Influence of Soil Parameters on Local Pier Scour Depth

By

Iqbal Singh Budwal

A thesis
presented to the University of Waterloo
in fulfilment of the
thesis requirement for the degree of
Master of Applied Science
in
Civil Engineering

Waterloo, Ontario, Canada, 2021

Author's Declaration

I hereby declare that I am the sole author of this thesis. This is a true copy of the thesis, including any required final revisions, as accepted by my examiners.

I understand that my thesis may be made electronically available to the public.

Abstract

Bridge scour is a phenomenon where erosion of the sediment bed surrounding bridge foundation occurs due to fluid forces arising from currents, waves, and turbulence. Scour around foundation components such as piers, piles and abutments may lead to structural instability and possible collapse. Scour has been documented as the leading cause of bridge failures; thus, the prediction, monitoring and mitigation of scour is paramount for safe and cost-efficient bridge design. The current methods of estimation of pier scour do not properly use information about soil parameters in the calculations. However, soil parameters among other factors play an important role in the scour process. Neglecting inputs of soil parameters leads to significant underestimation of pier scour depths and overtly expensive bridge foundation designs. To develop more accurate methods of scour prediction, parametric studies are required to systematically investigate the effects of soil parameters, such as grain size distribution, mineral composition, cohesion, angle of repose, and void ratio, and incorporate them in the scour prediction equations. Most published scour studies utilized scaled down laboratory experiments although there has been some limited research on scour using numerical simulations. Numerical studies on scour are less expensive and provide the opportunity to investigate a wide variety of scenarios through systematic parametric studies.

In this thesis, a comprehensive review on the existing bridge scour theories and scour estimation methods are made. Subsequently, numerical simulations of pier scour are performed using the software SSIIM. Parametric studies are conducted using SSIIM to quantify the influence of sediment parameters on pier scour and to provide recommendations on the most appropriate scour prediction methods. The review performed in this thesis covers the existing literature on scour including the controlling mechanisms and the scour types that occur at bridges. Relevant soil, fluid, and structural factors and their influence on scour are examined. The most influential soil parameters on scour were found to be the grain size, angle of repose, and cohesion. However, the only soil parameters currently considered by empirical methods is the grain size or gradation. Also discussed in detail are the common empirical equations used for estimating equilibrium scour depths and scouring rates. The review covers laboratory-scale studies, numerical modeling, and soft computing techniques, such as artificial neural networks, used to investigate scour. A brief discussion is made on scour monitoring techniques and countermeasures to mitigate scour.

Numerical simulations in this study were performed using the software SSIIM (Sediment Simulation in Intakes with Multiblock option). The ability of SSIIM to estimate pier scour was first investigated and the optimal modeling parameters required for accurate predictions of scour were determined. It was found that SSIIM was able to accurately model flow past piers with rigid beds and predict equilibrium scour depths with errors not exceeding 12.6% when compared to observed experimental scour depth.

A parametric study was subsequently conducted using SSIIM investigating the effect of soil parameters on pier scour depths. To cover a range of structure sizes, numerical domains were created with pier diameters set as 0.1 m, 0.25 m, 0.5 m, and 0.8 m. Each of the four piers were simulated with two flow intensities of 0.5 and 0.75 for a total of eight flow scenarios. Each flow scenario was simulated with 16 different types of soils for a total of 128 cases. The soils tested were clean sands with control parameters of a 1 mm grain size, 30° angle of repose, and 0 Pa cohesion. While two soil parameters were kept constant, the third was varied to investigate the influence on scour depth. The scour depths for ten grain sizes were examined to evaluate the performance of 12 empirical methods for predicting pier scour. Of the empirical equations examined, the TAMU (Texas A&M University) method was found to be the best scour depth prediction equation. The angle of repose was modeled using stable slope angles between 20° and 40°. Variation of the stable slope angle was found to vary scour depths by –41.9% to +145.1%. Cohesive strength was added to the sediment to simulate the presence of fines and was found to significantly impact scour depths. A cohesion of 0.5 Pa was enough to reduce scour depths by about 90%. The significant variations in scour depth as functions of angle of repose and cohesion highlighted the need for their inclusion in scour prediction equations and methods. Discussions on the SSIIM's numerical scour modeling established that the current numerical sediment models require improvement in their ability to capture soil behaviour based on the angle of repose and cohesion. Better sediment modeling and accurate numerical scour simulations are required for the development of accurate scour depth prediction models for safe and cost-efficient bridge designs.

Acknowledgements

I would like to thank my supervisor Dipanjan Basu for their advice and guidance throughout the research process. I also want to thank my family and friends for their support.

Table of Contents

List of Figures

List of Tables

List of Abbreviations

Abbreviation	Description
ANN	Artificial Neural Network
BPN	Back-Propagation Neural Network
CFD	Computational Fluid Dynamics
CSU	Colorado State University
DEM	Discrete Element Method
DES	Detached Eddy Simulation
EFA	Erosion Function Apparatus
FEM	Finite Element Method
FHWA	Federal Highway Administration
FVM	Finite Volume Method
GEP	Gene Expression Programming
GMDH	Group Method of Data Handling
GSN	Geotechnical Scour Number
HEC	Hydraulic Engineering Circular
OMS	Observation Method for Scour
PIV	Particle Image Velocimetry
RANS	Reynolds-Averaged Navier–Stokes
RQD	Rock Quality Designation
SIMPLE	Semi-Implicit Method for Pressure Linked Equations
SPH	Smoothed Particle Hydrodynamics
SRICOS	Scour Rate In Cohesive Soils
SSE	Sum Of Squares Error
SSIIM	Sediment Simulation In Intakes with Multiblock Option
TAMU	Texas A&M University
TDR	Time-Domain Reflectometry
UE	Underprediction Error

List of Symbols

Symbol	Definition	Units
c	Sediment Concentration	kg/m^3
D	Pier Diameter/Width	m
D_{50}	Median Grain Size, 50% Passing Grain Size	mm
D_{84}	84% Passing Grain Size	mm
D^*	Dimensionless Particle Diameter	
d_s	Scour Depth	m
ε	Rate Of Dissipation of Turbulent Kinetic Energy	m^2/s^3
Fr	Froude Number	
g	Acceleration Due to Gravity	m/s^2
H	Wave Height	m
I	Flow Intensity	
k	Turbulent Kinetic Energy	m^2/s^2
k_s	Wall Roughness	m
K_c	Keulegan–Carpenter Number	
L	Pier Length	m
σ_g	Gradation	
ρ_f	Fluid Density	kg/m^3
ρ_s	Soil Density	kg/m^3
Re	Reynolds Number	
s	Specific Gravity	
t	Time	s
t_e	Equilibrium Time	s
T	Wave Period	s
τ	Hydraulic Shear Stress	Pa
τ_b	Bed Shear Stress	Pa
τ_c	Critical Shear Stress	Pa
ϕ	Angle Of Repose	°
θ	Shields Parameter	
θ_{cr}	Critical Shields Parameter	-
u_*	Friction Velocity	m/s
μ	Dynamic Viscosity	Pa s

v	Kinematic Viscosity	m^2/s
v_t	Eddy Viscosity	m^2/s
V	Mean Flow Velocity	m/s
V_c	Critical Velocity	m/s
V_{cu}	Velocity Of Current	m/s
V_{lp}	Live-Bed Peak Velocity	m/s
V_w	Wave Induced Flow Velocity	m/s
V_{cw}	Wave-Current Velocity	m/s
V_x	Horizontal Velocity	m/s
V_z	Vertical Velocity	m/s
ω	Sediment Fall Velocity	m/s
x	Horizontal Distance from Pier	m
y	Flow Depth	m
$\dot{z}$	Erosion Rate	mm/hr
z	Elevation	m

Chapter 1: A Review on Bridge Scour in Geotechnical Engineering

1.0 Introduction

The importance of understanding the process and impacts of scour at bridges is essential for safe and efficient engineering design. Scouring is defined as the erosion or removal of sediment bed material around marine structures due to fluid forces. The scouring process over time weakens the lateral resistance of bridges and has been responsible for around 60% of bridge collapses (Lagasse 2007). Wardhana and Hadiprio (2003) investigated the causes of 500 bridge failures in the US between 1989 and 2000 to identify the primary causes. Flooding and scouring were the largest contributors and found to be responsible for 48.31% of the bridge failures. Significant scouring reduces effective foundation depths and expose foundation footings as shown in Figure 1.1.

Figure 1.1: Scoured bridge foundation (MTO 1997)

This Chapter discusses theory and methods used for predicting scour rates and equilibrium depths at bridge foundations. The interactions between soils, fluids and structures cause and control the scour phenomena. Researching the influences and interactions of factors stemming from the three elements is vital to understanding bridge scour. Experimental laboratory testing, numerical simulations, and various data-driven algorithms have been used to investigate how scouring occurs and the best practices for estimating scouring. Most current day techniques for

predicting scour are severely limited in their application and often lead to overly conservative designs to account for the inherent unpredictability of scour. Existing methods consider only a limited number of factors and are not applicable for complex foundation geometries, cohesive soils, rocks, and wave-current interactions. While the overall issue is accuracy, the primary knowledge gap is the understanding of how all soil parameters can influence scour. Methods currently used to predict scour depths are empirical formulae developed with limited data from laboratory experiments. Newer research techniques for scour estimation focus on using numerical tools to model full scale bridge scour to overcome scale effects. The primary focus of this review is bridge scour in channels which consists of contraction scour, local pier scour and local abutment scour. Long term channel degradation, lateral migration, and stream stability analysis are precursors to bridge scour analysis, therefore not within the scope of discussion. In addition to scouring depth predictions, there is a need for research into scour mitigation and monitoring technology at scour critical bridges. Both existing and newly researched techniques for scour monitoring and mitigation are reviewed for their accuracy and effectiveness. Some reviews on bridge scour have been conducted on literature published at the time (Deng and Cai 2010, Wang et al. 2017).

1.1 Scour Phenomena

This section discusses the types of scour occurring in channels at bridge sites along with the influencing factors. First a brief overview of the topics is covered, followed by the impacts of soil parameters, structure types, flow conditions, and other special considerations. Scouring is a subtopic within sediment transport, so the basic theories of sediment transport are summarized herein.

1.1.1 Scour Types

While scour is defined as the erosion of sediment beds due to flowing water, there are different types based on what is generating the erosive flows. The three types of scour occurring in channels are general scour, contraction scour, and local scour (Richardson and Davis 2001). Firstly, general scour occurs in all waterways with moving water regardless of the presence of any structure. General scour describes the long-term bed degradation and aggradation due to the removal and deposition of sediment by fluid forces. The amount of general scour will be

dependent on the soil parameters, channel geometry, water velocity and water depth. General scour is expected to have already occurred prior to the introduction of a bridge; thus, the channel bed is assumed as steady provided that flow conditions do not significantly change. Therefore, when considering the addition of a new bridge structure in a channel, contraction and local scouring together make up the total predicted scour. The second scour type is contraction scour which behaves as an increase in erosion of the channel bed near structures due to a reduction in channel width. The presence of bridge foundation structures constricts the flow resulting in an increase in water velocity and the additional kinetic energy results in deeper scouring at foundation structures. The factors controlling contraction scour are the same as those for general scour while considering the amplification of flow velocity due to a contraction. Figure 1.2 illustrates the process of contraction scour at channel embankments or abutments.

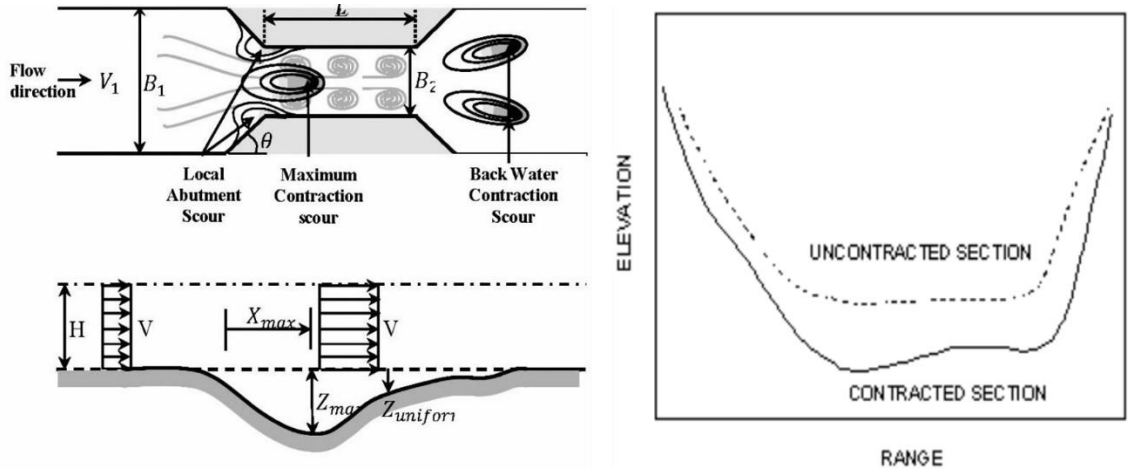

Figure 1.2: Flow and scouring at a contraction (MTO 1997)

The third type of scour, local scour, occurs adjacent to objects such as piers to form localized scour holes. Flow accelerates around and downwards at these obstacles to forms turbulent eddies which erode soil material. Local scour is the most complex type due to turbulence and requires the most future research into methods of prediction. Other structures vulnerable to local scour include abutments, pile groups, complex piers, spurs dikes, and cofferdams. Getting accurate predictions of localized scour around foundation components such as piers is paramount as it can significantly decrease effective depths and lateral structural stability. Severe scour cases can also increase the chance of buckling under vertical loading due to self-weight, vehicles, and snow (MTO 1997). For local scour flow at a circular pier in a channel, flow approaches the front

of the pile and accelerates around the pile and creates lee wake vortices downstream of the pier (Dargahi 1990). Local scour flow around a bridge pier is demonstrated in Figure 1.3.

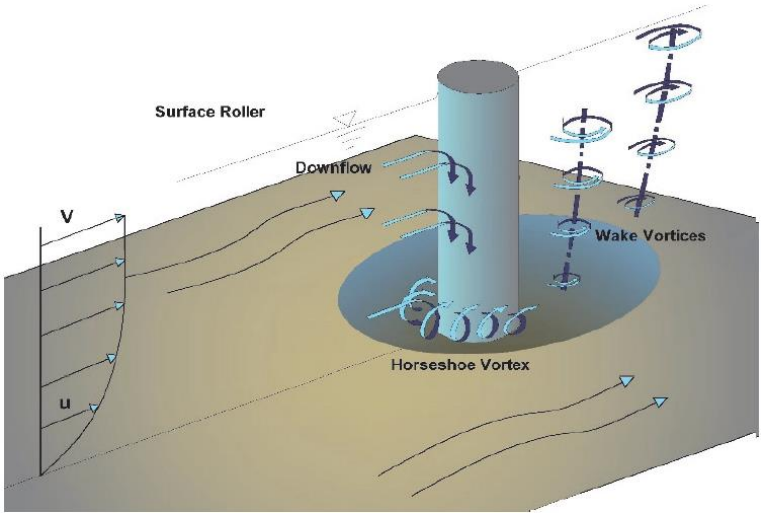

Figure 1.3: Flow and scour at single pier (Akib et al. 2014)

Before the scour hole is formed the upstream wake vortices start to erode soil material eventually resulting in the scour hole which will alter the flow conditions. As the scour hole starts to form in front of the pile, down flow into the hole will create horseshoe vortices which deepen the scour hole. The term horseshoe refers the how the vortices will wrap around the pier in a U-shaped formation (Dargahi 1990). The combination of the turbulent flow around the pile and into the hole both contribute to the formation of the scour hole. As with general and contraction scour, the amount of local scouring is dependent on the soil parameters, flow conditions and geometry of the structure. As the scour hole approaches maximum depth, the strength of the horseshoe vortices decreases, and once the shear stress exerted by the flow is less than the critical shear stress of the soil, maximum depth is achieved (Deng 2010). Local abutment scour has similar properties to that of local piers scour where flow acceleration and turbulent vortices develop a localized scour hole. The large-scale turbulence and scouring occurring at bridge abutments are illustrated in Figure 1.4.

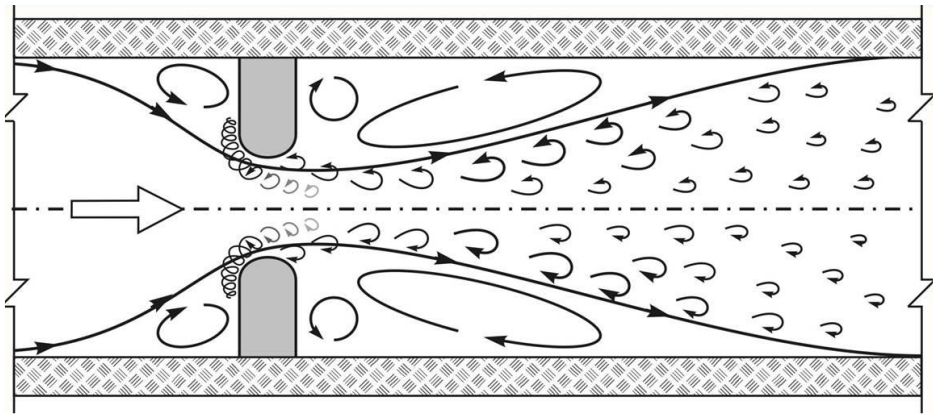

Figure 1.4: Flow and local scour at abutment (Richardson and Davis 2001)

Figure 1.4 illustrates the turbulent flow field with wake vortices and the primary vortices at the upstream face acting similar to horseshoe vortices occurring at piers. As with piers, the primary scouring agent is the upstream primary vortices and downwards flow occurring at the abutment sides (Melville 1992). Larger abutments also create channel contractions which increase flow velocity and thus the degree of scouring. In addition to the three types of scours, the sediment bed is said to be in one of two scour conditions. The bed is in the clear-water condition when there is no motion upstream of the structure. Thus, for clear water condition, no upstream material is transported, and no deposition is expected to occur at the scoured area. The other bed condition is live-bed scour in which there is active scouring occurring upstream thus, deposition may occur at the scoured site. Live-bed scour occurs if the upstream flow velocity, V, is larger than the critical velocity of the soil, V_c. The critical velocity of a soil is velocity at which sediment motion is incited, so if the flow velocity is less then the critical value then the bed is in a clear water state. Figure 1.5 depicts the general relationship recorded between live-bed and clear-water scour depths over time given steady flow conditions.

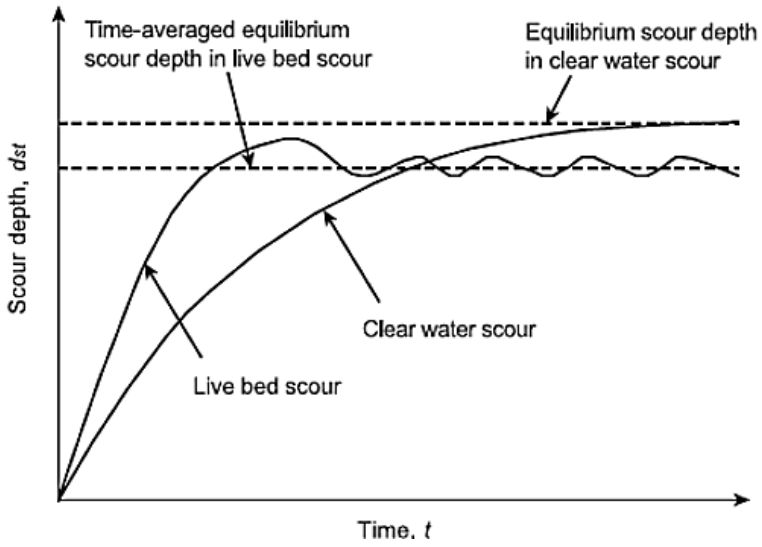

Figure 1.5: Live-bed and clear-water scour over time (Richardson and Davis 2001)

Although live-bed scour occurs at a higher velocity the accumulation of upstream deposits will decrease scour depth and may lead to a lower time-averaged equilibrium scour depth. For local scour, the maximum scour depth is expected to occur near threshold condition, where $V = V_c$, (Melville 1997). If flow velocity continues to increase past threshold conditions the depth will asymptotically approach a depth near the maximum depth at threshold conditions as shown in Figure 1.6 for local pier scour.

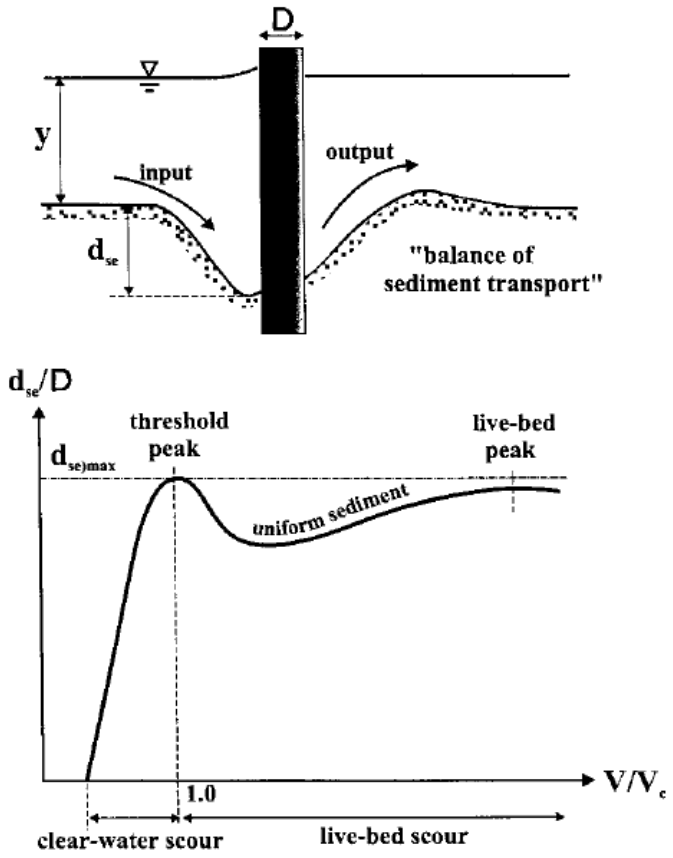

Figure 1.6: Live-bed and clear-water scour comparison on time (Melville 1999)

As the maximum scour depth is often near threshold conditions, most experiments are conducted with velocities at that level.

1.1.2 Soil Influences on Scour

In analyzing scour, a major consideration is the sediment bed and its soil parameters influencing its behaviour under fluid forces. Soils have many characteristics or factors impacting its general behaviour such as its median grain size, gradation, cohesion, shear strength, angle of repose, porosity, and many more. In scour research these parameters are factors influencing the erosive behavior by controlling a soil's critical shear stress, failure mechanism, armouring potential, erosion rate, and transport behaviour. Understanding the nature of scouring requires investigation into what fluid conditions erode particles, particle transport behaviour and particle to particle interactions. Most existing research on sediment transport and scour deal with coarse sands, though some findings have been made on scour in cohesive soil and rocks.

Firstly, a soils resistance to fluid shear forces must be quantified and comparable to applied fluid force to determine the state of sediment motion. Whether due to waves and/or currents, flowing water will exert a shear stress on the sediment bed which is further discussed in Chapter 1: Section 1.1.3. The shear stress at which sediment bed become mobile is termed the critical shear stress, τ_c. Describing critical shear stresses of soils starts with analyzing the all the force acting on a soil particle on a sediment bed. Early research into evaluating soil grains on stream beds consisted of conducting a force balance on individual grains (White 1940). Non-cohesive grains are under forces of gravity, grain to grain friction, and fluid shear forces. Motion is expected to occur once the fluid forces overcome gravity and granular frictional forces. In the case of clean sand, critical shear stress is primarily a function of the internal frictional angle which has also been referred to as the angle of repose. With clay and other soil types, the cohesive strength and other parameters must be considered to describe the critical shear stress. In the case of sediment resuspension and transport the most import parameters of the soils are its grain size and its density (Van Rijn 1993). To encapsulate the influence of viscosity, density and gravity on soil, the dimensionless particle diameter D^* is introduced with the following expression

$$D^* = [\frac{(s-1)g}{v^2}]^{1/3} D_{50} \tag{1.1}$$

where g is acceleration due to gravity, s is the specific gravity, v is the fluid viscosity and D_{50} is the median soil grain size (Van Rijn 1993). In order to find the critical shear stress or the threshold shear stress initiating movement of particles, the flow past the sediment needs to be analyzed. The fluid velocity needs to be large enough to overcome the shear strength to initiate motion and large enough to overcome gravity to suspend the particle. Thus, suspension of particles is a two-step process in which the lateral fluid forces surpasses lateral strength and secondly the vertical eddy velocity surpasses the particle falling velocity (Van Rijn 1993). The fluid forces exerted on a sediment particle are a combination of viscous shear skin friction and pressure forces. The pressure forces arise from pressure difference and are composed of lift and drag components. The forces acting on a single soil grain are illustrated in Figure 1.7.

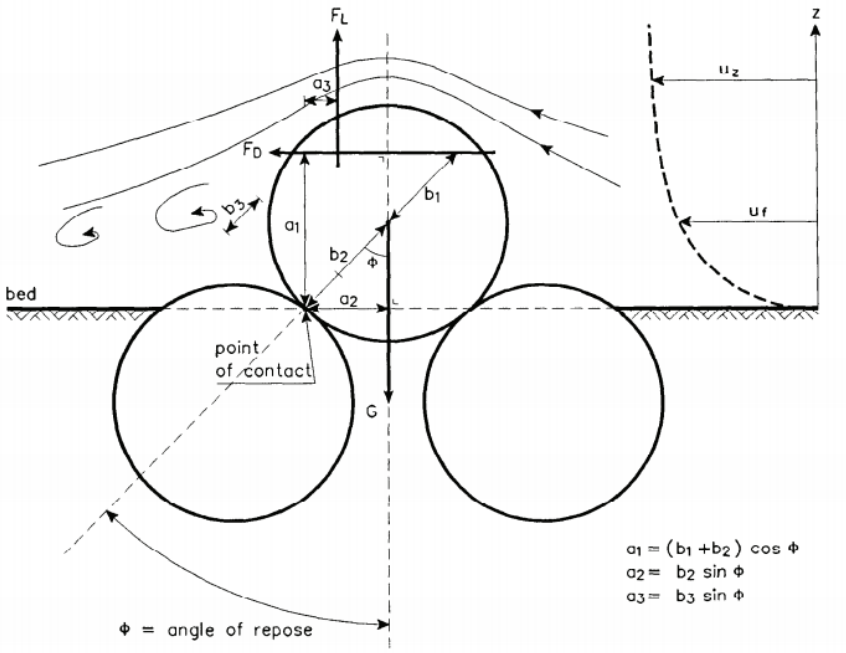

Figure 1.7: Forces acting on a bed sediment particle (Van Rijn 1993)

In Figure 1.7 the fluid velocity is directed to the left as indicated the by velocity profile and streamlines around the sediment. The acting forces due to gravity, G, lift, F_L, and drag, F_D, are illustrated along with the moment arms relative to a point of contact with a neighbouring particle. The angle of repose, ϕ, is measured from the channel bed normal to the point of contact of particles. The angle of repose is a function of both soil grain shapes and sizes. After flowing over the top of the sediment, Figure 1.7 illustrates that there is flow separation and the production of turbulent wake where the rotating streamlines are drawn. For small Reynold's number flow the viscous forces are strong and flow separation is less likely. For large Reynolds number flow the pressure forces dominate the viscous forces so there is slow separation and more turbulence. A moment balance was conducted on a sediment particle to derive closed form relations for determining when movement is initiated (Shields 1936). After conducting experiments, Shields (1936), was able to represent the forces acting on a sediment particle with a single parameter, referred to as the Shields parameter, θ. Motion was said to occur once θ was larger than or equal to the critical Shields parameter, θ_{cr}. The Shields parameter is defined using the following relationship

$$\theta = \frac{\tau_b}{(\rho_s - \rho_f) g D_{50}} \tag{1.2}$$

where ρ_s is the density of the soil, ρ_f is the fluid density, and τ_b is the bed shear stress (Van Rijn 1993). The Shields parameter represents the hydraulic conditions near the bed for a particular bed shear stress. Due to the variability in particle arrangement and size, empirical relationships were obtained from experiments for determining the critical Shields parameter in different situations. Bonnefille (1963) and Yalin (1971) were able to express the critical Shields parameter, θ_{cr}, in terms of the dimensionless particle diameter D^* with the following relationships,

$$\begin{aligned} \theta_{cr} &= 0.24D^{*-1} && \text{for} && 1 < D^* \leq 4 \\ \theta_{cr} &= 0.14D^{*-0.64} && \text{for} && 4 < D^* \leq 10 \\ \theta_{cr} &= 0.04D^{*-0.1} && \text{for} && 10 < D^* \leq 20 \\ \theta_{cr} &= 0.013D^{*0.29} && \text{for} && 20 < D^* \leq 150 \\ \theta_{cr} &= 0.055 && \text{for} && 150 < D^* \quad . \end{aligned} \tag{1.3}$$

While the relationships described in Equation (1.3) are useful they have high levels of uncertainty. Due to the empirical nature and limited soil data used to develop the relationship it should be used with caution. After obtaining the critical Shields parameter using Equation (1.2), the time-average critical bed shear stress, τ_c, can be obtained with the expression

$$\tau_c = \theta_{cr}(\rho_s - \rho_f)gD_{50} \quad . \tag{1.4}$$

The force balance displayed in Figure 1.7 was derived for a horizontal bed and needs to be corrected for the slope of the channel. Redoing the derivation of forces acting on a particle with the channel bed at angle α lead to the following formulation for critical bed shear stress,

$$\tau_c = \frac{sin(\phi - \alpha)}{sin(\phi)}\tau_{c,0} \tag{1.5}$$

where ϕ is the angle of repose and α is the channel bed downwards slope, and $\tau_{c,0}$ is the critical shear stress for a flat horizontal bed (Van Rijn 1993). The obvious limitation to using Shield's parameter is the lack of many soil parameters such as gradation, cohesion, water content, and shear strength, which can have a significant impact on scour. For non uniform soil, the various effects of gradation must be considered during scour analysis. The most common method for describing the effects of gradation on the critical shear stress of a soil is using the geometric standard

deviation. For soils the geometric standard deviation, is defined using the median grain size D_{50} and the 84% passing size D_{84} as

$$\sigma_g = D_{84}/D_{50} \tag{1.6}$$

where σ_g is used for expressing a soils shear strength and armouring capabilities. The armouring of a soil occurs after some sorting which leads to the removal of finer soil particles near the top of the bed resulting in a resilient and coarse armour layer. Raudkivi and Ettema (1985) investigated the influence of coarse armor layers on pier scour. They found that although armor layers usually assist in reducing scour, they can have an adverse impact in the armour break case. The case of armour break scour can occur where the entire armor layer is removed then finer unlaying material is eroded to a larger depth than had there been no sorting effects. Raudkivi and Ettema (1985) also provided empirical formulae based on laboratory experiments for estimating scour depth in armour layer soil as a function of soil grain sizes, flow properties and pier size.

In addition to the effects of grain size, the other soil parameters must be investigated. Coarse grain soils such as sands are the most understood when it comes to scouring behavior as they are the most common riverbed material. As sand does not experience any significant cohesive forces and erodes grain by grain, its shear strength against fluid forces is most significantly influenced by the median grain size (Richardson and Davis 2001). The lack of cohesion in sand also impacts the time-depth relationship of scour as equilibrium depth occurs rather quickly for a given flow state. Finer soils such as clay and silt possess a cohesive strength and other parameters such as plastic behaviour not exhibited by coarser soils. The cohesion between clay particles also leads to more complicated erosion patterns where scour holes are dug chunk by chunk as opposed to individual grains in sand. The cohesion leads to slower scour rates and smaller scour depths, thus equations developed for sands are usually conservative when applied to clay. The larger equilibrium depth times imply that understanding the depth-time relationships of scour is more important for cohesive soils. A comparison of local pier scouring in sand and clay is shown in Figure 1.8.

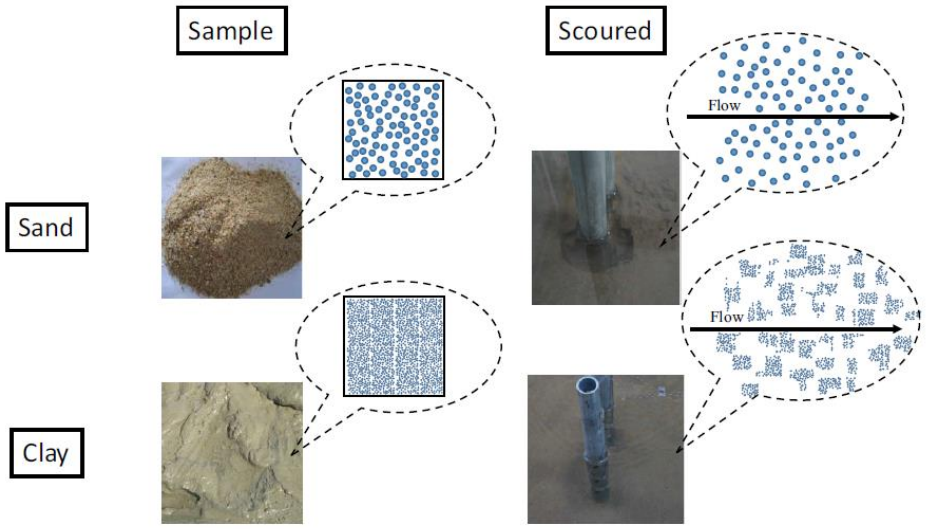

Figure 1.8: Difference between scour in sands and clays (Wang et al. 2017)

As seen in Figure 1.8, sands will be looser and transported as single grains while clay with cohesion will be transported as chunks of grains. Most existing methods of estimating scour account for median grain size, unit weight and gradation while neglecting other parameters. Other parameters such as cohesion, void ratio etc. are either too difficult to measure in field or research has not provided reliable representation of their influence on scouring. Briaud studied scour in cohesive materials including developing the SRICOS method (Briaud et al. 1999, Briaud et al. 2004, Briaud et al. 2005, Briaud et al. 2011) and the TAMU method for scour prediction (Briaud 2015a, 2015b). Briaud's research involved conducting a multitude of laboratory tests of local scour and contraction scour in cohesive material to determine the effects of soil parameters. The equations developed by Briaud are discussed in Section 1.2.2. Briaud et al. (2011) summarized many findings including the critical shear stress and critical velocity of a soil as a function of the grain size as displayed in Figure 1.9 and Figure 1.10.

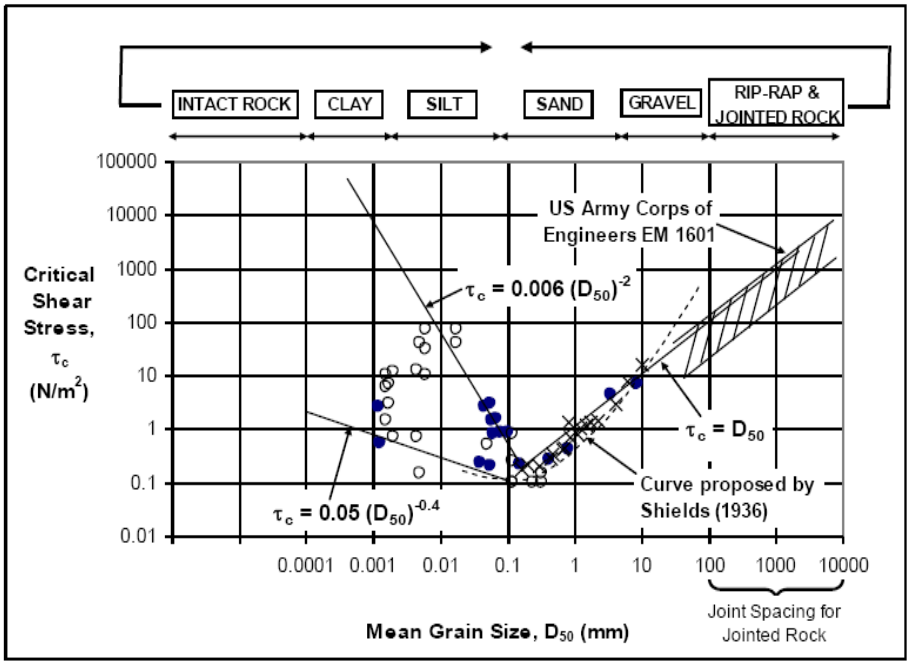

Figure 1.9: Critical shear stress as a function of mean grain size (Briaud et al. 2011)

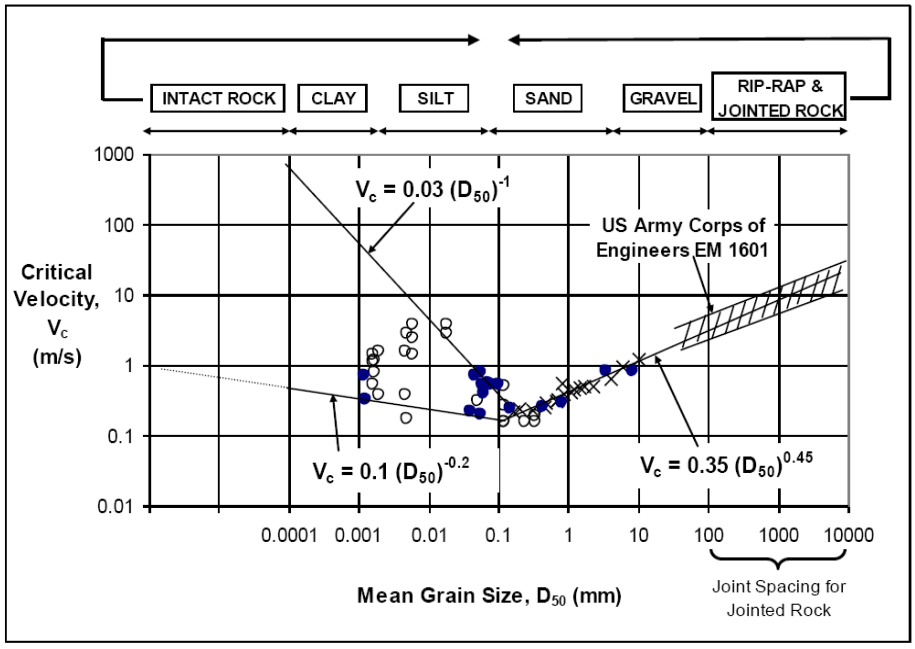

Figure 1.10: Critical velocity as a function of mean grain size (Briaud et al. 2011)

Figure 1.9 and Figure 1.10 display the different empirical relationships used to describe critical states of soil which are discussed in detail by Briaud et al. (2011). The critical shear stress of soils

versus grain size on a log plot formed a V-shaped relationship where a median grain size of 0.2 mm had the least resistance. This revealed that the as soil grains become larger than 0.2 mm their increase in self weight would overcome the fluid shear forces and lead to a larger value for critical shear stress. Interestingly as soils also got smaller than 0.2 mm in size Briaud found an increase in soil resistance against fluid shear stresses. The finer silts and clays saw an increase in cohesive forces leading to the increase in critical shear stress. Unlike clean coarse sands, soils with cohesion will experience slower scouring so their erosion rates become more important for depth predictions. With varying flow conditions and flood events, assuming a constant rate of erosion over long periods of time is not a reasonable assumption in cohesive soils and layered soil profiles. Briaud et al. (2011) created plots to describe the general erosion rates of different soil types from laboratory data which is shown in Figure 1.11 and Figure 1.12.

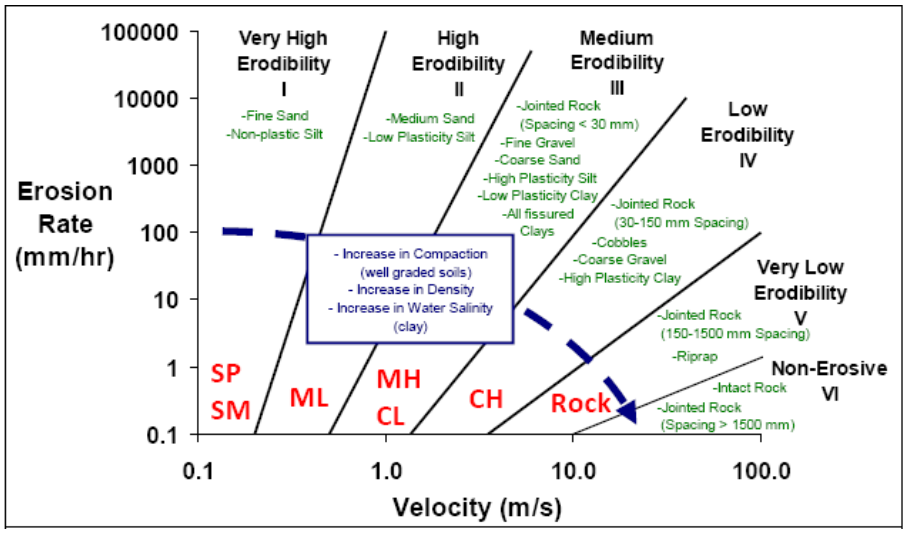

Figure 1.11: Erosion rates versus flow velocity for soils (Briaud et al. 2011)

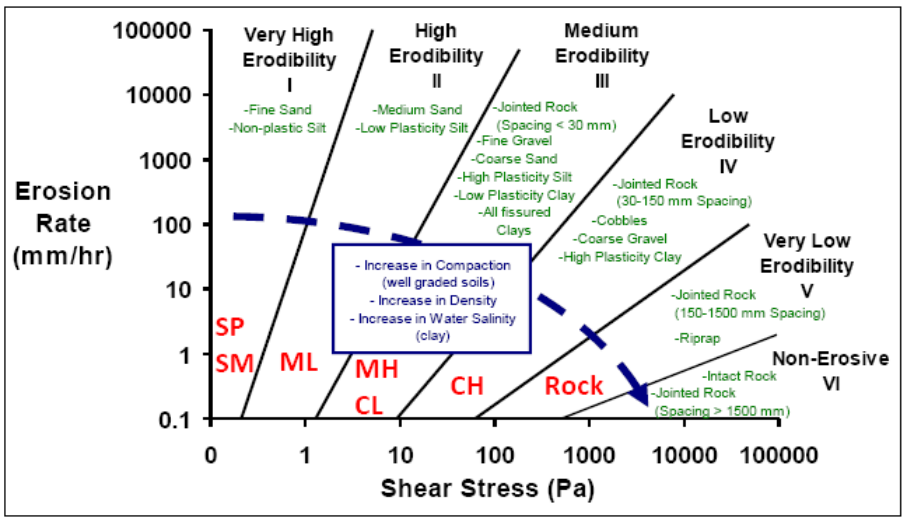

Figure 1.12: Erosion rates versus applied shear stress for soils (Briaud et al. 2011)

Richardson and Davis (2001) reviewed the findings of NCHRP reports on scour in the HEC-18 manual. These reports included investigations on the effect of many soil parameters on erosion. The general findings on how erodibility was impacted were summarized in Table 1.1.

Table 1.1: Soil factor influences on erosion (Richardson and Davis 2001)

When this Parameter Increases	Erodibility
Soil water content	*
Soil unit weight	decreases
Soil plasticity index	decreases
Soil undrained shear strength	increases
Soil void ratio	increases
Soil swell	increases
Soil mean grain size	*
Soil percent passing sieve #200	decreases
Soil clay minerals	*
Soil dispersion ratio	increases
Soil cation exchange capacity	*
Soil sodium absorption ratio	increases
Soil pH	*
Soil temperature	increases
Water temperature	increases
Water chemical composition	*
*unknown	

With some parameters, limited data can reveal contradictory relationships and a low level of confidence in correlations. The cohesion due to fines passing the #200 sieve has been recorded as describing erodibility as seen in Table 1.1. While it is understood that cohesion increase soil critical shear stresses and reduce scour there is not enough data to include cohesion as a factor in predicting scour. The complex nature of cohesion is why scour in clean sands is understood so

much better than finer soils. The variety of soil types and composition lead Briaud to develop a laboratory test to determine the erosion parameters of a soil sample obtained from the site of interest. Briaud et al. (2001a) described the development and use of the Erosion Function Apparatus (EFA). The EFA was developed for testing finer grains soils but is also applicable for coarser soils and soft rock. Briaud et al. (2001a) stated that for finer soils D_{50} was not enough to describe the critical shear stress. Therefore, tests replicating the in-field erosion conditions would provide more meaningful results. The EFA was meant to acquire a soil's critical shear stress and erosion rate as described by the erosion function. The erosion function is defined as the relationship between the erosion rate, $\dot{z}$, and the hydraulic shear stress, τ, as seen in Figure 1.13.

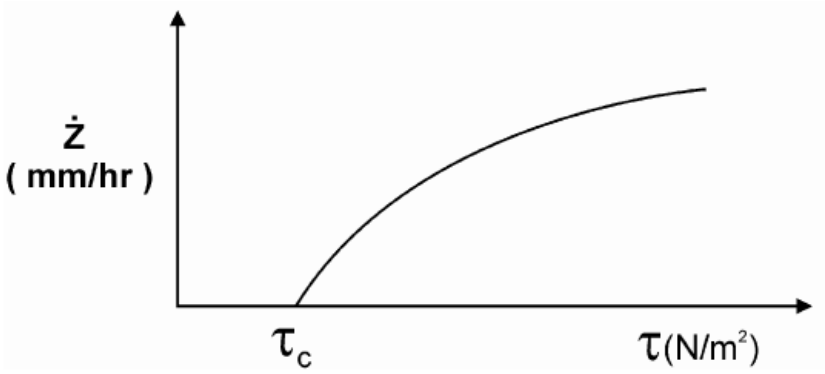

Figure 1.13: Erosion function plot from EFA (Briaud et al. 2001a)

The EFA was specifically developed for performing site specific scour prediction studies while minimizing sample disturbance. A photo and schematic drawing of the EFA is shown in Figure 1.14.

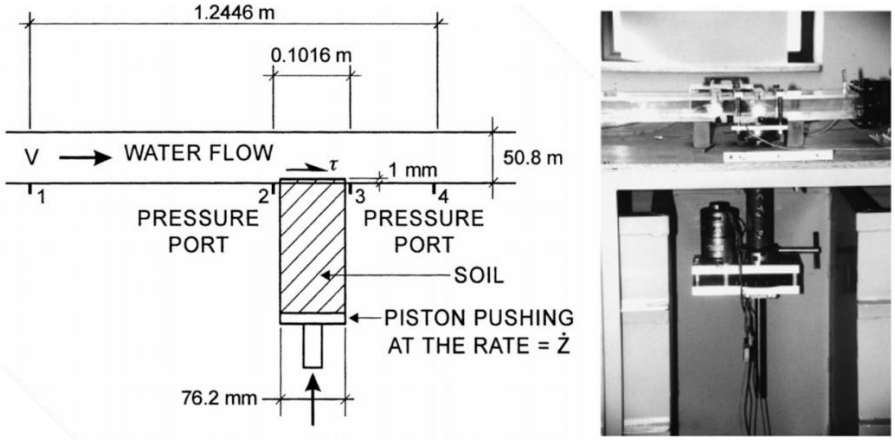

Figure 1.14: EFA detail (Briaud et al. 2001a)

The EFA consists of a Shelby tube which can be pushed into the soil to obtain a sample or have a soft rock core placed inside from the bridge site. The sample should of be taken close to the expected scour holes on site to be the most representative of in field soil conditions. The tube is then attached to the bottom of a rectangular pipe containing the eroding water flow driven by a pump. The sample is pushed into the channel such that only 1 mm protrudes and then a controlled water flow is ran through the pipe eroding the sample while monitoring how long it takes to erode. The sample is repeatedly pushed in in further with increasing flow velocities to plot the erosion function in Figure 1.13. Shear stress was obtained using the Moody chart as it proved more accurate for fine grained soils then manometers or transducers readings. As the water velocity is controlled and steadily increased through-out testing the plot also reveals the critical shear stress at which erosion for the sample begins. The shear stress would then be used with the actual channel dimension to calculate the critical velocity of the channel, and the expected erosion rate of the channel velocity. The maximum scour depth z_{max} is then calculated and inputted with the initial scour rate, $\dot{z}_i$, into a hyperbolic model describing the scour depth versus time curve, which is explained in the SCRICOS method (Section 1.2.2). The erosion rate of clean sands and gravels is measured in tens of thousands of mm/hours, while for finer soils the EFA reported rates ranging from 0.3 to 30 mm/hour. Some test on clays reveal that the increase of velocity changed the erosion of clays from grains to blocks as the higher shear stress was enough to dislodge larger blocks.

Although limited there had been other studies into the scour behaviour of soil types other than coarse sands. Debnath et al. (2007) researched the re-suspension and transportation of cohesive bedload. Rambabu et al. (2003) conducted experiments on pier scour in cohesive soil and found that higher shear strengths result in smaller scour depths. Experimental results were used to develop depth prediction equations as a function of the flow Froude number while not considering cohesion as an input. Debnath and Chaudhuri (2010a, 2010b) used some limited data of scour around cylinders in clay and clay-sand mixed beds to develop a predictive equation. The equation included soil factors such as clay content in the range of 20–100%, water content in the range of 20%–45.92% and the soil shear strength. Debnath and Chaudhuri (2010a, 2010b) found that higher clay content reduced both the width and depth of scour holes. Higher shear strength decreased scour depths while larger water content increased scour depths. Sonia Devi and Barbhuiya (2015) compiled a review on scour in cohesive soils while covering past literature, the influence of soil parameters and predictive equations. For beds composed of mixed sediments, ad

hoc engineering judgement is recommended alongside investigative soil testing with boreholes. In addition to mixed soil compositions, a bed maybe composed of a series of several layers. For layered beds, a step-by-step analysis on the scouring of each layer should be conducted to find the true equilibrium or maximum scour depths. Debnath and Chaudhuri (2010a, 2010b) investigated scour in layered profiles due to currents and Sumer et al. (2007) analyzed scour due to waves in layered profiles. Briaud et al. (2001b) discussed the application of the SRICOS method to multilayered soils and multi-flood flow events. Briaud et al. (2001b) discussed the importance of addressing scour in stages for accurate predictions.

Rock Scour

Due to bridge foundations being generally built-in soils, and the large variance in rock behaviour there is a limited number of methods for predicting rock scour. Rock scour is approached differently from soil due to its unique strength properties and failure mechanism during erosion (Richardson and Davis 2001). A continuously perfect rock could be defined by its mass strength, but the true strength is variable due to mineral compositions, crystal structures, and cracks. As opposed to grain-by-grain erosion for non-cohesive soils, and the erosion by chunks for cohesive soils, rock erosion involves a multitude of failure modes. For the case of layered soil profiles, a strong bedrock may act as a protective limiting layer for the overlaying soil. Scour in soft rocks may be approached with cohesive soil methods if adequate values for critical shear stresses and erosion rates are obtained through laboratory testing (Richardson and Davis 2001).

The American Federal Highway Administration (FHWA) Hydraulic Engineering Circular number 18 (HEC-18) manual discusses the compositions and classifications of rocks for the purposes of scour analysis (Richardson and Davis 2001). The information includes the different types of rock failure modes along with methods for quantifying rock strength and scour depth. In a case with constant flow conditions the equilibrium scour depth for sand may be achieved in hours, for clay it may take days to weeks, while for rock the process may range from months to years. Bridge foundations built in rock would require extension surveying including boreholes to identify the composition, orientation, and fractured state of rocks. Data from surveying would then allow a quantification of the rock's erosive strength using rating systems. The four modes of rock scour are dissolution of soluble rocks, cavitation, quarrying and plucking of durable jointed rock, and abrasion with grain-scale plucking of degradable rock. Soluble rock is not typically

going to dissolve in the engineering time of bridge foundations and cavitation is not likely to occur in typical natural channels. Thus, quarrying/plucking, and abrasion of rock have been investigated as the most probable failure modes to consider during scour analysis. The rock's resistance would then be compared to the stream power which characterizes the erosive potential of the flowing fluid to determine the resulting scoured depth.

Rock quality and strength quantification methods in the HEC-18 manual include the Erodibility Index Method (Annandale 1995) and the Rock Mass Rating System (Bieniawski 1989). The Rock Mass Rating System is used to describe the in-situ strength of rock using individual ratings of the intact strength of rock, the Rock Quality Designation (RQD), spacing of joints, condition of joints and groundwater conditions. The RQD is a parameter used to quantify a rock's degree of fracturing by examining the length of fractures from a drilled core sample. After obtaining a sample, the RQD is calculated as the ratio of the sum of rock piece lengths longer than 0.1 m to the total core length. The percentage values for RQD typically ranged from 5% to 100%, where a higher percentage indicates a higher quality of rock. Apart from RQD, the rocks on site would need to be tested for their compressive strength, joint status, and the present groundwater conditions. The numerical Rock Mass Rating is then calculated as the sum of the five relative ratings prescribed to the five categories aforementioned for which the ratings can be obtained from Table 1.2.

Table 1.2: Rock mass classifications (Richardson and Davis 2001)

PARAMETER	RANGES OF VALUES							
1. Strength of intact rock material	Point load strength index	>1,200 psi	600 to 1,200 psi	300 to 600 psi	150 to 300 psi	For this low range – uniaxial compressive test is preferred		
	Uniaxial compressive strength	>30,000 psi	15,000 to 30,000 psi	7,500 to 15,000 psi	3,600 to 7,500 psi	1,500 to 3,600 psi	500 to 1,500 psi	150 to 500 psi
Relative Rating		15	12	7	4	2	1	0
2. Drill core quality RQD	90% to 100%	75% to 90%		50% to 75%		25% to 50%	<25%	
Relative Rating	20	17		13		8	3	
3. Spacing of joints	>10 ft	3 to 10 ft		1 to 3 ft		2 in. to 1 foot	<2 in.	
Relative Rating	30	25		20		10	5	
4. Condition of joints	• Very rough surfaces • Not continuous • No separation • Hard joint wall rock	• Slightly rough surfaces • Separation <0.05" • Hard joint wall rock		• Slightly rough surfaces • Separation <0.05" • Soft joint wall rock		• Slickensided surfaces - or - • Gouge <0.2 in thick – or - • Joints open 0.05-0.2" • Continuous joints	• Soft gouge >0.2" thick - or - • Joints open >0.2" • Continuous joints	
Relative Rating	25	20		12		6	0	
5. Ground water conditions (use one of the three evaluation criteria as appropriate to the method of exploration)	Inflow per 30 ft tunnel length	None		<400 gallons/hr		400 to 2,000 gallons/hr	>2,000 gallons/hr	
	Ratio= joint water pressure/ major principal stress	0		0.0 to 0.2		0.2 to 0.5	>0.5	
	General Conditions	Completely Dry		Moist only (interstitial water)		Water under moderate pressure	Severe water problems	
Relative Rating		10		7		4	0	

After calculating the base Rock Mass Rating value, it is adjusted for joint orientation by summing it with the rating from Table 1.3.

Table 1.3: Joint orientation rating (Richardson and Davis 2001)

Orientations of Joints		Very Favorable	Favorable	Fair	Unfavorable	Very Unfavorable
Ratings	Tunnels	0	-2	-5	-10	-12
	Foundations	0	-2	-7	-15	-25
	Slopes	0	-5	-25	-50	-60

Lastly, the rock's quality description/class is obtained from Table 1.4 using the final adjusted Rock Mass Rating.

Table 1.4: Rock mass classes (Richardson and Davis 2001)

RMR (Note 1)	100 to 81	80 to 61	60 to 41	40 to 21	<20
Class No.	I	II	III	IV	V
Description	Very good rock	Good rock	Fair rock	Poor rock	Very poor rock

To quantify a rock's resistance specifically against erosion, Annandale (1995) proposed the Erodibility Index Method. Although the method were designed for both soils and rocks, only the rock portion is discussed herein. The rock erosion process of quarrying and plucking occurs when fluid force breaks apart jointed and fractured rocks. In addition to the hydraulic shear forces, rough boundaries with bridge foundations would create turbulent vortices intensifying the stress on rock beds. Water penetrating joints leads to hydrostatic pressure buildup which will also act as an erosive force. Blocks of rock would then be weakened, dislodged, and eventually displaced downstream. Continuous displacement of rock blocks leads to the formation of scour holes. The Erodibility Index, K, rates a rocks resistance to erosion by multiplying factors from standard tables using the equation

$$K = M_s K_b K_d J_s \tag{1.7}$$

where M_s is the earth mass strength factor, K_b is the block/particle size factor, K_d is the discontinuity/shear strength factor, and J_s is the relative orientation factor. The earth mass strength factor is a function of the unconfined compressive strength and is obtained from Table 1.5.

Table 1.5: Rock mass strength parameter M_s (Richardson and Davis 2001)

Hardness	Identification in Profile	Unconfined Compressive Strength (MPa)	Mass Strength Number (Ms)
Very soft rock	Material crumbles under firm (moderate) blows with sharp end of geological pick and	Less than 1.7	0.87
	can be peeled off with a knife; is too hard to cut triaxial sample by hand.	1.7 – 3.3	1.86
Soft rock	Can just be scraped and peeled with a knife; indentations 1 mm to 3-mm show in the	3.3 – 6.6	3.95
	specimen with firm (moderate) blows of the pick point.	6.6 – 13.2	8.39
Hard rock	Cannot be scraped or peeled with a knife; hand-held specimen can be broken with hammer end of geological pick with a single firm (moderate) blow.	13.2 – 26.4	17.70
Very hard rock	Hand-held specimen breaks with hammer end of pick under more than one blow.	26.4 – 53.0 53.00 – 106.0	35.0 70.0
Extremely hard rock	Specimen requires many blows with geological pick to break through intact material.	Larger than 212.0	280.0

The block size factor K_b is a function of joint spacing represented by the RQD and the number of joints sets represented by the joint set number J_n. A joint set is defined as a group of joints with the same dip and strike angle. The joint set number is obtained from Table 1.6.

Table 1.6: Rock joint set number J_n (Richardson and Davis 2001)

Number of Joint Sets	Joint Set Number (J_n)
Intact, no or few joints/fissures	1.00
One joint/fissure set	1.22
One joint/fissure set plus random	1.50
Two joint/fissure sets	1.83
Two joint/fissure sets plus random	2.24
Three joint/fissure sets	2.73
Three joint/fissure sets plus random	3.34
Four joint/fissure sets	4.09
Multiple joint/fissure sets	5.00

After determined the values for RQD and J_n, the block size factor, K_b, is calculated using the equation

$$K_b = \frac{RQD}{J_n} \quad . \tag{1.8}$$

The discontinuity/shear strength factor K_d represents the shear strength at the discontinuities in rock as a function of joint wall roughness, J_r, and the degree of joint wall alteration, J_a. Alterations in rock refers to the amendments of the rock surfaces from weathering or the presence of cohesive material in-between joints. Values for J_r and J_a are listed in Table 1.7 and Table 1.8 respectively.

Table 1.7: Joint roughness number J_r (Richardson and Davis 2001)

Condition of Joint	Joint Roughness Number J_r
Stepped joints/fissures	4.0
Rough or irregular, undulating	3.0
Smooth undulating	2.0
Slickensided undulating	1.5
Rough or irregular, planar	1.5
Smooth planar	1.0
Slickensided planar	0.5
Joints/fissures either open or containing relatively soft gouge of sufficient thickness to prevent joint/fissure wall contact upon excavation	1.0
Shattered or micro-shattered clays	1.0

Table 1.8: Joint alteration number J_a (Richardson and Davis 2001)

Description of Gouge	Joint Alteration Number (J_a) for Joint Separation (mm)		
	1.0 (1)	1.0 –5.0(2)	5.0(3)
Tightly healed, hard, non-softening impermeable filling	0.75	-	-
Unaltered joint walls, surface staining only	1.0	-	-
Slightly altered, non-softening, non-cohesive rock mineral or crushed rock filling	2.0	2.0	4.0
Non-softening, slightly clayey non-cohesive filling	3.0	6.0	10.0
Non-softening, strongly over-consolidated clay mineral filling, with or without crushed rock	3.0	6.0**	10.0
Softening or low friction clay mineral coatings and small quantities of swelling clays	4.0	8.0	13.0
Softening moderately over-consolidated clay mineral filling, with or without crushed rock	4.0	8.00**	13.0
Shattered or micro-shattered (swelling) clay gouge, with or without crushed rock	5.0	10.0**	18.0
Note: (1) Joint walls effectively in contact. (2) Joint walls come into contact after approximately 100-mm shear. (3) Joint walls do not come into contact at all upon shear. **Also applies when crushed rock occurs in clay gouge without rock wall contact.			

The discontinuity/shear strength factor K_d is calculated using the equation

$$K_d = \frac{J_r}{J_a} \tag{1.9}$$

where J_r is the joint wall roughness and J_a is the degree of joint wall alteration. The relative orientation factor, J_s, describes the erosive impact of the dip and strike of the rock relative to flow orientation. The factor specifically uses the material unit, dip, and dip direction of the weakest discontinuity relative to the flow direction. Rocks dipped against the flow are not eroded as easily as those dipped in the flow direction because flow cannot penetrate under to dislodge blocks. The shape of material unit refers the ratio of length to width between joints, *r*, where a larger ratio or length results in more resistance. This occurs because longer blocks are more difficultly removed than equisized blocks by flow. The relative orientation factor, J_s, is obtained from Table 1.9 using the dip direction, dip angle and ratio of joint spacing.

Table 1.9: Relative orientation parameter J_s (Richardson and Davis 2001)

Dip Direction of Closer Spaced Joint Set (degrees)	Dip Angle of Closer Spaced Joint Set (degrees)	Ratio of Joint Spacing, r			
Dip Direction	Dip Angle	Ratio 1:1	Ratio 1:2	Ratio 1:4	Ratio 1:8
180/0	90	1.14	1.20	1.24	1.26
In direction of stream flow	89	0.78	0.71	0.65	0.61
In direction of stream flow	85	0.73	0.66	0.61	0.57
In direction of stream flow	80	0.67	0.60	0.55	0.52
In direction of stream flow	70	0.56	0.50	0.46	0.43
In direction of stream flow	60	0.50	0.46	0.42	0.40
In direction of stream flow	50	0.49	0.46	0.43	0.41
In direction of stream flow	40	0.53	0.49	0.46	0.45
In direction of stream flow	30	0.63	0.59	0.55	0.53
In direction of stream flow	20	0.84	0.77	0.71	0.67
In direction of stream flow	10	1.25	1.10	0.98	0.90
In direction of stream flow	5	1.39	1.23	1.09	1.01
In direction of stream flow	1	1.50	1.33	1.19	1.10
0/180	0	1.14	1.09	1.05	1.02
Against direction of stream flow	-1	0.78	0.85	0.90	0.94
Against direction of stream flow	-5	0.73	0.79	0.84	0.88
Against direction of stream flow	-10	0.67	0.72	0.78	0.81
Against direction of stream flow	-20	0.56	0.62	0.66	0.69
Against direction of stream flow	-30	0.50	0.55	0.58	0.60
Against direction of stream flow	-40	0.49	0.52	0.55	0.57
Against direction of stream flow	-50	0.53	0.56	0.59	0.61
Against direction of stream flow	-60	0.63	0.68	0.71	0.73
Against direction of stream flow	-70	0.84	0.91	0.97	1.01
Against direction of stream flow	-80	1.26	1.41	1.53	1.61
Against direction of stream flow	-85	1.39	1.55	1.69	1.77
Against direction of stream flow	-89	1.50	1.68	1.82	1.91
180/0	-90	1.14	1.20	1.24	1.26

Notes:
1. For intact material take $J_s = 1.0$.
2. For values of r greater than 8 take J_s as for r = 8.
3. If the flow direction FD is not in the direction of the true dip TD, the effective dip ED is determined by adding the ground slope to the apparent dip AD: ED = AD + GS

The rock strength as evaluated by the Erodibility Index Method or the Rock Mass Rating System are used in scour depth predictive equations. The equations for depth prediction are further discussed in Section 1.2.1.

1.1.3 Fluid Flow Influences on Scour

As discussed in Section 1.1.2, soil parameters were used to describe the critical shear stresses, critical velocities, erosive parameters, and failure mechanisms. Thus, fluid flow properties must be used to describe the shear stress exerted on the sediment bed and its capacity for sediment transport. In the cases of contraction and local scour the flow acceleration and turbulent vortices generation will amplify bed shear stresses and change the sediment transport behaviour of the flow.

Currents

Most scour research has been focused on current generated scour occurring at bridges in rivers and channels. Scour in coastal areas would need to consider the effect of waves and wave-current interactions which is discussed later in this section. The fluid factors to consider are density, viscosity, and the acceleration due to gravity acting on the fluid. The simplest factors of the flow to consider is the depth and velocity in currents. In the process of dimensional analysis for developing equations predicting scour, factors are arranged in non-dimensional forms. For scouring, a factor of interest is the flow intensity, *I*, which is calculated using the expression

$$I = \frac{V}{V_c} \tag{1.10}$$

where V is the mean flow velocity and V_c is the critical velocity of the soil (Sheppard and Miller 2006). The flow intensity describes the bed condition as live bed when greater than one or clear water if less than one. A common non-dimensional flow factor is the Reynolds number, R_e, which for a pier can be found using the expression

$$R_e = \frac{DV}{\nu} \tag{1.11}$$

where D is the pier width as the length scale, V is the mean flow velocity as the velocity scale, and ν is the kinematic viscosity. Larger Reynolds numbers indicate higher turbulent levels whereas lower values characterize laminar flow. In addition to structures such as piers, R_e can be used to

describe the turbulence around soil with a grain size length scale and at vortices using vorticity sizes as length scales. The formation of the bed shape can alter local flow conditions and thus the amount of local scour. The existence and shape of upstream dunes can accelerate flow approaching piers and result in deeper scour (Sheppard and Miller 2006). The formation of dunes can be attributed to several factors, one of which being the Froude number. The Froude number, F_r, is the ratio of flow inertia to gravity defined as,

$$F_r = \frac{V}{\sqrt{gy}} \tag{1.12}$$

where V is the mean flow velocity as the characteristic velocity, g is the acceleration due to gravity as the externally acting field, and y is the water depth as the characteristic length. A flow with a Froude number larger than one is classified as supercritical and a flow with a Froude number smaller than one is classified as subcritical. For a given mean velocity, V, a Froude number of 1.0 indicates a length termed the critical depth, y_c. Subcritical flow would result in dune formations in the bed form and supercritical flow would result in antidune formation in the bedform. Van Rijn (1993) discusses in detail the formations of dunes and the different bed conditions which can exist. As bed shape and dunes impact the near bed velocities and bed shear stresses it is a factor to consider when predicting scour.

Using basic channel flow theory, the velocity profile and bed shear stresses can be expressed. To determine the bed shear stress, examine the basic representation of shear stress in a fluid as modeled by Newton's Law of friction

$$\tau = \mu \frac{du}{dz} \tag{1.13}$$

where τ is the shear stress, $\frac{du}{dz}$ is the velocity gradient in the fluid layer, and μ is the dynamic viscosity of the fluid. The fluid viscosity is a function of temperature and pressure. The dynamic viscosity, υ, can be related to the fluid's kinematic viscosity by the relationship

$$\upsilon = \frac{\mu}{\rho_f} \tag{1.14}$$

where ν is the kinematic viscosity and ρ_f is the fluid density. Shear stresses in open channels are a function of the fluids viscous properties, channel dimensions and fluid velocity. In a channel the no-slip boundary condition is assumed as seen in Figure 1.15.

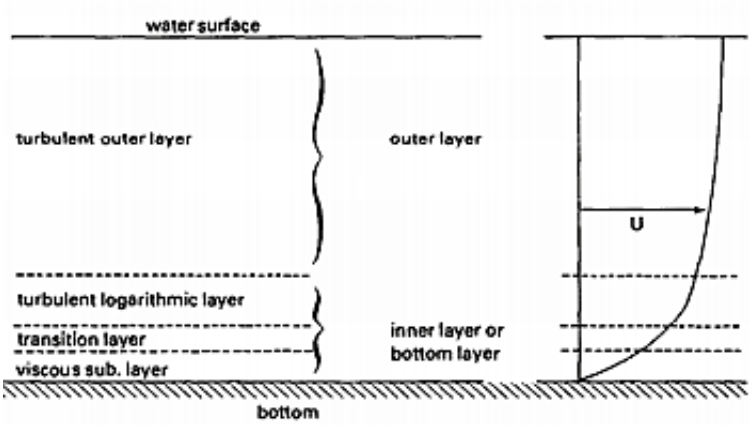

Figure 1.15: Open channel flow profile (Van Rijn 1993)

Figure 1.15 displays the different layers of flow occurring in a channel and the expected velocity profile shape. The shear stress in a fluids viscous sublayer is modeled by Equation (1.13). In a channel with a perfectly smooth bed, the flow could be treated as laminar, but the roughness of sediment will produce turbulence which will be proportional to the degree of roughness. The amount of turbulence is dependent on the ratio of inertial forces to viscous forces. Any turbulence will indicate that there are eddies forming and the swirling flow in these eddies contributes to the suspension of sediment particles. The viscous sublayer transitions into the turbulent log layer which has shear stress governed by the following relationship

$$\tau = \rho_f \upsilon_e \frac{du}{dz} \tag{1.15}$$

where ν_e is the eddy viscosity and ρ_f is the fluid density (Van Rijn 1993). Equation (1.15) looks very similar to Equation (1.13), but it uses the kinematic eddy viscosity based on turbulent theory. Past experiments have revealed that the turbulent log layer behaviour dominates the fluid shear stresses for a channel. To find the kinematic eddy viscosity, a characteristic velocity, u_*, was introduced which has also been referred to as the friction velocity or shear velocity in literature. In turbulent flow the velocity field is complicated and variable, so the characteristic velocity can

be used to describe the average velocity in turbulent flow. The characteristic velocity is related to the velocity gradient by the following relationship

$$u_*{}^2 = \upsilon_e \frac{du}{dz} \quad . \tag{1.16}$$

Next, Equation (1.16) was substituted into Equation (1.14) to obtain the following expression,

$$\tau = \rho_f u_*{}^2 \tag{1.17}$$

where the shear stress is expressed in terms of the characteristic velocity, u_*. In river systems, the energy was evaluated to obtain the following closed form formula for the characteristic velocity,

$$u_* = (g\ y\ sin(\alpha))^{1/2} \tag{1.18}$$

where *g* is acceleration due to gravity, *y* is the water depth and α is the slope of the channel. In the case of the open channels, Equation (1.18) can simply be substituted into Equation (1.17), to obtain the bed shear stress, τ_b, as

$$\tau_b = \rho_f\ g\ h\ sin(\alpha) \quad . \tag{1.19}$$

Equation (1.19) is applicable only for open channels or rivers, for a more general case Prandtl's hypothesis is used to relate the characteristic velocity to the kinematic eddy viscosity using the following relationship

$$\upsilon_e = k u_* z \tag{1.20}$$

where *k* is the Von Karman constant equal to 0.4, and *z* is the distance above the bed. This relationship states that the level of turbulence is proportional to the distance above the bed of the point of interest. Then by substituting Equation (1.20) into Equation (1.17), and integrating with respect to u and z the following formula is obtained

$$u = \frac{u_*}{k} ln(z) + C \tag{1.21}$$

where C is the constant of integration which was set as $-ln(z_0)$, and z_0 is the roughness length. The roughness length is the proportional to the thickness of sediments on the bed and represents the *z*

value at which velocity is zero. This leads to the general expression for velocity distribution over depth as

$$u = \frac{u_*}{k} ln(\frac{z}{z_0}) \tag{1.22}$$

(Van Rijn 1993). The type of flow occurring is dependent on the roughness of the bed and Figure 1.16 shows the velocity profile for smooth and rough flow cases.

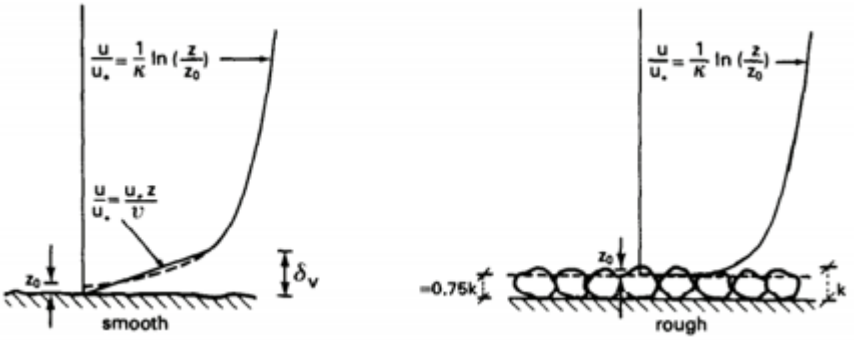

Figure 1.16: Channel velocity profile (Van Rijn 1993)

This velocity distribution was found for the log layer and describes the entire flow depth for fully developed flow. The average velocity over the depth $\bar{u}$ is obtained by integrating Equation (1.22) and dividing by the water depth to obtain,

$$\bar{u} = \frac{u_*}{k}\left[\frac{z_0}{y} - 1 + ln(\frac{y}{z_0})\right] \tag{1.23}$$

where y is the water depth. A new parameter called the Nikuradse roughness, k_s, is introduced to find z_0. The Nikuradse roughness is found from conducting a grain size analysis on samples of soil sediment. In literature there have been numerous formulas developed for the Nikuradse roughness as functions of water body dimensions, surface materials and grains sizes. In the cases of open channel flow, Nikuradse roughness may be approximated as D_{50} which is the sieve size at which half the soil passes through or the median grain diameter. It can also be argued that D_{84} is a better representation because the larger grains will sit higher resulting in a larger influence on the amount of turbulence (Cheng 2015). For hydraulically smooth flow, the size of the roughness is very small compared to the viscous sublayer thickness, thus the roughness does not affect the velocity distribution (Van Rijn 1993). The equation for z_0 is,

$$z_0 = 0.11\frac{\nu}{u_*} \qquad \text{for} \qquad \frac{u_* k_s}{\nu} \leq 5 \quad . \tag{1.24}$$

For the case of hydraulically rough flow, the roughness is so large that the viscous sublayer does not exist, and the fluid viscosity has no impact on the velocity distribution, only the eddy viscosity does. The following relationship describes the location of the zero-velocity level in hydraulically rough flow,

$$z_0 = 0.033k_s \qquad \text{for} \qquad \frac{u_* k_s}{\nu} \geq 70 \quad . \tag{1.25}$$

The third flow regime is hydraulically transitional flow where both roughness and fluid viscosity impact the velocity distribution as seen in the following equation

$$z_0 = 0.11\frac{\nu}{u_*} + 0.033k_s \qquad \text{for} \qquad 5 < \frac{u_* k_s}{\nu} < 70 \tag{1.26}$$

(Van Rijn, 1993). Instead of examining just the mean flow velocity of a channel with the resulting bed shear stress, the stream power of a channel is used for scour calculations in rock (Richardson and Davis 2001). The stream power describes the rate of energy dissipation or work done by the stream on the channel bed. The stream power used in conjunction with rock erosive strength rating methods for estimating the scour depth in rock. The stream power can be expressed using different variables as shown in the following equation

$$P = \gamma q S = \gamma q \Delta E = \tau V \tag{1.26}$$

where P is the instantaneous stream power, γ is the unit weight of water, q is the unit discharge, S is the slope of the energy grade line, ΔE is the energy loss per unit distance, τ is the representative shear stress, and V is the representative velocity. When the stream power is expressed using the shear stress and velocity, the values chosen must be representative of the location being evaluated for local scour. For the cases of local scour at piers, equations have been developed to specially calculate the pier stream power at the upstream face. Based on rock properties a critical stream power can be defined and then compared to the pier stream power to attain the degree of scouring. The stream would erode the rock at the pier and as the depth increase the pier stream power decreases until it is less than the critical stream power at which the equilibrium scour depth is achieved (Richardson and Davis 2001).

The basics of flow in channels understood very well regarding the turbulent boundary layer development and log velocity profile. The complexities in flow arise in contraction scour and especially local scour where flow becomes significantly turbulent, and vortices impact the bed shear stress and sediment transport. Research into flow effects on scour are often conducted in lab settings with different techniques and equipment to visualize the turbulent processes. As these complex flows are dependent on the structural obstructions, further discussion is made in Section 1.1.4. Experiments have generally consisted of scaled down flume tests where various equipment is used to measure velocity fields, measure bed shear stresses and track particle paths. Dargahi (1990) investigated the controlling mechanism of scour by experimentally analyzing the horseshoe vortex and wake vortices. Dargahi (1990) found that varying roughness of bed soil grains influences the water boundary layers and thus also affects the formation of the vortices conducting scour. Dargahi (1990) also describes in detail the three phases of scour as initial scour, primary scouring, and then gradual reduction with the cyclic horseshoe and wake vortex sheading over time.

Unlike deterministic factors such as structural dimensions, the true soil and flows conditions are actually probabilistic. With limited site soil samples and estimates of mean flow velocities, scour predictions are often conducted with approximations and averages. To simplify the stochastic problem, many design methods are frequently overly conservative to account for unknowns. However, the case can occur where a deterministic formula under predicts scour leading to structural instability due to unexpected soil bed weakness or intense flood conditions. Brandimarte et al. (2006) conducted a stochastic flow analysis which couples a synthetic river flow simulation technique with a cohesive soil model. The analysis used historical flow records to create hydrologic series with the same statistical properties as observed flows to perform probabilistic design and risk analysis of bridge foundations exposed to scour. Briaud et al. (2007) investigated the probability of scour depth predictions being exceeded due to hydrologic uncertainty. Briaud et al. (2007) continued the work of Brandimarte et al. (2006), using historical data to create thousands of future velocity hydrographs all equally likely to occur. Using the future velocity hydrographs and SRICOS method (Section 1.2.2), scour depths are calculated and analyzed for the probability of a depth being exceeded. Briaud et al. (2014) continued their investigation of statistical, risk, and reliability analyzes of bridge scour. Briaud et al. (2014) used scour databases to quantify statistical parameters relating the scatter between predicted and

measured scour depths. Then the parameters were used to develop a reliability-based load and resistance factor (LRFD) design for shallow and deep foundations subjected to scour. Khalid et al. (2019) performed a reliability-based assessment of live bed scour at bridge piers the using Sheppard and Miller (2006) equations combined with a first-order reliability method (FORM) reliability analysis. Factors such as the pier diameter, flow depth, flow velocity and median soil grain size were analyzed for their mean values and coefficients of variation (COV). Results revealed flow velocity to be the most dominant variable and the flow depth the least influential for scour depths. Results were also used to develop an equation for safety factors in terms of a reliability index based on the variability of factors.

Waves

In the case of structures located in coastal areas, scour occurs due to waves and wave-current combined flow. Waves generated due to gravity and wind will influence the flow field and thus also the bed shear stresses, and sediment transport occurring around structures. Waves mixed with currents result in very complex flow fields and bed conditions with cyclic properties of erosion and deposition. The analysis of wave scour involves using the kinetic and potential energy within waves along with wave characteristics as factors for methods predicting the scour depth. In addition to flow depth, y, and mean flow velocity of current, V_{cu}, wave factors for scour include the wave induced flow velocity, V_w, wave period, T, wave height, H, and wavelength, L (Wang et al. 2017). A common non-dimensional number used in wave scour research is the Keulegan–Carpenter number, K_c, which is defined as

$$K_c = \frac{V_w T}{D} \tag{1.27}$$

where T is the wave period, D is the length scale such as pier width, and V_w is the maximum velocity of the undisturbed wave-induced oscillatory flow. The Keulegan–Carpenter number describes the relative strength of drag forces over inertia forces for bluff objects in oscillatory fluid flow (Sumer et al. 2000). Different cases of wave-current interactions include waves following current, waves opposing currents, waves perpendicular to currents or any relative direction in between. Simpler and conservative methods for predicting scour in waves involve combining the current velocity, V_{cu}, with the wave velocity, V_w, to obtain an equivalent wave-current velocity,

V_{cw}, to use in traditional scour equations like those in Section 1.2. The difficulty in obtaining an appropriate value for V_{cw} is the non-linearity in wave-current interactions.

Sumer et al. (1992a) ran experiments of wave scour around single piles to formulate a scour depth prediction equation. The lee wake and horseshoe vortices were the primary scouring agents, and their development was mainly dependent the on Keulegan-Carpenter number. Further examining of K_c values revealed that for values of $K_c<6$ scour was negligible and increasing K_c deepened scour depths until $K_c=100$ where scour depth become steady state. Sumer et al. (1992b) examined the time scale of pile scour hole evolution and the importance of boundary layers on the velocities and bed shear stresses. Sumer et al. (1993) expanded on their prior research and scour depth equation to include square piles cross sections and the flow angle of attack. Sumer and Fredsoe (1998) experimented with wave scour at various group piles arranged side-by-side, in tandem, triangular groups, and square groups. Different pile spacings and K_c values were tested for influence on scour depths. Sumer et al. (2000) conducted a review on scour around coastal structures while covering sediment transport, non-linear waves, wave-induced pore pressure on soil, wave kinematics, soil liquefaction, wave steepness effects on scour, scour protection methods, and numerical modeling of coastal flow around piles. Sumer et al. (2000) stated that scour in linear waves can be determined as function of K_c while for non-linear waves a coefficient was required to describe asymmetry of wave velocity. Sumer and Fredsøe (2001) performed rigid and mobile bed experiments at a large diameter cylinder with progressive waves. Scour at a 1 m diameter cylinder was found to increase with K_c and the diffraction parameter, D/L, where D is the pier diameter and L is the wavelength. Sumer et al. (2007) investigated soil influence with live-bed wave scour experiments with a pile in sand, medium density silt, and high-density silt. Tests ranged in K_c values of 0 - 20, and results showed scour to be 1.6 - 2.0 times deeper and faster in dense silt when compared to medium density silt and sand. Babu et al. (2003) also performed flume experiments of wave scour around single piles in cohesive silty-clay sediment. Pile diameters ranged between 50 mm - 110 mm and flows tested were varying combinations of different waves properties and current velocities. Parametric studies were performed on the scour depths and its non-dimensional factors such as the Froude number which is a major dynamic factor causing movement of soil particles. The other factors tested were the wave steepness, $H/$L, which influences local vertical flows lifting sediments from bed and the Ursell parameter, $U_p=HL^2/D^3$, which signifies the magnitude of wave energy transmitted to the soil bed. Scour depth prediction

equations were developed using the non-dimensional factors. Zanke et al. (2011) performed experiments on wave-current scour in non-cohesive sediments and developed a depth equation as a function of K_c ranging from 6 - 105 and flow intensity, I, ranging from 0.6 - 4.5. Qi and Gao (2014) examined wave and current scour at large diameter monopiles while focusing on the effects of wave induced pore pressure. In addition to eroding and transporting sediment, fluid can influence scour through seepage flow within the bed. Figure 1.17 shows wave-induced upward seepage surrounding monopiles which can lower the soil's buoyant unit weight thus increasing the degree of scouring.

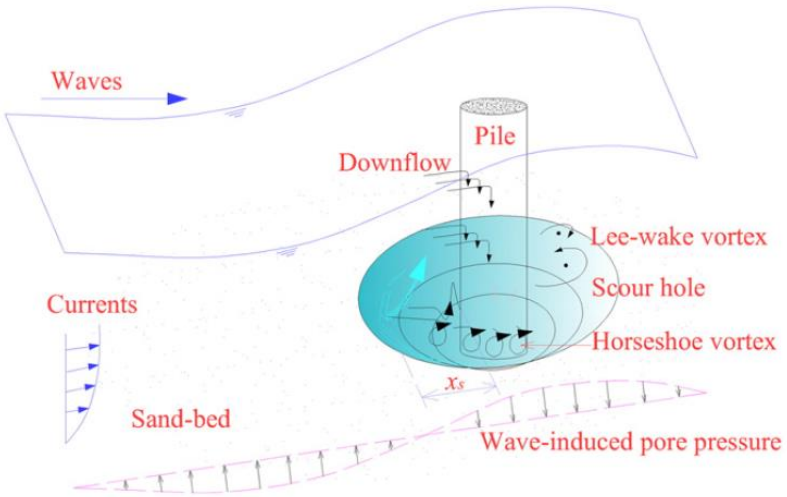

Figure 1.17: Wave and current coupled scour at a monopile (Qi and Gao 2014)

Qi and Gao (2014) found that waves following currents produced higher velocity in boundary layers while waves opposing current reduced velocity. For smaller values of K_c, the horseshoe vortex effects are lowered and its impact on scour is much less than steady currents where $K_c \approx \infty$. Due to the non-linear effects when waves and currents interact, the linear sum of current scour with wave scour was found to underestimate the actually rate and depth of scouring. For a detailed analysis into the effects of wave–current interaction on the current profile, Olabarrieta et al. (2010) examined the effects of wave–current on a water column and the free surface. Results were recorded on how the typical logarithmic velocity profile of pure currents was altered in experiments with following, opposing, and perpendicular waves. Olabarrieta et al. (2010) analyzed the non-linear effects of waves with a Eulerian wave–current model and verified the model with experimental results. Following waves increased velocity while opposing and

perpendicular waves decreased velocity in the upper column areas between wave crests and troughs. Velocity below the wave trough level decreased for following waves and increased for opposing's waves and these effects were seem amplified for larger wave heights and shorter wave periods.

1.1.4 Structural Influences on Scour

In the case of general scour where no structures are present to obstruct flow, the flow and soil parameters are the only factors controlling scour. Structural contractions and localized obstructions accelerate flow while creating turbulent vortices which amplify bed shear stress and modify sediment transport behaviour. This section will cover the experimental and field study research which has been conducted into understanding and predicting bridge scour. Details on the prediction equations is further discussed in Section 1.2. Unlike the soil bed and flow behavior the structural factors of interest are deterministic dimensions.

Contraction Scour

The presence of abutments and embankments reduce channel widths at bridge foundations and form a contraction responsible for scour as shown in Figure 1.2. The contraction would have a similar flow rate to the approaching flow and the reduction in flow width is compensated by an increase in flow velocity. The higher flow velocity increases bed shear stresses which will scour the bed in the area of the contractions in addition to local scouring effects at the structures. The primary objective of research into the analysis and prediction of contraction scour is quantifying the level of velocity amplification based on the geometry of the contraction. The factors of interest for contraction scour are the soil parameters, channel approach width, contraction width, channel approach depth, channel approach velocity, channel approach flowrate, and contraction length. The common non-dimensional factor proportional to the maximum contraction scour depth is the contraction ratio defined as the channel approach width divided by the contraction width (Richardson and Davis 2001). Further discussion on prediction methods is done in Section 1.2, where the importance of channel types and geometry is emphasized. Depending on whether the channel a simple rectangular shape or compound channel the approach and methods will be significantly different. The HEC-18 manual (Richardson and Davis 2001) covers theory and some

methods for predicting clearwater and live-bed scour at different types of contractions. Experimental investigations of contraction scour have been conducted by Laursen (1960), Laursen (1963), Neill (1973) and Sturm at al. (2011). Methods for estimating contraction scour in cohesive soils were presented by Briaud et al. (2005) and Briaud et al. (2011).

Local Scour at Piers

The scour case with the most literature and need for further research is local scour at bridge piers. Unlike general and contraction scour, the local scouring around piers is caused by the formations of turbulent horseshoe and wake vortices as illustrated in Figure 1.3. The flow acceleration around piers and the downwards flow of the horseshoe vortices erode the surrounding soil to form scour holes. In addition to soil parameters the main factors of interest for pier scour are the flow depth, flow velocity, pier shape and pier width normal to flow. The earlier research into pier scour includes Laursen and Toch (1956), Neill (1964), Melville and Raudkivi (1977), Jain and Fischer (1979), Jain (1981), Dargahi (1987), Dargahi (1989), Froehlich (1988), and Ahmed and Rajaratnam (1998). The earlier work consisted of fitting laboratory data to obtain simple empirical equations for estimating the maximum scour depth at single cylindrical piers. Over the years with more experimental and field data, methods for scour prediction have become more comprehensive by including the effects of flow directions, sediment parameters, and different pier types. Other experimental works have been conducted with a focus on analysing the turbulent flow field and understanding the behaviour of the primary horseshoe vortex. Breusers et al. (1977) reviewed pier scour and discussed the effects of different scour shapes on local scour. The controlling factor for pier scour was found to be the shape and size of the upstream pier face. For piers aligned with the flow the length of the pier had no impact as it did not interact with the primary horseshoe vortex. The tail end of piers would produce lee wake vortices however scour would be the deepest at the front face. Round nosed piers helped lower the horseshoe vortex strength and produce scour depths 70% - 90% of those at rectangular piers of the same width. Sheppard et al. (2004) performed large scale clear water local scour experiments with piers of diameters of 0.114 m, 0.305 m, and 0.914 m. Results were recorded for a range of flow depths, flow velocities and sediments sizes of 0.22 mm, 0.80 mm, and 2.90 mm. The pier scour prediction equations discussed in Section 1.2 were from the works of Breusers (1963), Colorado State University (1977), Melville and Sutherland (1988), (Richardson and Davis, 2001), Sheppard and

Miller (2006), Breusers et al. (1977), Melville and Raudkivi (1997), Melville and Chiew (1999), Briaud et al. (1999), Briaud et al. (2001a), and Briaud (2015a, 2015b).

Experimental studies on local scour flow were conducted by Manes and Brocchini (2015) to analyze the turbulence effects on sediment. By merging theory and empirical observations of the fluid stresses on sediment erosion and transport, a prediction formula was developed for maximum scour at cylindrical piers. Guan et al. (2018) studied the horseshoe vortex in a developing scour hole with Particle Image Velocimetry (PIV). Measurements were made of velocity fields, turbulence intensities and Reynolds's shear stresses over time to examine the different stages of scour. The primary horseshoe vortex started as one small vortex which grew in size and strength before evolving into three vortices. The tests were done in a flume with a cylindrical pier of 80 mm diameter, flow intensity of 0.53, and flow depth of 200 mm. The area of maximum downflow was found to be $-0.5<y/D<0$ upstream of the pier, where D was the pier diameter and y was the distance from pier. The region of maximum turbulence intensity and Reynolds's shear stress occurred at upstream head of the main horseshoe vortex, where large turbulent eddies have the highest probability of occurring. Through some promising results were obtained they were limited for the particular scaled setup and the turbulence behavior can greatly vary for other pier shapes and flow intensities. Further experimental tests and numerical studies would be required to completely comprehend the vortex system at piers for depth design and protection against scour. Chen et al. (2019) statistically investigated the horseshoe vortex system with time-resolved PIV. Using flows with varying Reynolds numbers, the horseshoe vortex was tracked as it traveled downstream and weakened. The mean lifespan was estimated to be $5D/V$, where D is pier diameter and V is the mean approach velocity.

When prediction equations from the formerly mentioned sources were applied to wide piers, scour depths were significantly over predicted. This occurred due to the scale effects arising in laboratories and limited field data of scour at large piers. As piers get larger, the width influence on scour depth decreases, so new relationships must be described for the cases of wide piers or long skewed piers. Whitehouse (2004) studied scour around large 20 m diameter monopile wind turbine foundations. Sheppard et al. (2011) performed an in-depth study on scour at wide and long skewed piers as part of NCHRP REPORT 682. Large sets of existing data on field and lab scour were compiled to evaluate the performance of common formulae. Two equations with good

performance from Sheppard and Miller (2006) and Melville (1997), were combined to form a new equation referred to as the Sheppard/Melville or S/M equation. The new S/M equation performed better than any other existing equation for predicting scour at wide and skewed long piers. For consideration of temporal effects, the S/M equation was inputted into the Melville and Chiew (1999) scour evolution equation to form the M/S equation. The M/S equation performed very well in modeling the evolution of scour hole depth over time. Zhao et al. (2012) used experiments to study the local scour around rectangular subsea caissons in steady currents. The flow skew angle was evaluated with tests at 0°, 45° and 90°, where 0° represents flow parallel to the long boundary of the caisson and 90° representing flow parallel to the short boundary of the caisson. Rectangular shape effects revealed that the horseshoe vortex had less of role in scouring compared to flow acceleration at upstream corners where the scour started. Results were also used to develop an empirical equation where a hyperbolic function fit the data than an exponential function.

Local Scour at Complex Piers and Pile Groups

Most of the research conducted has been on pier of uniform diameter but many structures are composed of compound sections. Compound piers as those in Figure 1.18 may be composed of lower foundation sections of larger diameters or multigroup piles as those in Figure 1.19, which will change the flow system and scour hole shape.

Figure 1.18: Compound pier shapes (Whitehouse 2004)

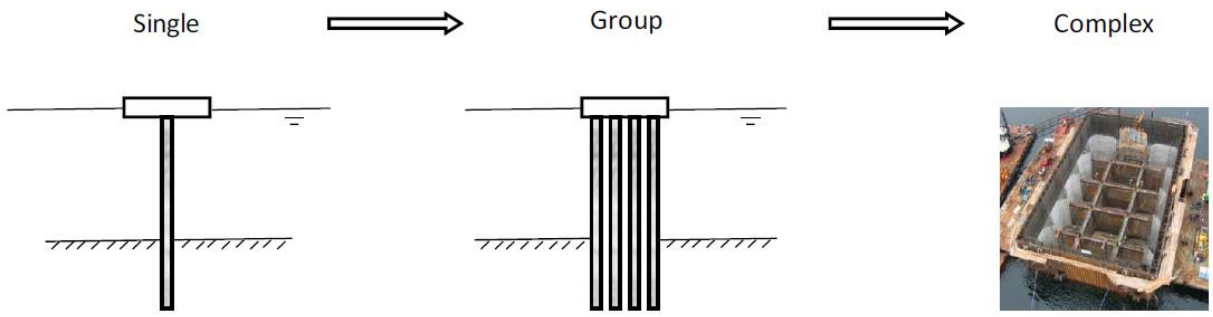

Figure 1.19: Single pile, pile group, and complex foundation example (Wang et al. 2017)

Different scour cases can occur based on the relative elevations of the sediment bed, water depth, and pier height. The scour cases are defined by which sections of structures are exposed to flow. Scour at pile groups include factors such as spacing and arrangement types which cause flow effects such as jetting and shielding. Piles at the upstream face will shield downstream piles from the flow, therefore the scour depth at piles upstream are larger than those shielded behind. Jetting at pile groups is the acceleration of flow in the contraction between piers which increases with closer spacing. Mutual interactions between piles and the pile cap are also important to consider for close spacings and pile caps exposed to flow (Wang et al. 2017). Many scenarios with different shapes, arrangements and relative heights of structures are possible. Different states of elevation and exposure are illustrated by a pier with pile group foundation example in Figure 1.20.

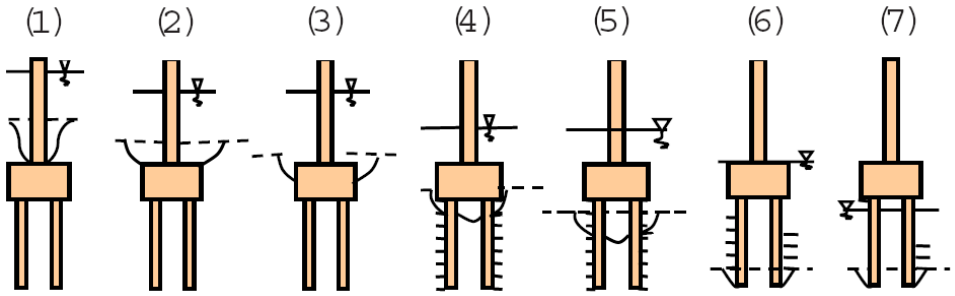

Figure 1.20: States of scour at complex piers due to elevations (Ataie-Ashtiani et al. 2010)

In Figure 1.20 the water elevation is shown with a solid line, the sediment bed is indicated with a dashed line, and the expected scour hole shape is drawn. In case (1), scour is controlled by the top pier, case (2) has a lower sediment bed and a smaller scour depth because the pile cap acts

a protective layer to limit the scour depth. With lower flow and bed depths, case (3) and case (4) see the cap exposed and scour starting to go underneath towards the pile groups. As the water elevations goes below the pier with cases (5) - (7), the piles and pile cap interactions with the flow control the vortex system and scouring. Ataie-Ashtiani et al. (2010) experimentally investigated pile cap elevation influence on clear water scour at the compound pier types shown in Figure 1.20. It was found that scour increased with cap exposure and maximum scouring occurs when pile cap is undercut, and flow penetrates below as in case (4). Common pile arrangements include side by side rows (normal to flow), tandem lines (parallel with flow), triangular, and rectangular grids. If piles are grouped close enough then scour may be approximated using equations for wide piers by treating the group a single large pier. On the other end, piles spaced far enough such that their flows do not interact may be treated as single piers. Ataie-Ashtiani and Beheshti (2006) observed that the group acts as a single pier for spacings of $S/D < 1{:}25$, where S is the spacing and D is the pile diameter.

When researching non-uniform piers, Melville and Raudkivi (1996) performed experiments of scour on compound piers with diameters of D situated on larger cylinder foundation of diameter D^*. A solution tested was to predict scour with an equivalent diameter as a function of D and D^*. However, the equivalent diameter was found to excessively overpredict scour depth. Instead, Melville and Raudkivi (1996) proposed a method addressing the threes possible cases for compound piers and using equations specific to the cases as those in Figure 1.20. Briaud et al. (2004) expanded the single pier SRICOS method to solve for scour at pile groups in cohesive soils. Melville and Coleman (2000) published a text on pier and pile group scour with a predictive equation also referred to as the New Zealand Equation. Coleman (2005) updated the New Zealand Equation with new expressions for correction factors obtained from additional experimental testing. The new equation was applicable for scour at complex piers, uniform piers, caisson-founded piers, pile groups with debris rafts, and pile groups with various cap elevations. Ashtiani and Beheshti (2006) ran 112 experiments of clear water scour at side-by-side and rectangular arrangements of piles. The case of cap above water was tested with quartz sand of 0.25 mm and 0.98 mm size, varying spacing, and varying flow conditions. The amplification of local scour at piles in a group was referred to as the interference effect and it was seen reduced for spacings $S/D>2\text{-}4$, where D is the pile diameter and S is the pile spacing. Relative to single pile, scour depth increased by a factor of 1.5 for two piles side by side with spacing $S/D \cong 0.25$, a factor of 1.2

for two piles in tandem with spacing $S/D \cong 2$, and a factor of 2 for a 2x4 pile group with spacing $S/D \cong 0.25$. As with single piers, the width normal to flow dominated the scour depth, in the case of group piles the width was controlled by the number of piles arranged normal to flow. The results were used to derive a correction factor for pile groups and when incorporated with the HEC-18 and New Zealand equation, a good agreement was found when compared with lab scour depths. Kumar et al. (2012) put together a review on local scour at uniform and compound circular piers. Suggestions were given on what methods to select when evaluating local scour with temporal considerations. Amini et al. (2012) conducted experiments on pile group scour with submerged and unsubmerged caps. To obtain the maximum scour depth, flow intensity was set to near threshold conditions. The shielding effect of upstream piles reduced velocity and coupled with deposition lead to lower depths at the downstream piles. An equation for estimating scour depth was developed as a function of pile arrangement, spacing and submergence ratio, $Sr=h/y$, where h is the pile height, and y is the flow depth. Scour holes became interconnected forming a larger scour hole for spacings $S/D < 3.5$. The interference between piles and other group effects diminished for spacings $S/D > 3.5$. Akib et al. (2014) experimentally evaluated local scour around complex pier groups and combined piles at semi-integral bridge. Flow and depth measurements revealed that scour developed faster at upstream faces although the time until equilibrium depth at upstream and downstream sides was same. Liang et al. (2019) tested the effects of pier widths, types, and configurations on scour in non-cohesive soils. Most tests were in deep water and some numerical models were used to evaluate scour at piers too large to test experimentally.

Local Scour at Abutments, Spur-Dikes and Groynes

Apart from piers the local scour often of concern at bridge foundation is at abutments. Local scour at abutments occurs due to a combination of lateral channel migrations, flow contraction, and vortex formation due to abutments obstructing flow as piers do. Acting as flow obstructions, abutments form primary vortices upstream running along the abutment toe and wake vortices downstream as described in Figure 1.21.

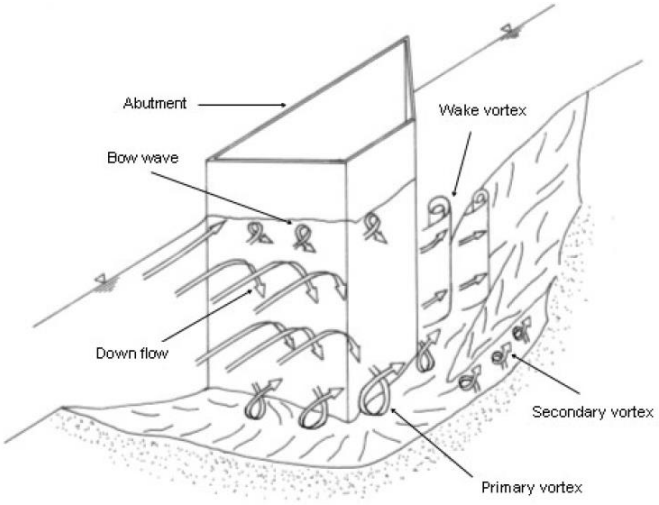

Figure 1.21: Flow around scoured abutment (Barbhuiya and Dey 2004)

As scour holes begin to form at abutments, the combination of downward flow and vortices will continue to deepen the scour until a maximum depth is reached provided flow conditions are steady state. Evaluating local abutment scour is complex as there are many factors to address starting with the channel cross section which for compound channels consists of a main channel and flood plains. Scour in a compound channel is illustrated in Figure 1.22, where analysis includes different sections with their own flow rates, velocities, and dimensions.

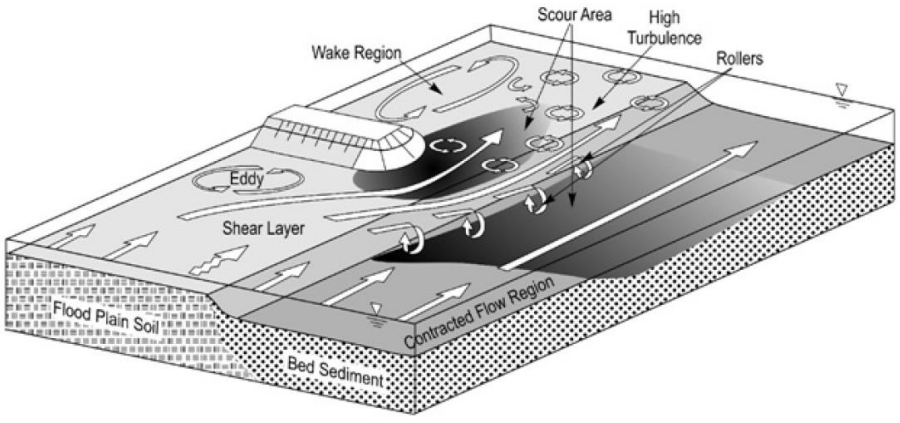

Figure 1.22: Abutment scour in a compound channel (Richardson and Davis 2001)

The next major factor is the geometry of the abutments which influence the level of flow contraction along with vortices size and strength. The common abutments shapes are spill through abutments, vertical wall abutments, and wing-wall abutments as displayed in Figure 1.23.

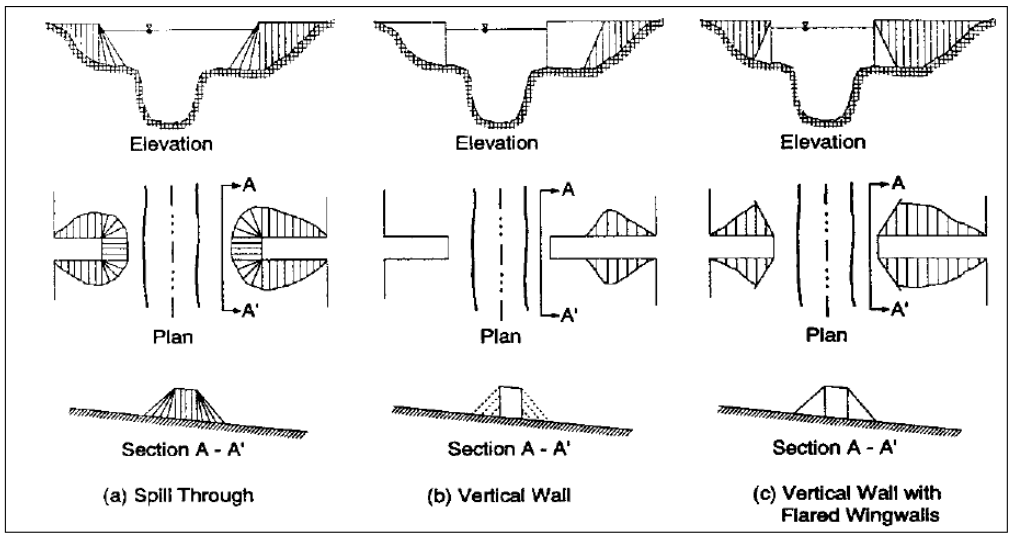

Figure 1.23: Abutment shapes (Richardson and Davis 2001)

The approach to studies for abutments scour follows the process for any other local scour as such as local piers scour. Local scour occurs while the shear stress exhibited on the bed from the flow is larger than the critical value of the soil. Barbhuiya and Dey (2004) compiled information on local abutments scour and found that scour is the largest for vertical wall abutments, followed by wingwall abutments and the lowest for spill through abutments. Apart from the abutment shape, the length normal to flow will significantly impact scour as its redirection of flow causes flow acceleration. The flow field at abutments is comparable to groynes or spur-dikes as they are all large wall-like structure forcing flow around.

Equations for predicting local abutment scour are discussed in Section 1.2 including Froehlich (1989), HIRE equation (Richardson and Davis 2001), NCHRP 24-20 approach (Ettema et al. 2010), Melville (1992), Melville (1997), and the TAMU method (Briaud 2015a, 2015b). Other published literature includes Coleman et al. (2003), who conducted experiments of clear water scour at vertical wall abutments near threshold velocity conditions. An equation was developed for dimensionless equilibrium time as a factor of flow intensity and relative abutment length, y/L, where y is the flow depth and L is the abutment length. Results with short abutments, $y/L>1$, revealed a flow pattern similar to piers with downflow at upstream face and a principal vortex analogous to the horseshoe vortex at piers. For long abutments, $y/L<1$, the downflow was significant to scour and a large eddy was seen generated ahead of the abutment. Sturm et al. (2011) reviewed contraction scour and local abutment scour prediction methods, discussed the gaps of

knowledge, and the need for safe and cost-effective design of bridge foundations. Debnath at al. (2014) investigated abutment scour in a clay/sand-mixed cohesive sediment bed, with 87 experiments at vertical wall abutments and 29 experiments at 45° wing wall abutments. Depth prediction equations were created as functions of clay content, C, water content, Wc, bed shear strength, and flow Froude number. Water content was tested in the range of $0.19 < Wc < 0.44$, and clay content ranged in between $0.35 < C < 1$. Results revealed that for $Wc < 0.24$ the scour depth decreases with an increase in clay content. For $Wc > 0.24$ an increase in clay content decreases scour depth until $C = 0.5$, at which point further increases in the clay content increased scour depth. Pandey et al. (2018) compiled a review on scour at spur dike structures which stem from banks into stream to deflect flow and defend the bank against stream erosion. The shape and scour process at spur dikes is very similar to abutments due to their shape and orientation in a channel.

Debris and Icing

Other than the bridge structure itself, local debris and icing can accumulate and increase the amount of contraction and local scour. Debris consists of plant material or ice forming a raft or becoming stuck at bridge foundation components such as piers. The presence of debris further contracts flow and may increase the effective widths of pier which will then enhance the effects of local scouring. If not accounted for, significant amounts of debris may lead to bridge instability or even failure. By measuring or estimating the dimensions of debris it can be considered as extensions of the structures, for example a pier with ice near the surface may be treated as a compound pier. Structural design may incorporate considerations to minimize debris and icing through field monitoring and analysis. The HEC-18 manual (Richardson and Davis 2001) provides some recommendations for estimating pier scour with debris which is covered in Section 1.2.1. Wu et al. (2015) conducted experiments on scour at ice covered bridge abutments. Abutments with square and semi-circular ends were investigated along with ice roughness effects on scour. Wu et al. (2016) conducted experiments on ice covered piers to develop a depth estimation equation and found that scour hole sizes increased with larger ice cover. Ice cover was more influential for shallow flows, as it was more likely to interact with turbulent flow field causing scour near the bed. Namaee and Sui (2019) studied local scour around two side-by-side cylindrical bridge piers under ice-covered conditions.

1.2 Scour Estimation Methods

The most common method for formulating predictive empirical equations for scour prediction is fitting experimental data. This section will cover common methods used for predicting equilibrium depths and time rates of contraction and local scour. General scour, the long-term degradation/aggradation is expected to have already occurred prior construction, thus its prediction is not necessary. Empirical formulae have generally been rough estimates of scour depths and limited in their consideration of all factors relating to the soil, fluid, and structure interaction. The earliest of the empirical equations only considered structural dimensions and are overtly conservative to account for uncertainly in flow and soil parameters. Over time with further research and more experimental data, the empirical equations have been updated to include factors related to flow depths, flow velocities and soil parameters.

To obtain meaningful relationships and fit measured data, dimensional analysis was conducted in scour studies. The approach to developing equations for estimating scour depth most often involved using the Theorem of Vaschy-Buckingham (Buckingham Pi) to perform dimensional analysis. Papers covering the dimensional analysis of scour include Breusers et al. (1977) and Chiew and Melville (1987). The dimensional analysis process identifies all possible variables or factors impacting scour depth to express non-dimensional pi parameters and then curve fitting measured data. The equilibrium depth for scour at a pier in function form can be written as

$$d = f(\rho_f, \nu, \rho_s, b, g, V, y, L, D_{50}, \theta, \sigma_g, Sh, t, t_e) \tag{1.28}$$

where ρ_f is the fluid density, ν is the fluid viscosity, ρ_s is the soil density, b is the pier width, g is the acceleration due to gravity, V is the flow velocity, y is the flow depth, L is the pier length, D_{50} is the median soil grain size, θ describes the flow angle of attack, σ_g is the soil gradation, Sh describe the pier shape, t is the time of scouring, and t_e is the equilibrium scour time. These are generally the most common factors considered for the formation of local pier scour equations. The dimensional analysis would require running experiments with different values for each factor to conduct a sensitivity analysis. Once all individual factors are identified, the theorem of Vaschy-Buckingham involves rewriting Equation (1.28) with the factors in non-dimensional forms as

$$\frac{d}{b} = f_1(\frac{y}{b}, \frac{D_{50}}{b}, \Delta, \frac{V^2}{gb}, \frac{Vb}{\nu}, \sigma_g, Sh, Al, \frac{t}{t_e}) \quad (1.29)$$

where $\Delta=(\rho_s-\rho)/\rho$ is relative submerged density. The left side of the equation has the equilibrium scour depth normalized with the pier width which is commonly done as is has been proven to be the most influential length factor. Included in Equation (1.29) are classical parameters in studies of sediment transport, the Froude number and Reynolds number written with the pier width. Also included are the non dimensional factors σ_g, *Sh*, and the alignment factor *Al* which would account for the flow angle of attack θ. For methods in cohesive soils where flood times are important the scouring time, *t*, is analyzed relative to an equilibrium scour time, t_e. As Equations (1.28) and (1.29) are just examples, many methods for estimating scour focus only on some specific factors for scour at different structures. For abutments, the channel dimensions become more influential and for pile groups the spacings would be considered. Some studies also have included many soil factors and scour in waves would involve the K_c number.

For general scour, contraction scour and some cases of local abutment scour, a large-scale evaluation of the channel flow must be performed. Unlike pier scour, a mean flow velocity and flow depth is not enough information to describe the flow. Software such as BSDMS (The Bridge Scour Data Management System) and HEC-RAS (River analysis system) help with simulating river flow and determining the flow rates at different sections (Richardson and Davis 2001). The software include data on the bed shapes and water elevations so velocities and flowrates can be obtained throughout the channel. The software are used in conjunction with scour prediction methods to obtain flow rates to input into equations such as Laursen's (1960) equation for contraction scour or the TAMU equation for abutment scour (Briaud 2015a, 2015b). Govindasamy et al. (2013) created a statistical method for predicting scour called the observation method for scour (OMS). The advantages of the OMS were that it did not require site-specific erosion testing of the soil and it accounted for time dependent scour. The method extrapolated measurements of past scour depths during floods to predict scour in specified future floods. Past flowrates and velocities were converted in between each other using HEC-RAS. Then the data was used to create Z-future charts to describe the scour depths corresponding to different flow rates. The OMS was applied to 16 bridges in the US which then revealed 10 were scour critical due to the possibility of future floods causing structural instability. Govindasamy and Briaud (2014) applied the OMS to

two additional bridges and found good agreement between predicted depths with OMS and field measurements.

The remainder of this section will describe equations predicting scour obtained from North American design manuals and newly published research. Over the years, past equations have been updated to include previously dismissed factors or to improve the performance by including new scour data in the dimensional analysis.

1.2.1 Scour Estimation Methods in Design Manuals

To review the current state of scour prediction methods used in North America, the methods in the MTO Drainage Management Manual (MTO 1997) and FHWA HEC-18 (Richardson and Davis 2001) Evaluating Scour at Bridges Manuals are summarized.

1.2.1.1 MTO Drainage Management Manual

In Ontario, Canada, the MTO (Ministry of Transportation) Drainage Management Manual has compiled the necessary information on designing for and analysing structures with scour. The manual includes some information on scour theory, monitoring, countermeasures, four methods for estimating contraction scour and three methods for estimating local scour at piers. The methods for determining contraction scour involve making assumption of scoured sediment bed shapes and flow conditions. The limitations to the methods are that they were developed based on laboratory testing with non-cohesive sandy soils. Influences of most soil parameters, waves, complex flow conditions are neglected and lead to highly conservative estimates for scour depths.

MTO Contraction Scour: Competent Velocity Method

The Competent Velocity Method assumes that a contraction area would continue to scour until the flow velocity decreases to a critical velocity. Firstly, the method requires obtaining the cross section of the channel with a set channel surface level, channel flow rate, and the critical velocity of the soil bed. The critical velocity is a function of the soil median grain size and scour depth as seen in Figure 1.24.

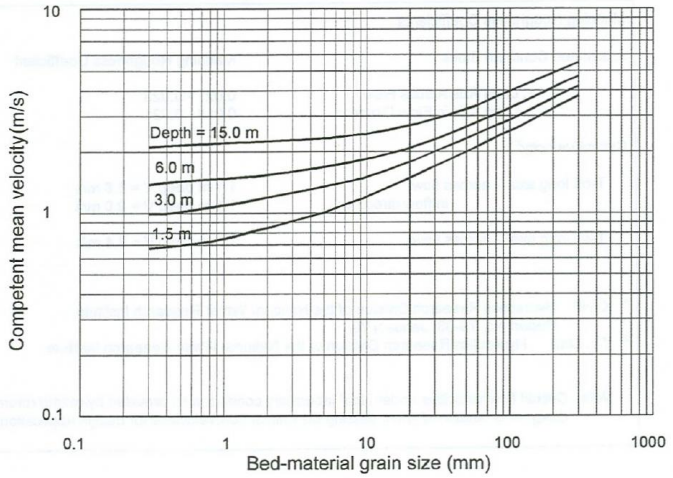

Figure 1.24: Competent velocity method design chart for critical velocity (MTO 1997)

The flow velocity is calculated from dividing the flow rate by the flow cross section. Next the channel's scoured cross section shape is estimated based on engineering judgment shape as either trapezoidal, parabolic, or triangular. A parabolic scoured area would be used for relativity straight channels and a triangular shape would be recommended for sharply curved regions. After assuming a scouring shape, the scoured area is calculated using the flow rate and critical mean velocity obtained. Once the scoured cross-sectional shape is determined it can be compared to the original cross section to calculate scour depths through the cross section.

MTO Contraction Scour: Mean Velocity Method (Neill 1973)

The second method is the Mean Velocity Method (Neill 1973), is used for channels having stabilised bed elevations and no longer experiencing degradation or aggradation. The method involves determining the bank-full mean velocity, assuming a scoured area as with the Competent Velocity Method and then compare these with the check flood flow condition to determine an approximate scour depth.

MTO Contraction Scour: Regime Method

The third method is the Regime Method, which incorporates site specific characteristics of channels including the bank-full flow rate, check flow rate determined using Manning's equation. The soil is considered in the calculations through the Manning roughness value, obtained from design tables. The equation for the Regime Method is

$$d_f = d_b(q_c/q_b)^m \tag{1.30}$$

where d_f is the total scoured depth, d_b is the bank-full depth of flow before scour, q_c is the check flow intensity, q_b is the bank full flow intensity and m is an empirical exponent equal to 0.67 for sand and 0.85 for gravel.

MTO Contraction Scour: Laursen Method (1960)

The last method recommended for predicting contraction scour is the Laursen Method (1960), which is used for narrow flood plains, openings set back from main channels and areas of sensitive flood plains. The method compares flows through a cross-section with and without the structural obstruction to solve for the scoured depth using the Laursen equation

$$d_s = d_2 - d_1 \quad , \quad \frac{d_2}{d_1} = \left(\frac{Q_2}{Q_1}\right)^{6/7}\left(\frac{W_1}{W_2}\right)^{0.64} \tag{1.31}$$

where, d_s is the average contraction scour depth, d_1 is the average depth upstream in the main channel, d_2 is the average depth in the contracted section, Q_1 is the flow rate upstream, Q_2 is the flow in the contracted channel, W_1 is the bottom width of the main channel upstream, and W_2 is the bottom width of the contracted section or bridge opening.

MTO Local Pier Scour: RTAC (1973)/Breusers (1963) Method

The MTO drainage manual provides three methods for estimating local scour at piers based on laboratory flumes tests. The methods are limited in their flow considers and only account for pier width, shape, and skew using empirical factors. Consideration for soil parameters, debris and complex flows conditions are recommended to be addressed by geotechnical expert judgements on site-specific conditions. The first method for estimating local scour is the RTAC Guide to Bridge Hydraulics (1973) Method. The method entails using the empirical equations seen in Figure 1.25, to estimate local scour depth as function of pier shape and size.

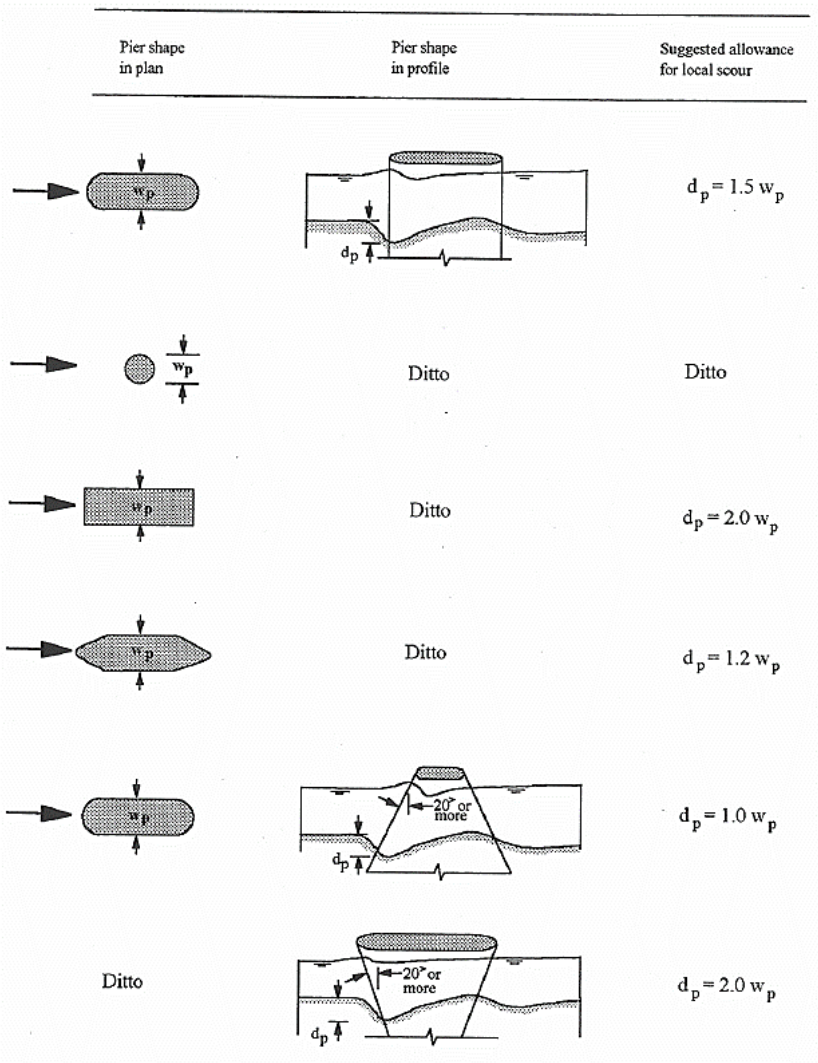

Figure 1.25: RTAC guide to bridge hydraulics (1973) method (MTO 1997)

In the empirical equations shown in Figure 1.25, d_p is the scour depth and w_p is the width of the pier normal to flow. The design chart was based off the data collected from laboratory flume tests by Larras (1963), Breusers (1963) and Neill (1973).

MTO Local Pier Scour: CSU (Colorado State University) (1977) Method

The second method for estimating local pier scour is the is the common Colorado State University (CSU) (1977) Method. The CSU equation is given as

$$\frac{d}{y} = 2.0 k_1 k_2 \left(\frac{b}{y}\right)^{0.65} {F_{rl}}^{0.43} \tag{1.32}$$

where d is the local scour depth, k_1 is the correction factor for pier shape, k_2 is the correction factor for angle of attack, b is the width of the pier, y is the flow depth, $F_{rl}=V/(gy)^{0.5}$ is the Froude number, g is the acceleration due to gravity, and V is the mean velocity. The two correction factors k_1 and k_2 are obtained from Figure 1.26.

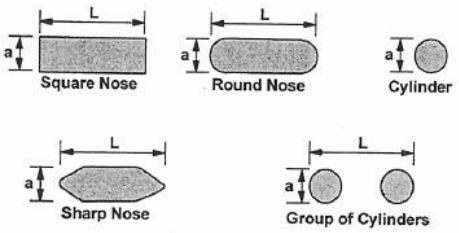

Pier Shape Factor k_1	
Shape	**k_1**
Square Nose	1.1
Round Nose	1.0
Circular Cylinder	1.0
Sharp Nose	0.9
Group of Cylinders	1.0

Correction Factor k_2			
Angle	**k_2**		
	L/a=4	**L/a=8**	**L/a=12**
0	1.0	1.0	1.0
15	1.5	2.0	2.5
30	2.0	2.5	3.5
45	2.3	3.3	4.3
90	2.5	3.9	5.0
Angle = skew angle of flow			

Note: The correction factor k_1 for pier nose shape should be determined using the table for angle of attack up to 5 degrees. For greater angles, pier nose shape loses its affect and k_1 should be considered as 1.0.

Figure 1.26: CSU (1977) method pier shape and angle of attack factors (MTO 1997)

The method is obviously more detailed than the RTAC as there is incorporation of flow depth, velocity, and angle of attack. The method is still limited in its consideration of soil parameters, as it was developed for sand it can also be applied to gravel beds. As shown in Figure 1.26, the correction factors include a conservative consideration for pier groups by treating them as one larger pier.

MTO Local Pier Scour: Melville and Sutherland (1988) Method

The third method for predicting local scour at piers is the Melville and Sutherland (1988) equation. This method is the most complete of the three it is the only one to account for the soil

gradation, mean grain size, and armoring abilities. The method was derived from experimental data which demonstrated a maximum scour depth of *2.4b* for clear water scour, where *b* is the pier width/diameter. Then using correction factors for flow and sediment parameters the maximum depth is adjusted for the specific conditions. The local scour depth equation is given as

$$\frac{d}{b} = k_i k_y k_d k_\sigma k_s k_\alpha \tag{1.33}$$

where d is the local scour depth, b is the pier width normal to flow, k_i is the flow intensity coefficient, k_y is the flow depth coefficient, k_d is the sediment size coefficient, k_σ is the sediment gradation coefficient, k_s is the pier shape coefficient, and k_α is the pier alignment coefficient. The method is based on the theory that bed paving would occur over time and through a sorting effect an armour layer would prevent further scouring. Consideration of the armour layer is part of the process for determining the flow intensity factor. The flow condition past which armoring does not occur is referred to as the limiting armour conditions. The coarsest or most stable armor bed occurs for a mean velocity of V_{ca} associated with a median grain size D_{50a}. The first step is calculating $D_{50a}=D_{max}/1.8$, where D_{max} is the maximum grain size in the soil. Next using both the grain sizes D_{50} and D_{50a}, shear velocities V_{*c} and V_{*ca} are respectively determined with the relationship

$$u_{*c} = 0.03 D_{50}^{1/2} \tag{1.34}$$

where $u*c$ is the shear velocity corresponding to a grain size of D_{50}. Using the shear velocity representing the bed shear stress, the corresponding mean flows V_c and V_{ca} are solved for using the following logarithmic velocity profile

$$\frac{V_c}{u_{*c}} = 5.75 \log\left(5.53 \frac{y}{D_{50}}\right) \tag{1.35}$$

where y is the flow depth and u_{*c} is the shear velocity corresponding to a grain size of D_{50}. It was found from sediment-recirculating flume tests that a mean value of $V_a=0.8V_{ca}$ was the best characterization of the limiting armour layer and the transformation from clear-water to live bed scour conditions for non-uniform sediments. The physical constraint of V_a would imply that it be checked to be less than V_c, otherwise it is set equal to V_c in which the sediment behaves as uniform. Sediment gradation effects were evaluated concurrently with the flow intensity, where larger

geometric stander deviations (σ_g = D_{84}/ D_{50}) lead to lower scour depths. The method takes the gradation factor k_σ as 1.0 because the gradation effects are considered in the flow intensity factor, k_i, by including the armor potential. The flow intensity factor k_i is determined using the following equation

$$k_i = \begin{cases} 2.4 \left| \frac{V - (V_a - V_c)}{V_c} \right| & , \quad \frac{V - (V_a - V_c)}{V_c} < 1.0 \\ 2.4 & , \quad \frac{V - (V_a - V_c)}{V_c} \geq 1.0 \end{cases} \tag{1.36}$$

where V is the mean flow velocity. The flow depth factor relationship was found from previously conducted experiments, and the relationship is including the upper limit described as

$$k_y = \begin{cases} 0.78 \left(\frac{y}{b}\right)^{0.255} & , \quad \frac{y}{b} < 2.6 \\ 1.0 & , \quad \frac{y}{b} \geq 2.6 \end{cases} \tag{1.37}$$

where y is the flow depth and b is the effective pier width. The sediment size factor considers the relationship between median sediment sizes and the pier width. Larger sediments were found to reduce the scour depth as described in the equation

$$k_d = \begin{cases} 0.57 \, log(2.24 \frac{b}{D_{50}}) & , \quad \frac{b}{D_{50}} < 25 \\ 1.0 & , \quad \frac{b}{D_{50}} \geq 25 \end{cases} \tag{1.38}$$

where D_{50} is the median grain size. The procedure states that for σ_g values larger than 1.3, the D_{50a} grain size should be used to determine k_d. For the pier shape factor, published relationships are used as displayed in Table 1.10.

Table 1.10: Pier shape correction factor (Melville and Sutherland 1988)

Shape in plan (1)	Length/ width (2)	Reference: Tison (1940) (3)	Laursen and Toch (1956) (4)	Chabert and Engeldinger (1956) (5)	Venkatadri (1965) (6)
Circular	1.0	1.0	1.0	1.0	1.0
Lenticular	2.0	—	0.97	—	—
	3.0	—	0.76	—	—
	4.0	0.67	—	0.73	—
	7.0	0.41	—	—	—
Parabolic nose	—	—	—	—	0.56
Triangular nose, 60°	—	—	—	—	0.75
Triangular nose, 90°	—	—	—	—	1.25
Elliptic	2.0	—	0.91	—	—
	3.0	—	0.83	—	—
Ogival	4.0	0.86	—	0.92	—
Joukowski	4.0	—	—	0.86	—
	4.1	0.76	—	—	—
Rectangular	2.0	—	1.11	—	—
	4.0	1.40	—	1.11	—
	6.0	—	1.11	—	—

It was recommended to use any of the shape factors, however for flow alignment angles larger than 10° the shape factor k_s should be taken as 1.0. Lastly the flow alignment factor, $k_{\alpha,}$ was based on the pier dimensions and angle of attack as shown in Figure 1.27.

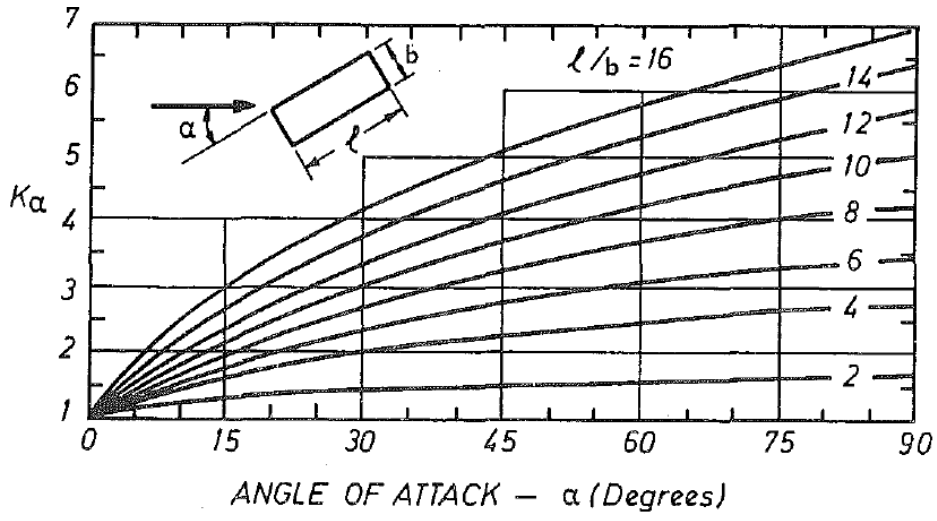

Figure 1.27: Flow alignment correction factor (Melville and Sutherland 1988)

The procedure is further discussed by Melville and Sutherland (1988), with details addressing turbulent boundary layer velocity profiles and shear stresses on soil beds.

1.2.1.2 FHWA HEC-18 Evaluating Scour at Bridges

The Federal Highway Administration of the US provides three manuals on scour, HEC-18 Evaluating Scour at Bridges, HEC-20 Stream Stability at Highway Structures, and HEC-23 Bridge Scour and Stream Instability Countermeasures. The HEC-18 document includes the recommended methods for estimating scour. HEC-20 discusses techniques for analysing steam instability and scour problems for designs of new bridges and evaluation of existing bridges. HEC-23 provides insight on bridge design recommendations with methods for scour countermeasures. Richardson and Lagasse (1996) discuss the state of scour at bridges in the USA and methods predictions and monitoring scour depths related to the FHWA manuals. All three documents are meant to be used collectively in the design and analysis of bridges as shown in Figure 1.28.

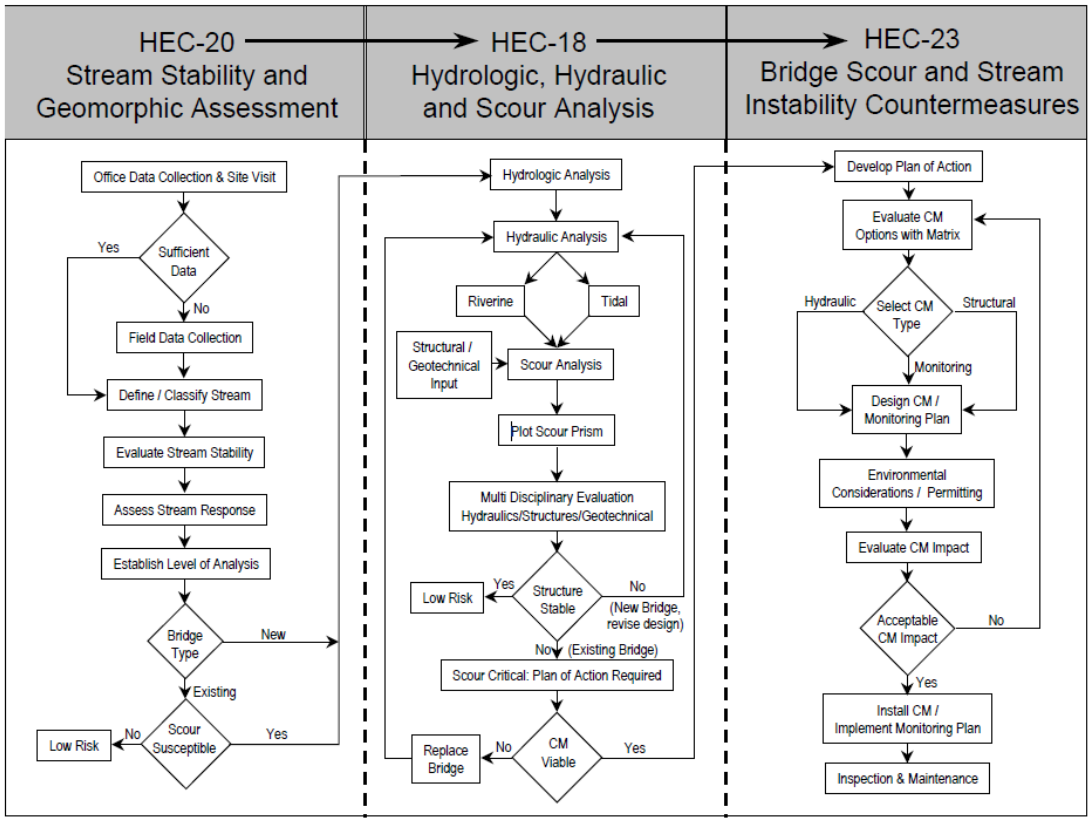

Figure 1.28: HEC-18, HEC-20, and HEC-23 manual summary chart (Richardson and Davis 2001)

The HEC-18 (Richardson and Davis 2001) manual provides methods for estimating contraction scour, local scour, and other considerations. Two methods are provided for local pier scour with additional methods and adjustment factors for scour dealing with wide piers, complex groups, erodible rock, and cohesive soil. The recommended method for local pier scour is the TAMU-Scour Method which is discussed in Section 1.2.2 (Briaud 2015a, 2015b). The manual also provides some information on evaluating scour in waves. There are four approaches for estimating contraction scour dependent on the type of contraction and whether there is overbank flow or relief bridges. For each case, an equation is provided for both live-bed and clear-water bed conditions, where depending on the case the flow rates are calculated differently. The four cases are differentiated by the cross-sectional shape of the channel, whether there is bank overflow and the locations of embankments. The first step is to compare the upstream critical and mean flow velocities to determine which bed condition equation to use. The HEC-18 document also provides contraction scour depth equations specific for open-bottom culverts and vertical contractions at decks/weirs. The equations are similar those used for bridges but are tailored to suit the different channel flow geometry. In addition to the two methods for estimating local pier scour, the FHWA HEC-18 manual provides methodology for predicting scour at pile groups and pile caps exposed to the flow. One method by Jones and Sheppard (2000) follows similar steps to those for single piers and using superposition of the scour at piles and pile caps while applying correction factors for spacing effects. Another method for estimating scour at different pile grouping was based on the work of Salim and Jones (1995, 1996, 1999) and Smith (1999).

FHWA Contraction Scour in Live-Bed Conditions

The live-bed equation for contraction scour is a modified version of the Laursen (1960) equation written as

$$y_s = y_2 - y_0 \quad , \quad \frac{y_2}{y_1} = \left(\frac{Q_2}{Q_1}\right)^{6/7} \left(\frac{W_1}{W_2}\right)^{k_1} \tag{1.39}$$

where y_s is the average contraction scour depth, y_1 is the average depth upstream, y_2 is the average depth in the contracted section, y_0 is the existing depth in the contracted section before scour, Q_1 the flow upstream transporting sediment, Q_2 is the flow in the contracted channel, W_1 is the bottom width upstream, W_2 is the bottom width of the contracted section, and k_1 is the exponent based on

sediment parameters. As the live-bed scour equation includes deposition of material at the contracted section from upstream, the fall behaviour of soil must be considered. The exponent k_1 is obtained from Table 1.11.

Table 1.11: Laursen (1960) Equation Sediment Exponent

$V_*/\ \omega$	k_1	Mode of Bed Material Transport
<0.50	0.59	Mostly contact bed material discharge
0.50 to 2.0	0.64	Some suspended bed material discharge
>2.0	0.69	Mostly suspended bed material discharge

In Table 1.11, V_* is the frictional velocity upstream and ω is the fall velocity obtained from Figure 1.29 as a function of the median grain size D_s (D_{50}).

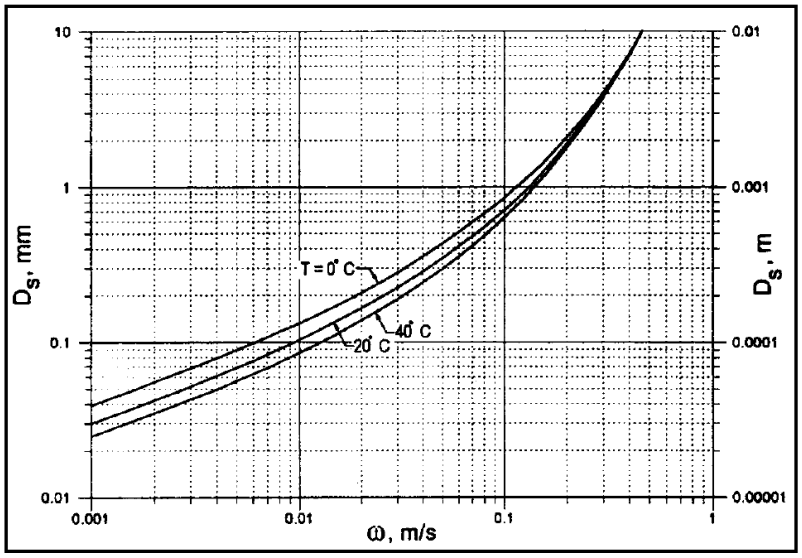

Figure 1.29: Sediment fall velocity versus grain size (Richardson and Davis 2001)

The changes from the original equation included removing the term containing Manning's coefficient which did not accurately reflect recent test results.

FHWA Contraction Scour in Clear-water Conditions

For the case of clear-water bed conditions a modified version of the Laursen (1963) equation is recommended as

$$y_s = y_2 - y_0 \qquad , \qquad y_2 = \left[\frac{K_u Q^2}{{D_m}^{2/3} W^2}\right]^{3/7} \tag{1.40}$$

where y_s is the average contraction scour depth, y_2 is the average depth in the contracted section, y_0 is the existing depth in the contracted section before scour, Q is the discharge through the bridge, D_m is the diameter of the smallest non-transportable particle in the bed material in the contracted section, W is the bottom width of the contracted section, and K_u is a constant equal to 0.025 for SI units.

FHWA Contraction Scour in Cohesive Soil

The recommended clear-water equation for contraction scour in cohesive soil was based on the analysis of laboratory data (Briaud et al. 2011). The equation for ultimate scour depth is given as

$$y_{s-ult} = 0.94 y_1 \left(\frac{1.83 V_2}{\sqrt{g y_1}} - \frac{K_u \sqrt{\frac{\tau_c}{\rho_w}}}{g n y_1^{1/3}} \right) \tag{1.41}$$

where y_1 is the upstream average flow depth, V_2 is the average flow velocity in the contracted section, n is the Manning roughness coefficient, τ_c is the critical shear stress of the soil, and K_u is valued at 1.0 for SI units. The critical shear stress for the cohesive soil would be obtained using experimental methods such as the EFA.

FHWA Local Pier Scour: HEC-18 Method

The FHWA developed their own method for local pier scour called the HEC-18 equation which is applicable for both live-bed and clear water conditions. By modifying the CSU equation, the HEC-18 formula was developed with the inclusion of a bed form factor. The HEC-18 formula is

$$\frac{d}{y_1} = 2.0 k_1 k_2 k_3 \left(\frac{b}{y_1}\right)^{0.65} {Fr_1}^{0.43} \tag{1.42}$$

where d is the local scour depth, k_1 is the correction factor for pier shape, k_2 is the correction factor for angle of attack, k_3 is the correction factor for bed condition, b is the width of the pier,

$Fr_1=V_1/(gy_1)^{0.5}$ is the Froude number, g is the acceleration due to gravity, V_1 is the mean velocity, and y_1 is the flow depth. The k_1 and k_2 correction factors can be obtained from Figure 1.26, or using the equation for k_2

$$k_2 = \left(\cos\theta + \frac{L}{b}\sin\theta\right)^{0.65} \tag{1.43}$$

where L is the pier length and θ is the angle of attack. The k_3 bed condition correction factor is obtained from Table 1.12 to account for the effects of flow acceleration over upstream dunes.

Table 1.12: HEC-18 dune correction factor (Richardson et al. 2012)

Bed Condition	Dune Height (m)	k_3
Clear-Water Scour	N/A	1.1
Plane bed and Antidune flow	N/A	1.1
Small Dunes	$3 > H \geq 0.6$	1.1
Medium Dunes	$9 > H \geq 3$	1.2 to 1.1
Large Dunes	$H \geq 9$	1.3

The dune correction factors indicate that even for plane-bed conditions, in field scour depths may exceed the estimate depth from Equation (1.42) by up to 10%. Therefore, the dune correction factor k_3 lead the HEC-18 method to be a more conservative version of the original CSU equation. Additional notes for the method state for angles of attack larger than 5°, k_1 is equal to 1.0, and for L/a values larger than 12, the k_2 factor for $L/a=12$ is used.

FHWA Local Pier Scour: Florida DOT Method

The second method discussed for local pier scour is the Florida DOT method which takes the consideration of many factors. A National Cooperative Highway Research Program (NCHRP) study in 2011 had been conducted and found though the HEC-18 equation for local scour performed well, the Sheppard and Miller (2006) equation was found to be more accurate in most cases. Then in a later NCHRP study, the Sheppard and Miller (2006) was modified to improve performance by including the flow angle of attack along with the pier geometry and shape. The improved method was expanded to form the Florida DOT method for estimating local pier scour. The Florida DOT relationship between scour depth and flow intensity is plotted in Figure 1.30.

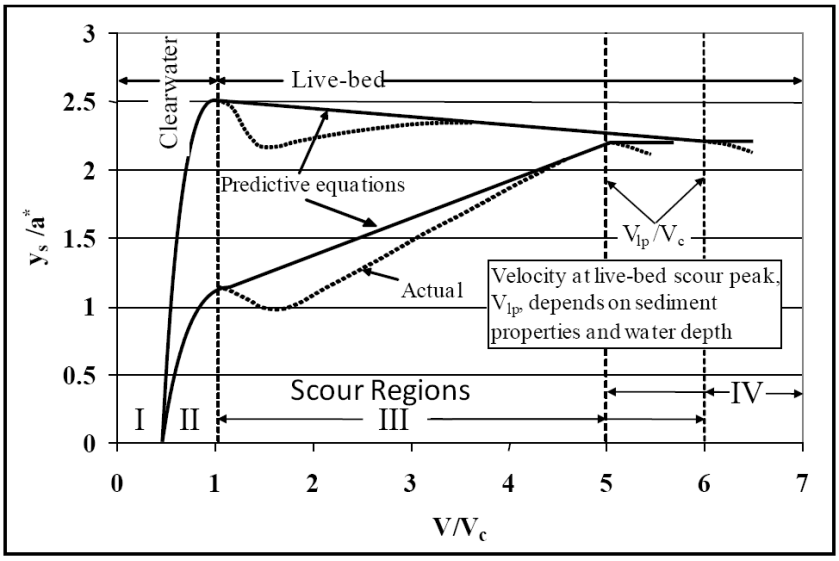

Figure 1.30: Florida DOT pier scour curve (Richardson and Davis 2001)

The method starts with calculating preliminary values using soil, flow, and structural properties. Firstly, the characteristic or shear velocity u_c^* is calculated using the following empirical equation

$$u_c^* = \begin{cases} 0.3048(0.0377 + 0.041D_{50}^{1.4}) & for\ 0.1\ mm < D_{50} < 1\ mm \\ 0.3048\left(0.1D_{50}^{0.5} - 0.0213/D_{50}\right) & for\ 1\ mm < D_{50} < 100\ mm \end{cases} \quad (1.44)$$

where D_{50} is the median grain size in mm. Next the critical velocity and live-bed peak velocity are calculated using

$$V_c = 5.75u_c^* log\left(5.53\frac{y}{D_{50}}\right) \quad (1.45)$$

$$V_{lp} = max\begin{cases} 5V_c \\ 0.6\sqrt{gy} \end{cases} \quad (1.46)$$

where u_c^* is the characteristic velocity, y is the flow depth, g is the acceleration due to gravity and D_{50} is the median grain size. The effects of angle of attack of the flow on the pier are considered by using the normal or projected width of the pier calculated using

$$b_{proj} = L\sin\theta + b\cos\theta \quad (1.47)$$

where L is the pier length, b is the pier width, and θ is the flow angle of attack in degrees. The method was tested for circular and square piers where the shape factor, K_{sf}, and the effective width, b^*, are calculated with the following equations

$$K_{sf} = \begin{cases} 0.86 + 0.97\left(\left|\frac{\pi\theta}{180} - \frac{\pi}{4}\right|\right)^4 & , \quad for\ square\ nosed\ piers \\ 1.0 & , \quad for\ circular\ nosed\ piers \end{cases} \tag{1.48}$$

$$b* = K_{sf} b_{proj} \tag{1.49}$$

where θ is the angle of attack in degrees. Once all the preliminary variables have been obtained the scour curve from Figure 1.30 is addressed. The scour curve was broken up by flow intensity values to distinguish between live bed and clear water scour. The curve is described using the equation

$$for\ V < 0.4V_c \quad , \quad d \cong 0$$

$$for\ 0.4 \le \frac{V}{V_c} < 1 \quad , \quad \frac{d}{b^*} = 2.5 f_1 f_2 f_3$$

$$for\ 1 \le \frac{V}{V_c} \le \frac{V_{lp}}{V_c} \ , \ \frac{d}{b^*} = f_1 \left[2.2 \left(\frac{\frac{V}{V_c} - 1}{\frac{V_{lp}}{V_c} - 1} \right) + 2.5 f_3 \left(\frac{\frac{V_{lp}}{V_c} - \frac{V}{V_c}}{\frac{V_{lp}}{V_c} - 1} \right) \right] \tag{1.50}$$

$$for\ \frac{V_{lp}}{V_c} < \frac{V}{V_c} \quad , \quad \frac{d}{b^*} = 2.2 f_1$$

where the variables f_1, f_2 and f_3 are defined as

$$f_1 = \tanh\left[\left(\frac{y}{b^*}\right)^{0.4}\right] \tag{1.51}$$

$$f_2 = \left\{1 - 1.2\left[ln\left(\frac{V}{V_c}\right)\right]^2\right\} \tag{1.52}$$

$$f_3 = \left[\frac{\left(\frac{b^*}{D_{50}}\right)^{1.13}}{10.6 + 0.4\left(\frac{b^*}{D_{50}}\right)^{1.33}}\right] \tag{1.53}$$

where d is the scour depth, V is the mean velocity, V_c is the critical velocity, V_{lp} is the live-bed peak velocity, b^* is the corrected pier width, y is the flow depth and D_{50} is the median grain size diameter. The steps to calculate the scour for a specific flow velocity is to first calculate the variables V_c, V_{lp}, b^*, f_1, f_2, and f_3. Next the mean velocity V, must be compared to V_c and V_{lp} to determine which scour zone the velocity intensity lies in. Using the in-field velocity intensity, Equation (1.50) is used to calculate the corresponding scour depth. If the mean velocity is such that $V<0.4V_c$, then the scour depth is said to be equal to zero for the initial clearwater conditions designated as zone I in Figure 1.30. However, there were some recorded non-zero scour depths in the field and lab for zone I, thus some ad hoc decisions should be made when designing using the Florida DOT method. Zone II was for large velocity intensity clear water scour conditions leading into Zone III live-bed scour. The final zone IV starts with the live-bed peak velocity, after which scour depth decreases with increasing velocity intensity.

FHWA Local Pier Scour: Wide Pier Correction Factor

The FHWA HEC-18 manual also provides additional information on predicting scour at wide piers and long skewed piers. For the case of wide piers in shallow flows the local scour was often overestimated because as the width of piers increased its influence on the scour depth decreased. Analysis of flume experiments conducted by Johnson and Torrico (1994) lead to the formulation of a wide pier correction factor, K_w, applicable for local pier methods. A pier was classified as wide if the ratio of flow depth to pier width was less than 0.8 ($y/b<0.8$), the ratio of pier width to medium grains size was greater than 50 (b/D_{50}), and the Froude number was subcritical ($Fr=V/(gy)^{0.5}<1$). The equation for K_w, dependant on the flow intensity is

$$K_w = \begin{cases} 2.58(y/b)^{0.34}Fr^{0.65} & for\ V/V_c < 1 \\ 1.0(y/b)^{0.13}Fr^{0.25} & for\ V/V_c \geq 1 \end{cases} \tag{1.54}$$

where y is the flow depth, b is the width of the pier, $Fr=V/(gy)^{0.5}$ is the Froude number, g is the acceleration due to gravity, V is the mean velocity, and V_c is the critical velocity.

FHWA Local Pier Scour with Effects of Debris

For certain channels, debris accumulation at bridge foundations is of concern as it increases the degree of local scour at piers. Debris would consist of wooden logs or ice surrounding piers

increasing the effective width for scour calculations. A NCHRP study was conducted to obtain an equation for the 'effective width" of piers with triangular and rectangular shaped debris as described in Figure 1.31.

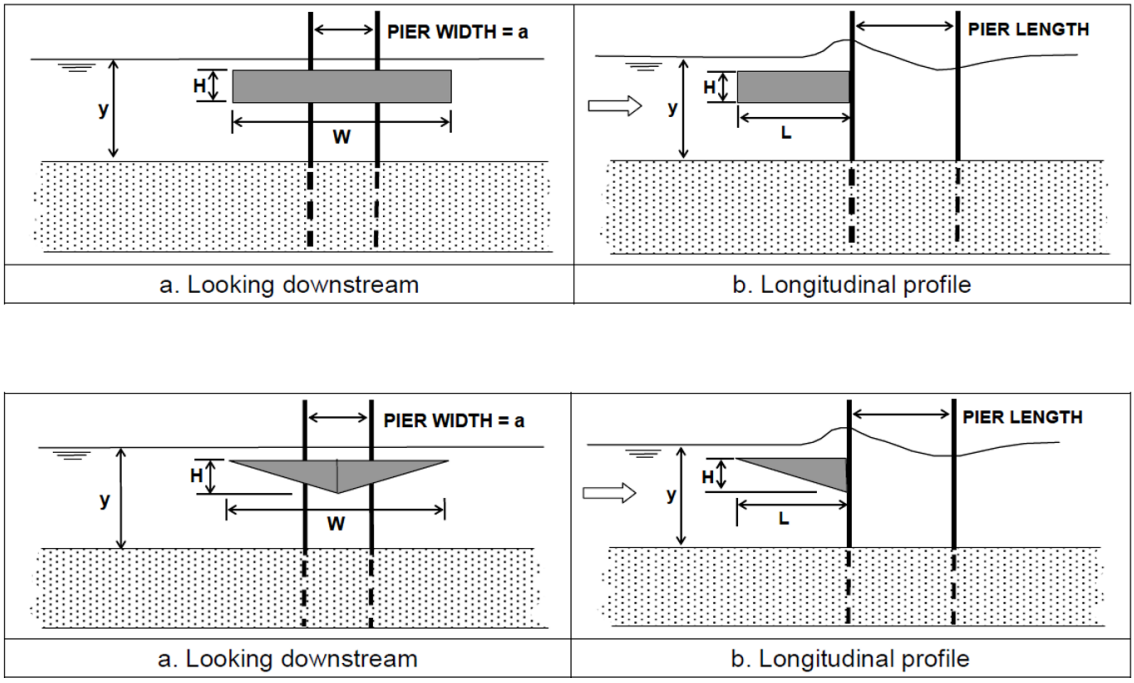

Figure 1.31: FHWA pier debris dimensions (Richardson and Davis 2001)

The debris would need to be evaluated on site to obtain the dimensions, and the debris is assumed to be floating at the water surface which is the most conservative case for calculating scour depth. Rectangular debris was found to produce significantly more scour than triangular as the disturbance to flow was much larger. The effective width equation was validated with the HEC-18 method but not the Florida DOT method. The equation for the effective width with debris b_d^* is

$$b_d^* = \frac{K(HW) + (y - KH)b}{y} \tag{1.55}$$

where y is the flow depth, b is the width of the pier, H is the height of the debris, W is the width of debris perpendicular to the flow direction as described in Figure 1.31, and K is the debris shape factor equal to 0.79 for rectangular debris and 0.21 for triangular debris. This effective width

would then be used in conjunction with the HEC-18 method to provide an estimate of scour depth with debris effects.

FHWA Local Pier Scour in Coarse Bed Materials Armour Layers

Section 1.1.2 discussed how coarser soil beds would produce an armored layer after some sediment sorting which would provide some protection against scour. A FHWA study was conducted on clear water scour conditions, ($V<V_c$), where laboratory and field data were used to include the effects of armour layers into the HEC-18 equation. The modified HEC-18 equation for coarse armor layers is

$$d = 1.1k_1k_2b^{0.62}y^{0.38}tanh\left(\frac{H^2}{1.97\sigma^{1.5}}\right) \tag{1.56}$$

where d is the local scour depth, y is the flow depth upstream, k_1 is the correction factor for pier shape from the original HEC-18 method, k_2 is the correction factor for angle of attack from the original HEC-18 method, b is the width of the pier, $\sigma = D_{84}/D_{50}$ is the sediment gradation coefficient, D_{50} is the median grain size, D_{84} is the 84% passing grain size, H is the densimetric particle Froude number defined as

$$H = \frac{V}{\sqrt{g(s-1)D_{50}}} \tag{1.57}$$

where V is the mean flow velocity, g is the acceleration due to gravity, and s is the specific gravity of the soil. This modified equation replaces the factor accounting for bed dunes, k_3, with a term containing the densimetric particle Froude number to encapsulate the effects the flow on the coarse grains. Due to the limited testing of the equation, it is only recommended for clear water conditions with a coarse bed where $D_{50} > 20\ mm$ and $\sigma > 1.5$.

FHWA Local Pier Scour in Erodible Rock

There are two different methods for calculating rock scour presented in the FHWA HEC-18 manual based on the two prevalent failure modes for rock scour discussed in Section 1.1.2. The first method predicts scour due to quarrying/plucking using the Erodibility Index Method developed by Annandale et al. (2006). In the case of quarrying/plucking erosion, rock

discontinuities have the greatest influence on scour depths. The quarrying/plucking scour of fractured rock around a pier is illustrated in Figure 1.32.

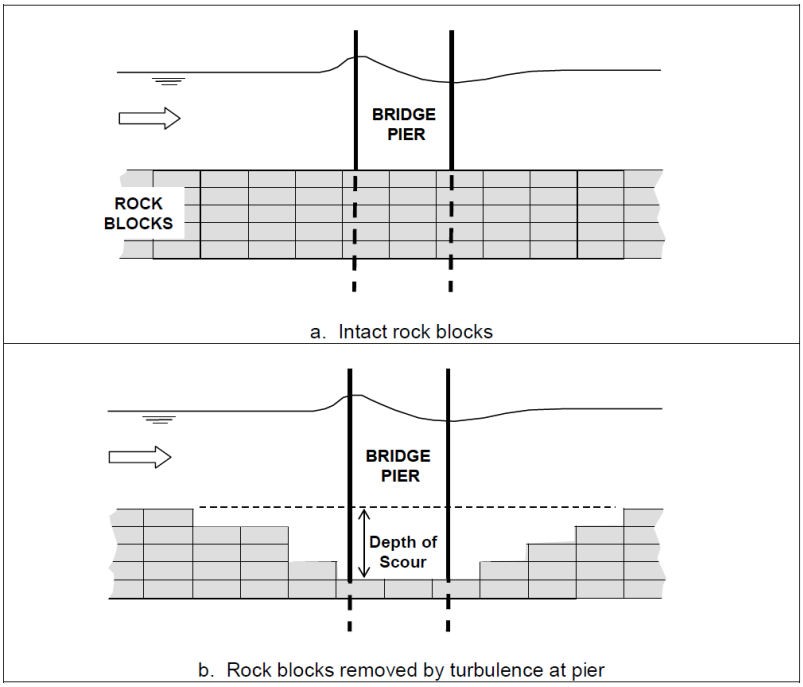

Figure 1.32: Rock quarrying scour around bridge pier (Richardson and Davis 2001)

The Erodibility Index Method starts with surveying and testing rock samples to determine the Erodibility Index *K* using the methods discussed in Section 1.1.2. Typical *K* values range from 0.1 for poor rock to greater than 10 000 good quality rock. The stream power which initiates rock scour is defined as the critical stream power is calculated using

$$P_c = K^{0.75} \tag{1.58}$$

where P_c is the critical stream power and *K* is the specific gravity of the rock. The stream power of the approach flow at a piers P_a is found using the equation developed by Annandale as

$$P_a = 7.853\rho\left(\frac{\tau}{\rho}\right)^{3/2} \tag{1.59}$$

where ρ is the mass density of water, $\tau=\gamma\, y\, S$ is the bed shear stress of the approach flow, *y* is the flow depth, γ is the unit weight of water, and *S* is slope of the energy grade line. The equation for the local pier scour depth was developed for piers of any shape as

$$\frac{P}{P_a} = 8.42e^{-0.712\left(\frac{d}{b}\right)} \tag{1.60}$$

where P is the stream power at the bottom of the scour hole, P_a is the stream power of the approach flow, d is the scour hole depth, and b is the pier width perpendicular to the flow. By substituting in the critical stream power P_c for P in Equation (1.60), then d can be solved for as the equilibrium scour depth.

The second method for estimating local pier scur in rock deals with the slower abrasion of rock surfaces caused by flowing bedload. Like quarrying/and plucking failure of rock, the vortices created by piers increases the amount of abrasion and thus the local scour depth as well. As the process of abrasive erosion is very slow and gradual, the design times of flood durations are very important. The stream power over a long period of time would need to be compared to the abrasion resistance of rock when predicting scour depth. The ASTM slake durability test evaluates a rocks resistance to weakening and disintegration caused by cycles of drying/wetting with abrasion. Though for the case for bridge foundations founded in rock the test is not suitable as the rocks would not experience a drying stage. To adapt the slake test for scour practices, Keaton et al. (2011) modified the test by relating the rock mass lost during testing with applied stream power. Keaton (2013) further discussed the modified slake test and its applicability in predicting rock scour. The modified slake durability test removed the oven drying step amongst other modifications to make the test more reflective of scour conditions so only weight loss due to abrasion was recorded. Keaton (2013) then related the weight loss data to an equivalent scour depth versus stream power relationship. The test provides a plot of data points for Equivalent Hourly Stream Power versus Equivalent Hourly Scour Depth, where the slope is the Geotechnical Scour Number (GSN). Lower values of GSN indicated a more resilient rock, and a relationship was developed for predicated scour depths and the GSN. For different values of GSN, the scour depth is dependent on the duration of the stream power as summarized in Figure 1.33.

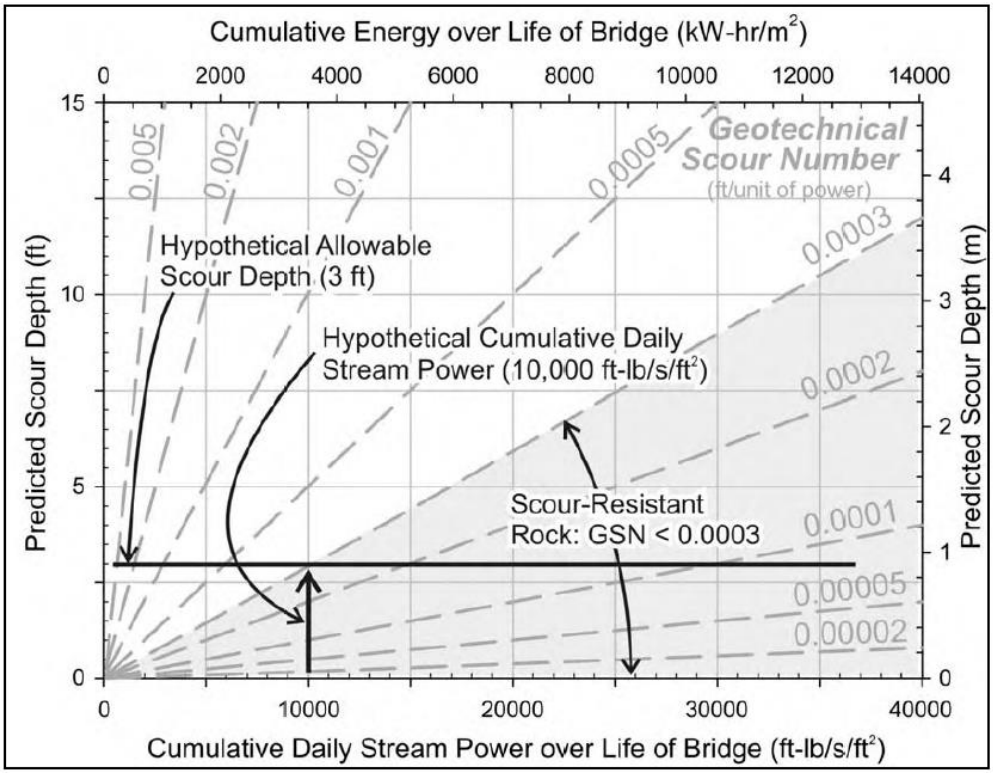

Figure 1.33: Pier scour in rock as a function P_c and GSN (Richardson and Davis 2001)

The work done on rock by fluid is the product of stream power and time, so integrating a time series of stream power can provide the most meaningful representation of flow work done. The integral was termed as Cumulative Daily Stream Power and was denoted using Ω [kW-hr/m^2]. The equation for pier scour in erodible rock due to abrasion was

$$d = (GSN)(\Omega) \tag{1.61}$$

where d is the scour depth, GSN is the Geotechnical Scour Number, and Ω is the Cumulative Daily Stream Power. Having obtained a daily discharge versus time chart for the design pier it must be converted into an effective discharge where effective discharge above a threshold value where bedload motion would occur. The effective stream power chart is then integrated over time to get the Cumulative Daily Stream Power Ω. The difficulty of this method that a value for Cumulative Daily Stream Power representing future events would need to be predicted for design. Engineering judgement is of upmost importance for coming up with an estimate for the future Cumulative Daily Stream Power value.

FHWA Local Abutment Scour: Froehlich's (1989) Equation

The FHWA HEC-18 manual provides insight on analyzing abutment scour and methods for depth estimation. Three methods were provided for estimating scour depth at bridge abutments, the first of which was Froehlich's (1989) equation. By performing regression analysis on 170 live-bed scour measurements Froehlich developed the equation as

$$\frac{y_s}{y_a} = 2.27K_1K_2\left(\frac{L'}{y_a}\right)^{0.43} Fr^{0.61} + 1 \tag{1.62}$$

where y_s is the scour depth, y_a is the flow depth of the floodplain, L' is the length of active flow obstructed by the embankment, $Fr=V_e/(gy_a)^{1/2}$ is the Froude number of the approach flow at the abutment, $V_e = Q_e/A_e$, Q_e is the flow obstructed by the abutment and approach embankment, A_e is the area of the approach cross section obstructed by the embankment, K_1 is the abutment shape factor obtained from Table 1.13, and $K_2 = (\theta/90)^{0.13}$ is the angle of embankment factor where θ is measured as described in Figure 1.34.

Table 1.13: Local abutment scour shape factor

Abutment Shape/Type	K_1
Vertical-wall abutment	1.00
Vertical-wall abutment with wing walls	0.82
Spill-through abutment	0.55

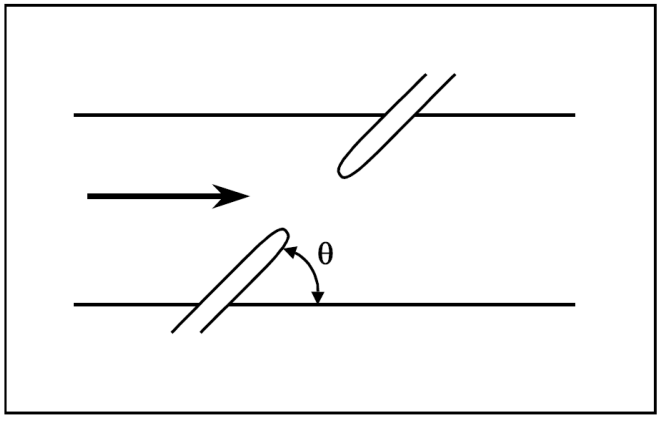

Figure 1.34: Abutment orientation angle (Richardson and Davis 2001)

FHWA Local Abutment Scour: HIRE Abutment Scour Equation

The second method for predicting abutment scour in the FHWA HEC-18 Manual is the HIRE equation. The method was based on a previous equation used to predict scour at the end of spurs in the Mississippi River. The HIRE equation is applicable for cases where the ratio of projected abutment length, L, to the flow depth, y_1, is greater than 25. The HIRE equation is defined as

$$\frac{y_s}{y_1} = 4Fr^{0.33}\frac{K_1}{0.55}K_2 \tag{1.63}$$

where y_s is the scour depth, y_1 is the flow depth at the abutment, $Fr=V/(gy1)^{1/2}$ is the Froude number of the approach flow at the abutment, V is the flow velocity at the abutment, K_1 is the abutment shape factor obtained from Table 1.13, and $K_2= (\theta/90)^{0.13}$ is the angle of embankment factor where θ is measured as described in Figure 1.34.

FHWA Local Abutment Scour: NCHRP 24-20 Abutment Scour Approach

The third method for predicting the total scour at abutments is the NCHRP 24-20 Abutment Scour Approach (Ettema et al. 2010). The method considers abutment types, abutment locations, flow conditions, and sediment transport conditions. The method first calculates the contraction scour and then applies a factor to include effects of local large-scale turbulence at abutments for local scour. The scour equations for both live-bed and clear water conditions are

$$y_{max} = \begin{cases} \alpha_A y_c & for\ live-bed\ conditions \\ \alpha_B y_c & for\ clear-water\ conditions \end{cases} \tag{1.64}$$

$$y_s = y_{max} - y_0 \tag{1.65}$$

where y_{max} is the maximum flow depth due to abutment scour, y_c is the flow depth including contraction scour, α_A is the amplification factor for live-bed conditions, α_B is the amplification factor for clear-water conditions, y_s is the abutment scour depth, and y_0 is the flow depth prior to scour. The approach differs depending on which of the three abutment conditions is applicable; *"(a) scour occurring when the abutment is in or close to the main channel, (b) scour occurring when the abutment is set back from the main channel, and (c) scour occurring when the embankment breaches and the abutment foundation acts as a pier*" (Richardson and Davis 2001).

Condition (a) is meet when the projected length of embankment, *L*, is greater than or equal to 75% of the floodplain width, *Bf*. The contraction scour equation for condition (a) is a modified version of the live-bed scour Equation (1.39), and is defined as

$$y_c = y_1 \left(\frac{q_{2c}}{q_1}\right)^{6/7} \tag{1.66}$$

where y_c is the flow depth including live-bed contraction scour, y_1 is the average depth upstream, q_1 the upstream unit discharge, and q_2 is the unit discharge in the constricted opening accounting for non-uniform flow distribution. The live-bed amplification factor α_A is obtained from the solid line in Figure 1.35 for spill through abutments and from Figure 1.36 for wingwall abutments.

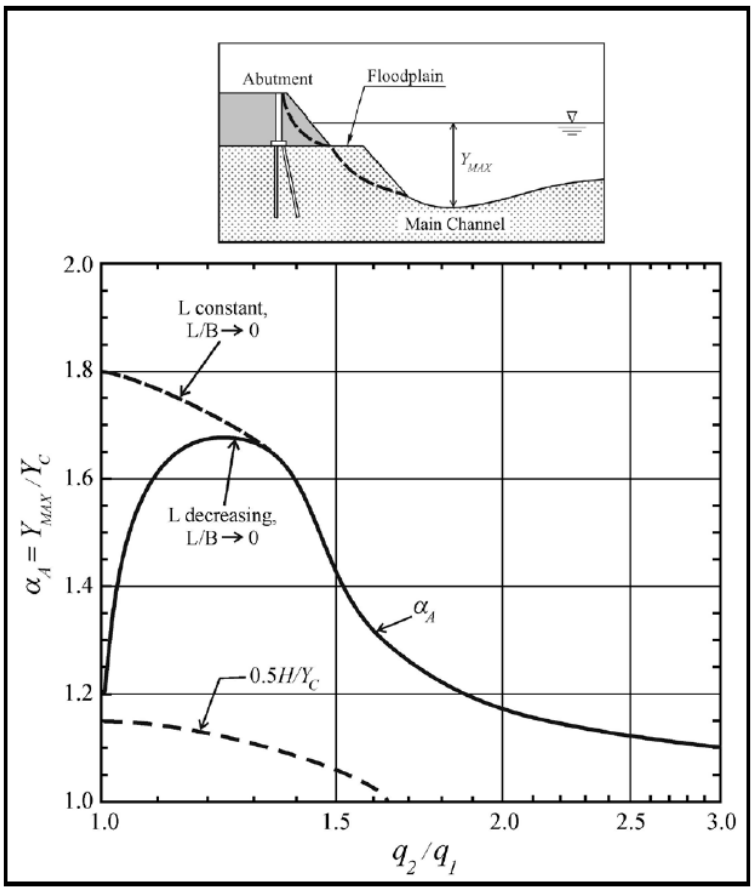

Figure 1.35: Scour amplification factor for spill-through abutments and live-bed conditions (Ettema et al. 2010)

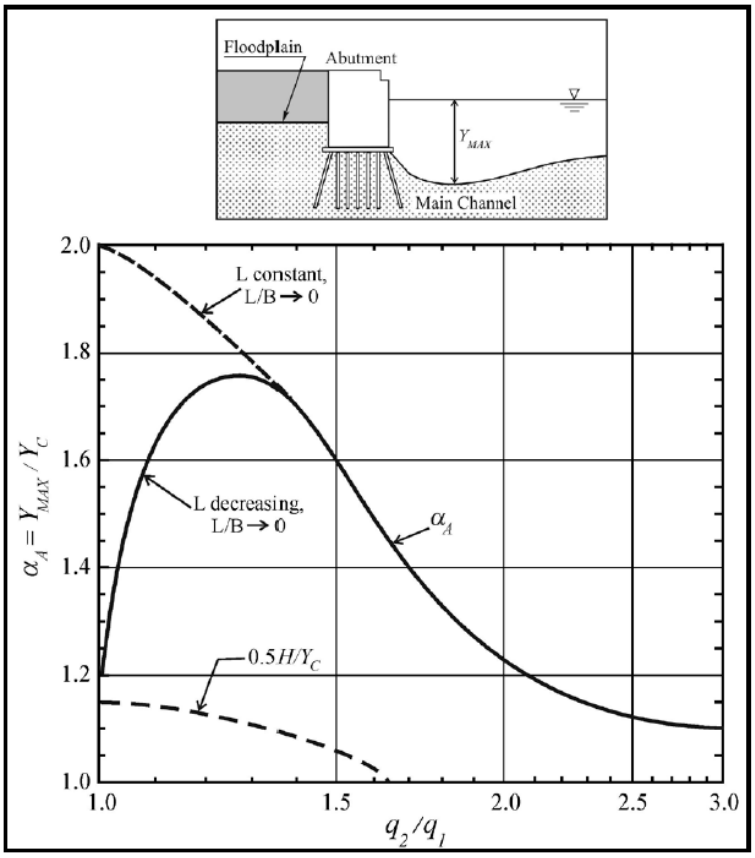

Figure 1.36: Scour amplification factor for wingwall abutments and live-bed conditions (Ettema et al. 2010)

The next condition (b) is meet when the embankment projected length, L, is less than 75 percent of the floodplain width, B_f. Condition (b) contraction scoured is calculated using the clear-water equation

$$y_c = \left(\frac{q_{2f}}{K_u D_{50}^{1/3}} \right)^{6/7} \tag{1.67}$$

where y_c is the flow depth including clear-water contraction scour, q_{2f} is the unit discharge in the constricted opening accounting for non-uniform flow distribution, K_u is a constant equal to 6.19 for SI units, and D_{50} is the median soil grain size. Equation (1.67) is recommended for coarse soils larger than 0.2 mm in diameter, whereas for finer soils with cohesion the following alternative clear water equation can be used

$$y_c = \left(\frac{\gamma}{\tau_c}\right)^{3/7} \left(\frac{nq_{2f}}{K_u}\right)^{6/7} \tag{1.68}$$

where y_c is the flow depth including clear-water contraction scour, q_{2f} is the unit discharge in the constricted opening accounting for non-uniform flow distribution, K_u is a constant equal to 1.0 for SI units, n is the Manning roughness of the channel bed, γ is the water unit weight, and τ_c is the soil's critical shear stress. The live-bed amplification factor α_B is obtained from the solid line on Figure 1.37 for spill through abutments and from Figure 1.38 for wingwall abutments.

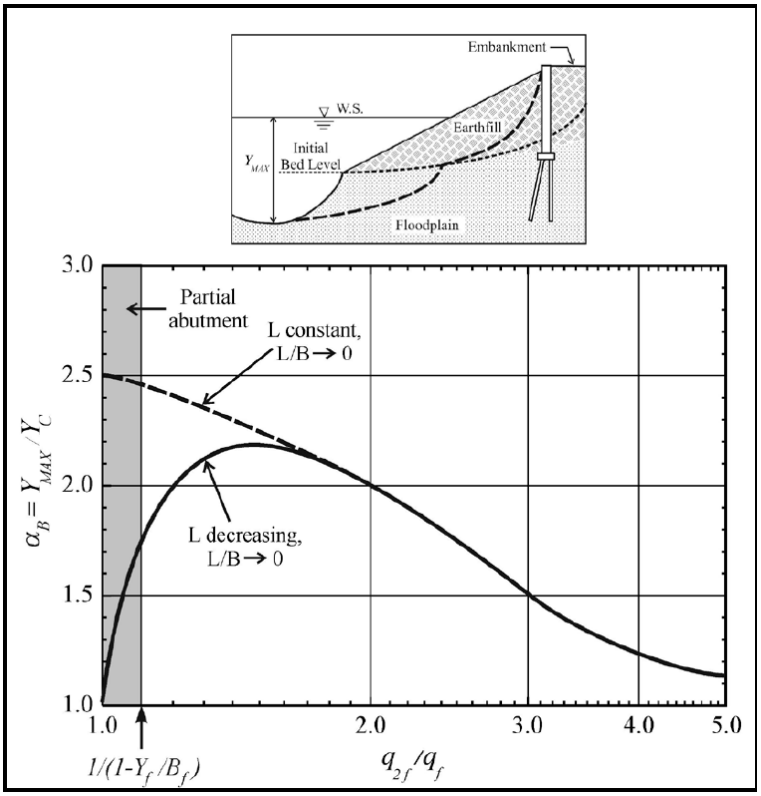

Figure 1.37: Scour amplification factor for spill-through abutments and clear-water conditions (Ettema et al. 2010)

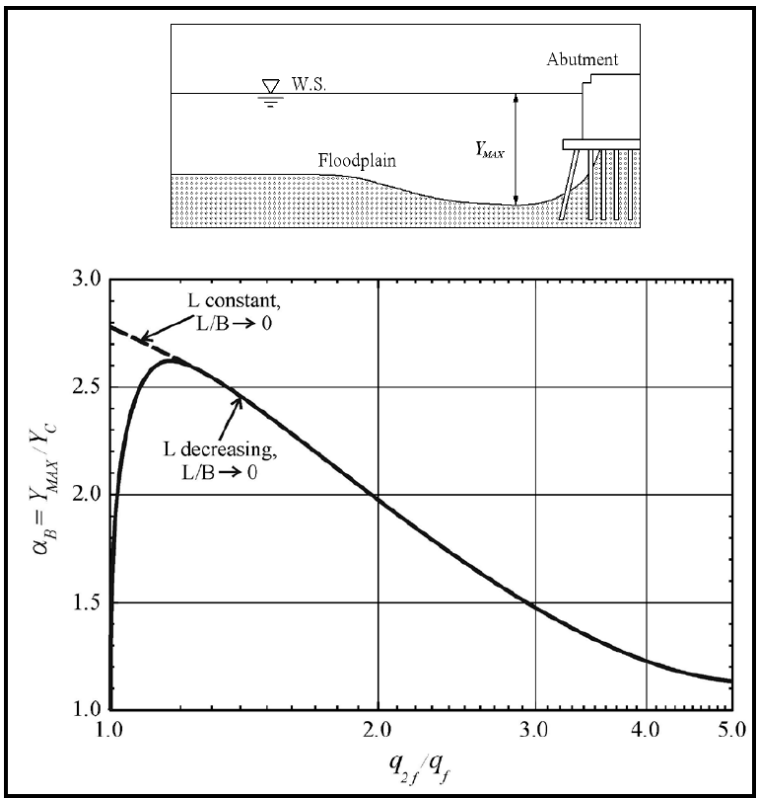

Figure 1.38: Scour amplification factor for wingwall abutments and clear-water conditions (Ettema et al. 2010)

For condition (c) the abutment is separated from the bank and its local scour is estimated using any of the suggested methods for piers. This method includes more details in the HEC-18 manual and recommendations of other factors geotechnical engineering should consider during design for scour. Ad hoc decisions are required as this method for estimating abutment scour considers flow, soil, and structural conditions along the entire channel width. Some of these additional factors to consider include channel bank/embankment stability, specifics of unit discharge calculations, and variation of critical shear stress in different areas of the contraction.

1.2.2 Other Methods for Contraction and Local Scour

Sheppard and Miller (2006): Local Pier Scour

Sheppard and Miller (2006) developed an equation for estimating live-bed scour at single circular piers, which has been often modified with new data to form other equations. The data used was obtained from a multitude of tilting flume test with varying flow depths, flow velocities

and two cohesionless sediments. Tests were running with flow intensity ratios V/V_c up to 6, near where the peak live-bed scour occurred for the examined sediments. The results of the tests were used to determine the general relationship between the flow intensity V/V_c and normalized scour depth d_{se}/D, where d_{se} is the scour depth and D is the pier diameter. The general scour curve found from testing is shown in Figure 1.39.

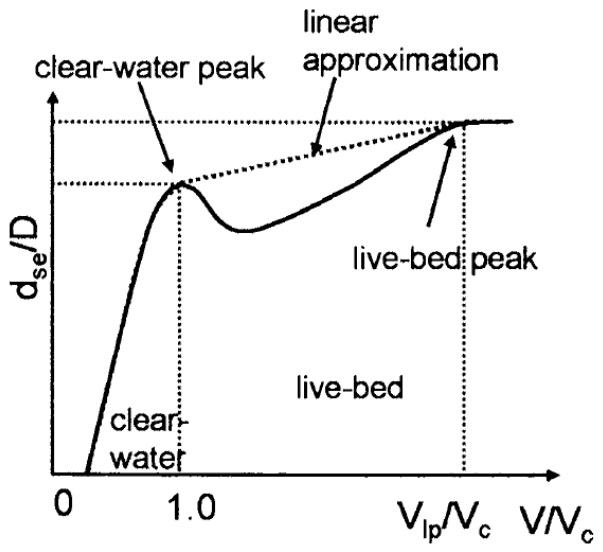

Figure 1.39: Normalized scour depth versus flow intensity (Sheppard and Miller 2006)

Figure 1.39 illustrates the transition from clear-water to live-bed scour, and the curve can be broken up using three different equations depending on the range of flow intensity. It was found that the live-bed peak scour occurs at a mean flow velocity of V_{lp}, which is denoted as the live-bed peak velocity. Sheppard and Miller (2006) define the live-bed peak velocity as when the flow Froude number, $F_r=V/(gy_0)^{1/2}$, is greater than 0.8 and the sediment transport parameter, $[(\tau_b- \tau_c)/\tau_c]$, is greater than 25. In the former condition statements, V is the flow velocity, y_0 is the flow depth, g is the acceleration due to gravity, τ_c is the critical shear stress of the soil, and τ_b is the bed shear stress. The velocity, V, which satisfies both conditions is the live-bed peak velocity, V_{lp}, for the given flow depth, and soil critical shear stress. After performing regression analysis, the scour depth curve described in Figure 1.39 was fitted with the following equation

$$0.47 \leq \frac{V}{V_c} \leq 1 \quad , \quad \frac{d_{se}}{D} = 2.5 f_1\left(\frac{y_0}{D}\right) f_2\left(\frac{D}{D_{50}}\right)\left\{1 - 1.75\left[ln\left(\frac{V}{V_c}\right)\right]^2\right\} \qquad (1.69)$$

$$1 < \frac{V}{V_c} \leq \frac{V_{lp}}{V_c} \quad , \qquad \frac{d_{se}}{D} = f_1\left(\frac{y_0}{D}\right)\left[2.2\left(\frac{\frac{V}{V_c}-1}{\frac{V_{lp}}{V_c}-1}\right) + 2.5 f_2\left(\frac{D}{D_{50}}\right)\left(\frac{\frac{V_{lp}}{V_c}-\frac{V}{V_c}}{\frac{V_{lp}}{V_c}-1}\right)\right]$$

$$\frac{V_{lp}}{V_c} < \frac{V}{V_c} \qquad , \qquad \frac{d_{se}}{D} = 2.2 f_1\left(\frac{y_0}{D}\right)$$

where the functions f_1 and f_2 are defined as

$$f_1\left(\frac{y_0}{D}\right) = \tanh\left[\left(\frac{y_0}{D}\right)^{0.4}\right] \tag{1.70}$$

$$f_2\left(\frac{D}{D_{50}}\right) = \frac{D/D_{50}}{0.4(D/D_{50})^{1.2} + 10.6(D/D_{50})^{-0.13}} \tag{1.71}$$

where d_{se} is the scour depth, V is the mean velocity, V_c is the critical velocity, V_{lp} is the live-bed peak velocity, D is the pier diameter, y_0 is the flow depth and D_{50} is the median grain size. For some validation of the new method, it was tested against experimental results and compared to three other common methods. The three other methods were the CSU (1977) equation, a method developed by Breusers et al. (1977), and Melville's (1997) method which was an updated version of the Melville and Sutherland (1988) method. The Sheppard and Miller (2006) method performed well with the smallest error amongst the four, although it under predicted scour for extremely low and high values of flow intensity.

Breusers (1977): Local Pier Scour

Breusers et al. (1977) investigated the turbulent flow occurring at circular piers and summarised the findings. Breusers also analyzed the existing equations for estimating local pier scour and provided their own recommended method based on different components of existing equations. The equation provided by the Breusers (1977) method is defined as

$$\frac{d}{b} = f_1\left(\frac{V}{V_c}\right)\left[2.0\tanh\left(\frac{y}{b}\right)\right] f_2(shape) f_3\left(\alpha, \frac{1}{b}\right) \tag{1.72}$$

where V is the flow velocity, V_c is the critical velocity of the soil, d is the scour depth, b is the pier width, y is the flow depth, and α is the angle of attack in degrees. The bed condition factor f_1 is defined as

$$\frac{V}{V_c} \leq 0.5 \quad , \quad f_1\left(\frac{V}{V_c}\right) = 0$$

$$0.5 < \frac{V}{V_c} \leq 1 \quad , \quad f_1\left(\frac{V}{V_c}\right) = \left(2\frac{V}{V_c} - 1\right) \tag{1.73}$$

$$1 < \frac{V}{V_c} \quad , \quad f_1\left(\frac{V}{V_c}\right) = 1$$

where V is the flow velocity, and V_c is the critical velocity of the soil. The pier shape factor f_2 is defined as 1.0 for circular/rounded piers, 0.75 for streamlined shapes such as lenticular, and 1.3 for rectangular piers. The angle of attack factor f_3 is obtained from Figure 1.40 for non-circular piers as a function of the angle of attack θ and pier shape ratio L/b, where L is the pier length and b is the pier width.

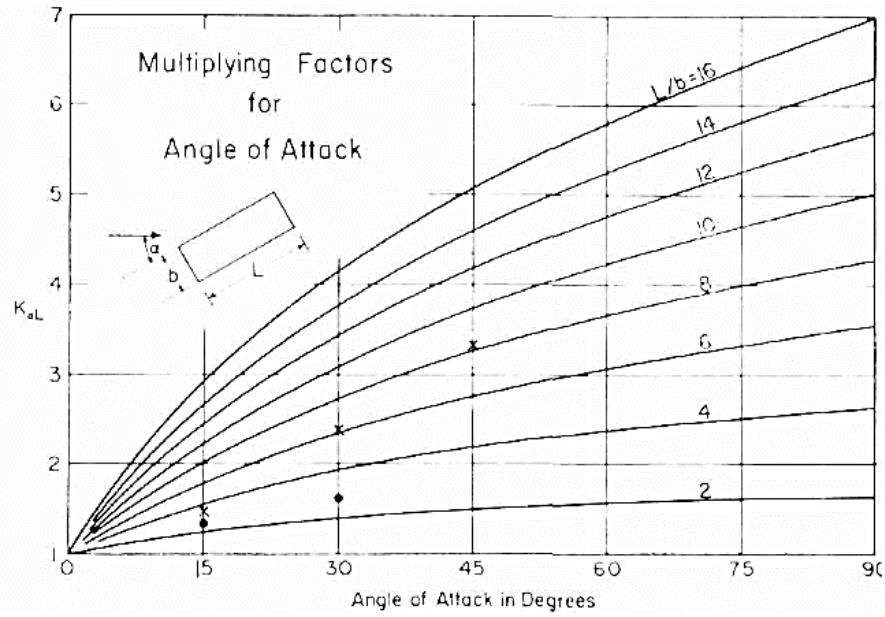

Figure 1.40: Angle of attack correction factor (Breusers 1977)

Breusers (1977) found that the relationship between d/b and y/b was best described by a tangent hyperbolic function as opposed to exponential relations used in the past. As shown in Equation (1.73), lower velocity intensity was found to produce insignificant amounts of scour, while the clear-water bed conditions were demonstrating a linear relation with velocity and scour depth. In live bed conditions the transport of soil into and out of the scour hole was assumed to be in equilibrium. Thus, for flow intensities above one, the scour hole depth was not expected to

increase at the time. A coefficient of 2.0 was placed in Equation (1.72) as a safety factor to account for unknowns and provide a conservative estimate. At the time, no significant findings for the influence of bedforms or sediment size were included within the method.

Melville (1992): Local Abutment Scour

Melville (1992) evaluated lab data and used dimensional analysis to develop equations for estimating the depth of local scour holes, *d*, at bridge abutments. The length of the abutments, *L*, was found to be the largest contributing factor for shorter abutments, however for long abutments, the flow depth, *y*, the most influential factor for scour depths. Therefore, equations for local scour at short and long abutments were written in terms of *d/L* and *d/y*, respectively. Melville defined short abutments as those with *L/y* ratios less than 1, and long abutments as those with *L/y* ratios greater than 25. Written in the same manner as the pier local scour equations developed Melville and Sutherland (1988), the equations for local scour at short and long abutments are

$$\frac{d}{L} = k_I k_y k_d k_\sigma k_s k_\theta k_G \tag{1.74}$$

$$\frac{d}{y} = k_I k_L k_d k_\sigma k_s k_\theta k_G \tag{1.75}$$

where *d* is the local scour depth, *y* is the flow depth, *L* is the abutment length, k_I is the flow intensity factor, k_y is the flow depth factor, k_L is the abutment length factor, k_d is the sediment size factor, k_σ is the sediment gradation factor, k_s is the abutment shape factor, k_θ is the pier alignment coefficient, and k_G is the approach channel geometry factor. The shape factors were obtained through regression analysis of laboratory data, where the vertical wall abutment is used as reference as it produces the largest scour depth. The shape factor k_s for abutment shapes is listed in Table 1.14.

Table 1.14: Local abutment scour shape factor (Melville 1992)

Abutment Shape	k_s
Vertical wall	1.00
Vertical wall with semicircular end	0.75
45° wing wall	0.75
Spill-through abutment (*H:V*)	
0.5:1	0.60
1:1	0.50
1.5:1	0.45

The shape factors in Table 1.14 include spill-through abutments of three different slope ratios where *H:V* is the width to height ratio of the sloped walls. The reduced flow restriction of abutments shapes other than vertical walls is captured in the shape factors. The shape factors in Table 1.14 are to be used only for short abutments and it was proposed that shape effects were negligible for long abutments. To distinguish between short, long, and in-between abutments, a corrected shape factor k_s^* was proposed as

$$\begin{aligned} \frac{L}{y} \leq 10 \quad &, \quad k_s^* = k_s \\ 10 < \frac{L}{y} < 25 \quad &, \quad k_s^* = k_s + (1 - k_s)\left(0.1\frac{L}{y} - 1.5\right) \\ \frac{L}{y} \geq 25 \quad &, \quad k_s^* = 1 \end{aligned} \tag{1.76}$$

where k_s^* is used in place of k_s in Equations (1.74) and (1.75). The alignment angle of abutments relative to flow was evaluated using previously recorded laboratory data from other researchers. A perpendicular abutment at 90° was used as reference for the alignment factor as shown in Figure 1.41.

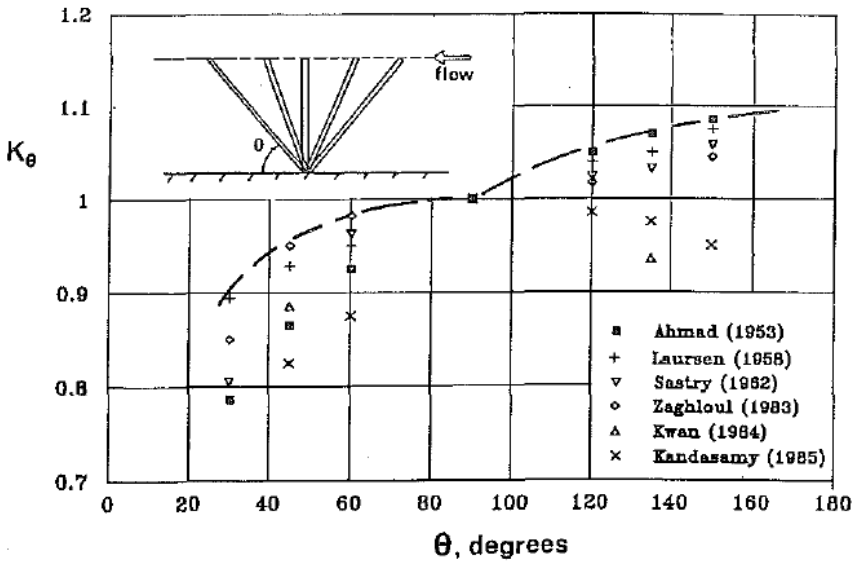

Figure 1.41: Abutment alignment angle factor (Melville 1992)

As seen in Figure 1.41, for smaller angles the abutment becomes more aligned with the flow reducing the scour depth and for angles larger than 90° flow produced larger scour depths. It was found that the impact of abutment alignment was diminished for short abutments, so a corrected alignment factor k_θ^* was recommend as

$$\begin{aligned} \frac{L}{y} \geq 3 \quad &, \quad k_\theta^* = k_\theta \\ 1 < \frac{L}{y} < 3 \quad &, \quad k_\theta^* = k_\theta + (1 - k_\theta)\left(1.5 - 0.5\frac{L}{y}\right) \\ \frac{L}{y} \leq 1 \quad &, \quad k_\theta^* = 1 \end{aligned} \tag{1.77}$$

where k_θ^* is used in place of k_θ in Equations (1.74) and (1.75). At the time there was a lack of research and laboratory data on the effects of soil grain size and gradation. Thus, both soil factors, k_g and k_d were set equal to 1.0. Testing results indicated the maximum scour depth ratios for the short and long abutments as *2L* and *10y*, respectively. As most abutments are neither short or long, but fall in between, the effects of both flow depth and abutment length needed to be addressed. For those abutments lying in between short and long, Melville (1992) found an envelope to describe the maximum depth as

$$d = 2(yL)^{0.5} \tag{1.78}$$

where d is the maximum scour depth for the given flow depth, y, and abutment length, L. Investigating the effect of flow intensity, Melville there was not enough data to express a strong relationship, so the k_I factor was set equal to 1.0. The channel shape factor k_G, accounts for channel geometry by evaluating the ratio of depth in the flood plain to the main channel and the ratio of floodplain width to abutment length. Once again due to the complexity of possible channel shapes and limited data at the time, the shape factor k_G was recommended to be taken as 1.0 as well. The remaining factors address were the depth and length factors k_y and k_L. There was no explicit expression for k_y and k_L, as the method uses the different shape and alignment factors to account for the effects. With the final expressions for the correction factors the simplified form of Equations (1.74) and (1.75) becomes

$$\begin{aligned} \frac{L}{y} < 1 \quad &, \quad d = 2k_s L \\ 1 \leq \frac{L}{y} \leq 25 \quad &, \quad d = 2\, k_s^*\, k_\theta^* (yL)^{0.5} \\ \frac{L}{y} > 25 \quad &, \quad d = 10 k_\theta y \quad . \end{aligned} \tag{1.79}$$

In summary, Equation (1.79) is used to predict local abutment scour while considering flow depth and abutment length ratios, which then in turn include how shape and alignment factors are applied. Factors relating to soil size, soil gradation, channel shape and flow intensity were recommended to be further investigated in later research.

Melville (1997): Local Pier and Abutment Scour

Melville provided a method to calculate both the local scouring at piers and abutments of bridges. The method was a follow up to the Melville and Sutherland (1988) local pier scour equation and the Melville (1992) local abutment scour equation. Using newly acquired laboratory data, Melville and Raudkivi (1997) were able to update the previous equations with new correction factors for soil and flow conditions. In addition to local single pier scour, some factors are provided for determining local scour at pile groups. The same general depth estimation equation

is used for both local scour at piers and abutments where the two are distinguished by the structural shape factors. The general local scour equation for the integrated approach is written as

$$d = k_{yW} k_I k_d k_s^* k_\theta^* k_G \tag{1.80}$$

where d is the local scour depth, the depth size factor is $k_{yw} = k_{yb}$ for piers and $k_{yw} = k_{yL}$ for abutments, k_I is the flow intensity factor, k_d is the sediment size factor, the foundation size factor is $k_s^* = k_s$ for piers and k_s^* for abutments, the flow alignment factor is $k_\theta^* = k_\theta$ for piers and k_θ^* for abutments, and the channel geometry factor k_G only applies to abutments. As with Melville and Sutherland (1988) method, the soil's critical velocities and armouring behaviour is addressed. The procedure starts with calculating the critical shear velocity, u_{*c}, and the critical armor shear velocity, u_{*ca}, with the equation

$$u_{*c} = \begin{cases} 0.0115 + 0.0125 D_{50}^{1.4} & , \quad 0.1\ mm < D_{50} < 1\ mm \\ 0.0305 D_{50}^{0.5} - 0.0065 D_{50}^{-1} & , \quad 1\ mm < D_{50} < 100\ mm \end{cases} \tag{1.81}$$

where D_{50} is the median grain size, $D_{50a} = D_{max}/1.8$ is used to obtain u_{*ca}, and D_{max} is the maximum soil particle size. Next the critical velocity, V_c, and critical armour velocity, V_{ca}, are calculated using Equation (1.35) and the mean approach flow velocity at the armor peak is calculated as $V_a = 0.8 V_{ca}$. The flow intensity factor k_I is determined using the following equation

$$k_I = \begin{cases} \left| \dfrac{V - (V_a - V_c)}{V_c} \right| & , \quad \dfrac{V - (V_a - V_c)}{V_c} < 1.0 \\ 1 & , \quad \dfrac{V - (V_a - V_c)}{V_c} \geq 1.0 \end{cases} \tag{1.82}$$

where V is the mean flow velocity. The sediment size factor, k_d, is calculated Equation (1.38), where for abutments the abutment length L is used instead of pier width b. The different foundation component classifications are described in Figure 1.42.

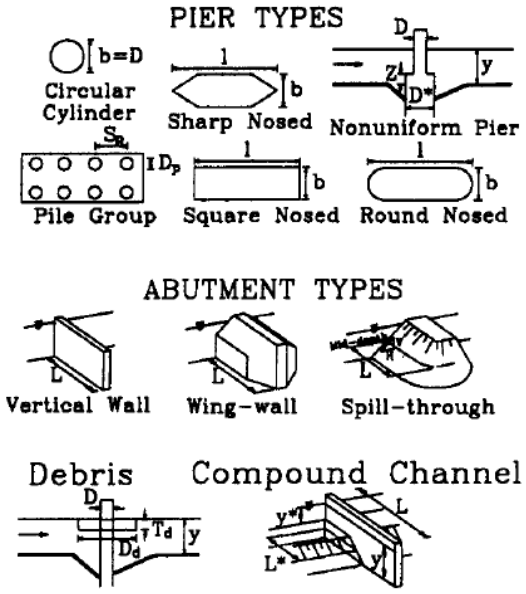

Figure 1.42: Pier and abutment classifications (Melville 1997)

The base shape factor, k_s, is 1.0 for round nosed piers, 1.1 for square nosed piers, 0.9 for sharp nosed piers and for abutments the shape factor is obtained from Table 1.14. For non-aligned flows where the angle of attack, θ, is greater than 5°, the shape factor is taken as $k_s=1.0$. For simple pile groups the shape and alignment factors are taken together and displayed in Table 1.15, where S_p is the spacing between piles and D_p is the pile width as illustrated in Figure 1.42.

Table 1.15: Multiplying factors (K_sK_θ) for group piles (Melville 1997)

Type (1)	S_p/D_p (2)	K_sK_θ θ < 5° (3)	θ = 5–45° (4)	θ = 90° (5)
Single row	2	1.12	1.40	1.20
	4	1.12	1.20	1.10
	6	1.07	1.16	1.08
	8	1.04	1.12	1.02
	10	1.00	1.00	1.00
Double row	2	1.50	1.80	—
	4	1.35	1.50	—

In addition to different cross-sectional shapes, Melville (1997) also provided a technique for estimating scour at nonuniform piers or piers with debris as displayed in Figure 1.42. From laboratory test data, an equivalent pier width D_e can be used in the method, where D_e is calculated using the equation

$$D_e = D\left(\frac{y - Z}{y + D^*}\right) + D^*\left(\frac{D^* + Z}{D^* + y}\right) \tag{1.83}$$

where D is the top pier section width, D^* is the bottom pier section width, y is the flow depth and Z is the height of the bottom pier section above the bed. For effects of floating debris, another relationship was developed for determining an equivalent pier width with the equation

$$D_e = \frac{0.52T_dD_d + (y - 0.52T_d)D}{y} \tag{1.84}$$

where T_d and D_d are the thickness and diameter of the floating debris raft. For abutments, the base shape factor k_s obtained from Table 1.14 is adjusted based on the behaviour of short and long abutments. The modified shape factor k_s^* is calculated using the following equation, which has been updated from the Melville (1992) method as

$$\begin{aligned} \frac{L}{y} \leq 10 \quad &, \quad k_s^* = k_s \\ 10 < \frac{L}{y} < 25 \quad &, \quad k_s^* = k_s + 0.667(1 - k_s)\left(0.1\frac{L}{y} - 1\right) \\ \frac{L}{y} \geq 25 \quad &, \quad k_s^* = 1 \end{aligned} \tag{1.85}$$

where L is the length of the abutments, y is the flow depth and k_s is the base shape factor. The base alignment factor k_θ is interpolated from Table 1.16 for abutments and piers as a function of the width to length ratio, L/b.

Table 1.16: Melville (1997) Flow Alignment Factor

Foundation type (1)		K_θ (°) θ = 0 (2)	15 (3)	30 (4)	45 (5)	60 (6)	90 (7)	120 (8)	150 (9)
Pier	l/b = 4	1.0	1.5	2.0	2.3	—	2.5	—	—
	8	1.0	2.0	2.75	3.3	—	3.9	—	—
	12	1.0	2.5	3.5	4.3	—	5.0	—	—
Abutment		—	—	0.9	—	0.97	1.0	1.06	1.08

As with the Melville (1992) abutment method, the impact of abutment alignment was diminished for short abutments, so a corrected alignment factor k_θ^* was recommend as

$$\frac{L}{y} \geq 3 \quad , \quad k_\theta^* = k_\theta$$

$$1 < \frac{L}{y} < 3 \quad , \quad k_\theta^* = k_\theta + (1 - k_\theta)\left(1.5 - 0.5\frac{L}{y}\right) \tag{1.86}$$

$$\frac{L}{y} \leq 1 \quad , \quad k_\theta^* = 1$$

where k_θ is the base alignment, L is the abutment length, and y is the flow depth. For local pier scour the channel geometry is unimportant as the only local flow effects matter for pier type obstructions, thus $k_G=1.0$ for all piers. However, for abutments the channel geometry will impact the local scouring as the location puts them at the floodplain, and to account for the effects of the compound channel design the k_G factor is used. The channel geometry factor is the ratio of scour depth at the actual abutment to the scour depth at an abutment in a rectangular channel. He equation for k_G is

$$k_G = \sqrt{1 - \frac{L^*}{L}\left[1 - \left(\frac{y^*}{y}\right)^{5/3}\frac{n}{n^*}\right]} \tag{1.87}$$

where n and n^* are the manning roughness coefficient of the main channel and floodplain respectively, y and y^* are the flow depths of the main channel and floodplain respectively, and L^* is the width of the flood plain as described in Figure 1.42. The last factor to address is the depth size factor, k_{yw}, which is also defined differently for pier and abutments. As for piers, $k_{yw} = k_{yb}$, and the equation for k_{yb} is as follows

$$\frac{b}{y} \leq 0.7 \quad , \quad k_{yb} = 2.4b$$

$$0.7 < \frac{b}{y} < 5 \quad , \quad k_{yb} = 2\sqrt{yb} \tag{1.88}$$

$$\frac{b}{y} \geq 5 \quad , \quad k_{yb} = 4.5y$$

where b is the effective pier width and y is the flow depth. Equation (1.88) demonstrates that for deeper flows the pier width dominates scour depth and for shallow flows the flow depth is more influential on scour depths. For abutments, the flow depth factor $k_{yw} = k_{yL}$ is obtained using the

same relationships based on abutment geometry from the Melville (1992) method, thus the equation is

$$\begin{aligned} \frac{L}{y} < 1 \quad &, \quad k_{yL} = 2L \\ 1 \leq \frac{L}{y} \leq 25 \quad &, \quad k_{yL} = 2\sqrt{yL} \\ \frac{L}{y} > 25 \quad &, \quad k_{yL} = 10y \end{aligned} \tag{1.89}$$

where L is the abutment length and y is the flow depth. Using all appropriate factors Equation (1.80) is then used to calculate local pier and abutment scour depths.

Melville and Chiew (1999): Local Pier Scour Evolution with Time

Melville and Chiew (1999) used laboratory test data to determine a time scale and time-depth relations for local scour holes at cylindrical bridge piers. The purpose was to observe temporal effects due to flooding events in order to create relationships for equilibrium scour depths and times. An expression for scour depth as a function of time, for constant density and negligible viscosity can be written as

$$\frac{d_s}{b} = f(\frac{V}{V_c}, \frac{y}{b}, \frac{D_{50}}{b}, \frac{t}{t_e}) \tag{1.90}$$

where t_e is the time for equilibrium scour depth, b is the pier diameter, and d_s is the scour depth at time t. Melville postulated and then confirmed from their findings that the equilibrium scour depth, d_e, and equilibrium scour time, t_e, are independent but rely on the same factors. To solve for the time, the following expression was written

$$\frac{Vt_e}{b} = f(\frac{V}{V_c}, \frac{y}{b}, \frac{D_{50}}{b}) \tag{1.91}$$

where $t^* = Vt_e/D$ was termed the equilibrium time scale. The laboratory data evaluated was limited to clearwater scour conditions, uniforms sediments, and cylindrical shape piers. As the true equilibrium scour depth is approached asymptotically over infinite time, a new definition for a reasonable equilibrium time is defined so a value can be achieved in experimental settings.

Melville and Chiew (1999) defined the equilibrium time as the time at which the increase of scour depth does not exceed 5% of the pier diameter, *b*, within a 24-hour period, the condition written as an expression is

$$\frac{d(d_{se})}{dt} \leq \frac{0.05b}{24\ h} \quad . \tag{1.92}$$

Findings from tests of various velocity intensities revealed a relationship between equilibrium depths and times as

$$\frac{d_s}{d_{se}} = \exp\left\{-0.03\left|\frac{V_c}{V}\ln\left(\frac{t}{t_e}\right)\right|^{1.6}\right\} \tag{1.93}$$

where d_s is the scour depth at time *t*, d_{se} and t_e are the equilibrium depth and time respectively. Next the effects of flow shallowness, *y/b*, were investigated and the following relationship was established

$$t^* = \begin{cases} 1.6 \times 10^6 \left(\frac{y}{b}\right)^{0.25} & , \quad \frac{y}{b} \leq 6 \\ 2.5 \times 10^6 & , \quad \frac{y}{b} > 6 \end{cases} \tag{1.94}$$

where *y* is the flow depth, *b* is the pier width, and t^* the equilibrium time scale. Flow shallowness was found to not be very influential for values larger than 3 and had no significant impact for values larger than 6. Using the remaining data, a relationship between velocity intensity and the equilibrium time scale was found as

$$0.4 < \frac{V}{V_c} \leq 1.0 \quad , \quad t^* = 4.17 \times 10^6 \left(\frac{V}{V_c} - 0.4\right) \tag{1.95}$$

where *V* is the flow velocity and V_c is the critical flow velocity. The data revealed that equilibrium depth was achieved the fastest near threshold conditions. Live bed scour led to longer equilibrium times as seen in Figure 1.43, which likely would have been due to the cycles of deposition of sediment in scour holes.

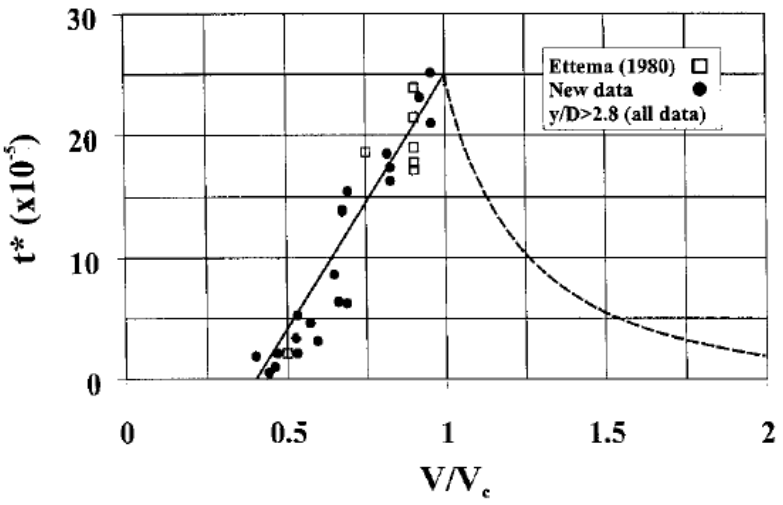

Figure 1.43: Influence of flow intensity on equilibrium time scale (Melville and Chiew 1999)

Melville and Chiew (1999) stated that the data set was not sufficient to provide a relationship between grain sizes and equilibrium scour depths at the time. To develop an equation for scour depth predictions, Melville and Chiew combined the time dependent relationships discussed herein with the Melville and Sutherland (1988) method for local pier scour. The new equation for time-dependent local scour depth at cylindrical piers is written as

$$d = k_{yD} k_I k_d k_t \tag{1.96}$$

where k_{yD} is the flow shallowness factor, k_I is the flow intensity factor, k_d is the sediment size factor, and k_t is the time factor. The flow shallowness factor k_{yD}, sediment size factor k_d factors are obtained using Equations (1.88) and (1.38) respectively. The flow intensity factor is obtained using a simple relation without considering bed armouring with the equation

$$k_I = \begin{cases} \dfrac{V}{V_c} & , \quad \dfrac{V}{V_c} \leq 1 \\ 1.0 & , \quad \dfrac{V}{V_c} > 1 \end{cases} \tag{1.97}$$

where V is the flow velocity and V_c is the critical flow velocity. The time factor k_t was relative to the equilibrium scour depth, d_e, as shown in the equation

$$k_t = \frac{d}{d_e} \tag{1.98}$$

where d is the scour depth at time t, and the factor can be solved for using Equation (1.93). The equilibrium time, t_e, must first be found using the relationships between the equilibrium time scale with flow intensity and flow shallowness. To solve for t_e, Equations (1.94) and (1.95) are combined to form

$$\begin{aligned} \frac{y}{b} \leq 6 \quad &, \quad t_e(days) = 48.26 \frac{b}{V}\left(\frac{V}{V_c} - 0.4\right)\left(\frac{y}{b}\right)^{0.25} \\ \frac{y}{b} > 6 \quad &, \quad t_e(days) = 30.89 \frac{b}{V}\left(\frac{V}{V_c} - 0.4\right) \quad . \end{aligned} \tag{1.99}$$

The range of velocity intensity for which the method is applicable is between 0.4-1.0, as suggested by earlier research scour inception generally occurs in that range. The method can be used to estimate scour depth over time and during flooding events provided accurate flow condition predictions.

Sheppard/Melville Equation: Local Pier Scour

Sheppard et al. (2014) conducted an analysis of 23 existing pier scour equations for their accuracy in predicting experimental and field scour depths. Along with analysis of existing equations, a new equation was developed by combining the Sheppard and Miller's (2006) and Melville's (1997) methods. The new method was termed the Sheppard/Melville or S/M method which was found to be the most accurate in the study by Sheppard et al. (2014). The S/M equations for pier scour depth are

$$\begin{aligned} 0.4 \leq \frac{V}{V_c} \leq 1 \quad &, \quad \frac{d_s}{D} = 2.5 f_1 f_2 f_3 \\ 1 < \frac{V}{V_c} \leq \frac{V_{lp}}{V_c} \quad &, \quad \frac{d_s}{D} = f_1 \left[2.2 \left(\frac{\frac{V}{V_c} - 1}{\frac{V_{lp}}{V_c} - 1} \right) + 2.5 f_3 \left(\frac{\frac{V_{lp}}{V_c} - \frac{V}{V_c}}{\frac{V_{lp}}{V_c} - 1} \right) \right] \\ \frac{V_{lp}}{V_c} < \frac{V}{V_c} \quad &, \quad \frac{d_s}{D} = 2.2 f_1 \end{aligned} \tag{1.100}$$

where the functions f_1, f_2 and f_3 are defined as

$$f_1 = \tanh\left[\left(\frac{y}{D}\right)^{0.4}\right] \tag{1.101}$$

$$f_2 = \left\{1 - 1.2\left[ln\left(\frac{V}{V_c}\right)\right]^2\right\} \quad (1.102)$$

$$f_3 = \frac{D/D_{50}}{0.4(D/D_{50})^{1.2} + 10.6(D/D_{50})^{-0.13}} \quad (1.103)$$

where d_s is the scour depth, V is the mean velocity, V_c is the critical velocity, V_{lp} is the live-bed peak velocity, D is the pier diameter, y is the flow depth and D_{50} is the median grain size. The live-bed peak velocity is determined using

$$V_{lp} = max\begin{Bmatrix} 5V_c \\ 0.6\sqrt{gy} \end{Bmatrix} \quad (1.104)$$

where g is the acceleration due to gravity. The critical velocity was estimated using

$$5 \le R \le 70 \quad , \quad V_c = 2.5u^*\ln\left(\frac{73.5y}{D_{50}\left\{R[2.85 - 0.58\ln(\mathrm{R}) + 0.002\mathrm{R}] + \frac{111}{R} - 6\right\}}\right) \quad (1.105)$$

$$R > 70 \quad , \quad V_c = 2.5u^*\ln\left(\frac{2.21y}{D_{50}}\right) \quad (1.106)$$

where the friction velocity, u^*, and R are defined as

$$u^* = \left(16.2D_{50}\left\{\frac{9.09 \times 10^{-6}}{D_{50}} - D_{50}[38.76 + 9.6\ln(D_{50})] - 0.005\right\}\right)^{1/2} \quad (1.107)$$

$$R = \frac{u^*D_{50}}{2.32 \times 10^{-7}} \quad (1.108)$$

.

SRICOS Method: Scour Rate In COhesive Soils

To investigate the time dependent scouring occurring in fine soils with significant cohesion, Briaud et al. (1999) proposed the SRICOS (Scour Rate In COhesive Soils) method. The method involves the formation of an equation to describe the scour rates and maximum depths of scour while including the effects of cohesion in soil erosion behaviour. To capture cohesive effects on scouring, the SRICOS method uses erosion rates obtained through testing with the EFA (Erosion Function Apparatus). The basic methods for local pier, complex pier, and contraction scour are discussed herein while Briaud has continuously expanded the method. One of these

expansions was the creation of the Extended-SRICOS method which evaluates scour with a random velocity-time history and a multilayer soil stratigraphy (Briaud 2001b). The methods starts with using formulae to estimate the maximum shear stress, τ_{max}, and the maximum scour depth, z_{max}. After which the EFA is used to the obtain the initial scour rate $\dot{z}_i$ corresponding to τ_{max}. Lastly, $\dot{z}_i$ and z_{max} are used to find the scour depth, d, after time, t, with a hyperbola relation.

SRICOS: Local Pier Scour

Briaud et al. (1999) first developed the SRICOS method for determine the local scouring over time at cylindrical piers. The method involves obtaining a site soil sample and utilizing the EFA to obtain the erosion function with initial scour rate $\dot{z}_I$ which would correspond with the maximum shear stress in the field, τ_{max}. To determine the maximum shear stress exhibited, τ_{max}, where the scour hole would form, numerical simulations were conducted to find an empirical formula for τ_{max}. The relationship for the maximum shear stress at piers was found as

$$\tau_{max} = 0.094\rho V^2 \left(\frac{1}{log\, R} - \frac{1}{10}\right) \tag{1.109}$$

where ρ is the water density, $R = (Vb/v)$ is the Reynold number, b is the pier diameter, V is the flow velocity, and v is the water viscosity. To find an expression for the expected maximum scour depths, laboratory flume tests were conducted with varying soil grain sizes, pier diameters, and flow velocities. During tests, scour depth was measure and plotted over time and a sample result is shown in Figure 1.44.

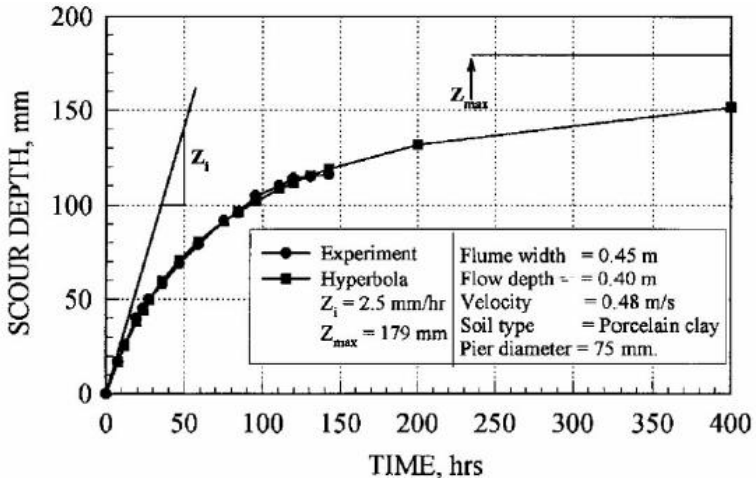

Figure 1.44: Example test results of scour depth versus time (Briaud et al. 1999)

Figure 1.44 also notes the initial scour rate and asymptotic maximum scour depth. Sets of experimental data was curve fitted to find the best fitting hyperbola equation as

$$z = \frac{t}{\frac{1}{\dot{z}_i} + \frac{t}{z_{max}}} \tag{1.110}$$

where z is the scour depth at time t, $\dot{z}_i$ is the initial scour rate corresponding to t_{max}, and z_{max} is the maximum scour depth at time $t = \infty$. An empirical relationship from the experiments was found for the maximum scour depth as

$$z_{max}(mm) = 0.18Re^{0.635} \tag{1.111}$$

where $Re = (Vb/v)$ is the Reynolds number for the flow past the pier. With the scour depth versus time curve, the scoured depth for floods can be determined using the associated flood duration and mean flow velocity. Additional findings from the research indicated that the maximum scour depths for sands and clay were both very similar even though their erosion rates were drastically different. The Reynolds number was included over the Froude number as the viscous forces influenced scour much more than gravitational forces.

SRICOS: Complex Piers Scour

Briaud et al. (2004) adapted the SRICOS method using additional flume tests and numerical simulations for estimating local scour at complex piers. The method was extended to include grouped rectangular piers with flows of different angles of attack in any flow depth. The method can also consider non-uniform velocities by transforming flow hydrographs into velocity hydrographs to describe the velocity over time. Firstly, a site soil sample is tested using the EFA to obtain the initial rate of scouring, $\dot{z}_I$, corresponding to τ_{max}. Next the maximum scour depth, z_{max}, and maximum shear stress, τ_{max}, must be addressed for complex piers. The original SRICOS method was limited for the deep-water condition where the depth ratio values are; $y/b>2$, where y is the flow depth and b is the pier diameter. Briaud et al (1999) found that larger depth ratios during laboratory tests had less of an impact on maximum scour depths. Shallow water depth effects on maximum scour depths were investigated for complex piers by several laboratory flume tests to develop a depth correction factor, K_w, defined as

$$K_w = \begin{cases} 0.85\left(\frac{y}{b}\right)^{0.34} & y/b < 1.62 \\ 1 & y/b > 1.62 \end{cases} \quad (1.112)$$

where y is the flow depth and b is the pier diameter. This and other correction factors would be applied to the z_{max} calculated from the original SRICOS method to account for complex pier effects. In addition to the maximum scour depth, the maximum shear stress exhibited by the bed, τ_{max}, is required to be computed and compared to the critical shear stress, τ_c. The effects of shallow water on the maximum shear stress were also investigated by running numerical simulations and performing a regression analysis to find a correction factor for the τ_{max} value calculated from the original SRICOS method. The correction factor for maximum shear stress, k_w, was defined as

$$k_w = 1 + 16e^{-\frac{4y}{b}} \quad (1.113)$$

where y is the flow depth and b is the pier width. These two correction factors reveal that if the shallow water condition lowers the maximum depth, then the maximum shear stress increases. The velocity versus depth test results for shallow water produced larger velocity gradients near the bed hence the larger shear stresses. As discussed in the formation of the erosion function, the initial scour rate is related to maximum shear stress, thus in shallow water, scour holes will develop faster, but the maximum scour depth will be lower. Additionally, for multigroup piers the spacing effects on the maximum scour depth and maximum shear stress must be considered. The scour depth at pier groups is increased due to the interaction of horseshoe vortices enlarging each other and flow acceleration caused by the contractions between the piers. The type of grouping examined in the study was single rows of piers lined perpendicular to flow with centre-to-centre spacings of S. The testing of up to four piers in a flume revealed that the ratio maximum scour depth for a group versus a single pier was proportional to the ratio of the width of the obstructed channel versus the unobstructed channel. This ratio was labelled the contraction ratio, and is also the spacing correction factor, K_{sp}, for which the equation is

$$K_{sp} = \frac{W_1}{(W_1 - nb)} \quad (1.114)$$

where W_1 is the unobstructed channel width, n is the number of piers, and b is the pier diameter. As seen in Equation (1.114), the controlling factor was not the spacing between the piers, but the contraction effect created by multiple piers. The effects of pier spacing on the maximum shear

stress as investigated by performing a regression analysis on the shear stress reported by simulation as a function of *S/b*. The correspond correction factor for maximum shear stress due to pier spacing effect k_{sp} was found as

$$k_{sp} = 1 + 5e^{-\frac{1.1S}{b}} \tag{1.115}$$

where *y* is the flow depth and *b* is the pier width. Next the pier shape effects on τ_{max} and z_{max} were investigated for piers using the *L/b* ratio where *b* is the width perpendicular to flow and *L* is the length of the rectangular pier. A cylindrical pier with a diameter equal to the width of the rectangular piers was used as a point of reference for flumes tests conducted using varying pier lengths. The shape effects on the maximum shear stress were expressed using the correction factor k_{sh} defined as

$$k_{sh} = 1.15 + 7e^{-\frac{4L}{b}} \tag{1.116}$$

where *L* is the pier length and *b* is the pier width. The last consideration for the rectangular multigroup piers is the angle of attack α effects on τ_{max} and z_{max}. The angle of attack is a more complex factor to consider as it is simultaneously interacting with the effects of the pier geometry and spacing. Firstly, the effective width *b'* shown in Figure 1.45, is calculated as

$$b' = L\sin\alpha + b\cos\alpha \tag{1.117}$$

where *L* is the pier length, *b* is the pier width, and α is the angle of attack.

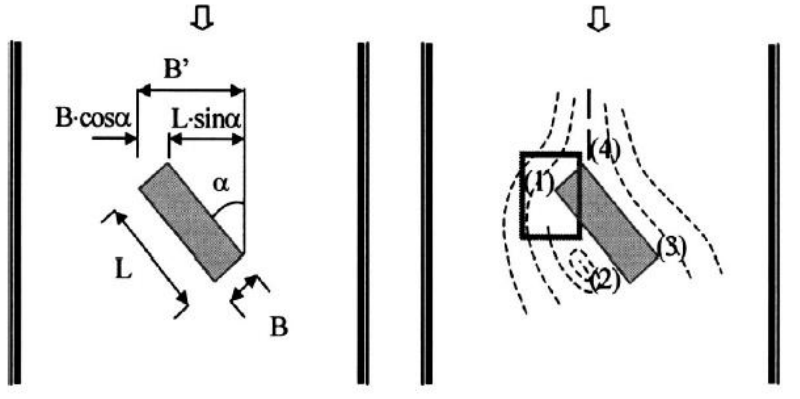

Figure 1.45: Projected width of rectangular pier (Briaud et al. 2004)

The angle of attack correction factor for maximum scour depth K_a is defined as the ratio of maximum scour depth for the angle of attack greater than zero to the maximum scour depth for an angle attack of zero. By using the effective width of the pier *b'* as opposed to the actual width b in the method, there is no need to calculate K_a as usage of the effective width inherently accounts for the effect of the angle of attack. The results of flumes tests on varying angles of attack also revealed where the deepest scour would occur on a rectangular pier as shown in Figure 1.46.

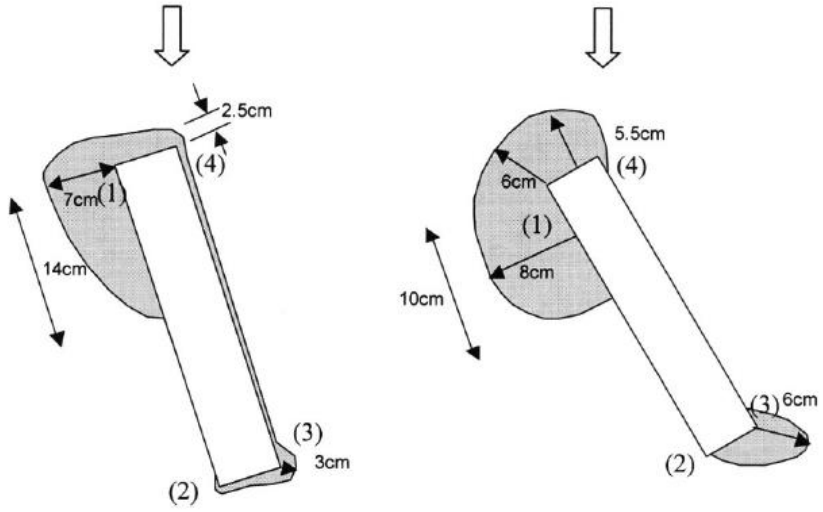

Figure 1.46: Scour hole shape at rectangular piers (Briaud et al. 2004)

As shown in Figure 1.46, the four corners of the rectangular pier are numbered, and the deepest scouring occurs at corner 1 for smaller angles and gradually moves to corner 3 as the angle of attack increases. The angle of attack correction factor for maximum shear stress, k_a, was also determined through regression analysis of simulation results. The equation for k_a was found to be

$$k_a = 1 + 1.5\left(\frac{\alpha}{90}\right)^{0.57} \tag{1.118}$$

where α is the angle of attack. Next the correction factors and the effective width were integrated onto the original equations for τ_{max} and z_{max}, to form the final equations for complex piers as

$$z_{max} = 0.18 K_w K_{sp} K_{sh} R^{0.635} \tag{1.119}$$

$$\tau_{max} = k_w k_{sp} k_{sh} k_a 0.094 \rho V^2 \left(\frac{1}{\log R} - \frac{1}{10}\right) \quad (1.120)$$

where $R=(b'V/v)$ is the flow the Reynolds number, ρ is the water density, b' is the pier's effective width, V is water velocity, and v is the water viscosity. For the maximum scour depth, the shallow water correction factor K_w and the spacing factor K_{sp} are calculated using b' while the shape factor K_{sh} is calculated using b. For the maximum shear stress, the shallow water correction factor k_w and the spacing factor k_{sp} are calculated using b' while the shape factor k_{sh} and the angle of attack k_a are calculated using b. Once the corrected τ_{max} and z_{max} values are obtained the rest of the process of SRICOS for complex rectangular piers follows the same steps as the original method by using Equation (1.111) to predict scouring over time.

SRICOS: Contraction Scour

The SRICOS method was adapted by Briaud et al. (2005) to be applicable for clear water contraction scour at bridges. The method was made to be used together with the SRICOS method for local pier scour and through superposition, obtain the total scour depth at a bridge foundation. The contraction scour here is defined as the maximum scour depth occurring in the centre line of a channel usually a short distance from the start of the contraction as seen in Figure 1.47.

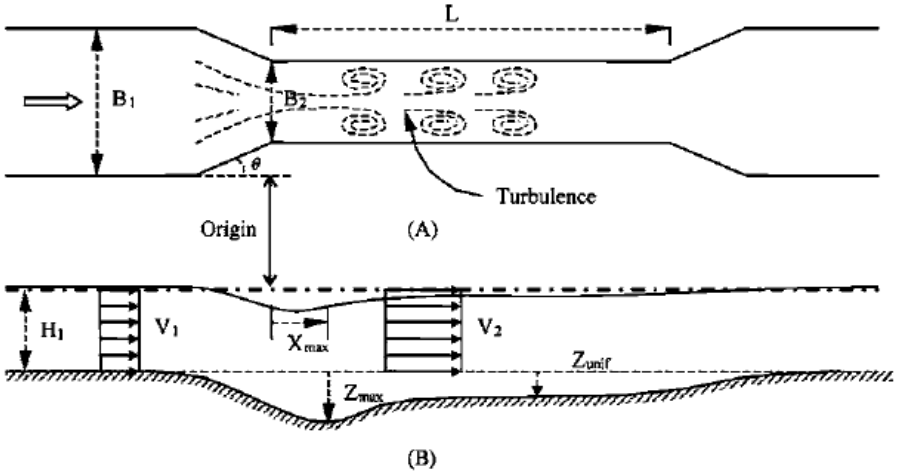

Figure 1.47: Contraction scour details (Briaud et al. 2005)

Figure 1.47 also defines channel features such as the width upstream as B_1, while the width at the contraction is B_2. Other dimensions of concern are the contraction angle, θ, contraction

length, L, the flow depth before contraction, H_1, and the upstream mean velocity, V_1. The maximum scour depth z_{max} occurs at a distance x_{max} downstream of the contraction and the uniform scour area has a depth of z_{unif}. The width ratio B_2/B_1 was investigated through flumes test and the results revealed how the ratio impacted the location of maximum scour depths. As the width ratio increased the maximum contraction scour depth location moved further downstream and was less likely to overlap with local abutment scour as shown in Figure 1.48.

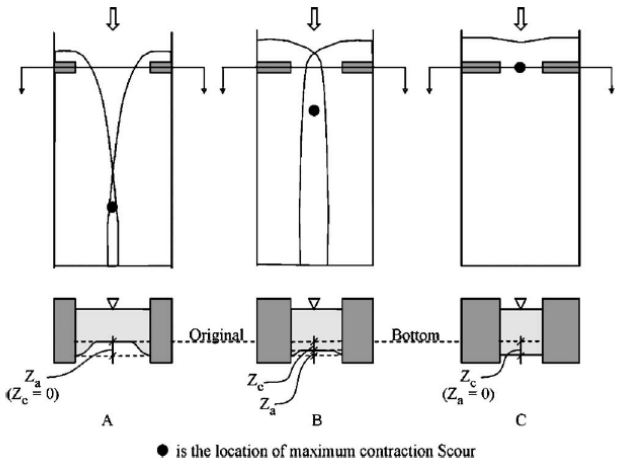

Figure 1.48: Location of maximum contraction scour (Briaud et al. 2005)

In addition to the flume tests, numerical simulations were conducted to investigate the effects of contraction ratio, contraction length, contraction transition angle, and water depth on the scour characteristics. As with the SRICOS method for complex piers, new equations were developed for the maximum scour depth z_{max} and the maximum shear stress τ_{max} at contractions. Firstly Briaud et al. (2005) examined a simple contraction, where the contraction angle, θ, was 90°. Using dimensional analysis and regression of the flumes tests a relationship was found for the maximum scour depth z_{max} and uniform scour depth z_{unif} as

$$z_{max} = 1.90\, H_1 \left(1.38 \left(\frac{B_1}{B_2}\right) \frac{V_1}{\sqrt{gH_1}} - \frac{\left(\frac{\tau_c}{\rho}\right)^{1/2}}{gnH_1^{1/3}} \right) \tag{1.121}$$

$$z_{unif} = 1.41\, H_1 \left(1.31 \left(\frac{B_1}{B_2}\right) \frac{V_1}{\sqrt{gH_1}} - \frac{\left(\frac{\tau_c}{\rho}\right)^{1/2}}{gnH_1^{1/3}} \right) \tag{1.122}$$

where ρ is the water density, B_1 is the channel width upstream, B_2 is the contraction width, H_1 is the flow depth before contraction, V_1 is the upstream mean velocity, g is the acceleration due to gravity, and τ_c is the critical shear stress obtained using the EFA. The depth Equations (1.121) and (1.122) were meant for straight and rectangular channels so Briaud et al. (2005) also developed additional equations for complex channel shapes which are detailed in the original paper. The location of the maximum scouring depth, z_{max}, was defined as x_{max} in Figure 1.47 and was calculated using

$$x_{max} = \frac{2.25}{B_1} + 0.15B_2 \tag{1.123}$$

where B_1 is the channel width upstream, and B_2 is the contraction width. Using z_{max}, x_{max}, and z_{unif}, the general scour profile is known and can be used in the design of the abutments and piers. The effects of the contraction angle were tested and revealed that θ had no significant impact on the depths of scour. However smaller contraction angles increased x_{max} and the correction factor for the contraction angle, $K_{\theta/Xmax}$, is calculated using

$$K_{\theta/Xmax} = 1 + 0.5/\tan\theta \tag{1.124}$$

where θ is the contraction angle ($K_{\theta/Xmax}$ = 1.0 for θ = 90°). The contraction length effects were examined and revealed no significant impact on the scoured depths or correlation with the location of maximum scour depth. Next an equation for the maximum shear stress was required while considering the effects of the contraction angle, contraction length, water depth and the contraction ratio. A preliminary value of interest was the reference shear stress at the bed of a channel without a contraction, τ_{ref}, and its expression is

$$\tau_{ref} = \gamma n^2 V^2 R_h^{-0.33} \tag{1.125}$$

where γ is the unit weight of water, n is the Manning's roughness coefficient, V is the mean depth velocity, and R_h is the hydraulic radius. Then τ_{ref}, is modified to solve for τ_{max} with correction factors obtained using numerical simulations as they provide more accurate stress measurements than measuring equipment in flume tests. The equation for the maximum shear stress is

$$\tau_{max} = k_\theta k_L k_H k_R \tau_{ref} \tag{1.126}$$

where k_θ is the contraction angle correction factor, k_L is the contraction length correction factor, k_H is the water depth correction factor, and k_R is the contraction ratio correction factor. The correction factor equations are

$$k_\theta = 1 + 0.9\left(\frac{\theta}{90}\right)^{1.5} \tag{1.127}$$

$$k_L = \begin{cases} 1, & \frac{L}{B_1 - B_2} \geq 0.35 \\ 0.77 + 1.36\left(\frac{L}{B_1 - B_2}\right) - 2\left(\frac{L}{B_1 - B_2}\right)^2, & \frac{L}{B_1 - B_2} < 0.35 \end{cases} \tag{1.128}$$

$$k_H = 1.0 \tag{1.129}$$

$$k_R = 0.62 + 0.38\left(\frac{B_1}{B_2}\right)^{1.75} \tag{1.130}$$

where B_1 is the channel width upstream, B_2 is the contraction width, H_1 is the flow depth before contraction, V_1 is the upstream mean velocity, g is the acceleration due to gravity, and τ_c is the critical shear stress obtained using the EFA. The water depth correction factor k_H was simply set equal to 1.0 as the effects of the water depth are captured in the hydraulic radius used to calculate τ_{ref}.

TAMU-Scour Method (Briaud 2015a, 2015b)

To understand and describe the influence of important soil parameters Briaud conducted 94 laboratory flume tests to find some relationships between the values of these parameters and the corresponding scouring (Briaud 2015a, 2015b). The method discussed is the Texas A&M University or TAMU-scour method and was an improvement to the CSU (1977) method with the inclusion of additional soil parameters as inputs. The TAMU method can calculate local scour at single piers, multigroup piers, abutments, and contractions. As with the SRICOS method, the TAMU method also includes depth over time relationships for scour. The method starts with using the EFA to test the soil on site and obtain the erosion function and critical shear stress. The EFA should be obtained locally at the abutment, pier, and contraction centre line to ensure accurate scour estimates as soil compositions on site may differ throughout the channel. Equations were developed through regression analysis of flume results for the maximum scour depth, z_{max}, and maximum shear stress, τ_{max}. Once calculated, the values of z_{max} and τ_{max} are substituted into the

time depth curve Equation (1.110). Using the time depth curve the scour depths would then be estimated for varying floods and soil layers with velocities and duration of floods. The equation for maximum local pier scour depth, $z_{max(pier)}$, was found as

$$z_{\max\,(pier)} = 2.2b'K_{pw}K_{psh}K_{pa}K_{psp}\left(2.6\,F_{(pier)} - F_{c(pier)}\right)^{0.7} \tag{1.131}$$

where b' is the pier's effective width from equation 1.109, K_{pw} is the water depth influence factor, K_{psh} is the pier shape influence factor, K_{pa} is the aspect ratio influence factor, K_{psp} is the pier spacing influence factor, $F_{(pier)}=V/(gb')^{0.5}$ is the pier Froude number, $F_{c(pier)}=V_c/(gb')^{0.5}$ is the critical pier Froude number, g is the acceleration due to gravity, V is the velocity, and V_c is the critical velocity of the soil. The aspect ratio influence factor is similar to factors correcting for the flow angle of attack and in this method is into account by using the effective width b' so $K_{pa}=1.0$. The flow depth and pier spacing influence factors are determined using the following equations

$$K_{pw} = \begin{cases} 0.89\left(\dfrac{h_w}{b'}\right)^{0.33}, & h_w/b' < 1.43 \\ 1.0, & h_w/b' \geq 1.43 \end{cases} \tag{1.132}$$

$$K_{psp} = \begin{cases} 2.9\left(\dfrac{S}{b'}\right)^{-0.91}, & S/b' < 3.22 \\ 1.0, & S/b' \geq 3.22 \end{cases} \tag{1.133}$$

where b' is the pier's effective width, S is the centre to centre spacing of piers, and h_w is the flow depth at the pier. The pier shape influence factor, K_{psh}, is obtained from Figure 1.26. The contraction scour equations were simplified by defining a few useful variables. Firstly, the contraction ration C_R reflects the contraction of flow rate and is defined as

$$C_{\mathrm{R}} = \frac{Q - Q_{block}}{Q} \tag{1.134}$$

where Q is the main channel discharge before the contractions and Q_{block} is discharge blocked by the abutments. The critical Froude number for the main channel, F_{mc}, contains an expression for the critical velocity as a function of the critical shear stress of the channel and is defined as

$$F_{\mathrm{mc}} = \frac{V_{mc}}{\sqrt{g h_{wm1}}} = \frac{(\tau_c/\rho)^{0.5}}{g n h_{wm1}^{0.33}} \tag{1.135}$$

where V_{mc} is the critical velocity of the main channel, h_{wm1} is the main channel water depth, τ_c is the critical shear stress, ρ is the soil mass density, g is the acceleration due to gravity, and n is the Manning's roughness coefficient. The maximum contraction scour depth $z_{max(cont)}$ is obtained using the equation

$$z_{\max\,(cont)} = 1.27 h_{wm1}(1.83\, F_{m2} - F_{mc}) \tag{1.136}$$

where h_{wm1} is water depth before contraction, $F_{m2}=(V/C_R)/(gh_{wm1})^{0.5}$ is the main channel contraction zone Froude number, C_R is the contractions ratio, F_{mc} is the critical pier Froude number defined previously, g is the acceleration due to gravity, V is the velocity, and V_c is the critical velocity of the soil. The abutment scour researched in the study was for typical abutment types and the details of geometry are described in Figure 1.49.

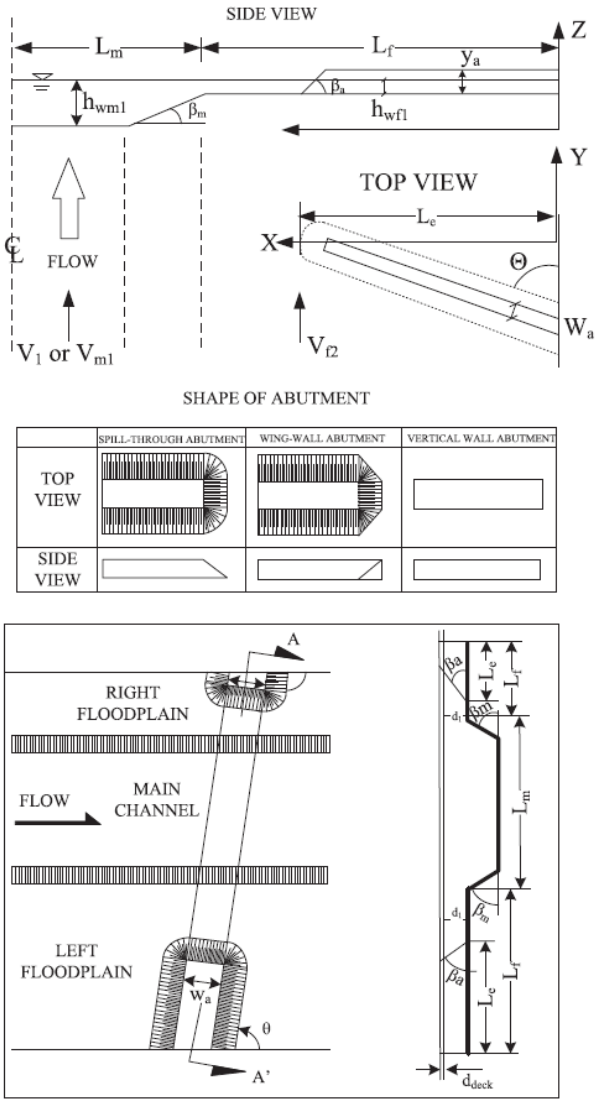

Fig. 11. Abutment parameter definitions

Figure 1.49: Abutment parameter details (Briaud 2015a)

For the abutment scour some variables were identified to simplify the final equation for the maximum scour depth. For abutments $Q_{0.5}$ is the flow in half the channel, calculated as half the upstream flow in the main channel such that $Q_{0.5}=0.5Q_{m1}$. The area in the contracted zone is denoted A_1 and the flow area on the floodplain at the contracted section is A_{f2}. As labeled in Figure 1.49, L_f is the width of the floodplain in the approach zone, and L_e is the length of embankment leading to the abutment. The local velocity near the abutment in the floodplain is dependent on the foundation geometry and is calculated using the following relationship

$$V_{\mathrm{f2}} = \begin{cases} Q_{0.5}/A_2 & , \quad \text{for short setback } \left[\left(L_f - L_e\right)\right. \\ Q_{f1}/A_{f2} & , \quad \text{for long setback } \left(L_e \leq 0.25\right. \\ \text{interpolate betwen } \left[\dfrac{Q_{0.5}}{A_2}, \left(L_f - L_e\right) = 5\right] \text{ and } \left[\dfrac{Q_{f1}}{A_{f2}}, \left(L_f - L_e\right) = 5\right] & , \quad \text{otherwise} \end{cases} \tag{1.137}$$

where h_{wm1} is the water depth in the approach channel near the abutment and the other variables were previously defined. Next the Reynolds number, Froude number and critical Froude number at the toe of the abutment were computed using the following relationships

$$R_{\mathrm{f2}} = \frac{V_{f2} h_{wf1}}{\vartheta} \tag{1.138}$$

$$F_{\mathrm{f2}} = \frac{V_{f2}}{\sqrt{g h_{wf1}}} \tag{1.139}$$

$$F_{\mathrm{fc}} = \frac{V_c}{\sqrt{g h_{wf1}}} \tag{1.140}$$

where V_{f2} is the local velocity near the abutment, V_c is the critical velocity of the soil, h_{wf1} is the main channel water depth, v is the kinematic viscosity of water, and g is the acceleration due to gravity. Finally, the equation for maximum abutment scour depth $z_{max(abut)}$ was defined as

$$z_{\max\,(abut)} = 243 h_{wf1} K_{ash} K_{ask} K_{al} K_{ag} R_{f2}^{-0.28} \left(1.65\, F_{f2} - F_{fc}\right) \tag{1.141}$$

where h_{wf1} is the floodplain water depth next to the abutment, K_{ash} is the shape factor, K_{ask} is the skew angle influence factor, K_{ag} is the geometry of channel influence factor, K_{al} is the proximity of the abutment to the main channel influence factor, R_{f2} is the Reynolds number around the toe of the abutment, F_{f2} is the Froude number around the toe of the abutment, and F_{fc} is the critical Froude number around the toe of the abutment. The shape factor K_{ash} accounts for geometry effects on scour as the equations was originally developed for wing wall abutments. The proximity of the abutment to the main channel influence factor, K_{al}, is used because testing revealed an increased scour depth when the abutment was closer to the main channel bank. The channel geometry factor, K_{ag}, was included because rectangular channels produced significantly less scour than compound channels. The equations for maximum abutment scour depth influence factors are

$$K_{\text{ash}} = \begin{cases} 1.0 & , \quad \text{for wing} - \text{wall abutment} \\ 1.22 & , \quad \text{for vertical} - \text{wall abutment} \\ 0.73 & , \quad \text{for spill} - \text{through abutment with } 2{:}\,1 \text{ slope} \\ 0.59 & , \quad \text{for spill} - \text{through abutment with } 3{:}\,1 \text{ slope} \end{cases} \tag{1.142}$$

$$K_{\text{ask}} = \begin{cases} 1.0 - 0.005(|\theta - 90°|) & , \quad \text{for } 60° \leq \theta \leq 120° \\ 0.85 & , \quad \text{otherwise} \end{cases} \tag{1.143}$$

$$K_{\text{al}} = \begin{cases} -0.23\dfrac{(L_f - L_e)}{h_{wf1}} + 1.35 & \dfrac{(L_f - L_e)}{h_{wf1}} < 1.5 \\ 1.0 & otherwise \end{cases} \tag{1.144}$$

$$K_{\text{ag}} = \begin{cases} 0.42 & , \quad for\ rectangular\ channel \\ 1.0 & , \quad for\ compund\ channel \end{cases} \tag{1.145}$$

where h_{wf1} is the floodplain water depth next to the abutment, θ is the skew angle as measured in Figure 1.49, L_f is the width of the floodplain, and L_e is the length of embankment. After the equations for the maximum scour depth, numerical simulations were conducted to obtain the equations for the maximum shear stress in the cases of pier, abutment, and contraction scour. As with the SRICOS method, the values for z_{max}, $\tau_{\max}$, and erosion function from the EFA can be used with Equation (1.110) to solve for scour depths over time. The TAMU method uses the same τ_{max} relationships as the SRICOS method therefore the τ_{max} for piers and contractions is determined using Equations (1.120) and (1.128), respectively. For the maximum shear stress at abutments, $\tau_{max(abut)}$, the TAMU method uses the equation

$$\tau_{\max\,(abut)} = 12.5 k_{acr} k_{aar} k_{aw} k_{ash} k_{ask} k_{al} \rho V_1^2 R^{-0.45} \tag{1.146}$$

where k_{acr} is the contraction ratio influence factor, k_{aar} is the influence factor for the aspect ratio of the abutment, k_{ash} is the influence factor for the abutment shape, k_{aw} is the influence factor for water depth or Froude number, k_{ask} is the influence factor for the skew angle, k_{al} is the influence factor related to the location of the abutment in the floodplain, ρ is the mass density of water, V_1 is the mean depth velocity of the water in the approach zone, $R=(V_1 W_a)/\nu$ is the abutment Reynolds number, W_a is the top width of the abutment, and ν is the water kinematic viscosity. The contraction influence factor k_{acr} is used to correct for the fact that the approach velocity V_1 is used instead of the contracted section velocity in Equation (1.134). The equation for k_{acr} is

$$k_{acr} = 3.65\left(\frac{Q_{tot}}{Q_{tot} - Q_{block}}\right) - 2.91 \tag{1.147}$$

where Q_{tot} is the total discharge, and Q_{block} is the part of the total discharge blocked by the approach embankments. The equations for the other influence factors are

$$k_{aar} = 0.85\left(\frac{L_e}{W_a}\right)^{-0.24} \tag{1.148}$$

$$k_{aw} = \begin{cases} 2.07F + 0.8 & \text{for } > 0.1 \\ 1 & \text{for } \leq 0.1 \end{cases} \tag{1.149}$$

$$k_{ash} = \begin{cases} 1.0 & , \quad \text{for vertical} - \text{wall abutment} \\ 0.65 & , \quad \text{for wing} - \text{wall abutment} \\ 0.58 & , \quad for\ spill - through\ abutment \end{cases} \tag{1.150}$$

$$k_{al} = \begin{cases} 1.0 & , \quad for\ \left(\frac{L_f - L_e}{h_{wf1}}\right) \leq -2 \\ 1.2 + 0.1\left(\frac{L_f - L_e}{h_{wf1}}\right) & , \quad for\ -2 \leq \left(\frac{L_f - L_e}{h_{wf1}}\right) \leq 0 \\ 1.2 - 0.2\left(\frac{L_f - L_e}{h_{wf1}}\right) & , \quad for\ 0 \leq \left(\frac{L_f - L_e}{h_{wf1}}\right) \leq 1 \\ 1.0 & , \quad for\ \left(\frac{L_f - L_e}{h_{wf1}}\right) \geq 1 \end{cases} \tag{1.151}$$

where h_{wf1} is the floodplain water depth next to the abutment, w_a is the top width of the abutment, L_f is the width of the floodplain, L_e is the length of embankment, $F=V_{f2}/(gh_{wf1})^{0.5}$ is the Froude number at the abutment, g is the acceleration due to gravity, and V_{f2} is the water velocity in the approach zone in line with the abutment. For the effects of the skew, the influence factor was set to unity as the most conservative case, therefore for all cases $k_{ask}=1.0$. Once the maximum shear stress values for piers, abutments and contractions are obtained, they are substituted in the SRICOS hyperbola Equation (1.101), and then scour depths corresponding to different floods would then be calculated. To deal with varying water velocities and soil layers, Briaud also discussed software tools and algorithms which aids in the use of the TAMU-scour method.

1.2.3 Performance of Scour Depth Prediction Methods

Determining the most accurate methods for scour depth prediction is vital for ensuring structural stability and cost-effective designs. Some research had been conducted into comparing the depths predicted by common methods with those measured in laboratory settings and in field

to determine which methods provide the most accurate estimates. Laboratory flume tests are often used because a variety of for soil and flow conditions are easy to test and many measuring instruments can be implemented. Field data measurements may be more difficult to measure but provide the best results with accurate scaling effects as scour around large structures can be investigated. This section will discuss the performance of existing scour prediction methods when compared with laboratory and field data. The HEC-18 manual (Richardson and Davis 2001) provides some comparisons of local pier scour prediction equations. Figure 1.50 shows a comparison of normalized scour depths versus normalized flow depth for a set Froude number of 0.3.

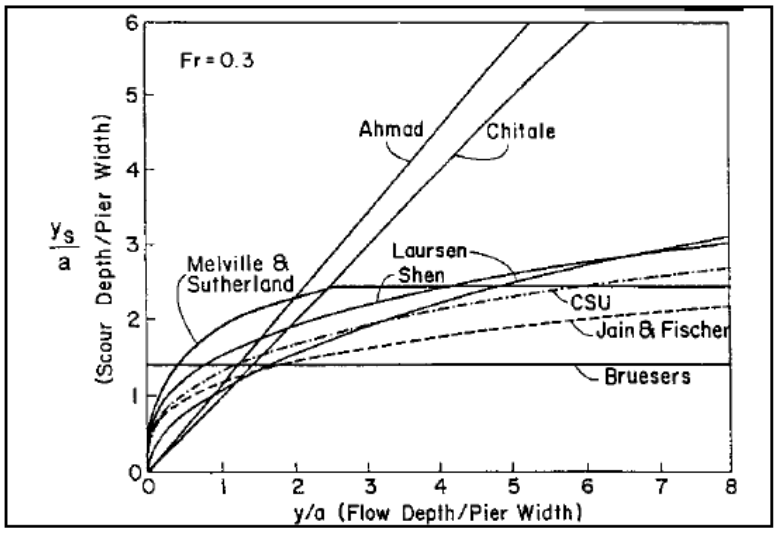

Figure 1.50: Pier scour equation relationship comparison (Richardson and Davis 2001)

The Ahmad and Chitale curves showed rapid increase in predicted scour depth with flow depth, leading to significant overestimations for wide piers. The Breusers equations, like those same from the RTAC guide, are only functions of pier width, and will underestimate scour depths for larger flow depths. The Colorado State University (CSU) equation addressed the most factors and provided the best results of those methods compared.

Mohamed et al. (2005) validated some bridge pier scour formulae using field and laboratory data. The equations compared were Colorado State University (CSU) (1977), Melville and Sutherland (1988), Jain and Fisher (1981), and Laursen and Toch (1956). Laursen and Toch (1956) and the CSU (1977) equations provided more accurate estimates while Melville and

Sutherland (1988), and Jain and Fisher (1981) over estimated scour depths. The Melville and Sutherland (1988) equation was the most accurate when compared with field measurements. Sheppard et al. (2014) performed an extensive evaluation of 23 equations for local scour at bridge piers with 441 lab and 791 field data sets. The study also reviewed results reported in NCHRP Report 682 (Sheppard et al. 2011) and focuses on the underprediction error by equations. Underprediction of scour depths is much more of issue than overconservative estimates simply because bridges failures are devastating. The primary objective in estimating scour should be to eliminate all cases of under predictions for safety and then address cost efficiency associated with overestimation. The underprediction error of the six best performing equations was plotted for laboratory and field data Figure 1.51 - Figure 1.54.

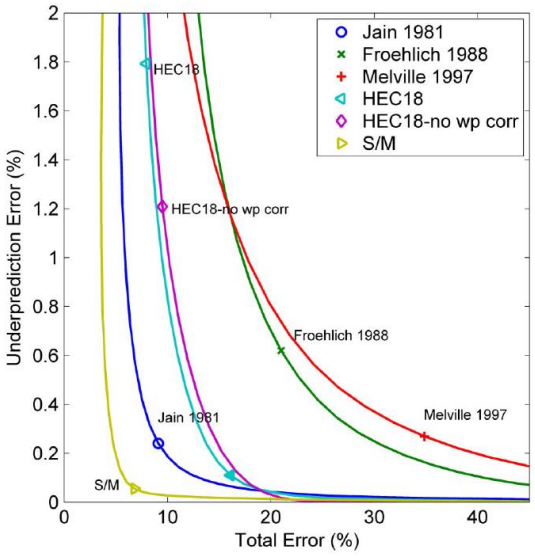

Figure 1.51: Underprediction error of dimensional scour depth versus total error for laboratory data (Sheppard et al. 2014)

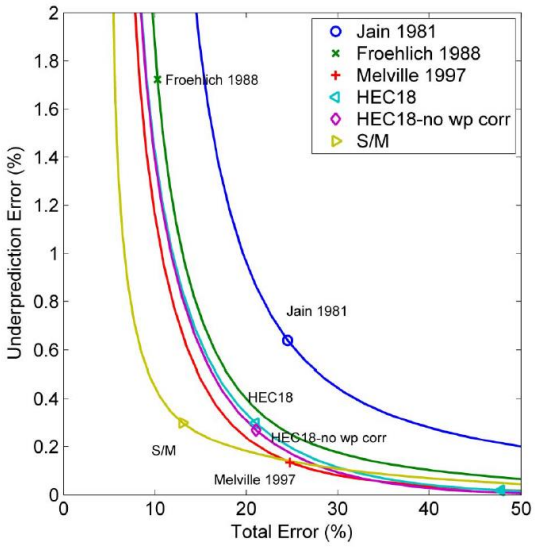

Figure 1.52: Underprediction error of dimensionless scour depth versus total error for laboratory data (Sheppard et al. 2014)

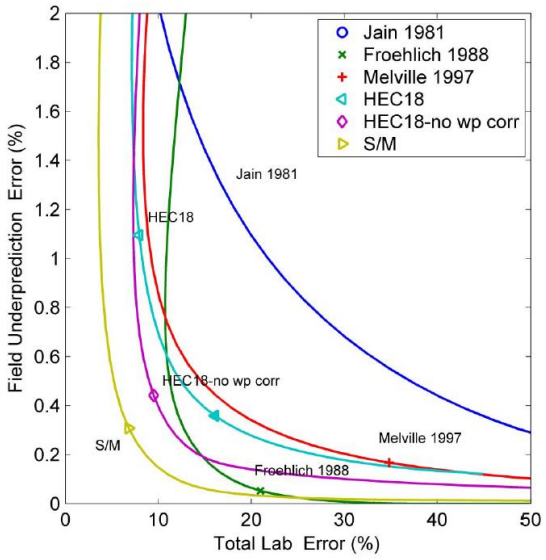

Figure 1.53: Underprediction error of field dimensional scour depth versus total error for laboratory data (Sheppard et al. 2014)

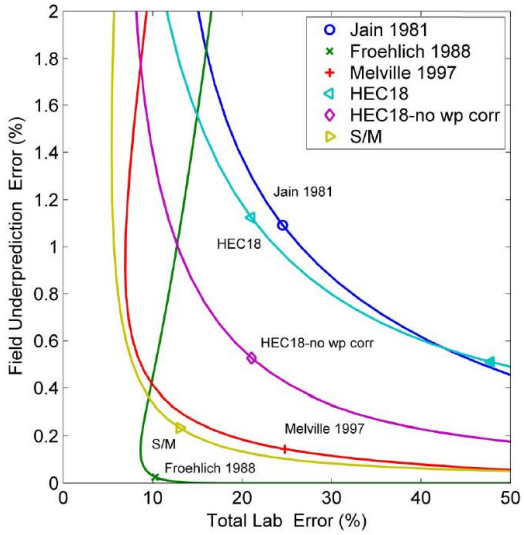

Figure 1.54: Underprediction error of field dimensionless scour depth versus total error for laboratory data (Sheppard et al. 2014)

The best performing equations were Jain (1981), Froehlich (1988), Melville (1997), HEC-18, HEC-18 with wide pier correction, and Sheppard/Melville. The Sheppard/Melville (2011) which was a combination of Sheppard and Miller's (2006), and Melville's (1997) equations was the most accurate of the 23 equations examined. Qi et al. (2016) also did a study on pier scour equations with comparisons to results of 126 laboratory and 408 field data sets. The equations studied were HEC-18, the 65-1R equation proposed by the Ministry of Railways of the People's Republic of China, the 65-2 equation recommended by the Ministry of Transportation of People's Republic of China, Melville and Sutherland (1988), and Melville (1997). The results of comparing the equation predictions with the lab and field measurements was summarized in Figure 1.55 and Figure 1.56.

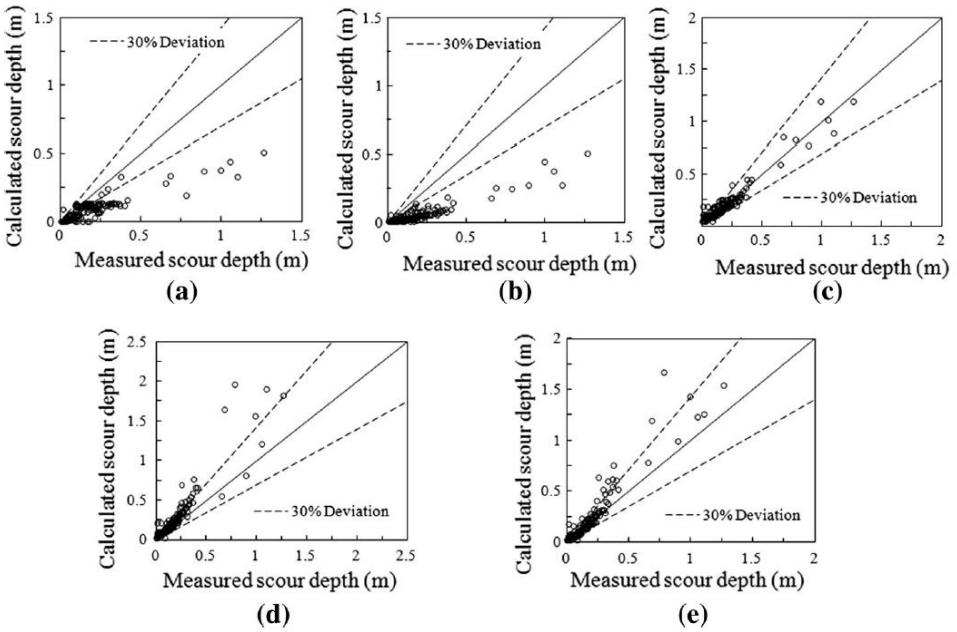

Figure 1.55: Comparisons of equations with laboratory scour measurements: (a) 65-1R; (b) 65-2; (c) HEC-18 4th;(d) Melville and Sutherland (1988); (e) Melville (1997) (Qi et al., 2016)

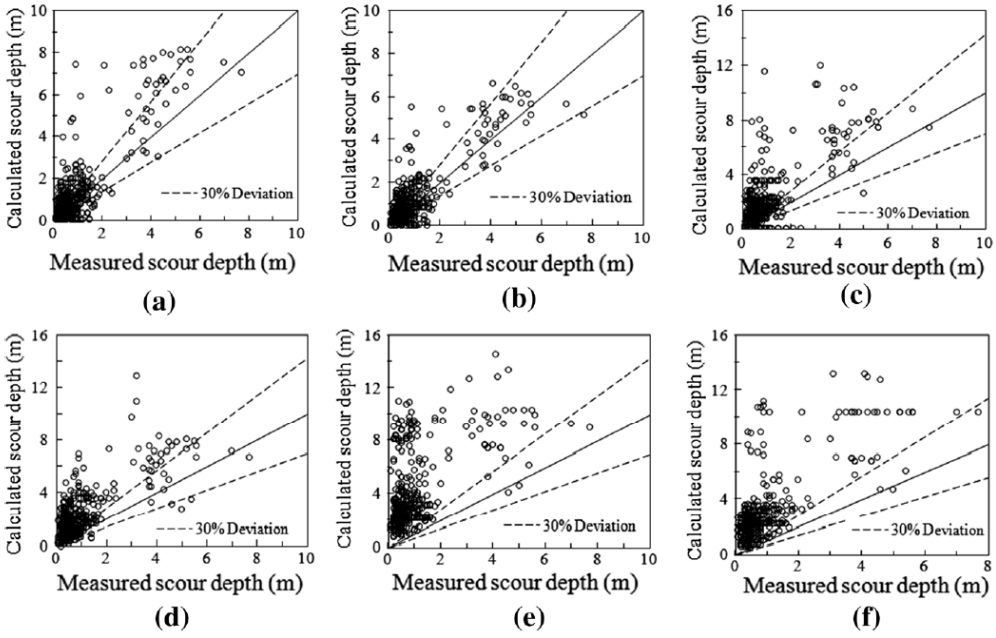

Figure 1.56: Comparisons of equations with field scour measurements: (a) 65-1R; (b) 65-2; (c) HEC-18 4th; (d) HEC-18 5th; (e) Melville and Sutherland (1988); (f) Melville (1997) (Qi et al., 2016)

The two Chinese equations were the most accurate for field estimates but underpredicted laboratory scour depths. The HEC-18, also referred to as the CSU equation in the study, was the most accurate in predicting laboratory pier scour depths. The Melville and Sutherland (1988), and Melville (1997) equations were generally conservative by over predicting scour in both field and lab. A parametric study was also conducted on the inputted factors and the resulting scour depth from the five equations. The influence of flow velocity, depth, pier width, and sediment size on the predicted scour depth were plotted and discussed in a similar manner to Figure 1.50. Liang at al. (2017) evaluated the performance of equations for predicting local scour at pile groups. Experiments were done with single, tandem, side by side and 3x3 pile groups with different spacings, flow velocities and flow depths. Baghbadorani et al. (2017) also compared pile group local scour equations and proposed a new approach which had 10% less prediction error than existing equations.

1.3 Numerical Research into Scour

Studies into analyzing and predicting scour at bridge foundations has been primarily conducted with laboratory flume experiments. A constraint with using laboratory sized experiments is that bridge foundation must be scaled down to fit in flume tanks. Thus, equations developed with data from laboratories include scaling effects when findings are applied to larger foundations in the field. The lack of field scour data and scaling effects have both resulted in overly conservative estimates of scour depth with the empirical formulae mentioned in Section 1.2. Some experimental investigations have attempted to bypass the issue of scaling effects with Froude similarity, but that technique does not address Reynolds and turbulence scale effects. The future of scour research requires methods of predictions which incorporate as many of the factors discussed in Section 1.1 and provide accurate depth estimates. The best means to approach future studies is with numerical modeling of the fluid and soil phases. Scour has been numerically modeled with tools such as computational fluid dynamics (CFD), finite volume method (FVM), finite element method (FEM), and the discrete element method (DEM). Numerical methods allow researchers to overcome the scaling issue by modeling full sized simulations while measuring scour development in real time.

A major obstacle to overcome is the limited availability of software capable of coupling the complex fluid and soil interactions during scour. Additionally, the CFD models which can

accurately depict the field conditions are computationally expensive with lengthy simulation times. CFD tools involve using the FEM or FVM to solve the Navier-Stokes (NS) equations governing fluid flow. The soil phase is modeled with a sediment model coupled with the fluid to allow fluid forces to erode the soil bed and model sediment transport. Sediment models used with CFD include morphodynamic models such as DEM or dynamic meshing techniques incorporating theory such as Shield's criteria. Ideally the sediment model should also consider various soil parameters such as cohesion changing the erosion mode from particles to chucks for clay. Cases of live bed scour also requires simulation of sediment transport with the use of equations such as Van Rijn's formulas or the Exner mass conservation equation. The most accurate simulations would solve the unsteady compressible NS equations with direct numerical simulation (DNS) and a coupled soil DEM model. However, this approach is unreasonable in most studies so some assumptions must be made to reduce computational cost. Simplifications to reduce computational costs include using the incompressible form of the Reynolds Averaged Navier-Stokes (RANS) equations. This would remove terms with varying fluid density and approximate the turbulence with models such as the k-epsilon or k-omega model. The meshing of flow past a pier would be optimized with a coarse general mesh with refinements around the bed and pier to capture the horseshoe vortex and flow turbulence around sediment. An example of the numerical boundaries for scour around a bridge pile in currents is illustrated in Figure 1.57.

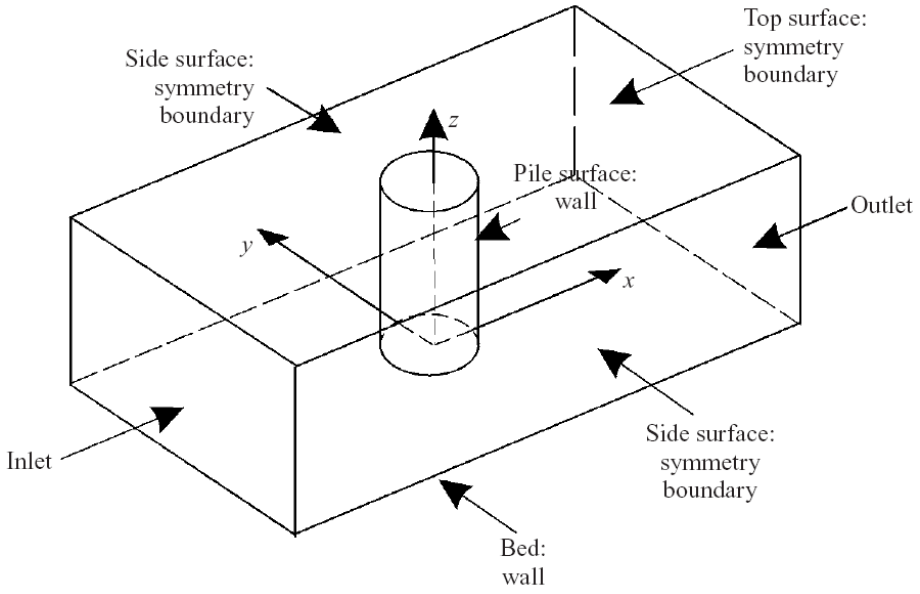

Figure 1.57: Numerical model boundaries of flow around a pile (Roulund et al. 2005)

Different types of boundary and initial conditions can be used depending on the context of the simulation. For the cases of wave scour, a free-surface model is required especially for shallow flows with larger velocity variation near the bed. Figure 1.58 displays the development of a scour hole around a bridge pier with a numerical simulation.

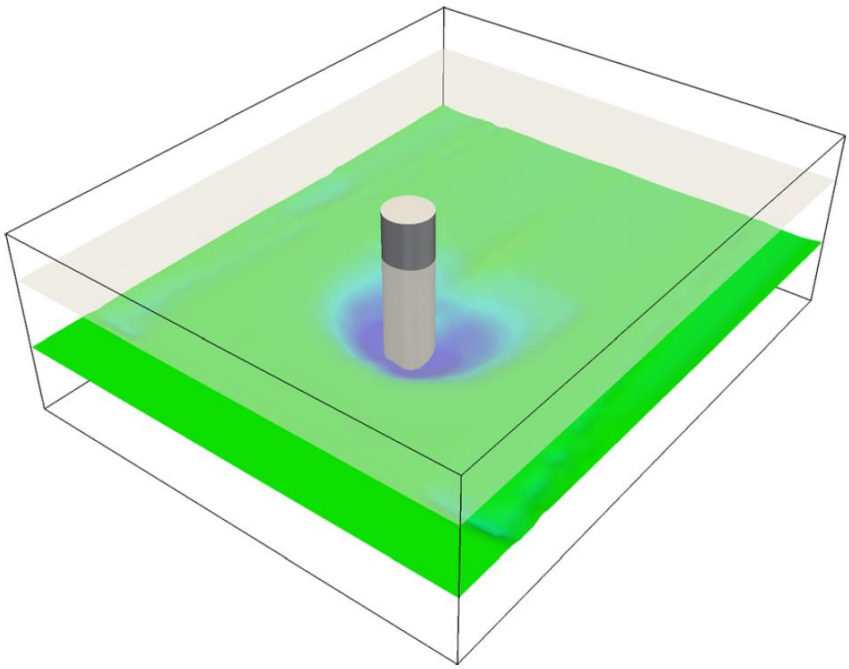

Figure 1.58: Numerical model of scour hole around a bridge pier (Afzal et al. 2015)

Richardson and Panchang (1998) used FLOW-3D to simulate scour-inducing flow at bridge piers and verified findings with the experimental results of Melville and Raudkivi (1977). As with some of the earlier studies limited by software capabilities this study was only of the fluid phase. Instead of an erodible soil bed, the bottom boundary condition was set as a rigid bed to evaluate the flow field at three different stages of scour. The scour stages included a flat bed, a 5 cm deep intermediate scour hole, and a 7 cm deep equilibrium hole from the results of Melville and Raudkivi (1977). Comparing the velocity field of the model with experimental results showed a good agreement. Wu at al. (2000) investigated the general scour and sediment transport in open channels with their own numerical model. The suspended-load transport was simulated through the general convection-diffusion equation and the free surface was determined from a 2D Poisson equation. The model was tested for net entrainment from a loose bed and with net deposition leading to a good match with experiments. Salaheldin et al. (2004) numerically modeled scour at

piers with Ansys-Fluent to investigate which modeling parameters best match results from experiments. Bed shear stresses and velocity fields were compared with results from Melville and Raudkivi (1977), Ahmed and Rajaratnam (1998), and Dargahi (1987). The influence of turbulence model choice was studied by comparing five different models including the one-equation Spalart-Allmaras model, Reynold's stress model (RSM), standard k-epsilon model, renormalization group (RNG) k-epsilon model, and realizable k-epsilon model. The one-equation Spalart-Allmaras model was the simplest option and performed very poorly in modeling the three-dimensional separated flows around a pier. The RSM model provides closure of the RANS equations and the best results but was computationally expensive. The three k-epsilon turbulence models have similar transport equations for turbulent kinetic energy and dissipation rate but use different expressions for the turbulent viscosity. The k-epsilon models overestimated velocity near the bed, especially the realizable k-epsilon model which provided the least satisfactory results of the three k-epsilon models. The fluid domain also included air for the free surface modeling and the recommended composition was a 1:2 ratio of air layer thickness to the water layer thickness. Ge and Sotiropoulos (2005a, 2005b) used a chimera overset grid flow solver to model the flow around a complex bridge foundation. Just the fluid phase was simulated to see how well large-scale simulations capture vortex sheading in the full-scale setting. Results of the mean flow velocities and turbulent intensities showed good agreement with field measurements. Roulund et al. (2005) conducted experiments of cylindrical pier scour to validate numerical simulations with EllipSys3D CFD code. Transient models captured complex flow structures with vortices more accurately but required a long time to simulate. Steady-state simulations were completed quickly but underpredicted maximum pier scour by 15%, and downstream scour up to 30%. Of the turbulence models tested, the k-omega Shear Stress Transport (SST) model performed the best due to its accurate simulation of near boundary flows. The turbulent flow around piers and bed-shear stresses are the most important processes for scouring, thus the k-omega SST model was recommend over the standard k-omega and k-epsilon models. Additionally, a comparison was made between smooth bed and rough bed models where roughness was approximated as the median soil grain size. The smooth bed simulation reported inaccurate flow velocities and directions, so the rough bed was deemed necessary for numerically modeling scour flows.

The numerical fluid-sediment coupling is very complex and the range of morphodynamic soil models provide many options. All particle-particle and fluid-particle interactions are still

difficult to capture realistically within current computational limits. For example, the seepage flow in soil has the possibility of lowering the buoyant weight and increasing how susceptible the bed is to scour (Zanke et al. 2011). Bierawski and Maeno (2006) used a DEM-FEM model to study highly saturated soil motion due to seepage force. The numerical model combined FEM for pore-water pressure fluctuations, poroelastic equations for soil, and DEM to simulate the transport phenomena inside highly saturated discrete soil. Zhu et al. (2007) reviewed the theory and literature on discrete particle simulation. They discussed the acting forces on particles in a fluid with the influence of different time and length scales. The scale effects on particle modeling were summarised in Figure 1.59.

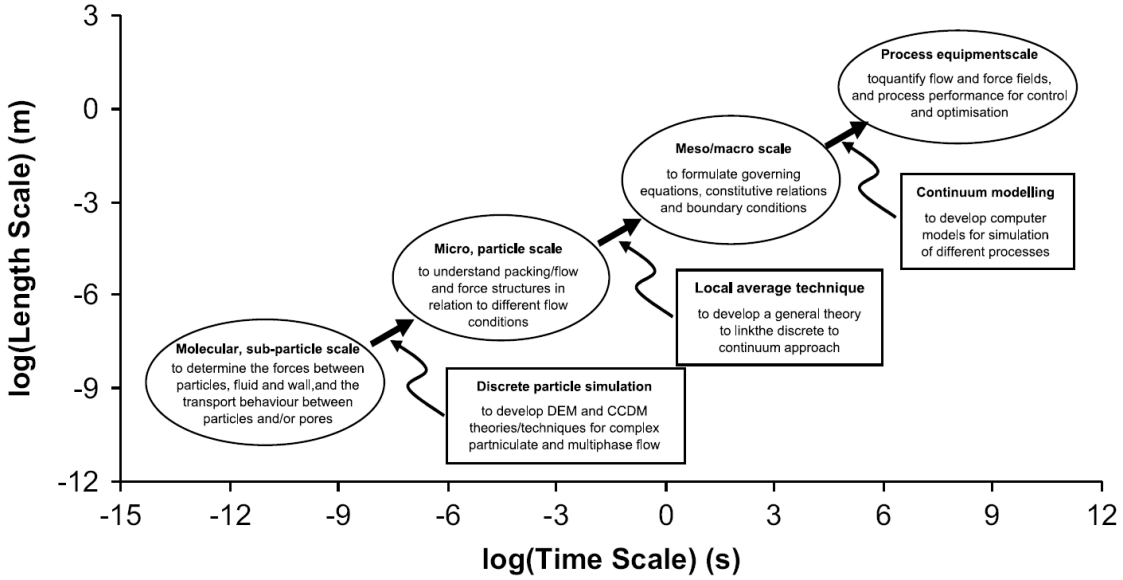

Figure 1.59: Particle modeling approaches at different time and length scales (Zhu et al. 2007)

The level of analysis and choice of discrete versus continuum particle modeling at different scales are described in Figure 1.59. Zhu et al. (2011) continued their study into linking discrete particle simulation to continuum process modelling for granular matter. Zhu et al. (2011) recommended using the continuum approach at a macroscopic scale and the discrete approach at a particle scale. A novel hybrid particle model was proposed and applied to a particle flow in a hopper and particle-fluid flow in an ironmaking blast furnace.

Huang et al. (2009) studied CFD modeling of scale effects on turbulence flow and scour around bridge piers with Ansys-Fluent. Escauriaza and Sotiropoulos (2011) used a detached eddy

simulation (DES) to examine the initial stages of erosion around a pier due to the horseshoe vortex. A novel morphodynamic model was comprised of the Exner equation coupled with a new bed transport model integrated with the effects of the instantaneous flow field. The model included nonlinear effects between the flow field and the bed while providing a better description of bed load transport flux. Bed ripples and velocities in the simulation closely matched experimental results. Zhi-wen and Zhen-qing (2012) modeled the sediment bed around a pier with a boundary adaptive mesh technique to modify the grid system with changed river-bed boundary. Comparing results with Melville and Raudkivi (1977) showed a good agreement in flow velocities and maximum scour depth at the pier. However, the boundary adaptive mesh technique provided a different scour hole shape due to not capturing the slope collapses in the hole accurately. Dynamic meshing compared the bed shear stress with the soil's critical shear to simulate the erosion while excluding some soil phenomena such as avalanching.

Abdallah Mohamed et al. (2013) numerically and experimentally researched into effects of contraction ratios and entrance angles on bridge abutment scour. The numerical tool used was SSIIM (sediment simulation in water intake with multiblock option). Testing entrance angles between 10° and 90° revealed that smaller contraction ratios and smaller entrance angles produced less scour. Local abutment scour was seen reduced by 92% after changing the entrance angle from 90° to 10°. Karami et al. (2014) verified SSIIM 2.0 simulations of non submerged spur dike scour with experimental data. The structure arrangement consisted of three parallel spur dikes where the horseshoe vortex produce the deepest scour as the at the first spur dike and wake vortices procured the second most scour at the third spur dike. As the second spur dike was shielded by the other two, recommendations were to prioritize scour protection at the first spur dike and then the third or last.

Ehteram and Meymand (2014) compared experimental and numerical results obtained using SSIIM 2.0 for scour depths at side piers of bridges. Comparing turbulence models indicated that the k-epsilon RNG model performed better than the standard k-epsilon as the RNG did a better job of capturing turbulence at a range of scales. The results for maximum scour depth from numerical simulations were 15% less than experiments, indicating a significant error and room for improvement of simulation. However, numerical results provided satisfactory predictions for location of scour holes, water levels and velocity profiles. Xiong et al. (2016) employed a

dynamic-mesh updating technique with Ansys-Fluent code to analyze clear water scour around piers. The mesh updating through-out simulations was node by node as opposed to a general boundary condition for a more accurate riverbed model. Jiang et al. (2017) analyzed how simulation parameters influenced the results of flow past a circular cylinder. Different boundary conditions and domain dimensions relative to the cylinder diameter, *D*, were tested to ensure that wake vortices were not restricted in development. A span length of at least *10D* was recommended for accurate modeling of unrestricted wake structures and hydrodynamic forces. Alemi and Maia (2018) investigated numerical simulation of flow and local scour around single and complex bridge piers. As large times steps can decrease computation time, they hinder the accuracy by excluding unsteady flow structures. Using SSIIM, multiple tests were performed for different pier configurations to find the steady state solution for maximum scour depth. Up stream scour geometry was accurately predicted but depths at downstream sides of the pier were underpredicted. Alemi and Maia (2018) assumed that this implied that the horseshoe vortex may not have been accurately represented using the turbulence models. Ahmad et al. (2018) used REEF3D to model wave-induced scour around piles in a side-by-side arrangement. The level set method was used to simulate the free surface along with the Exner formula to model evolution of the sediment bed. Zaid et al. (2019) used Ansys-Fluent to perform steady-state simulations of flow past a pier mounted on a rigid bed. Circular and square piers were tested with the numerical results compared to the experiments by Daragahi (1989). Nagel et al. (2020) developed a three-dimensional sediment scour model based within the framework of the open-source CFD platform OpenFOAM. Nagel et al. (2020) discussed the formation and coupling of their morphodynamic model for sediment with OpenFOAM's fluid modeling. The novel model demonstrated the need for more accessible and versatile sediment-fluid coupled software for scour simulation.

The bulk of numerical research has been limited and with the goal of simulating scour rather than using results to form predictive methods. Earlier simulations were conducted solely with rigid beds to examine the flow around obstacles such as piers. For example, Briaud et al. (1999) used CFD results to develop an expression the maximum bed shear stress around a pier in the SRICOS method. As numerical flows were well represented the next problem was including a mobile bed. Research into morphodynamic models and dynamic meshing techniques was performed to simulate the sediment bed erosion. For live bed scour, sediment transport equations were used to model the bed load transport. A robust coupled fluid-sediment model should be

developed to account for all soil and water interactions. Optimizing simulations require testing of parameters such as bed roughness, turbulence models, domain sizes and boundary conditions. Recent numerical studies have replicated the development of scour hole very well. The next steps involve using a capable software to run multitude of simulations with varying fluid, soil, and structural properties. A parametric study of full-scale numerical scour would support in the development of novel reliable scour prediction methods.

1.4 Computational Algorithms for Predicting Scour

As an alternative to traditional dimensional analysis, the use of artificial neural networks and gene expression programming have been used to study the relationships between scour depths and influencing factors (Lee et al. 2007). A benefit to the use of computational algorithms is that the physical scour theory does not need to be analyzed to provide accurate predictions of scour depths. Artificial Neural Networks (ANNs) haven proven useful in overcoming the complex non-linear relationships between scour factors. ANNs process data sets of inputs and outputs using algorithms based on a simplified version of the biological nervous system. In the case of scour, the outputs are scour depths and inputs are the factors relating to flow, structure, and soil. A typical three-layer ANN with an input layer, hidden layer and output layer is illustrated in Figure 1.60.

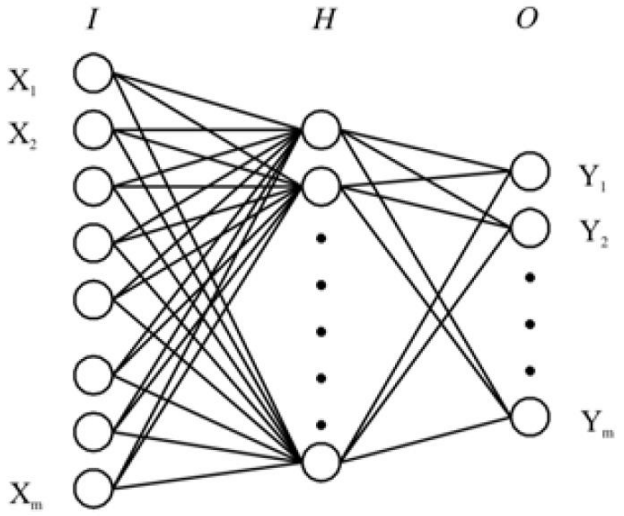

Figure 1.60: Three-layer artificial neural network structure (Lee et al. 2007)

The initial inputs are entered into a transfer function and the inner hidden layer contains more functions describing the relationships between inputs and outputs. Each layer contains several neurons, and these layers are correlated with weights. Like an artificial intelligence, as data is feed into the ANN it will learn to adjust weights, node connections, and functions. The learning process is referred to as training, and more data sets will improve the performance of the ANN in predicting futures scour depths. Lee et al. (2007) used a Back-Propagation Neural Network (BPN) to estimate pier scour depths. Lee et al. (2007) used non-dimensional forms of inputs and outputs where the scour factors considered included pier widths, flow velocity, critical velocity, flow depth, soil grain size, and soil gradation. In the BPN, errors at the output layer propagate backwards into the input layer though the hidden layer to train the ANN. The BPN model's scour predictions were found to be more accurate then five traditional pier scour equations. Kaya (2010) used Levenberg–Marquardt back-propagation algorithm with MATLAB's Neural Network Toolbox to study scour depths around bridge piers. A FHWA data set of 380 measurements at 56 bridges was used to train the ANN with dimensional data inputs. A portion of the data was used to train the ANN and the rest was used to predict and compare the depth values with those obtained from the HEC-18 equation. The ANN performed well with live bed scour but had overpredicted clear water scour with coefficient of determination of $R^2 = 0.60$. The overpredictions were suggested to have occurred because experimental scour depths were not the peak depths for the given conditions. A sensitivity analysis was conducted on the inputs to examine the influence on depth prediction accuracy. After the sensitivity analysis, the number of inputs would be reduced to those which primarily controlling scour. Kaya (2010) found that reducing the number of variables from 14 to 9 had a negligible impact on the coefficient of determination, (0.73 versus 0.72). The optimal number of inputs was four, consisting of pier width, skew angle, flow depth and flow velocity. The four inputs provided the highest coefficient of determination of $R^2 = 0.81$ overall and $R^2 = 0.89$ for live bed scour. The two most influential variables of flow depth and flow velocity provided a coefficient of determination of $R^2 = 0.66$. Pal et al. (2011) applied the use of support vector machines and two other ANNs to study and predict pier scour. The results of the models were compared with four traditional pier scour equations including HEC-18, where the support vector regression performed the best. From a sensitivity analysis of the support vector regression, dimensional inputs were recommended over non-dimensional, and the most influential factors were flow depth and pier width. Toth and

Brandimarte (2011) used a multi-layer feedforward network to predict pier scour which performed better than traditional pier scour equations.

Khan et al. (2012) used the artificial intelligence based soft computing technique gene expression programming (GEP) to predict bridge scour. GEP is a search technique that incorporates mathematical expressions, decision trees and logical expressions. The primary advantage of GEP over ANN is that GEP provides an explicit mathematical expression for calculating pier scour. The GEP expression can be readily used in engineering design and performed well against an ANN and traditional empirical formulae. Ismail et al. (2013) used a feed-forward neural network with an adaptive activation function to predict the evolution of scour depth at piers. With temporal considerations the model performed slightly better than the Melville and Chiew (1999) method. Najafzadeh et al. (2013a) used a new application of group method of data handling (GMDH) to predict scour at piers in cohesive soils. The properties inputted into the GMDH were initial water content, *IWC*, shear strength, compaction of cohesive bed materials, clay percentage, *Cp*, and the flow Froude number. The model performed well for soil in the range of 36.3%< *IWC* <42.28% and 35% < *Cp* < 100%. A sensitivity analysis revealed that clay percentage was the most influential factor on scour depth while non-dimensional shear strength had the least influence. Najafzadeh et al. (2013b) expanded their studies and applied the GMDH model to predict abutment scour in cohesive soil. After testing two types of montmorillonite and kaolinite clay soils, the GMDH model had the higher performance for unsaturated montmorillonite clay with *IWC < 25%* than ANNs and empirical formulae. Park et al. (2017) discussed the importance of training ANNs to prevent scale effects and accurately predict scour at both thin and wide piers. With both laboratory and field data sets, different types of training and testing were evaluated for the ANN. The ANN model trained with laboratory data overestimated field scour depths just as traditional empirical formulae. The ANN trained with field data produced severe scattering of results when attempting to predict scour depths of the laboratory experiments. The best performing ANN was trained with 50% of laboratory and 50% of field data. The large range on inputs of pier size and flow depths trained the ANN to be robust and applicable for all scales.

1.5 Scour Monitoring Technologies

An important part of controlling scour and ensuring adequate performance of bridges is monitoring the depth of scour. Monitoring and measurements of scour depths can be done in

person with equipment or remotely with instrumentation installed on site for real time data. Research and development have been done into creating various devices which can be implemented to record the depth of scour holes over time. Monitoring can be vital for bridges which are scour critical or expected to experience large levels of flooding. Monitoring can be used to determine locals scour depths, exposure of footings, and the conditions of scour countermeasures in case of disturbances. In person equipment for measuring bottom elevations include probes/rods, surveying, underwater sounding, and Ground Penetrating Radar (GPR). In person monitoring may provide better confidence in measurements but is not continuous and difficult during floods. Monitoring devices fixed to structures provide depth measurements in real time without requiring on site personal. Fixed monitoring devices include sonar devices, buried rods, sliding magnetic collar devices, and float-out transmitters (Richardson and Davis 2001). Studies into monitoring equipment seek to improve accuracy of real time readings, cost efficiency and non-invasive implementation.

Zheng et al. (2017) conducted a study using multi-beam echo sounders (Seabat 7125) to map the riverbed topography around bridges. The sonar devices were used to track erosion and soil deposition in various parts of the Yangtze River Estuary. The sonar devices provided high resolution data for tracking the change in scour hole depths which would then be used to determine the structural state of bridges. Yankielun and Zabilansky (1999) used time-domain reflectometry (TDR) sensors as a method to constantly monitor scour depth with the ability to detect sediment depth changes smaller than 5 cm. A probe at the location of interest has a signal sent through wires and reflected in a measured time period. Then using the knowledge on the conduction of the surrounding soil the scour depths were determined. Using a computer an alarm can be triggered once a critical scour depth has been observed. TDR has the potential to provide real time and accurate results even during high-energy flow periods such as floods. Chen et al. (2015) investigated the use of magnetic sensors called smart rocks for monitoring the depth of scour holes. The ‘master’ smart rocks were attached to piers to serve as a reference point to displacement measurements. Then other spherical smart rocks were placed on the riverbed adjacent to the pier, where the distance from the master smart rock would be measured in real time based using a magnetometer within the smart rocks. As the scour hole grows the spherical smart rocks would move further down in elevation allowing for monitoring of the erosion rate and scour depth. Issues arise in managing the alignment of the magnets in the rocks and losing the smart rocks due to high-

speed flow. Lu et al. (2008) performed field measurements and simulations of scour at the Si-Lo Bridge in the lower Cho-Shui River, the longest river in Taiwan. Multiple monitoring devices were evaluated, the findings summarized in Table 1.17.

Table 1.17: Comparison of existing instruments for measuring bridge scour (Lu et al. 2008)

Instrument	Advantages	Disadvantages or limitations	Relative cost
Bridge mounted sonar	Continuous and accurate record of riverbed	Mild slope river/estuary	Medium
Acoustic Doppler current profilers (ADCP)	Portable; measuring both velocity profile and water depth	Not applicable to high sediment concentration conditions	High
Ground penetrating radar (GPR)	Continuous record of riverbed	Time consuming in operation; specialized training required	High
Fiber Bragg grating (FBG) sensor	Continuous monitoring of riverbed	Limited successful field tests, tests for extreme environment needed	High
Numbered bricks	Commercially available; applicable to highly turbulent or rapid flows	Excavation of riverbed required; suitable for ephemeral rivers	Low
Sliding magnetic collar (SMC)	Easy to operate	Excavation of riverbed required; high maintenance/repairing cost	Low
Steel rod	Easy to operate	Excavation of riverbed required; high maintenance/repairing cost	Low

Lu et al. (2008) also used the data measurements to propose a method for simulating the general, contraction, and local scour to determine the total scour at bridge foundations.

1.6 Scour Countermeasures

When designing with scour in mind, an adequate foundation depth can be supplemented with protective measures to mitigate and reduce scour. The types and implementation of scour countermeasures are discussed in design manuals such as the MTO Drainage Manual, the FHWA HEC-18 manual, and the FHWA HEC-23 manual. Further studies have been conducted to evaluate the effectiveness of existing countermeasures and develop novel countermeasures. Protective measures against scour are divided into two categories of active and passives countermeasures (Richardson and Davis 2001). Passive countermeasures are those which provide a physical barrier against scouring forces such as coarse armour layers, riprap, gabions, and collar plates. Active countermeasures seek to reduce the strength of scouring forces such as the downward flow and horseshoe strength vortex. Active countermeasures include manipulating the channel shape, aligning piers with the flow to reduce effective widths, and selecting low scour structural design choices such as round nosed piers. It is recommended to prioritize active countermeasures during preliminary stages of design and supplement with passive countermeasures if necessary (Richardson and Davis 2001).

A common method of scour control is metal plate collars attached at to bridge foundations for protection against local scour. Theses collars, as seen in Figure 1.61, would surround a pier and sit near the bed where down flow and the horseshoe vortex are active.

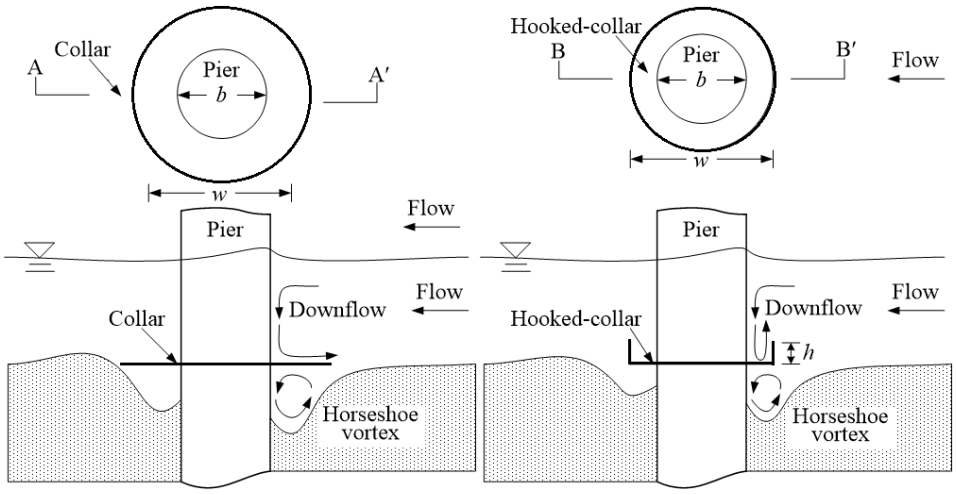

Figure 1.61: Circular and hooked collars for piers (Chen et al. 2018)

Jahangirzadeh et al. (2014) investigated the effectiveness of circular and rectangular shaped collars using experiments and numerical simulations. Using SSIIM 2.0, laboratory tests were numerically replicated and the CFD simulations were found to accurately predict the amount of scour. Square shape collars were found to be most effect for reducing scour as they lowered the horseshoe vortex strength more than circular collars. Testing the elevations of collars revealed that under-bed collars reduced scour much more than collars placed on or above the sediment bed. The most effective width of collars fell into the range of *3D - 3.5D*, where *D* is the pier diameter. Nasr-Allah et al. (2013) investigated different dimensions of collars for bridge abutments by comparing numerical and experimental results. Numerical simulations were conducted in SSIIM with non-compressible flow, k–ε turbulence model and Van Rijn's sediment formula. Findings revealed an optimal collar of length *0.73L* relative to the abutment length, *L*, reduced the maximum scour depth by 69%. For validation, results from SSIIM matched experimental results with average correlation coefficient of 95%. Chen et al. (2018) tested the use of hooked shaped collars where the outer edge of the collar bends upwards as seen in Figure 1.61. The hooked collar dimensions were set to a width of *1.25D* and a height of *0.25D*, where *D* was the pier diameter. Collars with hooks were proven to further reduce the strength of the horseshoe vortex and turbulent kinetic energy thus leading to reduced scour depths. The optimal collar arrangement was found to

be a double collar setup with one buried at a depth of *0.25D* and a second collar placed at bed level. Nielsen et al. (2013) investigated the flow, bed shear stresses, and different layer configurations of stone scour protections around a pile in a current. The scour protection consisted of a coarse stone layer covering a filter layer with fine stones, analogous to a coarse armour layer. Nielsen et al. (2013) discussed how bed sediment transport around scour protection can lead to misalignment of the protection and potential structural instability. Using numerical simulations in FLOW-3D, Nielsen et al. (2013) developed a method for determining critical stones size used in protection to prevent motion of the base sediment.

1.7 Conclusions

An exhaustive review on bridge scour analysis and predictions is covered in this chapter. The influences of factors from the soil, fluid, and structural interactions are discussed in detail. The most influential factors for scour include flow depth, flow velocity, flow direction, structural dimensions, median soil grain size, soil gradation, and soil cohesion. Further parametric studies must be conducted on soil parameters as the current scour data is limited for cohesive soils. The need for further investigations into stochastic scour analysis with varying soil compositions and flow rates is highlighted. Common equations for estimating contraction and local scour at piers, piles, and abutments are discussed in detail. The disadvantage of the empirical formulae is their basis on limited laboratory data which has led to overestimates of field scour. Most scour prediction methods were developed for coarse sand at laboratory scales, thus further research into field scour at all soil types and rock is recommended. Studies comparing predictive equations revealed the best performing pier scour equations to be the HEC-18 equation based on the CSU equation and the Sheppard/Melville (2011) equation. Other methods for analyzing scour depths examined are soft computing techniques like ANNs and GEPs which have been shown to perform better than empirical formulae. Although ANNs and GEPs do not provide information on the physics behind scour they are powerful statistical tools for identifying patterns in data. GEPs are recommended in addition to traditional dimensional analysis as they can provide a compact equation for depth predictions. Current methods are lacking in accuracy due to scale effects from the lab data used to develop equations and due to the exclusion of many soil parameters. In addition to accurate scour predicting, scour monitoring and countermeasure are vital for scour

critical bridges. Research into the testing of monitoring technologies and proposed countermeasures designs were discussed.

Techniques and studies conducted into numerically modeling simulating scour were reviewed. Numerical techniques are the future of scour studies to overcome scale issues in laboratory and difficulty of obtaining field data. Earlier studies focusing on capturing the flow field at piers while newer work has looked to include sediment modeling. Most existing numerical research into scour has focused on the validation of numerical algorithms with experimental scour data as coupling realistic sediment models with fluids is extremely difficult. Sediment algorithms capturing all soil vital behaviour such as cohesion, critical shear stress, slope behaviour, and transport are still in development. Future work is recommended into developing coupled numerical fluid-soil solvers with ability of simulating scour hole development and sediment transport. These tools should include a detailed morphodynamic model with all particle-particle interactions, fluid-particle interactions, and influential soil parameters such as clay content, shear strength, angle of repose, and water content. The robust numerical software should serve as the basis for performing a multitude of full-scale simulations to investigate the influence soil parameters on scour to develop novel scour depth prediction methods. Of the available copen scour software SSIIM appeared as the best choice for preliminary investigations into the influence of soil parameters on pier scour. The objective in this thesis is to conduct a sediment parametric study with different soils to quantify the effects on pier scour depths, evaluate the performance of current equations for soil parameter consideration and discuss the numerical modeling of sediment and fluid in SSIIM.

Chapter 2: Modeling and Validating Pier Scour in SSIIM

2.0 Introduction

Scour is a very complicated issue to quantify due to the non-linear interactions between the structural, fluid and sediment interfaces. In addition to the large number of parameters, scour is a probabilistic problem due to potential variations in flows and sediment bed compositions (Wang et al. 2017). The ideal investigative method would be measuring scour at bridge piers, but it is impossible to control all field conditions concerning fluid and sediment characteristics. To provide control over all input parameters, laboratory flume experiments has been the primary method of obtaining scour data. However, with laboratory investigations all structures must be scaled down to fit within laboratory and install measuring equipment. Smaller laboratory models introduce scaling errors which create discrepancies when conducting dimensional analysis. To safely account for these limitations, empirical depth prediction equations based on laboratory data are inherently conservation. Scour prediction at bridge foundations needs significant improvement to provide reliable estimation while considering the influences of all soil parameters. Accurate scour depth prediction methods will reduce the construction costs of bridges foundations and prevent possible bridge failures due to underprediction of scour depths. Thus, to control all parameter inputs and avoid scale effects, numerical scour simulation is the recommended tool. The numerical modeling of scour is still incredibly challenging due to the large number of inputs when coupling sediment transport and fluid flow models. Numerical scour simulation is still in its novel stages where the emphasis is on creating reliable numerical sediment models which consistently replicate laboratory and field results. Scour has been numerically modeled with tools such as computational fluid dynamics (CFD), adaptive meshing techniques, and the discrete element method (DEM). CFD is used to model the fluid phase while morphodynamic models such as DEM or dynamic meshing techniques describe the sediment bed. A discrete particle model such as DEM may provide more precise simulations, but the soil phase modelled as a continuum with adaptive meshing techniques provides a computationally cheaper option. CFD solves a flow field with prescribed boundary conditions reporting the bed shear stresses on a sediment bed and the velocity field which influences sediment transport. A mobile sediment bed boundary conditions would

compare the soil's critical shear stress with the fluid bed shear stress and then the adaptive meshing techniques would update the bed shape with erosion and deposition effects. Richardson and Panchang (1998) used FLOW-3D to simulate scour-inducing flow at bridge piers and verified findings with the experimental results published by Melville and Raudkivi (1977). Salaheldin et al. (2004) numerically modeled scour at piers with Ansys-Fluent and their own adaptive meshing algorithms. Roulund et al. (2005) conducted experiments of cylindrical pier scour to validate numerical simulations with EllipSys3D CFD code. Roulund et al. (2005) discussed how transient fluid models captured complex flow structures with vortices more accurately but were computationally expensive. Steady-state simulations were completed quickly but underpredicted maximum pier scour by up to 15% due to the exclusion some of non steady turbulent behaviour.

With powerful computers and robust numerical scour modeling tools, parametric studies may be conducted to develop novel scour prediction equations or update current methods. Depth prediction equations would be based on simulations with to-scale structures, soils of various compositions, sizes, cohesive strengths, and repose angles. The present objective was to a perform preliminary investigation into the effects of soil parameters on numerical scour and evaluate current methods. A decision was to be made on which tool to use for numerical modeling scour. Presently there exists a limited number of available CFD software coupled with sediment transport models. SSIIM (Sediment Simulation in Intakes with Multiblock option) was selected as it was an open source CFD software with built-in sediment transport modeling ideal for scour simulations. Over the years Olsen had updated and improved the software with more capabilities and a newer version SSIIM 2.0, which is used in this thesis to model scour. SSIIM is capable of modeling sediment transport with various soil sizes, gradations, repose angles, and cohesive strengths amongst other sediment parameters. Before SSIIM could be used for the parametric study, it was to be validated for its performance by verifying simulations with published experimental results. Three SSIIM models of flow past piers were simulated with rigid beds to validate the flow field and then with a mobile sediment bed to validate scour hole depths. SSIIM was able to accurately replicate the flow field around a pier in a rigid bed with good matches against published experimental results as seen later in Chapter 2. During validations of the SSIIM models tests were conducted to determine the best performing numerical parameters. Model inputs for domain sizes, mesh refinement, solver settings and sediment modeling were optimised for accuracy and computational efficiency. A total of four models were created in SSIIM to compare

with published experimental data. Cases 1, 2 and 3 were used for rigid bed validations while Cases 2, 3 and 4 were used for the mobile bed validations.

2.1 SSIIM Theory

SSIIM is a CFD (computational fluid dynamics) program coupled with solvers for sediment transport making it an ideal tool for simulating scour (Olsen 2018). SSIIM has been used to model complex flows, sediment transport, and different types of scours. SSIIM, specifically SSIIM 2.0, was selected because it was a readily available CFD open-source tool with built in sediment transport solvers. SSIIM solves the fluid flow field described by the 3D (three-dimensional) incompressible Reynold's Averaged Navier-Stokes (RANS) equations

$$\frac{\partial u_i}{\partial x_i} = 0 \tag{2.1}$$

$$\frac{\partial u_i}{\partial t} + u_j \frac{\partial u_i}{\partial x_j} = -\frac{1}{\rho}\frac{\partial P}{\partial x_i} + \vartheta\left(\frac{\partial^2 u_i}{\partial {x_j}^2}\right) - \frac{\partial u_i' u_j'}{\partial x_j} \tag{2.2}$$

where i and $j = 1, 2$ and 3 represent the dimensions of (x), (y) and (z) spatial directions respectively, x_i and x_j are the spatial coordinates, u_i and u_j are the time-averaged velocity components, u'_i and u'_j are the fluctuation components of velocity, P is the non-hydrostatic pressure, ρ is the fluid density, ϑ is the kinematic viscosity, and t is the time (Olsen 2018). The Reynold's stress term, $u'_i u'_j$, was modeled with the Boussinesq-approximation as

$$-u_i' u_j' = \vartheta_t\left(\frac{\partial u_j}{\partial x_i} + \frac{\partial u_i}{\partial x_j}\right) - \frac{2}{3}k\delta_{ij} \tag{2.3}$$

where ϑ_t is the eddy viscosity, k is the turbulent kinetic energy, and δ_{ij} is the Kronecker delta equal to 1 if $i=j$ and 0 otherwise (Olsen 2018). SSIIM uses the standard k-epsilon turbulence model to estimate the eddy viscosity as

$$\vartheta_t = C_\mu \frac{k^2}{\varepsilon} \tag{2.4}$$

where C_μ is a constant coefficient, and ε is rate of dissipation of turbulent kinetic energy. Through the uses of the Boussinesq-approximation and a turbulence model some minor errors are introduced for the sake of computational efficiency. To solve Equations 2.1 and 2.2 the SIMPLE

(Semi-Implicit Method for Pressure Linked Equations) algorithm was implemented into SSIIM for computationally efficient steady-state simulations (Olsen 2018). Further details on the formulation of the SIMPLE method are described by Patankar (1980). The SIMPLE method is a numerically stable technique for solving the flow with the unknown pressure field while excluding some transient flow effects. The flow effects neglected are related to turbulence generation, advection, and dissipation such as wake vortices shedding. The SSIIM models were constructed as rectangular channels with a solid cylindrical pier as illustrated in Figure 2.1.

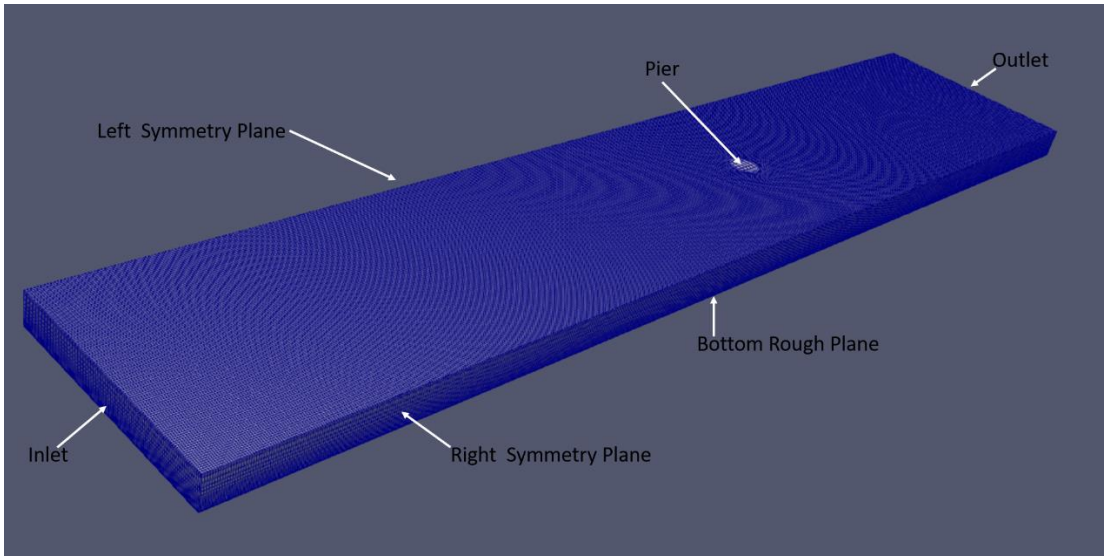

Figure 2.1: Case 1 model mesh and boundary conditions

SSIIM employed an unstructured grid with hexahedron shaped cells for solving of Equations (2.1) and (2.2) with the control volume method. The mesh was generated by first creating an orthogonal grid of the channel and then defining the pier area with a smooth elliptic grid around a circular cylinder. The meshing options in SSIIM were limited in geometry generation and localised refinement. The ideal grid would consist of a coarse mesh of the entire channel with a refined nested block at the pier which provides accurate result while reducing computational costs. However, the nested algorithm in SSIIM 2 lead to poor results when compared to those from the single refined block shown in Figure 2.1. Thus, the uniform and moderately refined grid was used in SSIIM. To improve stability and convergence, block-correction was employed in SSIIM. With block correction the solution is first solved for on a coarser grid and then iterated further on finer grid starting with interpolations from the coarse grid

solution. With block correction many instabilities may be avoided with fine grids and complicated geometries (Olsen 2018). To prevent additional instabilities and solution oscillations common in non-staggered grids, the Rhie and Chow (1983) interpolation was implemented into SSIIM (Olsen 1999).

The model shown in Figure 2.1 had inlets prescribed as a Dirichlet boundary condition with a flowrate calculated using a mean flow velocity and the cross-sectional area of the model (Olsen, 1999). The outlet and side walls were set to zero gradient boundary conditions. The top surface was also set as a wall with zero gradient boundary conditions as opposed to a free surface model to save on computational time. The lack of a free surface was justified as all models were of low-Froude number flows which experience negligible vertical velocities near the surface. Roulund et al. (2005) stated that for flow Froude numbers less than 0.209, the free surface may be removed with no substantial impact on scour depths. The pier and sediment bed were set as solid walls with smooth and rough surfaces, respectively. The velocity field near the wall boundaries were modeled with the standard wall functions equation

$$\frac{u}{u_*} = \frac{1}{K} ln\left(\frac{30y}{k_s}\right) \tag{2.5}$$

where u is the velocity, u_* is the shear velocity, K is the von Karmen constant equal to 0.4, k_s is the wall roughness, and y is the distance from the wall to the cell centre (Schlichting 1979). The bed shear stress on the sediment bed, τ, used for sediment transport calculations was determined using

$$\tau = \sqrt{C}_\mu \rho k \tag{2.6}$$

where k is the turbulent kinetic energy, ρ is the fluid density, and C_μ is a constant coefficient. The shear stress exerted by the fluid in Equation (2.6) was compared with the critical shear stress of the soil for the sediment transport calculations. The sediment transport solver in SSIIM is coupled with the fluid Equations (2.1) and (2.2) to solve for the sediment concentrations near the bed and suspended in the fluid. The concentration of the suspended load is governed by the transient convection-diffusion equation

$$\frac{\partial c}{\partial t} + u_j \frac{\partial c}{\partial x_j} + \omega \frac{\partial c}{\partial z} = \frac{\partial}{\partial x_i} \vartheta \left(\Gamma \frac{\partial c}{\partial x_i}\right) \tag{2.7}$$

where c is the sediment concentration, ω is the sediment fall velocity, u_j is the fluid velocity, x_i *and* x_j are the space dimension for dimension i=1, 2 and 3, and Γ is the turbulent diffusivity (Olsen 2018). For the sediment bed boundary to exhibit both sediment erosion and deposition, an equilibrium concentration in the cells close to the bed was required to be defined. To describe the equilibrium concentration near the bed, Van Rijn's formula was selected as

$$c_{bed} = 0.015 \frac{D_{50}}{a} \frac{\left[\frac{\tau - \tau_c}{\tau_c}\right]^{1.5}}{D_*^{0.3}} \tag{2.8}$$

where c_{bed} is the concentration of sediment near the bed, D_{50} is the median sediment size, a is the distance from the concertation point to the bed, τ is the bed shear stress from Equation (2.6), τ_c is the critical shear stress of the sediment, and D_* is the dimensionless particle diameter found using

$$D_* = \left[\frac{(s-1)g}{v^2}\right]^{1/3} D_{50} \tag{2.9}$$

where g is acceleration due to gravity, s is the specific gravity, and v is the fluid viscosity (Olsen 1999). To describe the threshold of sediment motion, SSIIM obtains the critical shear stress of soils based on a version of Shields's Diagram (1936), for which an example is displayed in Figure 2.2.

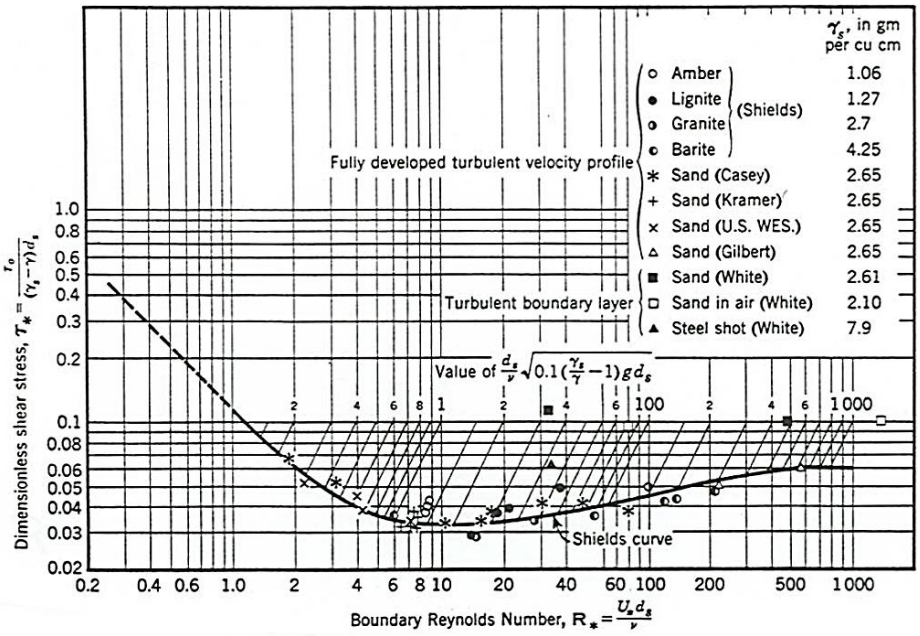

Figure 2.2: Shields diagram example (Vanoni 1975)

The Shields Diagram plots Shields curve based on laboratory tests examining what flow conditions caused sediment to begin motion. The x-axis in Figure 2.2 is the Boundary Reynolds number where U_* is the shear velocity, ν is the viscosity, and d_s is the particle diameter or D_{50}. The y-axis is the Shields parameter or the dimensionless shear stress where τ_o is the bed shear stress, γ is the fluid density, γ_s is the soil density, and d_s is the particle diameter D_{50}. The points making up the curve with different soils describe the critical Shields parameters for those soils and values lower than the curve indicate no motion. The critical Shields parameter may be used to solve for critical value of bed shar stress for given sediment and fluid properties. The diagram at the time was limited in the types of soils and flows tested so it has been modified by many researchers over the years to create curves with new data. Details on the version of the Shield's curve used in SSIIM is not mentioned in its manual. A limitation to the Shields diagram is that it was developed using a flat horizontal bed in a flume with no consideration of ripple effects or bed slope. Soil stability and resistance to flow decreases with steeped slopes as there is less unlaying material to provide support. To improve the accuracy of numerical scour hole shapes, SSIIM includes Brooks (1963) slope correction factor for the critical shear stress obtained from a Shields diagram. The Brooks (1963) correction factor, *K*, for the bed shear stress is defined as

$$K = -\frac{\sin\emptyset\sin\alpha}{\tan\theta} + \sqrt{\left(\frac{\sin\emptyset\sin\alpha}{\tan\theta}\right) - \cos^2\emptyset\left[1 - \left(\frac{\tan\emptyset}{\tan\theta}\right)^2\right]} \tag{2.10}$$

where α is the angle between the flow direction and a line normal to bed plane, $\emptyset$ is the bed slope and θ is an empirical parameter based on flume studies. The default values for Brooks parameters, inverse of *tan(θ)*, in SSIIM are 1.23 and 0.78 for uphill and downhill slopes respectively. Different values of for Brooks parameters were tested during validations to find the best values for clean sands. In additions to Brooks (1963), a correction for transverse slopes by Dey (2003) was also implemented into SSIIM. Without the Brooks (1963) correction factor to reduce a soil's flow resistance the scour depths in SSIIM were significantly underestimated. Another important aspect of sediment slopes in scour holes is avalanching or sand slides occurring due to slope instability. The sediment transport described by Equations (2.7) and (2.8) do not account for steep slopes collapsing and filling the scour hole. Without sand slides, numerical depths overpredict scour hole depths with very steep spike shaped scour holes. SSIIM implemented a sand slides algorithm to smooth out steep slopes and provide realistic scour hole shapes. The sand slide algorithm takes in

a stable slope angle where steeper slopes are adjusted to the stable slope angle. The algorithm acts as a grid correction iteratively searching the bed to correct slopes and then the adjacent areas to ensure all slopes are stable (Olsen 2018). The stable slope angle is often related to the angle of repose of the sediment but may vary as discussed in literature and this chapter.

As the numerical modeling of scour is in development and computationally demanding, there still exist many limitations on the accuracy of numerical scour simulations. The grid generation in SSIIM was limited in its refinement ability so the most computationally ideal grid pattern was not possible. Ideally a coarse orthogonal channel grid with an elliptic refined zone around the pier would provide efficient computation times while capturing the complex flows and a realistic scour hole at the pier. In SSIIM a moderately fine grid was used which was too fine in areas away from the pier and not quite fine enough at the pier. However even with the non-ideal grid pattern the flow fields and maximum scour depths at the piers in SSIIM matched experiment results well enough. The SIMPLE algorithm was also selected in SSIIM for its steady state like modeling which provides quicker computation times than algorithms capturing all transient flow behaviours. The upstream flow field of flow past a cylinder can be considered mostly steady state but the downstream flow consists of cyclic nonsymmetric wake vortices sheading. The wake vortices shedding is the main scour agent at the downstream of the pier, so SSIIM is expected to drastically underpredict the scour at the downstream side of the pier. However, as the maximum scour depth occurs at the upstream face of the pier, the downstream side was not of importance. Roulund et al. (2005) conducted steady state numerical simulations which underpredicted maximum pier scour by 15%, and downstream scour up to 30%. For the scope of this study, SSIIM predicted the maximum scour depth to within 12.8% of experiment values thus it successfully modeled numerical pier scour.

2.2 Rigid Bed Validations

To verify and optimise SSIIM models of flow past piers, three cases were compared with published experimental and numerical results. The SSIIM models used in the rigid bed validation were Case 1 from Roulund et al. (2005), Case 2 from Melville (1975), and Case 3 from Ahmed and Rajaratnam (1998). The experimental results provided measurements of the velocity field and bed shear stresses around the pier which were compared with results from SSIIM for validation.

To setup the rigid bed experiments tilted flumes with pumps were used to control inlet velocities and soil grains were glued to solid bed surfaces to mimic sediment bed roughness without erosion.

2.2.1 Rigid Bed Parameters and Inputs

The numerical models in SSIIM were setup with the solvers and boundary conditions discussed in Section 2.1. SSIIM is hardcoded with water properties at 20 degrees Celsius for the fluid's viscosity and density values (Olsen 2018). The parameters used to create the rigid bed models were the pier diameter, D, flow depth, y, mean inlet velocity, V, and bed roughness, k_s. In addition to the aforementioned parameters some decisions remained for the model dimensions and grid cell sizes. For the width of the SSIIM models the scour hole was to be fully captured so the experimental scour hole widths were used as reference. The ratio of scour hole width to piers diameters for Cases 2, 3 and 4 was 2.6, 1.3 and 1.5. Thus, a conservative domain width of $7D$ was selected where D is the pier diameter. During validations the inlet length and grid cell sizes were tested for to find the ideal values. The minimum distance from inlet to pier to ensure the turbulent flow was fully developed was found as $13y+4D$, where y is the flow depth. For the grid refinement various cell sizes were tested to reduce computational time but also capture the scour hole shapes well. The minimum ratio of horizonal cell size to pier diameter was determined as 10. Vertical cell refinement was tested to also ensure accurate results with computational efficiency. It was found that 14 vertical cells was adequate in predicting pier scour depths for Cases 2, 3 and 4. The inlet length and grid refinement conditions are further discussed with the validation results in Sections 2.3 and 2.4.

2.2.2 Case 1 Rigid Bed

Roulund et al. (2005) conducted experimental and numerical investigations into the flow at a single cylindrical pier in a rectangular channel. The purpose was to evaluate how well their EllipSys3D CFD code modeled flow past a pier when compared to experimental results. CFD models were ran with both smooth bed and rough bed conditions where the rough bed matched better with experimental results. SSIIM models were created to replicate rigid conditions and then compared with the reported results of Roulund et al. (2005) rough bed experiments to verify the results of SSIIM. The reported results included velocity plots in the centre plane vertical plane along the flow direction, an upstream velocity profile, and the bed shear stresses around the pier.

Case Model Parameters:

The SSIIM CFD model with its mesh was presented in Figure 2.1 with the labelled boundary conditions. The modeling parameters and dimensions for Case 1 are listed in Table 2.1.

Table 2.1: Case 1 Rigid Bed Model Parameters

Parameter	Value
Flow Depth: y [m]	0.54
Pier Diameter: D [m]	0.536
Mean Flow Velocity: V [m/s]	0.326
Channel Width [m]	4
Inlet Length [m]	12
Channel Length [m]	20
Bed Roughness: k_s [m]	0.007
Froude Number: Fr [-]	0.142
Reynolds Number: Re [-]	174127

Upstream Velocity Profile and Minimum Inlet Length

Roulund et al. (2005) provided experimental results of an upstream velocity profile in the centre plane. The purpose of the comparing the upstream velocity profile was to verify three components of the SSIIM CFD model. Firstly, if the law of wall was adequately modeling the bed roughness with a logarithmic velocity profile and secondly if the flow was fully developed before reaching the pier. The inlet in SSIIM is prescribed a mean or uniform flow rate, therefore the flow needs to development into the turbulent boundary layer flow after some length with the influence of the rough bed. The third component to the inlet length was the distance of influence for the pier's adverse pressure gradient upstream. The pier presence slows down all incoming flow and thus has a zone of influence on the upstream flow. The minimum inlet length would be the sum of development length as a function of flow depth and the areas of pier influence based on the pier diameter. The goal was for the SSIIM model flow to be fully developed before reaching not only the pier but also the zone of influence. A fully developed flow entering the pier and scour area is indicative of what may be seen in the field with a long upstream channel. The inlet length of the

Case 1 model was set to an extended distance to determine at what length into the model was the flow development and how far upstream the pier influenced the velocity profile. The SSIIM velocity profile at various distances downstream of the inlet was plotted along side the experimental velocity profile in Figure 2.3 and Figure 2.4.

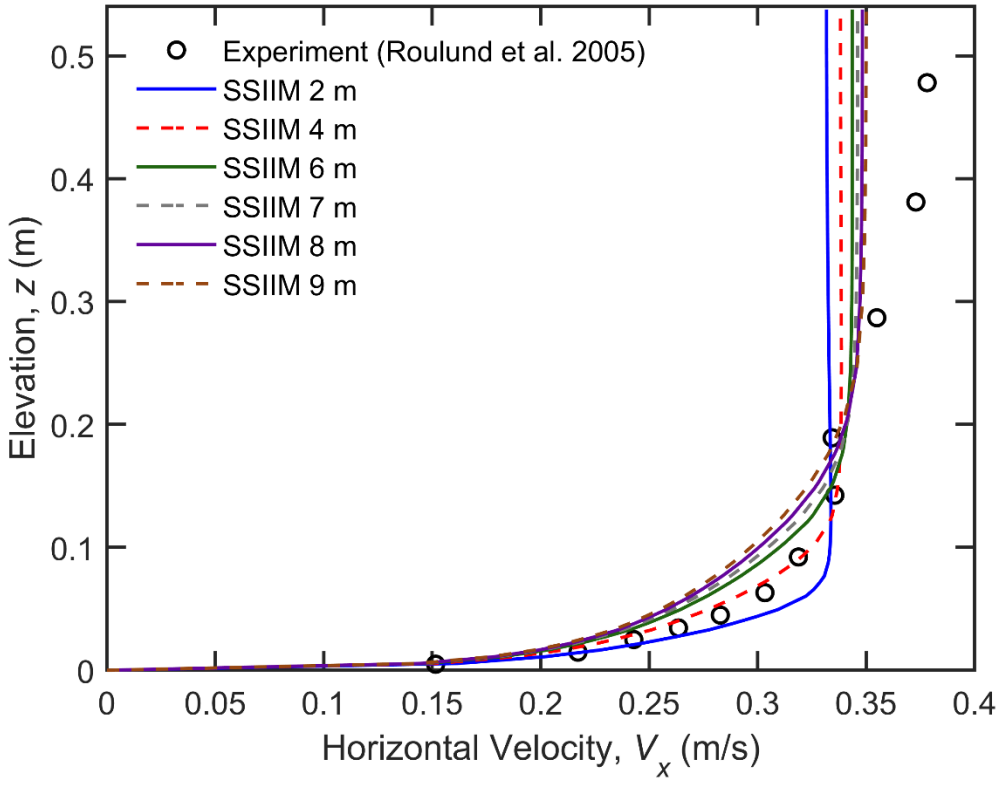

Figure 2.3: Case 1 Velocity profiles flow development

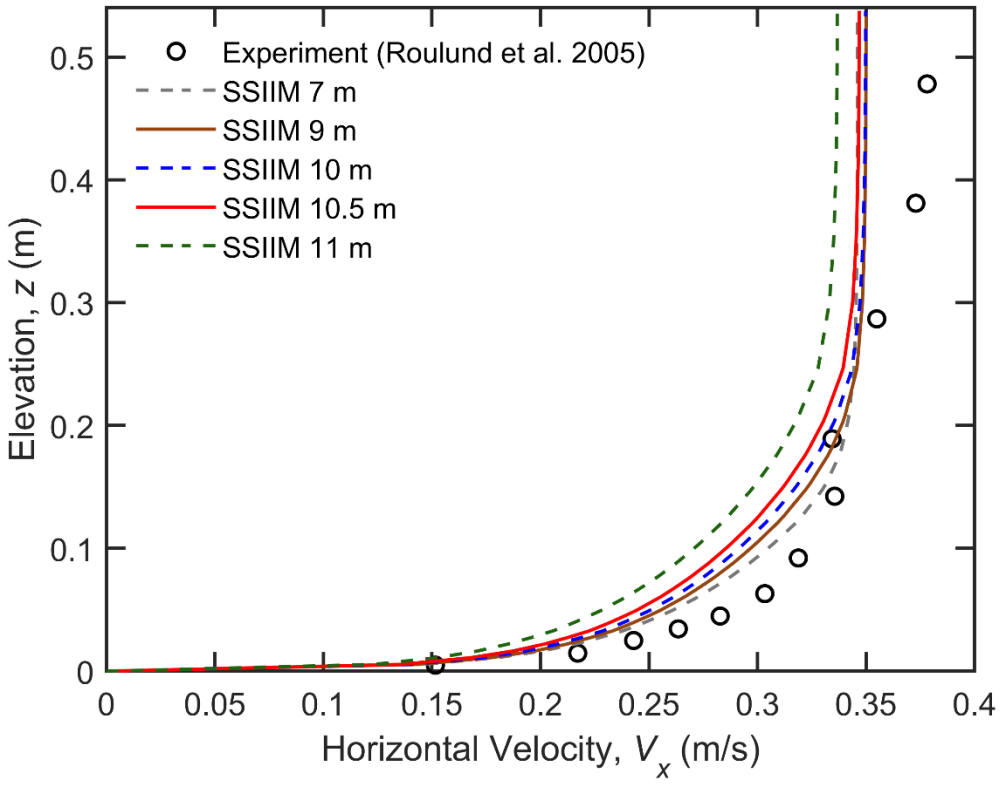

Figure 2.4: Case 1 velocity profiles pier influence

Although the experiment reported higher velocities the error was not of concern as the profile shape matched well near the bed. As seen in Figure 2.3, the velocity profile is obviously transitioning from 2 m – 6 m into the channel but seems to be near full development around 6 m – 9 m. An acceptable development length was estimated as 7 m or *13y* for Case 1 where *y* is the flow depth. From Figure 2.4 there is little change from 9 m to 10 m but at 10.5m the effects of the pier are noticeable with the lower velocity near the surface. A conservative estimate for the pier zone of influence was set as *4D*, where *D* is the pier diameter. Thus, the recommended minimum inlet length was determined as *13y+4D*. The recommended inlet length was not completely analyzed as the development length may vary with the bed roughness, pier sizes, and inlet velocities for the different cases. However, the estimate was justified for the study as the scour depths were accurately predicted in SSIIM as discussed in Section 2.3.

Velocity Plots

For a precise analysis, Roulund et al. (2005) compared experimental and numerical velocity plots at varying depths, *z*, in the centre plane. The velocity plots allowed examination of

the pier's effect on flow including the upstream downflow responsible for scour. The horizontal, V_x, and vertical velocities, V_z, from Roulund et al. (2005) are compared with the SSIIM results in Figure 2.5 and Figure 2.6 respectively.

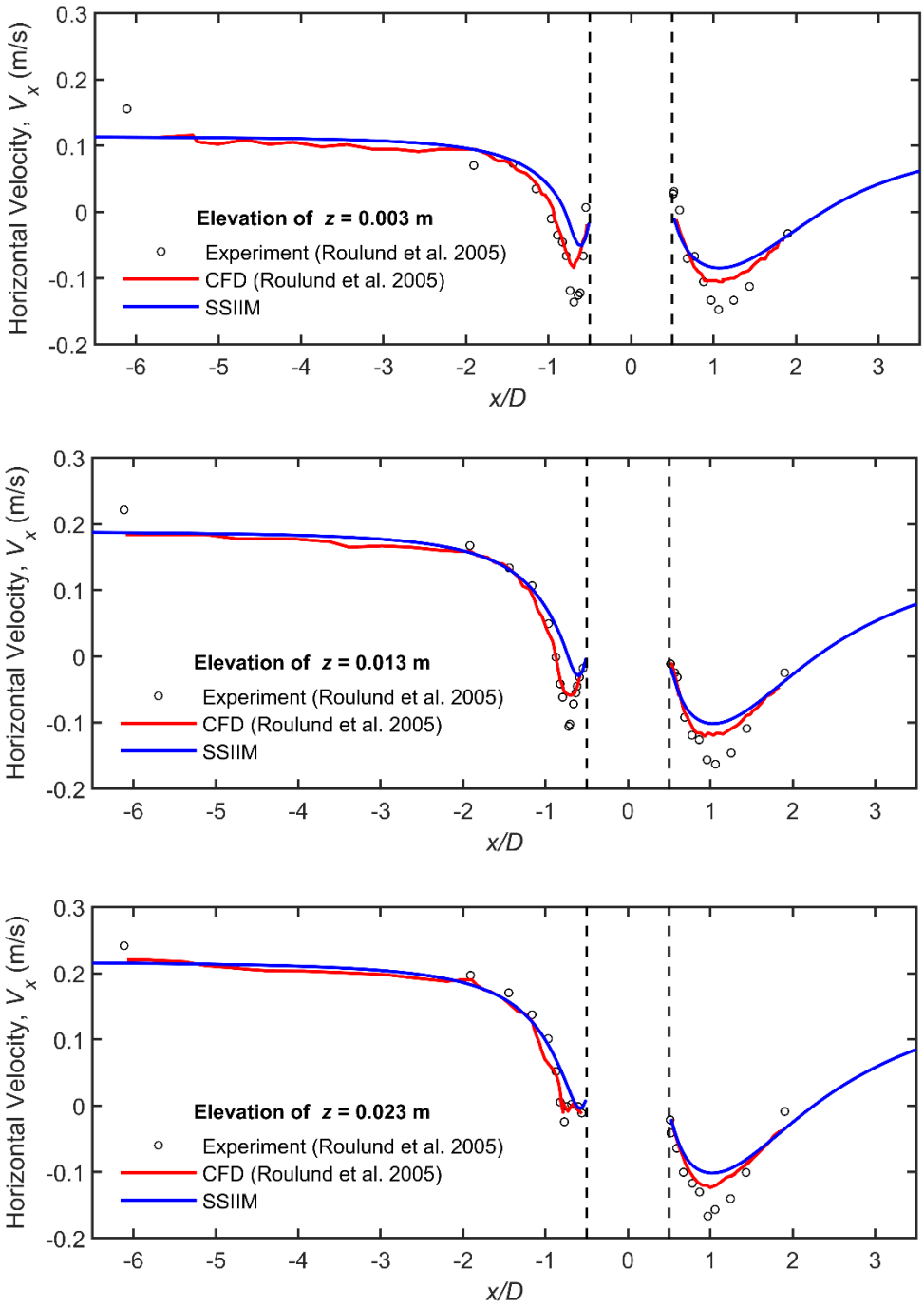

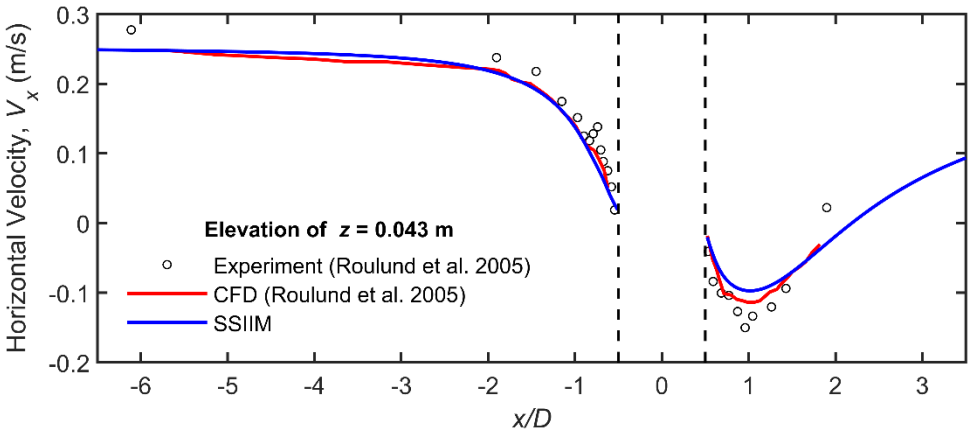
Horizontal Velocity, V_x (m/s)
0.3
0.2
0.1
0
-0.1
-0.2
-6
-5
-4
-3
-2
-1
0
1
2
3
x/D
Elevation of z = 0.043 m
Experiment (Roulund et al. 2005)
CFD (Roulund et al. 2005)
SSIIM

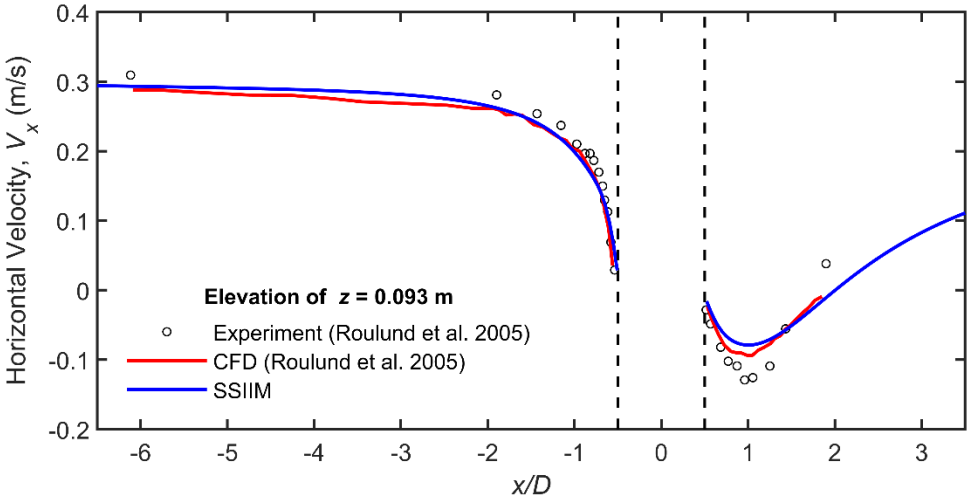
Horizontal Velocity, V_x (m/s)
0.4
0.3
0.2
0.1
0
-0.1
-0.2
-6
-5
-4
-3
-2
-1
0
1
2
3
x/D
Elevation of z = 0.093 m
Experiment (Roulund et al. 2005)
CFD (Roulund et al. 2005)
SSIIM

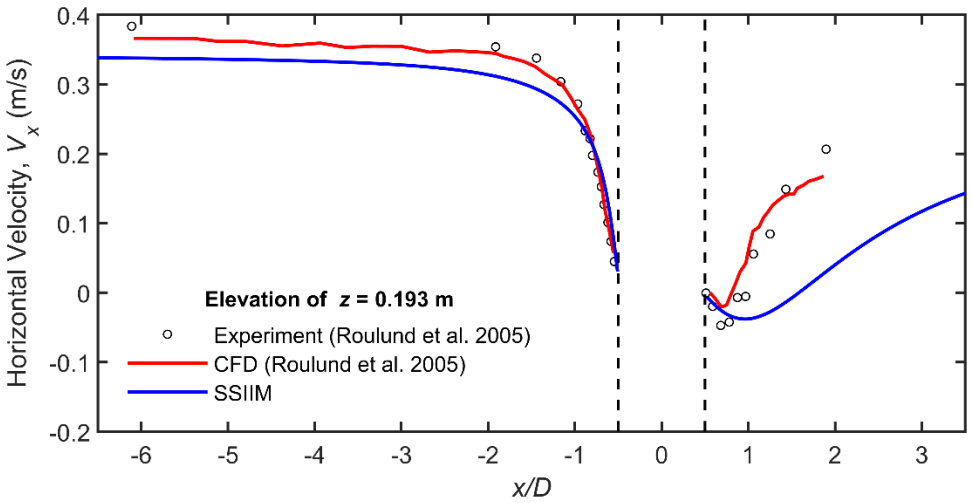
Horizontal Velocity, V_x (m/s)
0.4
0.3
0.2
0.1
0
-0.1
-0.2
-6
-5
-4
-3
-2
-1
0
1
2
3
x/D
Elevation of z = 0.193 m
Experiment (Roulund et al. 2005)
CFD (Roulund et al. 2005)
SSIIM

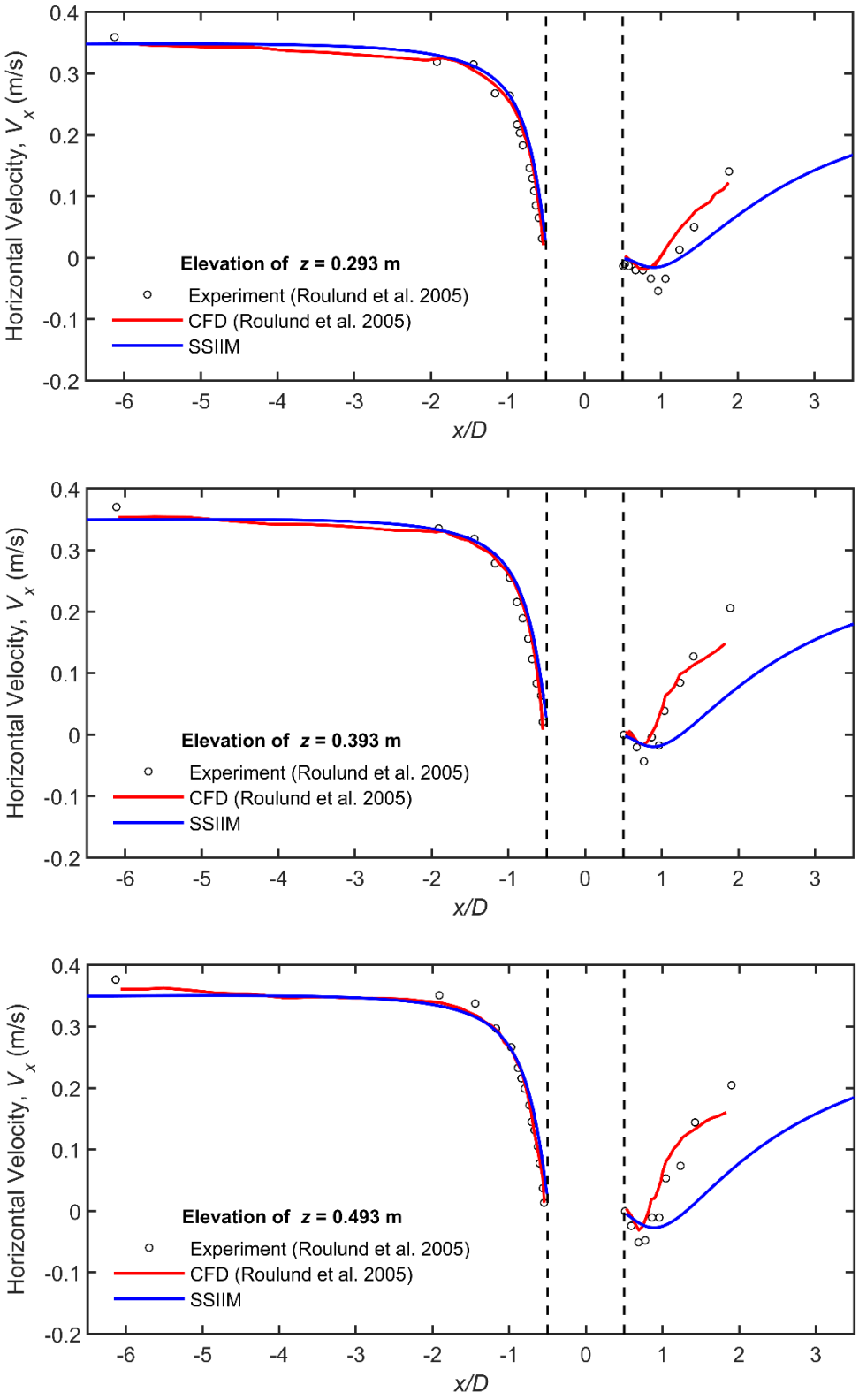

Figure 2.5: Case 1 rigid bed horizontal velocities

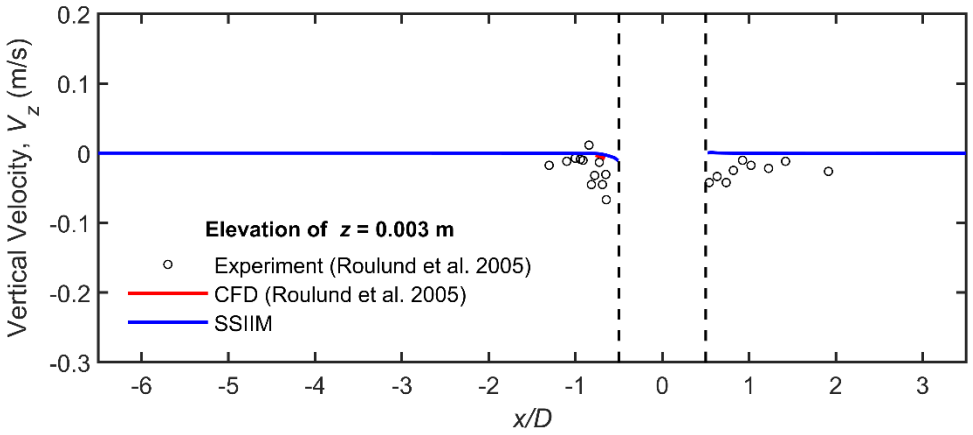
Vertical Velocity, V_z (m/s)
0.2
0.1
0
-0.1
-0.2
-0.3
-6
-5
-4
-3
-2
-1
0
1
2
3
x/D
Elevation of z = 0.003 m
Experiment (Roulund et al. 2005)
CFD (Roulund et al. 2005)
SSIIM

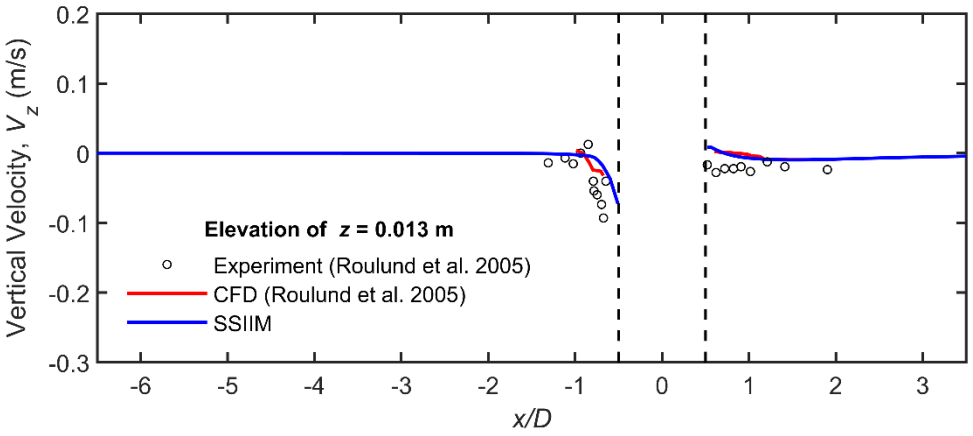
Vertical Velocity, V_z (m/s)
0.2
0.1
0
-0.1
-0.2
-0.3
-6
-5
-4
-3
-2
-1
0
1
2
3
x/D
Elevation of z = 0.013 m
Experiment (Roulund et al. 2005)
CFD (Roulund et al. 2005)
SSIIM

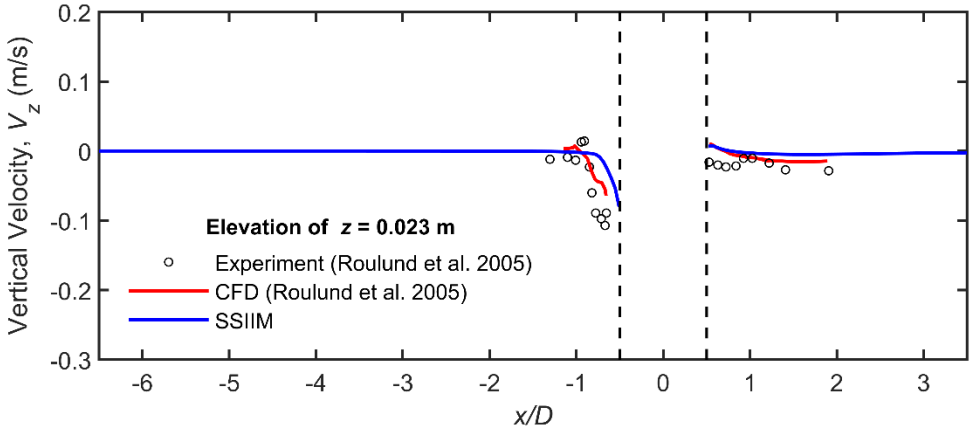
Vertical Velocity, V_z (m/s)
0.2
0.1
0
-0.1
-0.2
-0.3
-6
-5
-4
-3
-2
-1
0
1
2
3
x/D
Elevation of z = 0.023 m
Experiment (Roulund et al. 2005)
CFD (Roulund et al. 2005)
SSIIM

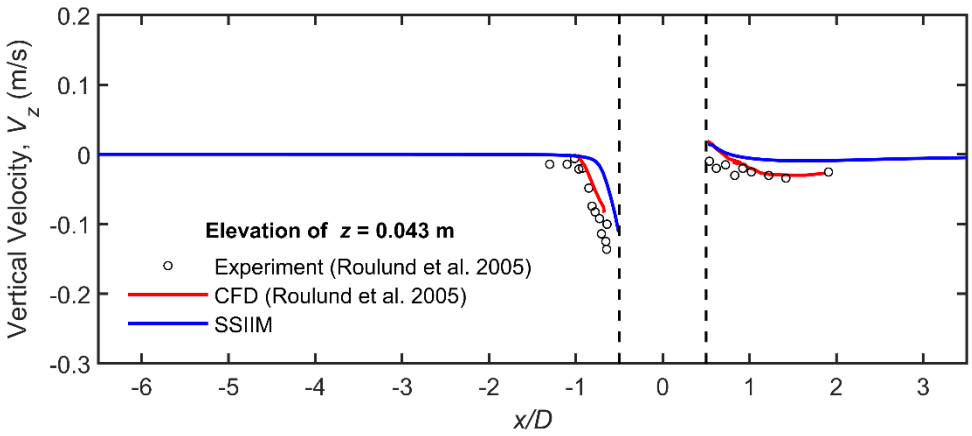
Vertical Velocity, V_z (m/s)
0.2
0.1
0
-0.1
-0.2
-0.3
-6
-5
-4
-3
-2
-1
0
1
2
3
x/D
Elevation of z = 0.043 m
Experiment (Roulund et al. 2005)
CFD (Roulund et al. 2005)
SSIIM

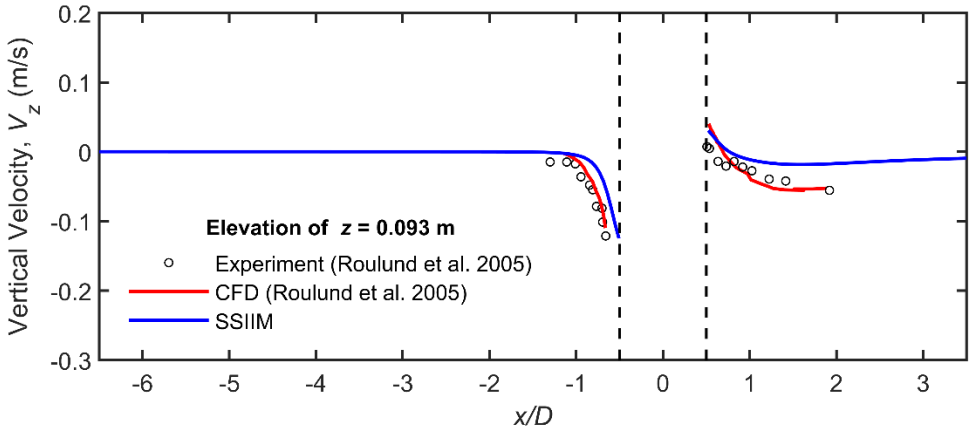
Vertical Velocity, V_z (m/s)
0.2
0.1
0
-0.1
-0.2
-0.3
-6
-5
-4
-3
-2
-1
0
1
2
3
x/D
Elevation of z = 0.093 m
Experiment (Roulund et al. 2005)
CFD (Roulund et al. 2005)
SSIIM

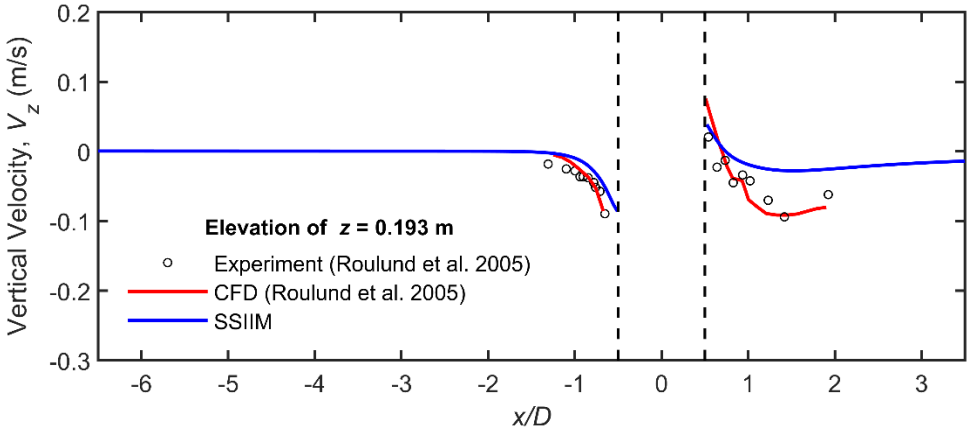
Vertical Velocity, V_z (m/s)
0.2
0.1
0
-0.1
-0.2
-0.3
-6
-5
-4
-3
-2
-1
0
1
2
3
x/D
Elevation of z = 0.193 m
Experiment (Roulund et al. 2005)
CFD (Roulund et al. 2005)
SSIIM

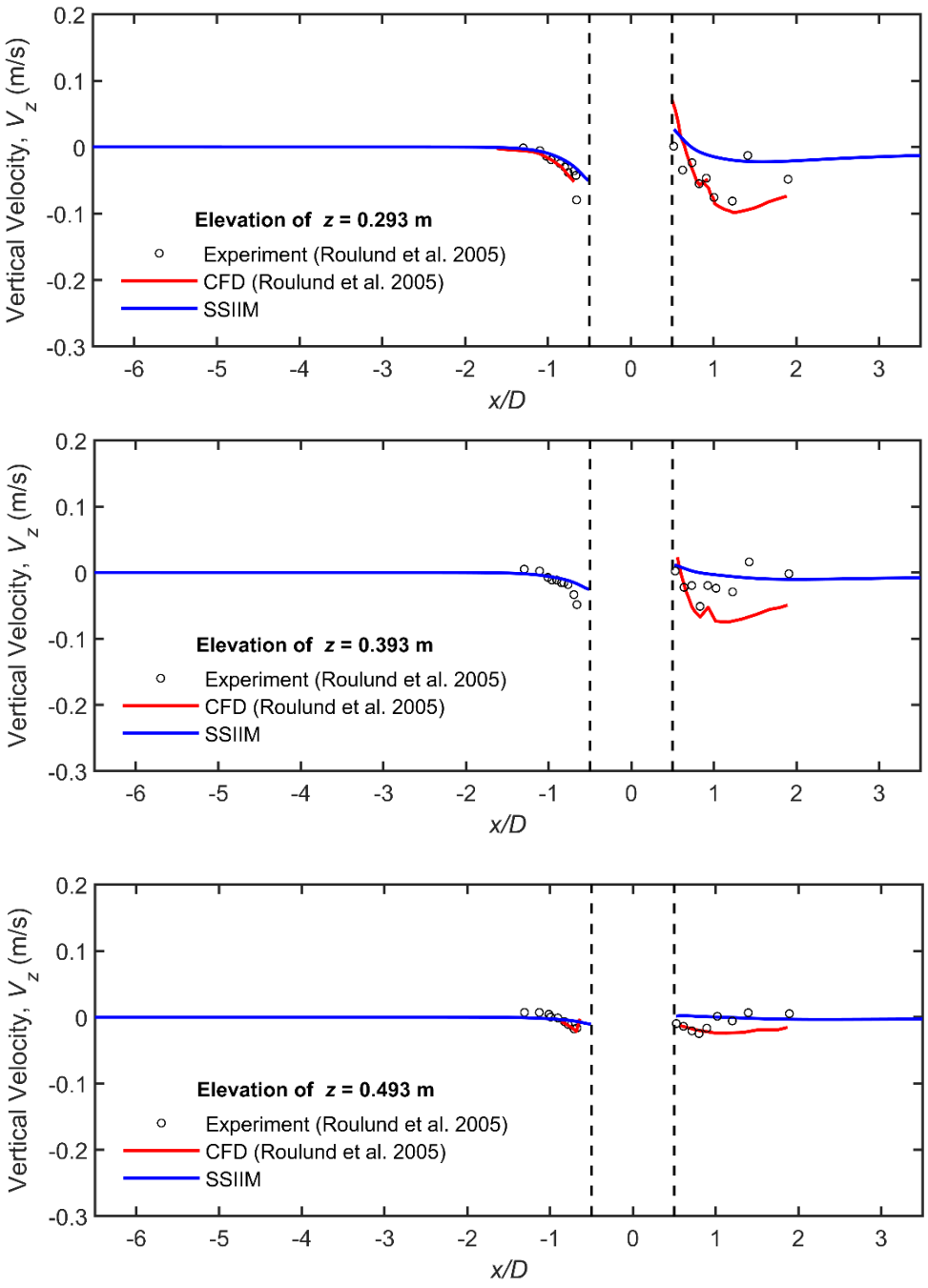

Figure 2.6: Case 1 rigid bed vertical velocities

The velocity fields upstream of the pier in SSIIM matched very well with the experimental results. The horseshoe vortex was seen depicted with the downflow although its size in SSIIM appears smaller than the experimental results. However, the downstream results in SSIIM do not match as well with the experiment but that was attributed to the time averaging of turbulent flows in the SIMPLE algorithm. A further refined mesh and transient solver would likely provide a

better match with experimental results. Velocities near the surface also experienced minor error from the exclusion of a free-surface model in SSIIM. The horseshoe vortex flow and upstream downflow flow was satisfactory captured in SSIIM.

Bed Shear Stress

In addition to the velocity field, Roulund et al. (2005) investigated the bed shear stress around the pier with a rigid bed. The pier's influence on the velocity fields leads to amplification of bed shear stress at upstream side of the pier. The locations of maximum bed shear stress amplification at the upstream corners is where scour holes start to form. Validating both the location and magnitude shear stress amplification will ensure SSIIM can realistically procures the initial stages of scour. The bed shear stress amplification was defined as the bed shear stress normalized with the undisturbed bed shear stress of τ_∞ = 0.353 Pa. Roulund et al. (2005) reported contour results from their numerical model along with experimental results from Hjorth (1975) as seen in Figure 2.7.

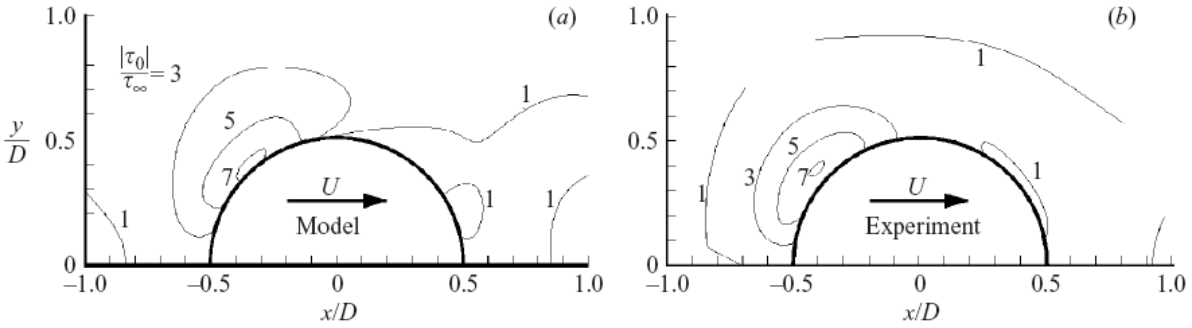

Figure 2.7: Case 1 bed shear stress amplification (a) Roulund et al. (2005) (b) Hjorth (1975)

Roulund et al. (2005) numerical results matched fairly well the experimental results of Hjorth (1975) in terms of magnitude although the location of maximum bed shear stress was slightly further upstream for Roulund et al. (2005). Figure 2.8 displays the bed shear stress amplification from SSIIM while Figure 2.9 overlays SSIIM results with those from Roulund et al. (2005) and Hjorth (1975).

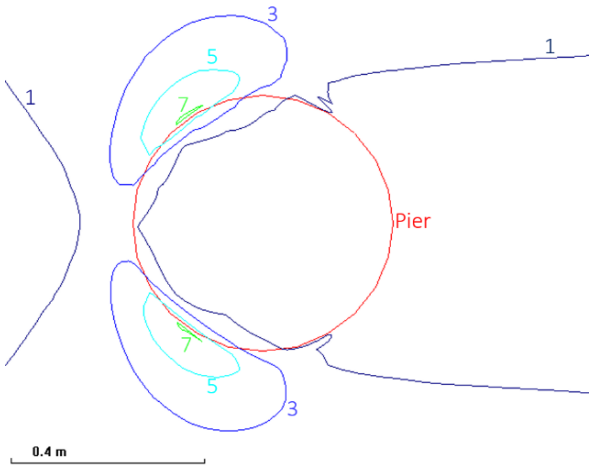

Figure 2.8: Case 1 bed shear stress amplification around pier in SSIIM

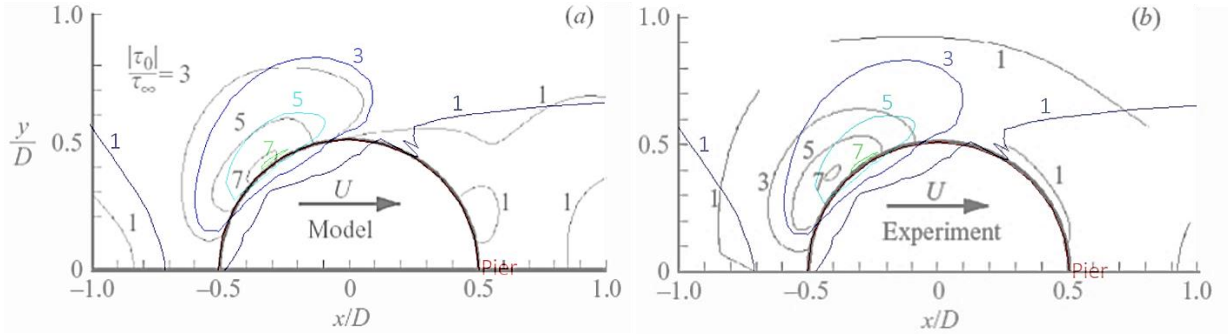

Figure 2.9: Case 1 bed shear stress amplification comparison (a) Roulund et al. (2005) (b) Hjorth (1975)

SSIIM matched very well with Roulund et al. (2005) in both magnitude and location of bed shear stress amplification. Thus, the SSIIM model for Case 1 was considered validated for rigid bed flow.

2.2.3 Case 2 Rigid Bed

Melville (1975) experimentally investigated the flow past a single pier. Melville's results have often been used in other numerical research for comparison and verification purposes. Two papers on numerical modeling of scour which reference Melville (1975) include Richardson and Panchang (1998) and Salaheldin et al. (2004).

Case Model Parameters:

The Case 2 numerical model was setup the same as Case 1 as described in Figure 2.1. The Case 2 model parameters are summarized in Table 2.2.

Table 2.2: Case 2 Rigid Bed Model Parameters

Parameter	Value
Flow Depth: y [m]	0.15
Pier Diameter: D [m]	0.0508
Mean Flow Velocity: V [m/s]	0.25
Channel Width [m]	0.5
Inlet Length [m]	3
Channel Length [m]	5
Bed Roughness: k_s [m]	0.0009625
Froude Number: Fr [-]	0.206
Reynolds Number: Re [-]	12656

Upstream Velocity Profiles

Melville (1975) reported upstream horizontal velocity profiles at multiple locations and comparisons with SSIIM are displayed in Figure 2.10.

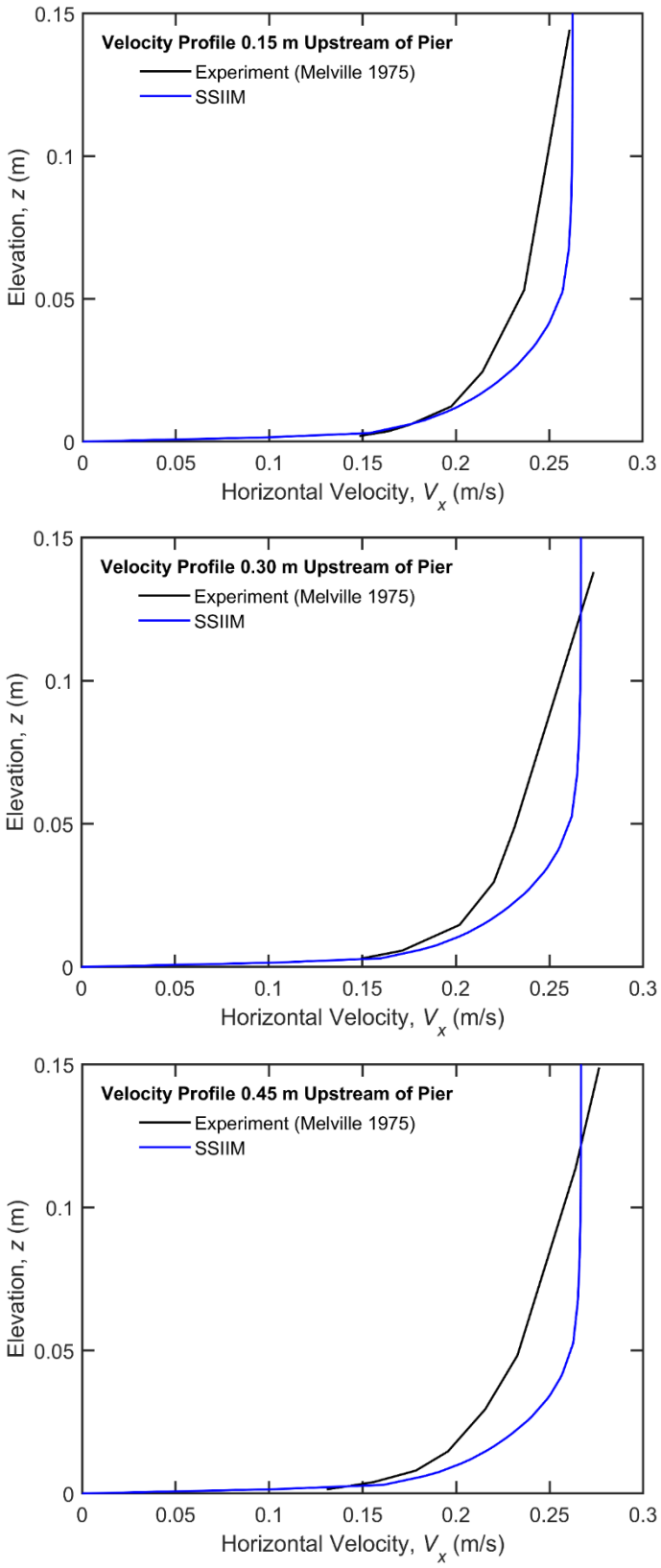

Figure 2.10: Case 2 upstream horizontal velocity profiles

Results show a satisfactory match between the experimental results and SSIIM. The profiles curves may differ in shape but the velocity gradient near the bed is captured well which is important for scour as it describes the bed shear stress. The difference on velocity profile chapes was also attributed to the limited number of data points from Melville (1975).

Bed Shear Stress

Melville (1975) reported contours of bed shear stress normalized with critical shear stress value of τ_c = 0.196 Pa as seen in Figure 2.11.

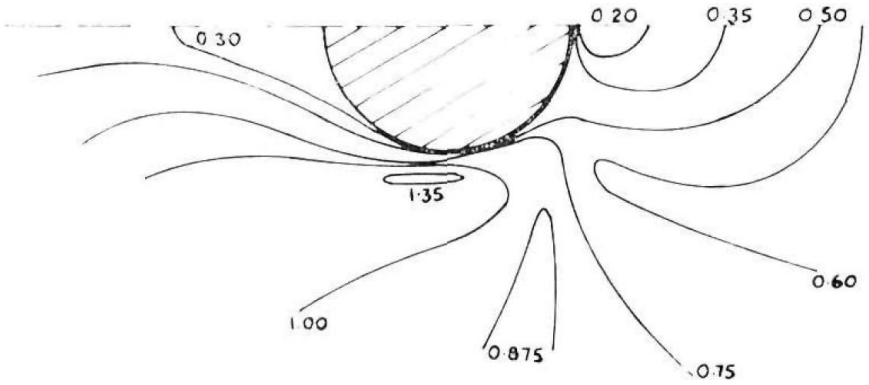

Figure 2.11: Case 2 experimental bed shear stress contour (Melville 1975) (flow towards left)

As seen in Figure 2.11 the point of maximum shear stress was located slightly downstream of the middle of the pier. Salaheldin et al. (2004) conducted CFD simulations and their numerical results for the bed shear stresses were compared with Melville's (1975) data in Figure 2.12.

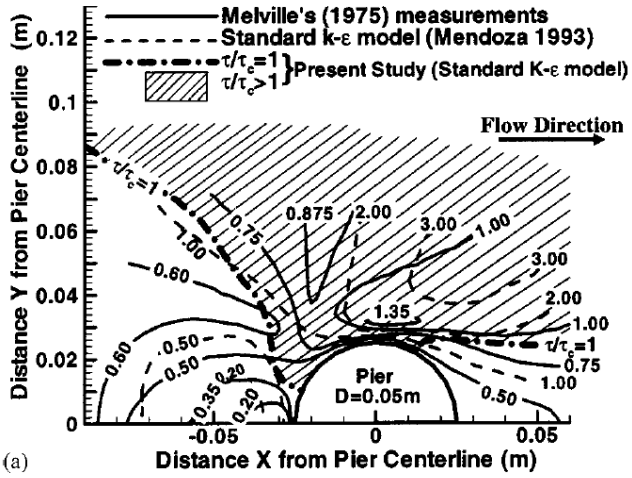

Figure 2.12: Case 2 bed shear stress contour comparison with Melville (1975) (Salaheldin et al. 2004)

The magnitudes of bed shear stresses reported by Salaheldin et al. (2004) were larger although the locations of maximum bed shear stress matched well with Melville (1975). Salaheldin et al. (2004) also reported larger areas of preliminary scour just as SSIIM numerical results. The bed shear stress amplification in SSIIM is displayed in Figure 2.13 and overlayed on top of Melville's contour in Figure 2.14.

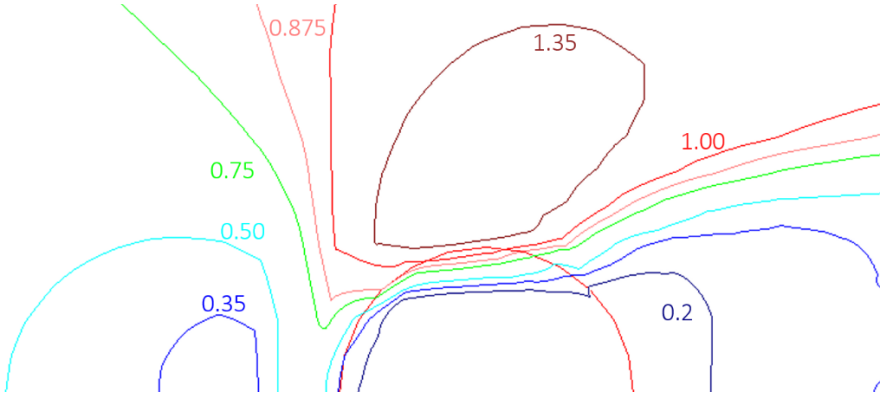

Figure 2.13: Case 2 bed shear stress in SSIIM (flow towards right)

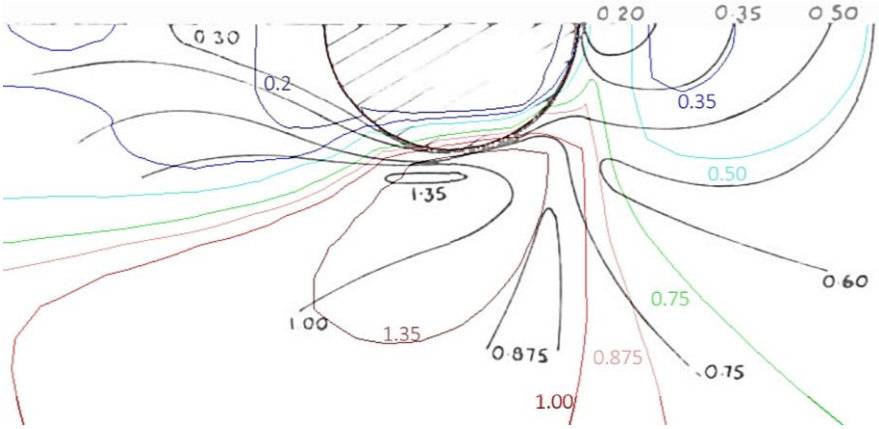

Figure 2.14: Case 2 bed shear stress in SSIIM compared with Melville (1975) (flow towards left)

The SSIIM results showed that the point of maximum shear stress was again located slightly upstream at the lateral sides of the pier, similar to the results from Case 1. The disparity in results was not deemed of concern for rigid bed results. Thus, as SSIIM results provided a satisfactory match, the SSIIM Case 2 rigid bed model was validated.

2.2.4 Case 3 Rigid Bed

Ahmed and Rajaratnam (1998) conducted experiments investigating flow past cylindrical piers with smooth rigid beds, rough rigid beds, and mobile beds. Ahmed and Rajaratnam (1998) experimental results were also used by Salaheldin et al. (2004) for verification of numerical research.

Case Model Parameters:

As with Case 2, the Case 3 SSIIM model was set up same as Case 1, with Figure 2.1 displaying the grid and boundary conditions. The Case 3 model parameters are listed in Table 2.3.

Table 2.3: Case 3 Rigid Bed Model Parameters

Parameter	Value
Flow Depth: y [m]	0.182
Pier Diameter: D [m]	0.089
Mean Flow Velocity: V [m/s]	0.2927
Channel Width [m]	0.7
Inlet Length [m]	4.2
Channel Length [m]	7
Bed Roughness: k_s [m]	0.0069
Froude Number: Fr [-]	0.219
Reynolds Number: Re [-]	25959

Upstream Velocity Profiles

Vertical and horizontal velocity profiles were reported at distances x/r=-2.25 and x/r=-10 upstream of pier where x is the measured distance from the pier and r is the pier radius. Comparisons of horizontal and vertical velocity profiles with SSIIM are illustrated in Figure 2.15 and Figure 2.16 respectively.

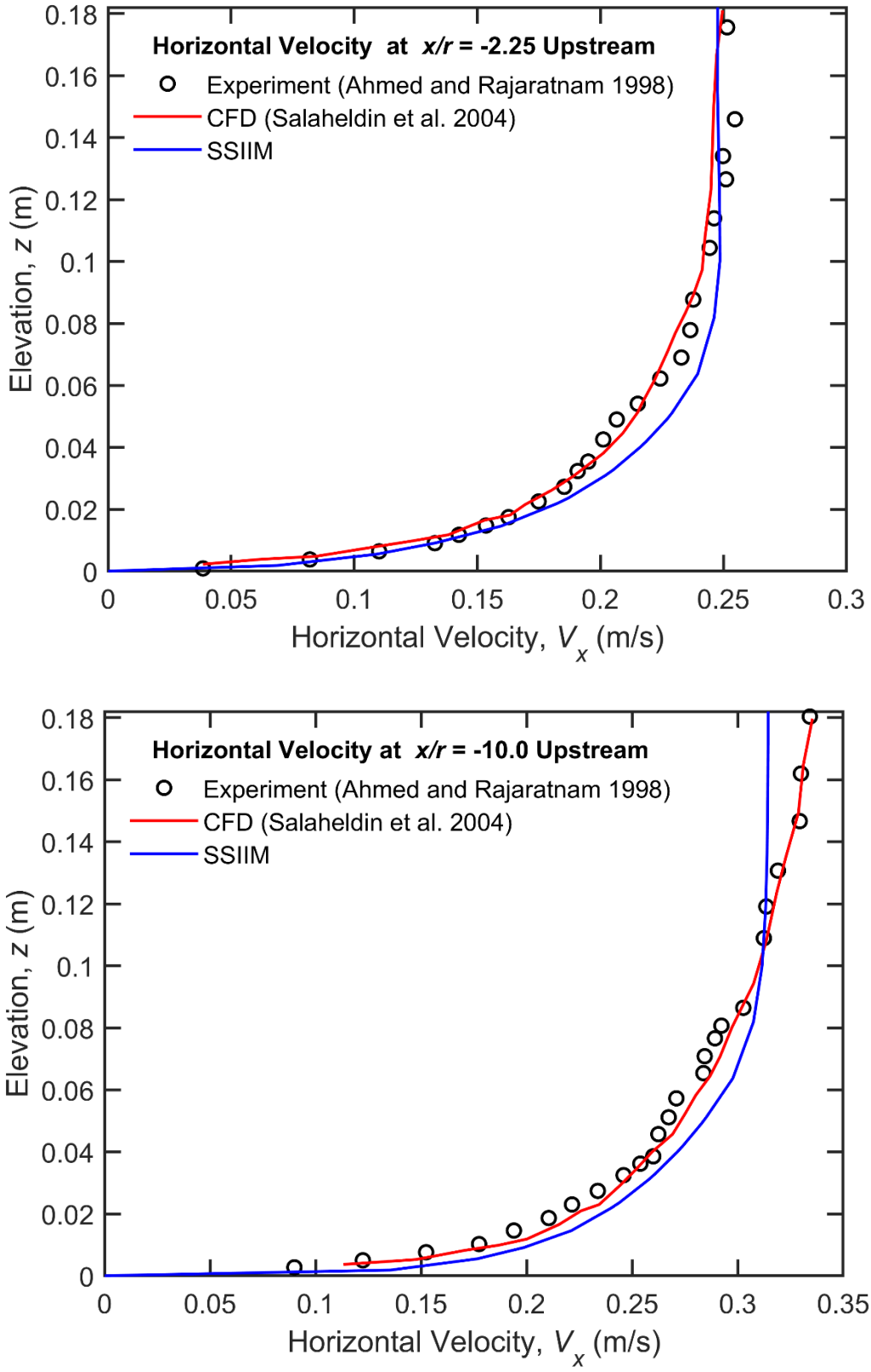

Figure 2.15: Case 3 upstream horizontal velocity profiles

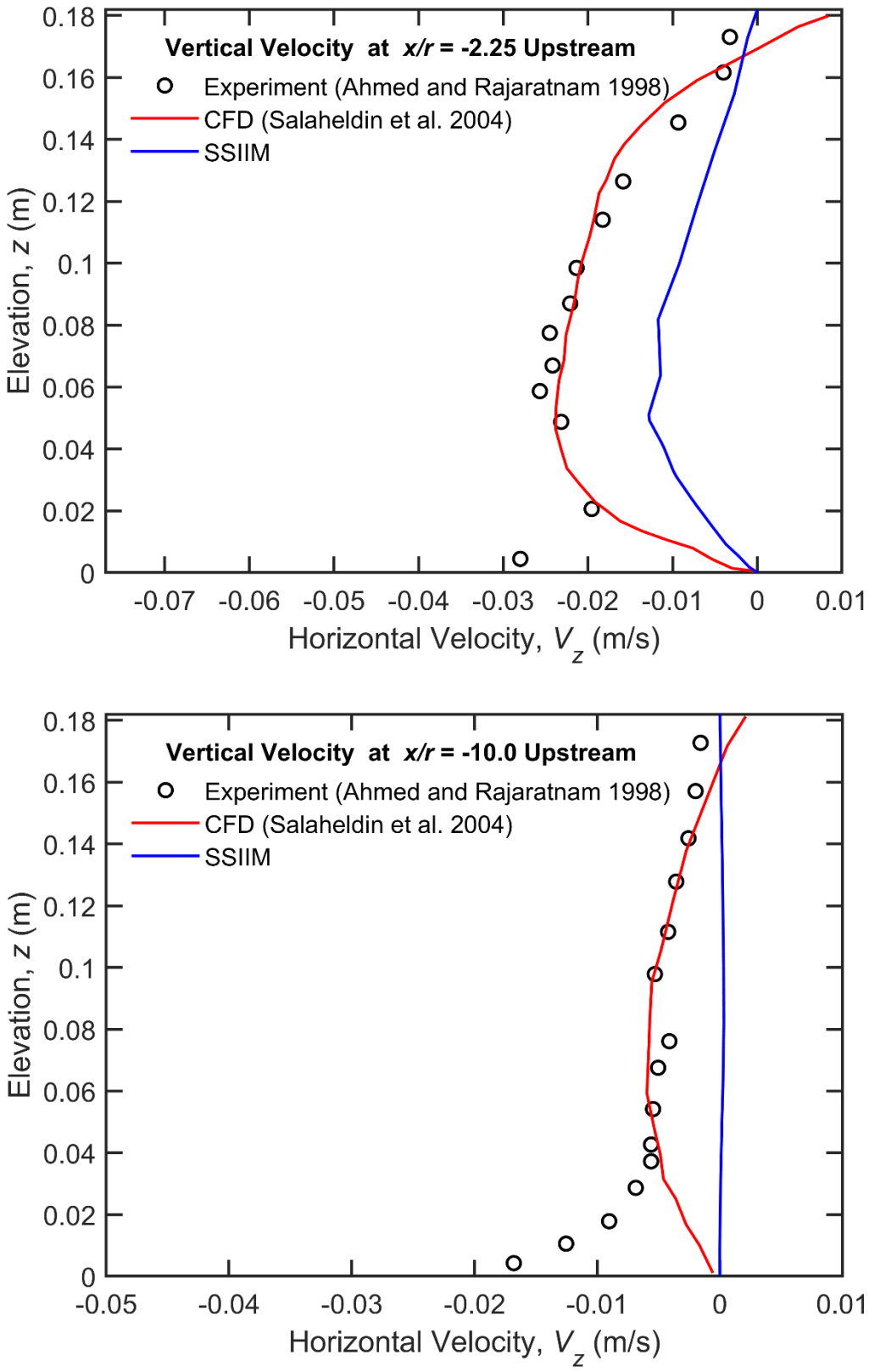

Figure 2.16: Case 3 Upstream vertical velocity profiles

At the distance of *10r* upstream the flow was developed, and results match well for SSIIM's horizontal velocity as seen in Figure 2.15. SSIIM also matches better with the velocity profile *2.25r* upstream in the area where the adverse pressure gradient of the pier is in effect. The vertical velocity profiles in Figure 2.16 show some discrepancy but due to the low magnitudes the difference in results was deemed insignificant. The flow's higher Froude number of 0.219, may have led to the underestimation of near surface velocity as SSIIM did not include the free surface. As the horizontal velocity profile in the vicinity to the pier matched very well especially near bed the SSIIM Case 3 rigid bed model was validated.

2.3 Mobile Bed Validations

Once rigid bed simulations were completed, the flow field in SSIIM was validated. The next step was to validate the SSIIM sediment transport and erosion with scour hole depth comparisons. Case 1 (Roulund et al. 2005) provided an ample amount result for a rigid bed flow past a pier but did not include mobile bed results with scour hole dimensions for Case 1. For a third case to compare SSIIM scour hole results with, another experimental model from Ahmed and Rajaratnam (1998) was used as Case 4.

2.3.1 Mobile Bed Parameters and Inputs

During validations different values were test for the empirical parameters in the critical shear stress slope reduction factor by Brooks (1963). The parameters which provided the best results during validation were then chosen as the fixed values moving forward with the parametric study in Chapter 3. Scour depth over time data was plotted to evaluate the rates of scour hole development over time in SSIIM. The depth over time plots were also used to develop a definition for numerical equilibrium depth. A slope value was interpolated from the plots to determine at what time equilibrium depth was reached. The structural and fluid flow properties were identical to those for the rigid bed validations discussed in Sections 2.1 and 2.2. For the inclusion of sediment transport and transient bed changes a number of parameters were added to the SSIIM models. The Van Rjin sediment transport Equations (2.7) and (2.8) required the median soil grain size, D_{50}, and sediment fall velocity, ω. The D_{50} values were obtained from the validation experimental papers and the fall velocities were obtained from Figure 1.29. SSIIM transient sediment computations were implemented with a time step of 10 s which was found to give very

similar results to a 1 s time step while reducing computation time. For localized scouring additional sediment behaviour needed to be addressed along with the sediment transport described by Van Rijn.

2.3.2 Case 2 Mobile Bed

Melville (1975) conducted mobile bed experiments with a median soil grain size of 0.385 mm. The fall velocity for that soil was interpolated as 0.055 m/s from Figure 1.29. The soil was inputted as uniform into SSIIM to simplify the simulation process although there was some gradation to the soil as shown in Figure 2.17.

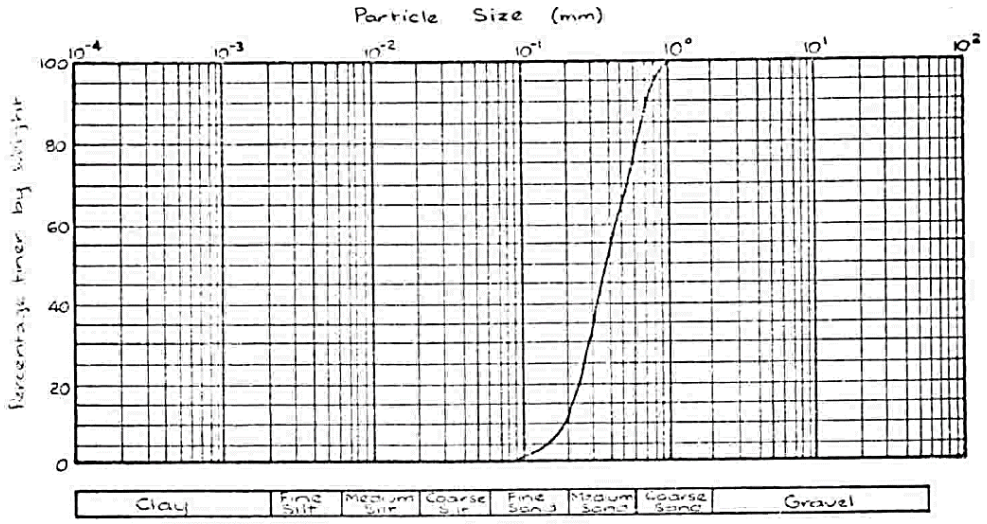

Figure 2.17: Case 2 soil gradation (Melville 1975)

A uniform soil gradation was as chosen for SSIIM as to remain consistent with the other validation cases and the parametric study which will focus solely on uniform soil gradations. Using the definition for critical velocity from Melville and Chiew (1999) equations, the velocity intensity was estimated as I=0.86. The velocity intensity fell into the peak range of 0.8-1.0 near live-bed conditions, thus large amounts of scour was expected (Sheppard and Miller 2006). Melville stated that the soil's angle of repose was 32° but a stable slope value of 32° in SSIIM significantly underestimated scour depths. Melville (1975) also measured the upstream slope of the scour hole and found a steeper slope of 38° which demonstrated how the underwaters slopes may differ from the traditional angle of reposes. Using a value of 38° for the stable slopes in SSIIM produced much better results for scour hole depths and shape in Case 2. Melville (1975)

measured a bed roughness of $2.5D_{50}$ during experiments, however this value was found to underestimate the initial scour rates in SSIIM. Thus, two SSIIM models were ran, Test A to stimulate the depth with control parameters and Test B to increase the initial SSIIM scour rates to determine the effects on equilibrium depth. One parameter of interest in SSIIM was the active sediment layer which is prescribed a thickness of D_{50} by default. The active sediment layer is the overlaying soil which is consider exposed to the flow for sediment transport this it influences the numerical rate of transport and scour. As the soil used in Melville's experiment included some grains larger then D_{50} it was assumed the default value was too small and may limit scour depth. Different values for the active sediment layer were tests range from D_{50} = 0.385 mm to $D100$ = 1 mm. The best results for initial erosion rates were with an active sediment layer thickness of 0.5 mm, it was also investigated with Test B.

Scour Hole Depth

Melville (1975) reported the Case 2 maximum scour depth was 6 cm and the maximum width of the scour hole was 13 cm. A photo of the experimental scour hole is displayed in Figure 2.18.

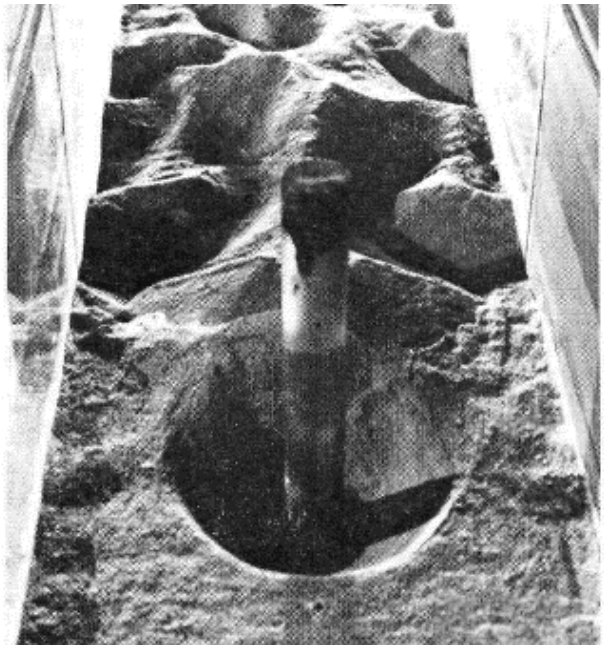

Figure 2.18: Case 2 experiment scour hole (upstream face view) (Melville 1975)

The parameters being tested with the two Case 2 SSIIM models are summarised in Table 2.4.

Table 2.4: Case 2 Test A and Test B Parameters

Parameter	Test A	Test B
Bed Roughness, k_s (m)	$2.5D_{50}$	$3D_{50}$
Active Sediment Layer Thickness (mm)	D_{50}	0.5
Stable Slope for Sand Slides (°)	38	38

SSIIM found the maximum depth as 5.95 cm for Test A and 5.8 cm for Test B which corresponded to errors of 0.8% and 3.4% respectively. The maximum scour depths at the upstream face matched very well and validated SSIIM's capabilities in predicting equilibrium scour depths. Significant underestimation of downstream depths was expected due to the solver nature. The scour holes in SSIIM are displayed in Figure 2.19.

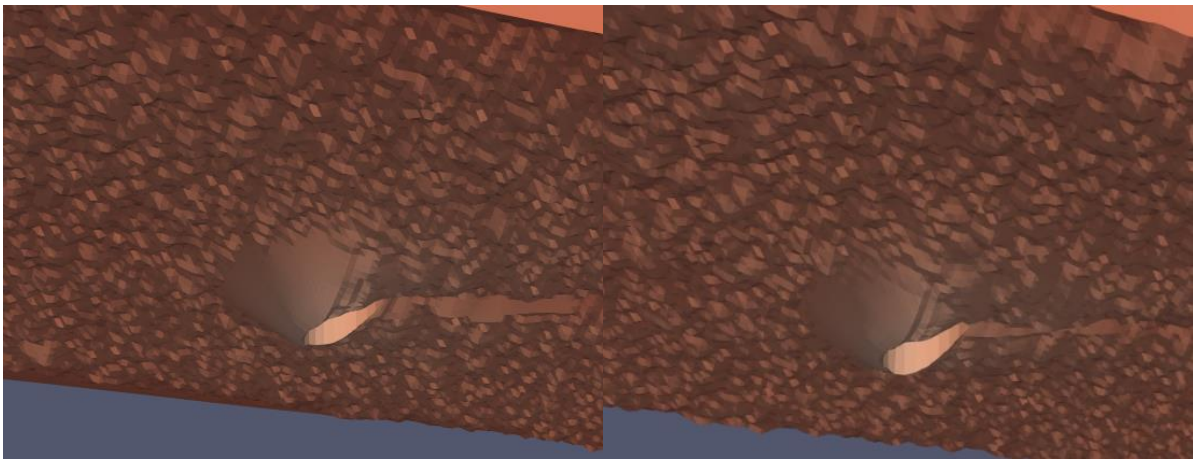

Figure 2.19: Case 2 SSIIM scour holes for Test A (left) and Test b (right) (flow towards right)

The scour holes were well formed although there is some general erosion of the bed around the pier in Figure 2.19. The experimental photo in Figure 2.18 showed plenty of bed ripples and erosion downstream of the pier and a clean upstream bed with very little bed forms until the flow reaches the pier. As both Tests A and B saw the upstream erosion, the higher bed roughness and larger active sediment layer in Test B were not the cause. The general erosion in SSIIM was likely caused by the flow being near the live-bed condition with the high flow intensity of *I=0.86*. The Shields diagram in SSIIM used to describe the critical shear stress is shown not to be the perfect

representation for the inception of bed motion. The experimental scour hole depth contours are shown in Figure 2.20 and the contours from SSIIM are displayed in Figure 2.21.

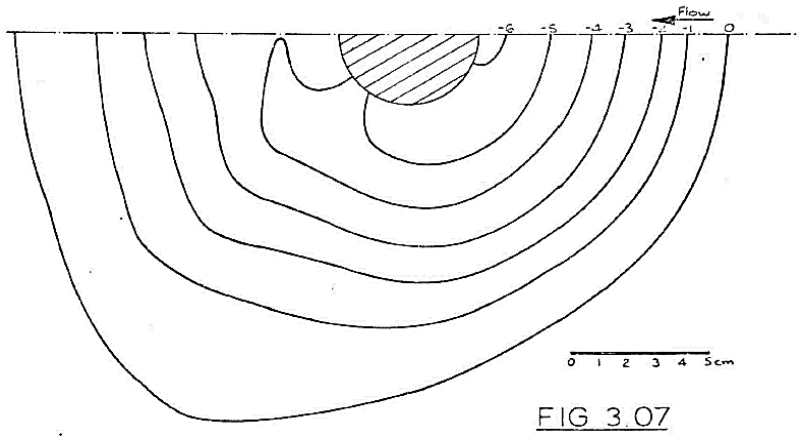

Figure 2.20: Case 2 experimental scour hole depth contours (units: cm) (Melville 1975)

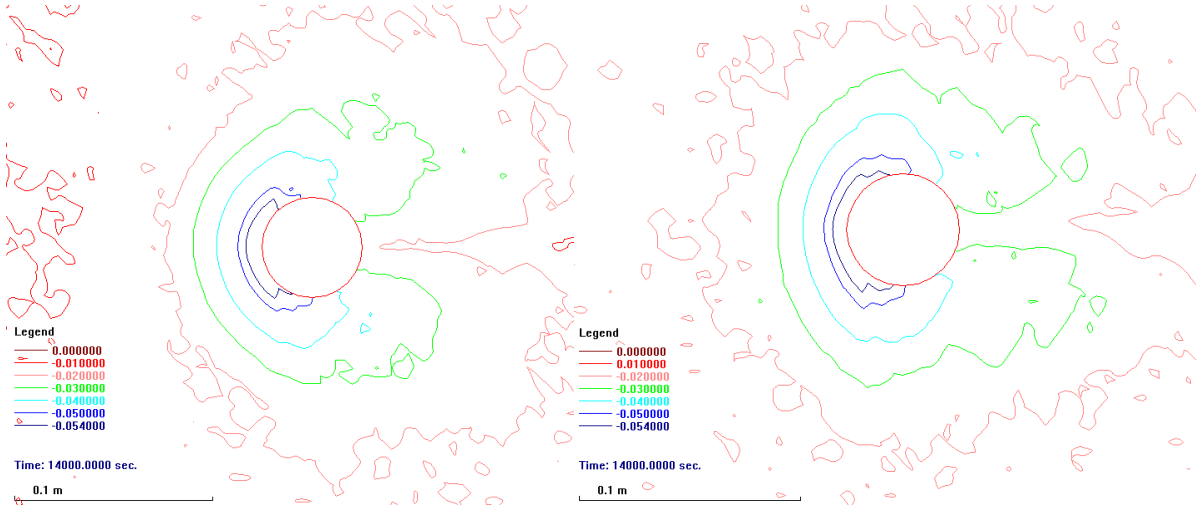

Figure 2.21: Case 2 SSIIM scour hole depth contours (units: m) (Test A left and Test B right)

The contour lines showing the deeper bands at the upstream face in SSIIM match very well with the experimental results. The messy bed erosion upstream observed in Figure 2.19 is shown to consist of 0 cm – 2 cm bed forms, but they were not of concern because the actual scour hole shape and depth matched well with Melville (1975) experiment. Test B contours matched better with Melville (1975) as the deep band of erosion extended farther downstream around the pier.

Scour Depth Versus Time

Melville (1975) stated that experiment equilibrium time was at 2.5 hours (9000 s) and recorded depth measurement for some time after to verify convergence to an equilibrium depth. To compare SSIIM with Melville's data, scour hole depth development over time for both Tests A and B were plotted in Figure 2.22.

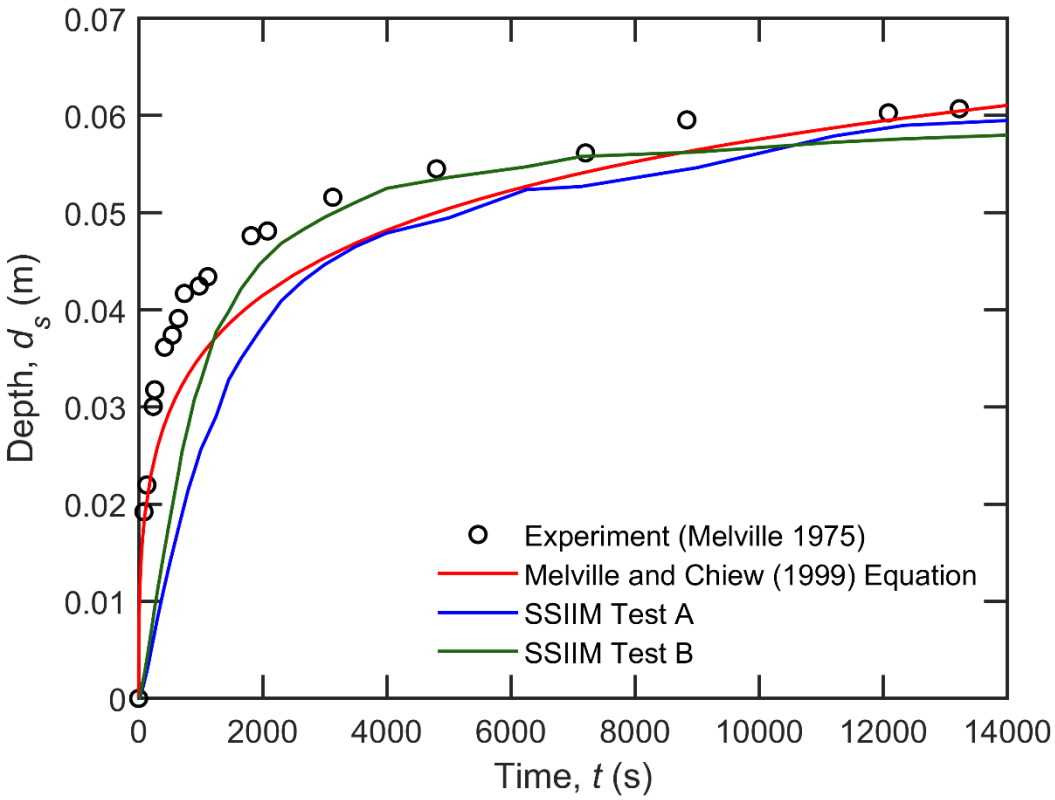

Figure 2.22: Case 2 scour depth over time

Both curves from Test A and B matched very well with Melville's experimental results although Test B was much closer for preliminary scour stages. Test A saw a dip in depth around 7000 s in, but the scour hole later deepened to closely match test B near the end of simulations at 14000 s. Although Test B exhibited higher initial scour rates the equilibrium depth was slightly lower than Test A. The thickness of the active sediment layer and higher roughness had little effects on the final depth which was dominated by the soil grain size, flow velocity and pier diameter. Additionally, Melville and Chiew's (1999) temporal equation was plotted in Figure 2.22 to evaluate how well the equation performed when compared with experimental and numerical results. The empirical formula closely followed the depth development initially and illustrated the

logarithmic relationship scour depth has with time. The empirical equation was known to overpredict equilibrium depth, as it deviated from both the experimental and numerical results after 13000 s.

The Figure 2.22 data was also used to develop a definition for numerical equilibrium scour depth. As Melville (1975) stated, the scour hole reached an equilibrium depth around 9000 s into the experiment which was also observed in SSIIM. Using Melville's data points the slope or erosion rate after 9000 s was found as 2.22e-7 m/s and the slope earlier was 2.09e-06 m/s. To define an equilibrium slope, a round value based on the pier width was desired which fell in between the two slope values of 2.22e-07 and 2.09e-06 m/s. For a sense of reference, the equilibrium condition from the Melville and Chiew (1999) method was an erosion rate of 0.05D/24h or a change in depth lower than five percent of the pier diameter over a day. For Case 2, the Melville and Chiew (1999) equilibrium erosion rate translated to 2.94e-08 m/s which was drastically stricter than Melville's (1975) observation. The Melville and Chiew (1999) equilibrium condition was much too stringent to reasonably reach with SSIIM numerical simulations. To reach such low scour rates SSIIM models would need to run for days-weeks real time which turns into weeks-months computationally. A reasonable value for equilibrium conditions in SSIIM was found as *0.6D/24h* which translated to 3.5e-07 m/s and perfectly described the Case 2 equilibrium observation by Melville (1975). With *0.6D/24h* as the equilibrium erosion rate going forward, the slope was used to find equilibrium runtimes for Cases 3 and 4 during validations and for the parametric study models.

Scour Hole Profiles

For a more precise comparison of the scour hole shapes, the profiles from Melville's (1975) experiment were plotted with the two SSIIM models. The cross sectional and longitudinal scour hole profiles were plotted in Figure 2.23 and Figure 2.24 respectively.

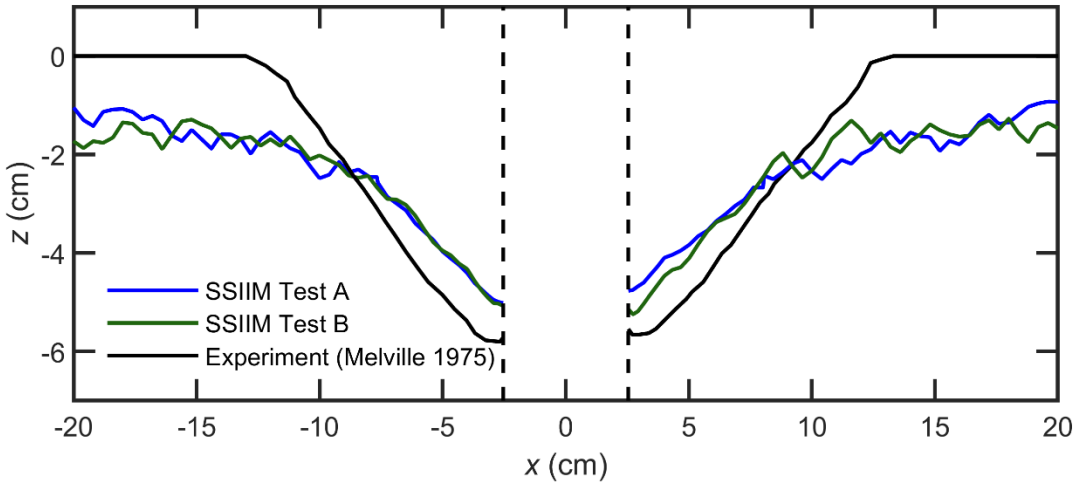

Figure 2.23: Case 2 scour hole cross section (view from upstream)

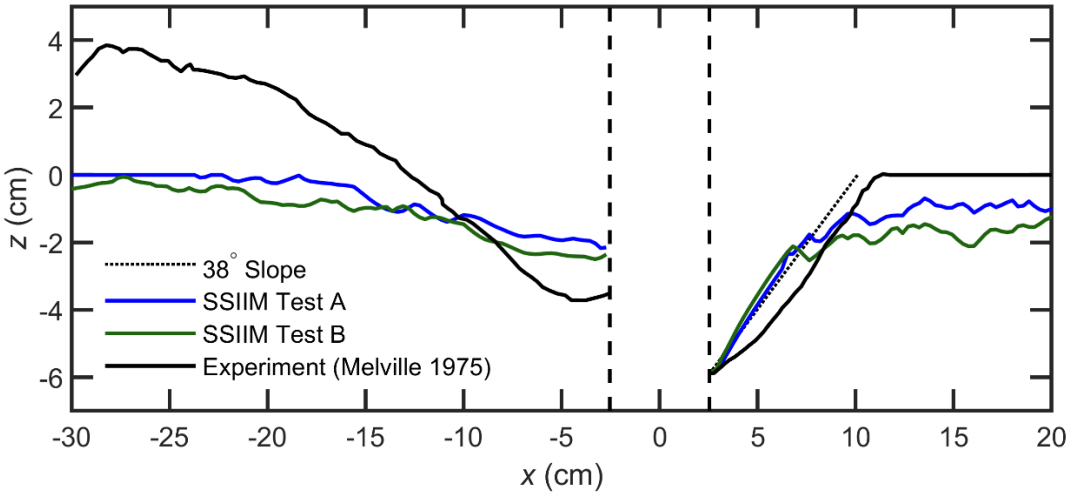

Figure 2.24: Case 2 scour hole longitudinal section (flows toward left)

Both figures show the rough match in hole shapes between SSIIM and the experiment. The general bed erosion is visible at the outer regions of the cross-section and upstream in the longitudinal profile. A 38° line was added near the upstream slope to demonstrate the performance of the sand slides algorithm. The downstream area emphasizes how SSIIM underpredicts both the scour at the pier and deposition at the mound due to the SIMPLE algorithm. However, the area of interest is the upstream face which exhibits a close match with the experimental results in depth and shape. As the maximum scour depth was well within 15% of the experiment, the Case 2 mobile bed SSIIM model was validated.

Grid Refinement Impact

During validations multiple grids were tested using the setup of Case 2 Test A with $2.5D_{50}$ bed roughness and default active sediment layer thickness of D_{50}. Earlier coarse grids were found to produce satisfactory results during the rigid bed validations but performed poorly in predicting scour hole shapes. Cell sizes in the horizontal direction were selected based on pier diameters to be proportional to scour hole sizes. The coarse initial grids were generated with a diameter to cell size ratio of eight, where eight cells fit into the pier width. The Case 2 test scour hole depth was only 5.31 cm, indicating an error of 11.5%. In addition to the scour underestimation, the scour hole shape did not match the experimental data of Melville (1975) as seen in Figure 2.25.

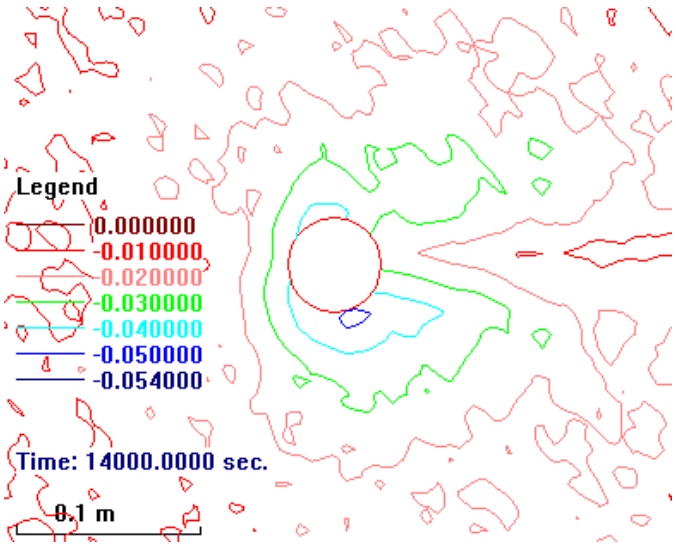

Figure 2.25: Case 2 coarse grid SSIIM scour hole depth contours (units: m)

The shape of the scour hole was not correct as it was non-symmetric with the maximum depth located at the downstream corner instead of the upstream face. Further refinement to a diameter to cell size ratio of 10 lead to satisfactory results previously discussed. Further horizontal refinement may have improved results, but the large increase in cells would have caused unreasonable computation times. The 0.8% error in Test A was satisfactory and did not require further refinement.

All SSIIM grids were created with 14 vertical layers and produced reasonable results. To demonstrate that further vertical refinement would not improve results, Case 2 was simulated with 20 layers and its depth contour is shown in Figure 2.26.

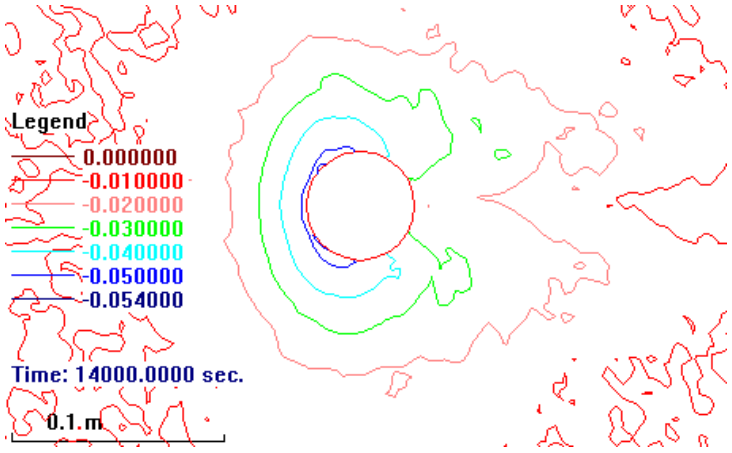

Figure 2.26: Case 2 20-layer grid SSIIM scour hole depth contours (units: m)

The increase in layers did not improve results but increased the error with a lower scour depth of 5.29 cm. As the 14-layer models produced the high-quality results with near zero error, the vertical grid choice was justified.

Critical Shear Stress Reduction on Slopes

The main sediment parameter in SSIIM which required significant testing was the critical shear stress reduction on slopes with Brooks (1963) correction factor. The Brooks correction factor in Equation (2.10) uses the default values for inverse of $tan(\theta)$ as 1.23 and 0.78 for uphill and downhill slopes respectfully. Case 2 Test A was first conducted with the defaults and but scour hole depths were too low. Different values were tested to determine which values for Brooks formula provide the best results for clean sands in Case 2, 3 and 4. First the downhill parameter was kept constant at 0.78 and the uphill parameter was tested with the corresponding depths for Case 2 plotted in Figure 2.27.

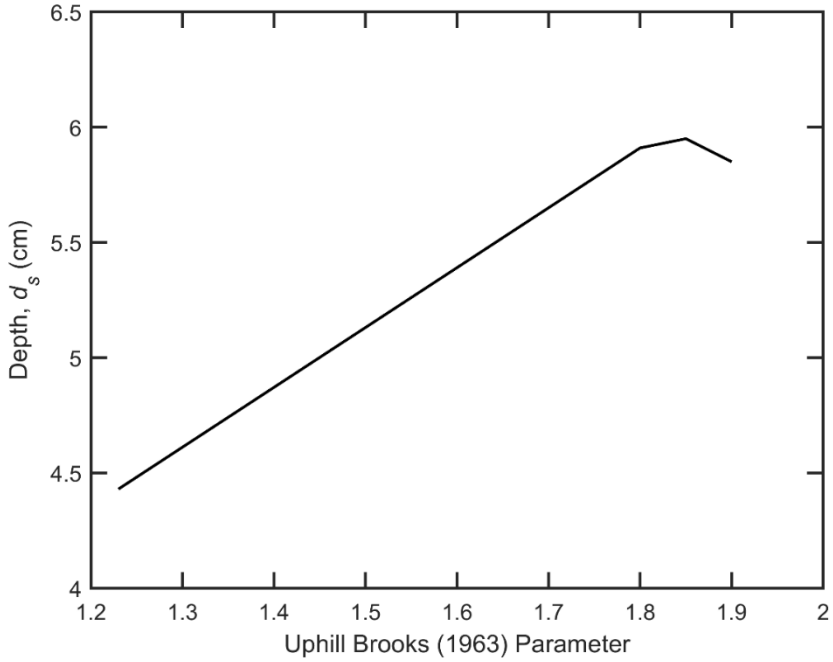

Figure 2.27: Case 2 Brooks (1963) uphill parameter test

Increasing the uphill parameter provided scour depths much closer to the experimental depth of 6 cm where a value of 1.85 was the closest. Once the optimal uphill parameter was selected, the downhill parameter was then tested with results illustrated in Figure 2.28.

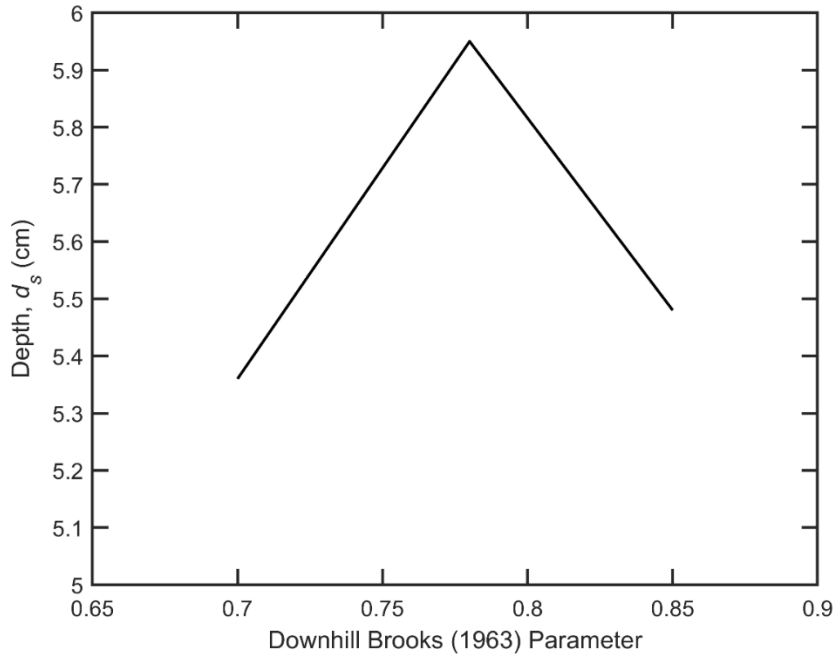

Figure 2.28: Case 2 Brooks (1963) downhill parameter test

The best value for the downhill parameter was determined as the default 0.78. Thus, the optimal Brooks parameters were found as 1.85 and 0.78 for Case 2. The chosen values produced good matches with Cases 3 and 4 SSIIM models as well so they were selected as the values for the parametric study with clean sands.

2.3.3 Case 3 Mobile Bed

Ahmed and Rajaratnam (1998) conducted the mobile bed scour experiments with a median grain size of 1.84 mm which corresponds to a fall velocity of 0.2 m/s from Figure 1.29. For the mobile bed results Ahmed and Rajaratnam (1998) only reported the limited results of scour hole depth and width. Using the definition of critical velocity from Melville and Chiew (1999), the velocity intensity was estimated as $I=0.52$. The soil was of uniform gradation and bed roughness in SSIIM was set to the measured value of $3.74D_{50}$ (Ahmed and Rajaratnam 1998). No data on the angle of repose was provided so an assumed value of 38° was chosen as the stable slope for sand slides. As both Cases 3 and 4 were from experiments by Ahmed and Rajaratnam (1998), the sediment and flow properties were identical. The only difference for Case 4 was a larger pier, validations for Cases 3 and 4 were conducted together to find the sediment parameters optimal for both cases.

Scour Hole Depth

Ahmed and Rajaratnam (1998) reported an experimental depth of 5.45 cm and width of 11.6 cm. SSIIM reported a depth of 6.13 cm which produced a moderate error of 12.6%. The overestimation in depth was deemed acceptable as Case 4 matched very well with the same soil parameters and the depth was within the 15% tolerance. Any changes of sediment parameters to reduce the SSIIM scour in Case 3 resulted in a significant underestimation in scour with Case 4. The Case 3 scour hole shape was well defined as seen in Figure 2.29.

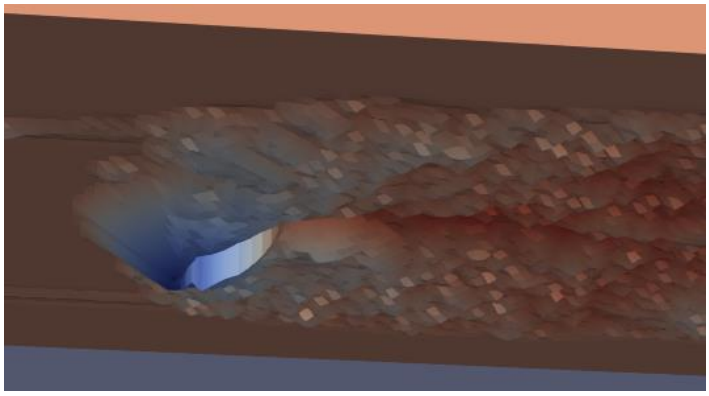

Figure 2.29: Case 3 SSIIM scour hole (flows to right)

The model produced much less outer general erosion when compared to Case 2 in Figure 2.19. Cases 3 and 4 were not close to live-bed conditions with velocity intensity estimates of 0.52 while Case 2 had a velocity intensity around 0.86. Thus, the lower velocity intensity was the probable cause for the cleaner upstream bed in Cases 3 and Case 4. The contour of the Case 3 scour hole in SSIIM is displayed in Figure 2.30.

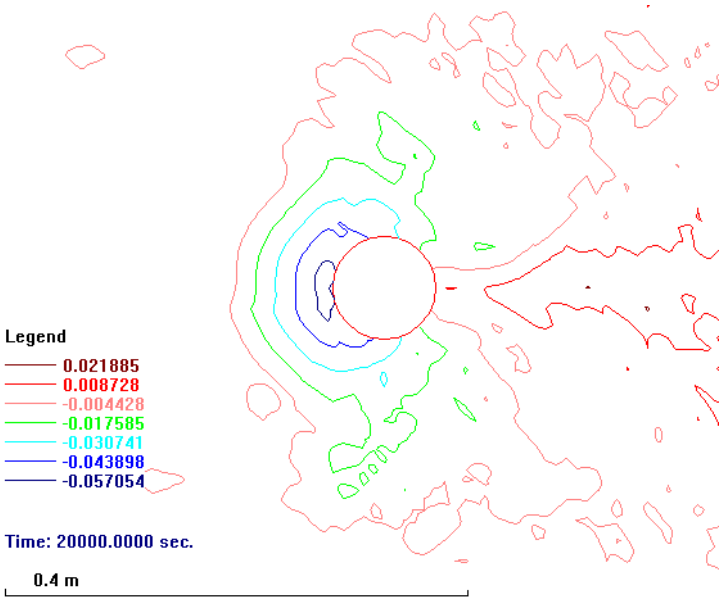

Figure 2.30: Case 3 SSIIM Scour Hole Contour (Units: m)

The scour hole contour for Case 3 revealed the peak depth at the upstream face and had significantly less scour at the downstream face as expected.

Scour Depth Versus Time

To ensure that SSIIM reported the equilibrium scour depth, depth over time was plotted compared with Melville and Chiew's (1999) equation in Figure 2.31.

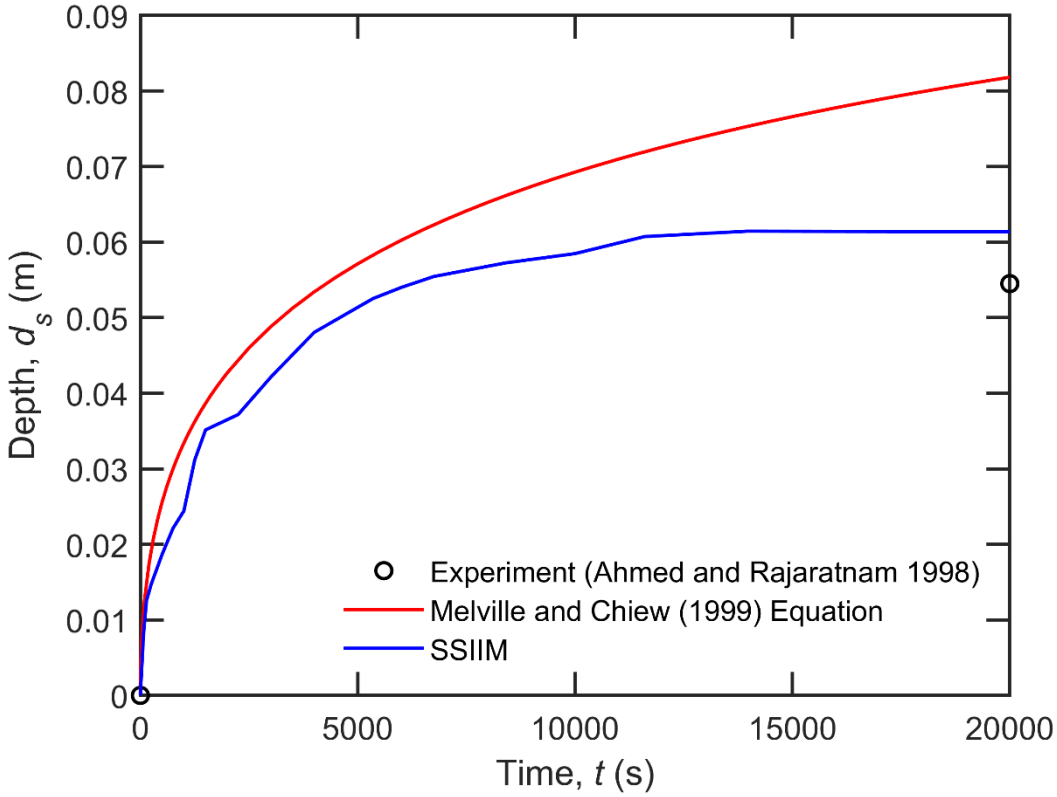

Figure 2.31: Case 3 Scour Depth over Time

Melville and Chiew's (1999) equation overestimated the depth significantly which was expected. Ahmed and Rajaratnam (1998) had ran their experiments for two to three weeks with a strict equilibrium erosion rate condition of less than 1 mm of scour over 24 hours. As seen visually in Figure 2.31, a reasonable equilibrium depth was reached much earlier just by inspection. Using the equilibrium erosion of *0.6D/24h* developed from Case 2, Case 3 had reached equilibrium depth at around 12500 s.

Scour Hole Profiles

The longitudinal profile for the Case 3 scour hole was plotted to confirm the upstream stable slope of 38° in Figure 2.32.

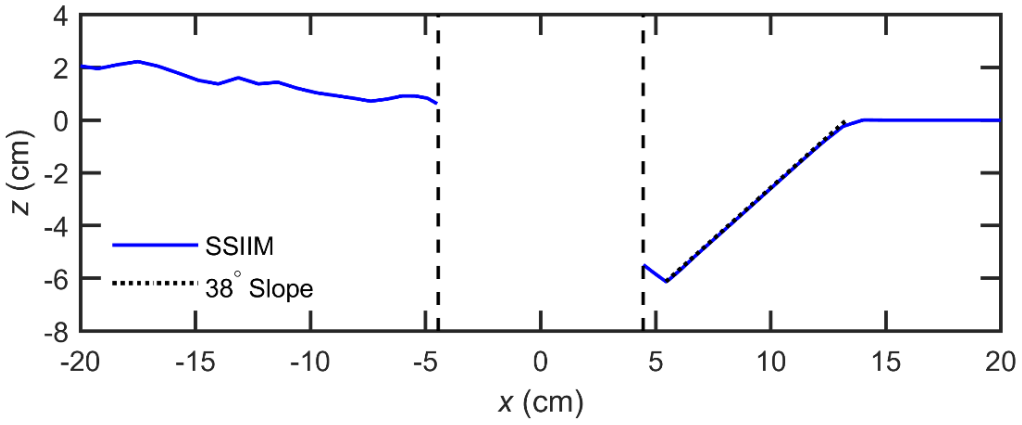

Figure 2.32: Case 3 scour hole longitudinal section (flows toward left)

SSIIM modeled the stable slope very well and the upstream portion of the scour hole was clearly defined.

2.3.4 Case 4 Mobile Bed

Ahmed and Rajaratnam (1998) conducted multiple experiments with differ piers sizes, flowrates, and sediment sizes. Case 4 was selected as the experiment which used the same flow and sediment type as Case 3. The difference was that Case 4 had a pier diameter of 0.108 m instead of the 0.089 m from Case 3. The SSIIM model had the same properties as Case 3 except the domain length and width were increased to account for the larger pier. The Case 4 SSIIM model was 10 m long and 1 m wide.

Scour Hole Depth

The experimental scour hole depth and width for Case 4 were 7.7 cm and 17.1 cm respectively. The scour depth from SSIIM was measured as 7.69 cm resulting in a very close match with only 0.2% error. As previously discussed, any attempt to improve the Case 3 match with the experimental depth also significantly lowered Case 4 scour as they shared the same sediment and flow properties. Thus, the overestimation of the Case 3 depth in SSIIM was acceptable as Case 4 matched so well. This disparity in errors between Case 3 and 4 further emphasizes the complicated and probabilistic nature of scour analysis and simulation. The scour hole shape for Case 4 is displayed in Figure 2.33 and the contour of the scour hole in SSIIM is displayed in Figure 2.34.

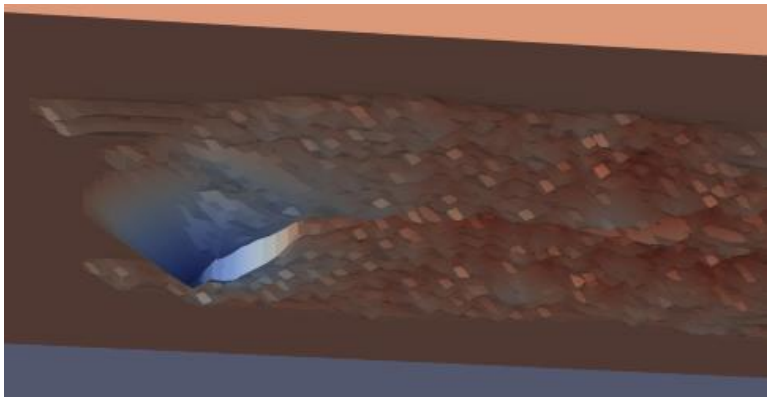

Figure 2.33: Case 4 SSIIM scour hole (flows to right)

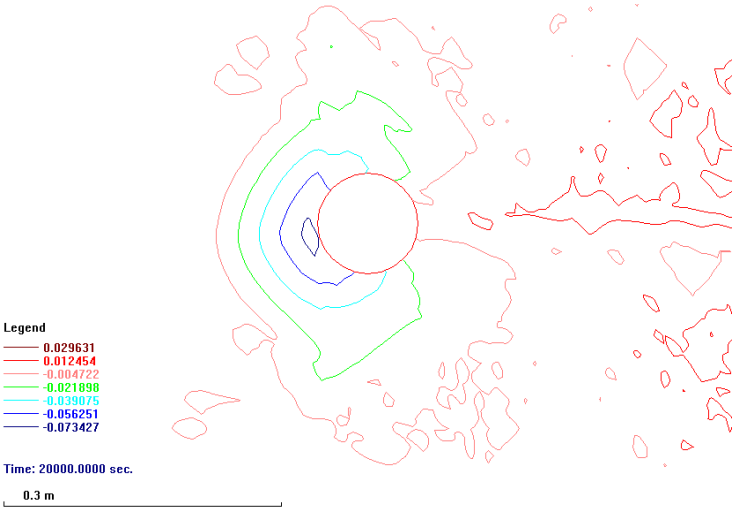

Figure 2.34: Case 4 SSIIM scour hole contour (units: m)

Just as Case 3 a distinct scour hole was developed with negligible erosion in areas upstream from the pier and the maximum depth was located at the upstream face.

Scour Depth Versus Time

The scour depth over time for Case 4 was plotted in Figure 2.35 for confirmation of equilibrium depth.

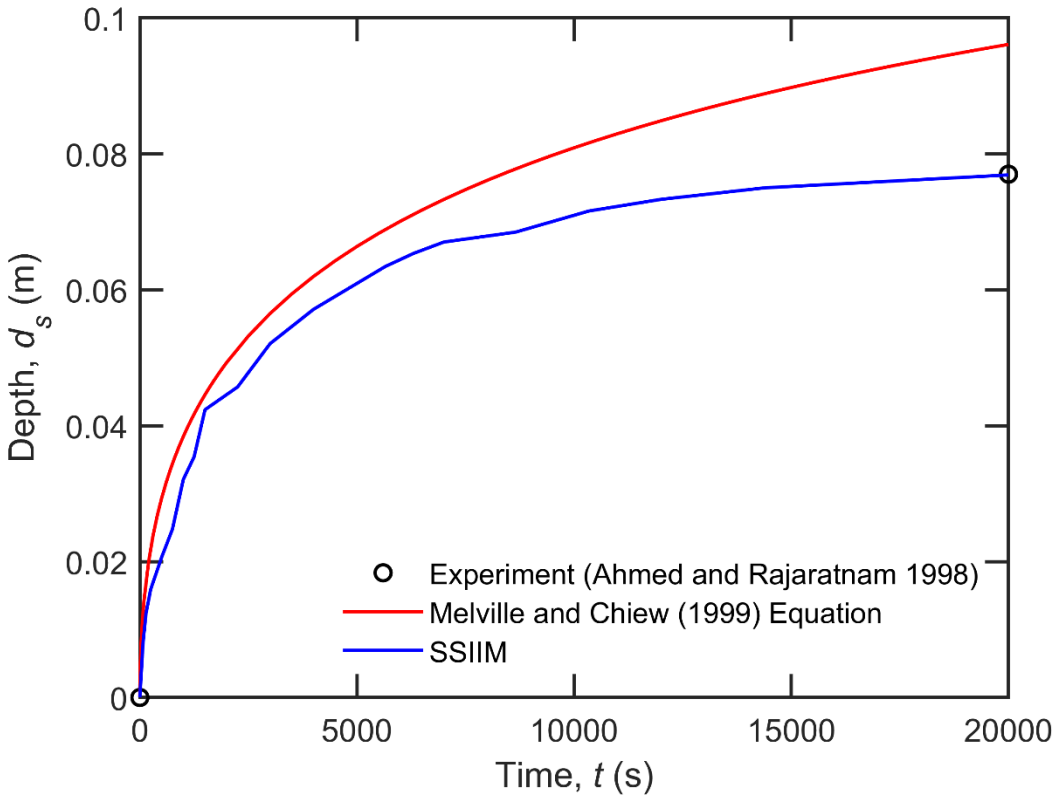

Figure 2.35: Case 4 scour depth over time

Case 4 scour was overpredicted again by Melville and Chiew's (1999) formula, especially later in the experiment. With the equilibrium slope of *0.6D/24h*, Case 4 reached equilibrium depth around 13000 s. With the close match in equilibrium scour depth with Ahmed and Rajaratnam (1998), the Case 4 mobile bed SSIIM model was validated.

Scour Hole Profiles

The longitudinal profile for the Case 4 scour hole was plotted to confirm the upstream stable slope of 38° in Figure 2.36.

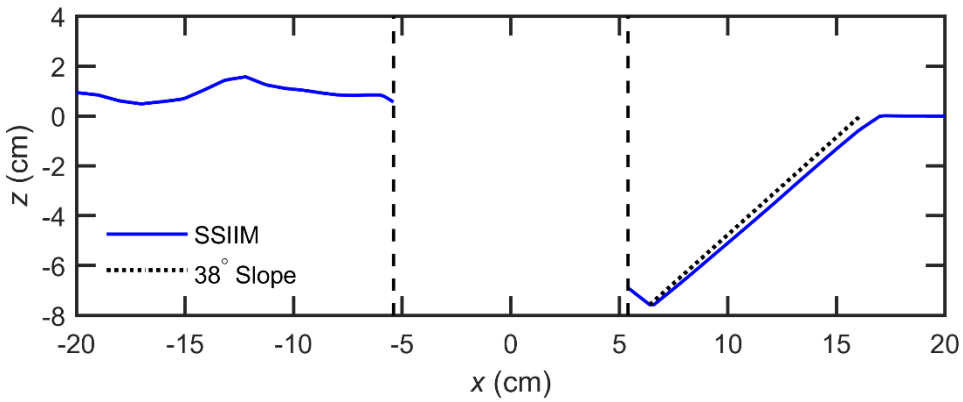

Figure 2.36: Case 4 scour hole longitudinal section (flows toward left)

The Case 4 upstream scour hole slope matched closely with the prescribed 38°s stable slope.

2.4 Conclusions

SSIIM was selected as the software tool to study numerical simulation of clear water pier scour as it was an open source CFD software with built in sediment transport models. To perform a soil parametric study on pier scour depths with clean sands SSIIM first needed to be validated with experimental results. SSIIM solves the 3D RANS equations coupled with Van Rijn's equations for sediment transport and the standard k-epsilon model. SSIIM used Shields diagram to describe the threshold for motion for sediments and included a sand slides algorithm to ensure slopes were realistically stable. Velocity fields and bed shear stresses from three rigid bed SSIIM models were compared with published experimental results to validate the CFD performance of SSIIM. During validations tests were also conducted to find the optimal parameters for accurate and computationally efficient simulations in SSIIM. Employing a uniform grid of cubic cells with 14 vertical layers and a horizontal cell size of *D/10* SSIIM provided accurate pier scour depth estimates where *D* as the pier diameter. A minimum domain width of *7D* and inlet of length of *13y+4D* was employed to fully capture scour holes and allow flow development where *y* was the flow depth. Due to the probabilistic nature of scour and the limitations of the current numerical scour model a 15% error in depth was deemed acceptable in SSIIM. The three mobile bed cases in SSIIM had sediment beds composed of clean sands with D_{50} values of 0.385 mm for Case 2 and 1.8 mm for both Cases 3 and 4. To address the reduction of critical shear stress on slopes, Brooks (1963) empirical correction factor was implemented in SSIIM. The optimal Brooks (1963)

parameters for the clean sands were determined as 1.85 for uphill slopes and 0.78 for downhill slopes. Higher values for active sediment layer thickness and bed roughness were found to increase initial erosion rates but had insignificant effects on equilibrium scour depths. SSIIM successfully predicted pier scour depths with errors of 0.8%, 12.6 % and 0.2% for Cases 2, 3 and 4 respectively. The large difference in errors between Cases 3 and 4 was interesting as both Cases used the same soils. The larger Case 3 error further demonstrated how scour is a complex issue and not perfectly modeled by the empirical sediment models used in SSIIM. The Shields diagram and Brooks (1963) correction factor are not universally applicable as they were empirically derived with limited soil types. SSIIM was validated as a good tool for preliminary investigations into the effects of soil parameters on pier scour as it allows full control of inputs and no scaling errors which are present in laboratory experiments. However, the current state of numerical sediment models are limited to empirical algorithms which cannot capture all complex soil parameters such as critical shear stress, gradations, cohesion, angle of repose, porosity. Further development into morphodynamic sediment models coupled with CFD is recommended for future studies into numerical scour simulations.

Chapter 3: Pier Scour Sediment Parametric Study in SSIIM

3.0 Introduction

Chapter 1 summarised the current state of knowledge on scour theory and presented the common equations used by engineers to estimate scour depths. The major gap in scour estimation methodology is the lack of soil parameter consideration leading to major inaccuracies. To improve methods for predicting scour further studies must be conducted into describing relationships between prominent soil parameters and scour depths. Past studies on pier scour have been conducted through laboratory flume tests where scaling effects produced inaccuracies when applying findings to the larger to-scale piers in the field. As field measurement of scour is difficult and limited to available sites an alternative approach was taken to model scour. The ideal method for future scour studies is numerical modeling which allows full control of input parameters and includes to-scale modeling. The main obstacle in numerical scour modeling is the availability of software which couple reliable sediment models with a fluid model such as CFD. With numerical scour modeling many scenarios and soil types may be investigated to develop novel scour estimation methods including soil parameters as inputs for more accurate depths. For a preliminary investigation into the influences of soil parameters on pier scour the software SSIIM was selected to conduct simulations.

Chapter 2 discussed the scour modeling capabilities in SSIIM along with the validation of three mobile bed cases from published experimental data. SSIIM was found to adequately simulate maximum scour depths at piers although the sediment modeling algorithms were limited in their ability to captures all soil behaviour accurately. Once SSIIM was validated for its acceptable pier scour modeling abilities, analysis into sediment effects was to be conducted. The first of two objectives was to quantify the influence of soil parameters on scour depth and emphasise that soil parameters not yet considered by current methods have significant impacts. The second objective was to evaluate current scour prediction methods and recommend the most accurate and safe methods for design engineers. The present study scope was set to clear water scour at four cylindrical piers in clean sands under two uniform flow conditions. The four piers had diameters of 0.1 m, 0.25 m, 0.5 m, and 0.8 m. Along with the four pier sizes, two flow intensities of 0.5 and

0.75 were tested with each pier for a total of eight models in SSIIM. The eight models were all simulated using 16 different types of soil for a total of 128 cases. The different soil types were included of clean sands with varying soil grain sizes, stable slope angles, and cohesive strengths. The control sediment for each model was selected as D_{50} =1 mm, a stable slope angle of 30° and cohesive strength of 0 Pa. The control case was simulated for each model after which a single parameter was varied to conduct a parametric analysis. The D_{50} values tested were 0.05 mm, 0.1 mm, 0.2, mm, 0.5 mm, 1 mm, 2 mm, 5 mm, and 10 mm. The stable slope angles were 20°, 35°, 30°, 35°, and 40°. Lastly the cohesive strength tested were 0 Pa, 0.05 Pa, 0.1 Pa, 0.25 Pa, and 0.5 Pa.

Conclusions were made on how influential soil parameters were and the performance of the empirical scour estimation equations. Resulting scour depths in each case were compared and analysed along side 12 empirical scour formulae in Chapter 3. Using the D_{50} results error analysis was conducted to score the performance of each empirical formulas as D_{50} was the only soil parameter included by any formulae. The best performing equations were the TAMU method, F-DOT method, SRICOS method and the Sheppard/Miller method. Soil parameters such as the stable slope angle and cohesion are not considered by any empirical equations but were found to have significant impact on scour depths. The larger variation in scour with the two soil parameters highlighted the need for their inclusion in scour prediction methods.

3.1 Empirical Equations for Pier Scour

To analyze the current state of methods for predicting pier scour, 12 equations were selected to include in the parametric study with SSIIM. Of the 12, five are industry standard equations used for bridge design by MTO and the FHWA. The methods suggested by FHWA are the HEC-18 and F-DOT (Richardson and Davis 2001) methods. The MTO recommended methods are the RTAC (1973)/Breusers (1963), CSU (Colorado State University), and Melville and Sutherland (1988) methods. Rest of the methods and equations are described in detail in Chapter 1: Section 1.2. Most equations used inputs such as the flow depth, pier diameter, and mean flow velocity for estimating pier scour depths while few also considered the soil grain sizes. In addition to those equations used by MTO and the FHWA, some equations which have been documented as high performing in Chapter 1: Section 1.2.3 were also included in the study. Equations not considering any soil parameters for calculation of equilibrium scour depth are the RTAC

(1973)/Breusers (1963) Method, CSU (Colorado State University) (1977) Method, HEC-18 (Richardson and Davis 2001) method, and the SRICOS (Briaud et al. 1999) method. Although the SRICOS method uses laboratory testing to quantify a soil's erosive behaviour over time, Equation (1.111) for the maximum depth is only a function of the pier Reynold's number. Equations which used D_{50} as an input included the F-DOT (Richardson and Davis 2001) method, Sheppard and Miller (2006) method, Sheppard/Miller (Sheppard et al. 2014) method, Breusers Method (1977) method, TAMU (Briaud 2015a, 2015b) method, and the temporal Melville and Chiew (1999) method.

Over the years past equations have been altered and updated with new data to improve performance. For example, the HEC-18 was just the CSU equations with an additional factor for bed forms. Both the F-DOT and Sheppard/Miller equation were derived from the Sheppard and Miller (2006). Once the best performing equations from the present study are identified they may be used as base equations for developing new methods. The results of future numerical scour studies should be used to refine and update current methods with factors accounting for reposes angles, cohesive strength, and other soil parameters. Papers which evaluated empirical equations with experimental and field scour data were reviewed in Chapter 1: Section 1.2.3. The best performing equations in literature were found to be the CSU, HEC-18, and Sheppard/Miller equations as discussed in Chapter 1: Section 1.2.3

3.2 SSIIM Models for Parametric Studies

Local scour occurs due to the non-linear interactions between the three elements of flow, structure, and sediment. The three elements themselves have many different parameters where varying combinations lead to near infinite possible scenarios. The variety factors discussed in Chapter 1: Section 1.1 contribute to the complexity of scour and difficulty in creating equations applicable to all scenarios. For the scope of this report only a sample of the possible pier scour situations was able to be investigated. The primary element of investigation from a geotechnical engineering perspective was the influence of soil parameters on scour. However different piers and flows are also vital to test to see the soil effects at different scales. Firstly, the sediment scope was selected as clean sands with a control size of D_{50} = 1 mm. Clean sands were often used in the development of the empirical scour equations mentioned in Section 3.1 and the validations conducted in Chapter 2. Future studies are recommended into scour in cobbles, rocks, and fine

sediment such as clays and silts. Once the control D_{50} value was selected, four piers and two flows were determined for a total of 8 SSIIM models. Each of the SSIIM models were simulated with varying sand grain sizes, cohesive strengths, and stables slopes angles for a total of 128 cases. Thus, results of this study will reveal the influence of soil parameters on clear water scour in clean sands at circular piers.

3.2.1 Pier Parameters in Parametric Study

For the piers type, circular cross sections were selected to remove any factors pertaining to pier shapes or flow angles of attacks. Equations developed for pier scour have usually started with circular piers after which correction factors were developed for non-circular piers, angled flow directions, and pile group effects. Thus, as a preliminary study circular piers were the rational choice to allow focus on soils and recommend future studies to explore other pier types. The sizes for Pier 1, Pier 2, Pier 2, and Pier 4 were selected as 0.1 m, 0.25 m, 0.5 m, and 0.8 m respectively. The smaller pier of 0.1 m was selected as it was in the range of smaller piers or piles usually used in laboratory experiments and the 0.8 m pier was more indicative of the larger piers at bridges. With a large range of pier sizes the performance of the empirical equations may be assessed in their versatility.

3.2.2 Flow Parameters in Parametric Study

The flow factors to consider for local pier scour are the flow depth and mean flow velocity. The study scope was set to constant flow conditions in the clear water range and low Froude numbers. The simulation of clear water scour was found to be more manageable numerically as upstream ripples and transport was not required to be modelled. Simulations for clear water scour were also simpler as an unambiguous maximum equilibrium depth is observable as opposed to live bed conditions. Live-bed scour consists of deposition and erosion cycles occurring at piers as described in Figure 1.5 so a time-averaged approach is more appropriate. To narrow down the range of flows two median flow intensities a-flow and b-flow were selected as 0.5 and 0.75 respectively. To determine inlet velocities for each flow intensity a soil critical velocity was required. However, the Shields diagram version used by SSIIM was unknown, so an approximation for the critical velocity, V_c, was made using different empirical formulae. With the control size of D_{50} = 1 mm, V_c was calculated by averaging the values for V_c obtained using the Melville and Sutherland (1988), Melville (1997), and the TAMU (Briaud 2015a, 2015b) methods.

The approximate critical velocity for the control case was calculated as 0.463 m/s so the a-flow and b-flow velocities were determined as 0.231 m/s and 0.346 m/s respectively. As the velocity intensity values were merely selected to provide a range of flow conditions, any errors in the approximation of V_c were trivial. Lastly the model flow depths were selected to remain in the low Froude number, *Fr*, range so free surface modeling could be neglected for computational efficiency. Roulund et al. (2005) stated that excluding a free surface model has negligible results on numerical scour results for $Fr < 0.219$. The model flow depths, *y*, were all set to 0.4 m to meet the Froude number requirement. The FHWA HEC-18 defines slender piers as those with depth to diameter ratios as $y/b > 0.8$ (Richardson and Davis 2001). Piers 1 and 2 were set as slender while the wider Pier 3 was set on the borderline value of $y/b=0.8$ and Pier 4 was classified as wide. The range of slenderness also proved a wider range of pier types to assess with the empirical formulae.

3.2.3 Soil Parameters in Parametric Study

The soil parameters selected for the parametric study were the grain size D_{50}, stable slope angle and cohesive strength. Theses parameters were selected as they were available in SSIIM, are regularly used to describe soil shear strength and were found to be the most influential on scour as discussed in Chapter 1: Section 1.2. The soil density was left as the default SSIIM value with a specific gravity of 2.65 which is representable of most sands (Melville 1975).

3.2.3.1 Soil Grain Size (D_{50})

The most influential soil parameter has been documented as the soil grain size, thus D_{50} was imperative to test in SSIIM. The soil grain size generally controls its resistance to fluid flow and critical velocity as documented by Shields (1936). It is the only soil parameter to be regularly inputted into empirical formulae when solving for scour depths as seen in Chapter 1: Section 1.2. According to the Massachusetts Institute of Technology (M.I.T) Soil Classification System, sand grain sizes range between 0.06 mm to 2 mm (Melville 1975). Thus, for a representative medium size the control sand grain D_{50} was selected as 1 mm. For a wide range of soils encapsulating all sands in between coarse silt and fine gravel the smallest D_{50} size was 0.05 mm and the largest D_{50} value was 10 mm. The intermediate soil grain sizes for the study were selected to provide well distributed data on a logarithmic plot. A logarithmic plot was selected because most methods such as Melville (1997) described a logarithmic relationship between D_{50} and V_c. The fall velocity for each D_{50} value was obtained from Figure 1.29 for input into SSIIM. The bed wall roughness

influences the velocity profile therefore also the bed shear stress influencing the scour. Wu at al. (2000) recommended that the roughness be set between a minimum of D_{50} and up to $3D_{90}$ as recommend by Van Rijn (1984). For the cases of the uniform soils in the parametric studies $D_{90} = D_{50}$ for all roughness calculations. From testing roughness values during validations, a roughness of D_{50} was found to significantly underestimate scour depths due to lower magnitudes of bed shear stress. Thus, the bed roughness values for the SSIIM models in the parametric study were set to $3D_{50}$. The study soil grain sizes, D_{50}, with the corresponding fall velocity, ω, and bed roughness, k_s, are listed in Table 3.1.

Table 3.1: Parametric study D_{50} values and numerical parameters (*control)

D_{50} (mm)	ω (m/s)	k_s (m)
0.05	0.003	0.00015
0.1	0.0095	0.0003
0.2	0.026	0.0006
0.5	0.07	0.0015
1*	0.14	0.003
2	0.2	0.006
5	0.37	0.015
10	0.46	0.03

To reduce the number of input parameters within the scope only uniform clean sands were examined. The large variety of gradation which may occur in natural soil is too large to evaluate in the present study. Non uniform graded soil may exhibit sorting effects which develop into armour layers. Scour in non-uniform soils with armour layers have been researched by Melville and Sutherland (1988), Raudkivi and Ettema (1985), and Melville (1997). Unlike DEM sediment models, SSIIM is unable to model the particle scale sorting effects which occur in non-uniform soils. Future numerical studies in the armour effects in non-uniform soils is recommended.

3.2.3.2 Stable Slope Angle

Chapter 2 discussed the sediment behaviour on sloped beds required for numerical scour simulations. The two behaviours on slopes was the reduction of critical shear stress and avalanching at steep slopes. The objective in the present study was to investigate the effects of

soil repose angles on scour in SSIIM. A soil's repose angle would influence both the stable slope and critical shear stress reduction on slopes. However, as the repose angle is not an explicit input into SSIIM, an alternative approach was taken to investigate its effects. The reduction of critical shear stress was implemented in SSIIM with Brooks (1963) empirical formula seen in Equation (2.10). During the validations in Chapter 2 with sands, the optimal uphill and downhill parameters for Brooks (1963) formula were found as 1.85 and 0.78 respectively. The parameters were defined as $tan(\theta)$, where θ was an empirical value similar to a soils repose angle. The optimal Brooks parameters in SSIIM were those which provided the deepest scour depths and best matches with published experiment results. However, the optimal uphill parameter of $tan(\theta) = 1.85$ did not correspond to the measured slope of 38°. This inconsistency posed a problem in using the Brooks formula to investigate the repose angle. As the Brooks (1963) formula was limited in its development it was difficult to implement the repose angle into the critical shear stress reduction on slopes formula. Therefore, the Brooks (1963) parameter values were kept constant for all cases and the repose angle effects were examined solely using the stable slope angle. As the values were tested with D_{50} values of 0.385 mm and 1.8 mm in Chapter 2 they were deemed acceptable for the present study with clean sands. The stable slope angle described the steepest slope which may exist before a grid correction algorithm simulates sand slides. Stable slope angles analyzed in the present study are within the typical range for sands (Al-Hashemi and Al-Amoudi 2018). The values for stable slopes angles tested are listed in Table 3.2 where 30° was the control value.

Table 3.2: Parametric study stable slope angle values (*control)

Stable Slope Angle (°)
20
25
30*
35
40

The sand slide algorithm in SSIIM reduced steep slopes and solved for slope stability as a function of the inputted stable slope value. Larger stable slope angles can maintain steeper sleeps before collapsing so the scour depths are expected to increase with higher stable slope angles.

3.2.3.3 Cohesion

The third soil parameter investigated in SSIIM was soil cohesive strength. Sands with graduation may be composed with fines lending some cohesive strengths. To model a graded sand with cohesion, a cohesive strength was prescribed to the clean uniform sands. However, SSIIM's sediment model is limited in how cohesion is considered. SSIIM allows cohesion to be assigned to increase the critical shear stress of a soil but has no impact on transport behaviour once suspended. As discussed in Chapter 1: Section 1.1 cohesion also effects the erosion failure mechanism in soil where instead of only grain by grain erosion, chunks of fine soils may be eroded at once. The cohesion effects on temporal scour may not be realistic but for investigating the effects on maximum scour depths, the SSIIM model is adequate. The range of cohesive strengths for the study was determined using the critical shear stress of the control sediment of $D_{50} = 1\ mm$. As the Shields diagram in SSIIM was unknown an estimate was made for the critical shear stress using Figure 1.9 by Briaud et al. (2014). From the data of US Army Corps of Engineers EM 1601 the critical shear stress for a 1 mm soil was approximately 1 Pa. The cohesive strength values were selected as fractions of the critical shear stress. The cohesive strength values tested are listed in Table 3.3.

Table 3.3: Parametric study cohesion values (*control)

Cohesion (Pa)	Approximate % of τ_c*
0*	0
0.05	5
0.1	10
0.25	25
0.5	50

The control cohesive strength was set as 0 Pa for cases investigating the effects of D_{50} and the stable slope angle. The default cohesion value was selected because sand typically does not exhibit cohesive strength due to its coarser grain size.

3.2.4 Summary of Study Model Parameters

Once the pier sizes and flow conditions for the eight models were established the SSIIM models were generated. The numerical model domains and grids were generated using relationships recommended from validations in Chapter 2. To ensure flow development from the inlet to pier the minimum inlet lengths for all models was *13y+4D*, where *y* is the flow depth and *D* is the pier diameter. The model widths were set to a minimum of *7D* to capture maximum scour hole widths. The horizontal and vertical grid refinement was based on values which accurately captured scour hole shapes while keeping simulation runtimes reasonable. The maximum horizontal cell size was *D/10*, and all model grids were comprised of 14 vertical layers. The structural and flow parameters for all eight models were summarised in Table 3.4.

Table 3.4: Parametric study SSIIM model parameters

Model	*D* (m)	*y* (m)	Flow Intensity	V_c* (m/s)	*V* (m/s)	*y/D*	*Fr*
1a	0.10	0.40	0.50	0.463	0.231	4.0	0.117
1b	0.10	0.40	0.75	0.463	0.347	4.0	0.175
2a	0.25	0.40	0.50	0.463	0.231	1.6	0.116
2b	0.25	0.40	0.75	0.463	0.347	1.6	0.175
3a	0.50	0.40	0.50	0.463	0.231	0.8	0.117
3b	0.50	0.40	0.75	0.463	0.347	0.8	0.175
4a	0.80	0.40	0.50	0.463	0.231	0.5	0.117
4b	0.80	0.40	0.75	0.463	0.347	0.5	0.175

With eight models and 16 different combinations of soil parameters, a total of 128 cases were simulated in SSIIM. The control sediment case for each model consisted of D_{50} = 1 mm, a 30° stable slope angle and 0 Pa cohesive strength. As two of the three sediment parameters was kept at the control values the third parameter was varied with those values listed in Table 3.1, Table 3.2, and Table 3.3. The original study scope included a third flow intensity c-flow with a magnitude of 0.9. The tests with different D_{50} values all used the velocity based on a flow intensity of 0.9 with D_{50} = 1 mm as the prescribed flow intensity was based on the control case. Thus, for the D_{50} values smaller than 1 mm the bed condition was far into in the live-bed range as illustrated in Table 3.5.

Table 3.5: Approximate flow intensities for D_{50} values (*control)

D_{50}	Approximate Velocity Intensity		
	a	b	c
0.05 mm	1.03	1.55	1.86
0.1 mm	1.00	1.50	1.80
0.2 mm	0.89	1.34	1.60
0.5 mm	0.67	1.00	1.20
1* mm	0.50	0.75	0.90
2 mm	0.36	0.54	0.65
5 mm	0.25	0.38	0.45
10 mm	0.20	0.29	0.35

With the large range of D_{50} values the flow intensity ranged from 0.2 to 1.86 for the three flow velocities. The condition of live-bed scour implies not only deposition at the local scour hole but also general erosion of the entire bed. Live bed scour in SSIIM exhibited erosion of the entire bed such that the local scour hole continuously shifted downwards while not becoming any deeper relative to the upstream bed level. For the smaller D_{50} sizes with flow intensity c the scour process in SSIIM consisted of very long equilibrium times. The equilibrium depths took over weeks to reach which was not reasonable within the present scope, so flow intensity c was removed. The removal simply eliminated tests with flow intensity higher than 1.55 so a good range was still covered with a-flow and b-flow intensities. The high flow intensity c was used to determine the model depth of 0.4 m with the Froude number requirement of $Fr > 0.219$.

3.3 Results

This section presents the results of the parametric study in SSIIM while further quantitative data analysis is discussed in Section 3.4. Results for all eight models and 128 cases were plotted to examine the influence of soil parameters while comparing results with empirical formulae. All scour depth results are available in Appendix A.

3.3.1 Scour depth over time

The first simulations conducted were with the control case of D_{50} = 1 mm and the smallest grain size of D_{50} = 0.05 mm to create scour depth over time plots. These cases were simulated

first to determine the run times for other D_{50} values ensuring that equilibrium depths were reached. Realizing that equilibrium depth times, t_e, are inversely proportion to the grain size the number of cases requiring depth monitoring over time could be reduced (Melville and Chiew 1999). By tracking the depths over time for two cases the equilibrium times found could be applied to larger soils to ensure that the equilibrium depth is reached in the clear water case. The equilibrium run time for the control 1 mm case was used as the runtime for the cases with D_{50} = 2 mm, D_{50} = 5 mm, D_{50} = 10 mm, all stable slopes cases, and all cohesion cases. The equilibrium run time for the D_{50} = 0.05 mm case was used as the runtime for the smaller intermediate D_{50} value cases of 0.1 mm, 0.2 mm, and 0.5 mm. To obtain the maximum scour depths around the pier in SSIIM, results were required to be exported manually exported at timesteps. Results were exported to Paraview for visual inspection of results as the maximum depth of the SSIIM models was not always the local scour hole at the pier. The need to manually export and examine depth data resulted in a tedious time-consuming process for developing depth over time plots. An unknown boundary condition issue would cause the inlet and outlets to experience local erosion deeper than the pier scour as seen in Figure 3.1.

Figure 3.1: Inlet and outlet erosion in model 1b (flow towards right)

Figure 3.1 shows how the inlet and outlet localized erosion depths may exceed the depth of the scour hole located approximately two thirds downstream of the inlet. The amount of erosion produced at the boundaries was generally related to the flow intensity where the larger sediment did not experience this issue. Therefore, result text files could not be simply searched for the lowest depth, the pier scour hole required visual examination to find the maximum depth for each time interval during plotting. Due to the extensive steps required to produce depth over time plots, the scope was limited to depth over time plots for only two D_{50} values. Originally the scour rate used to describe equilibrium depths was going to be the same as the one developed in Chapter 2. In Chapter 2 the SSIIM models were said to have reached equilibrium scour depths once the scour rate fell below *0.6D/24Hours*, where *D* is the pier diameter. The erosion rate was relatively larger

compared to that used by Melville and Chiew (1999) but was used to ensure numerical simulations did not run for weeks. However, the equilibrium erosion rate definition in the parametric study was revised from Chapter 2. The larger piers 3 and 4 produced what appeared as significant scour on the depth over time plots due to their large diameter. For the purposes of evaluating empirical equations in the parametric study, a stricter equilibrium erosion rate definition was warranted. Thus, the equilibrium erosion rate was reduced by 75% to *0.15D/24Hours* for the parametric study. The new equilibrium erosion rate provided a much better estimate of the true maximum depths at piers while only marginally increasing simulation times.

In addition to establishing runtimes the depth over time plots were compared with Melville and Chiew's (1999) temporal scour equation. Previously in Chapter 2, the Melville and Chiew (1999) equation was demonstrated to significantly overestimates pier scour depths just as most empirical equations. The depth over time data for all eight models was presented in Figure 3.2 – Figure 3.9.

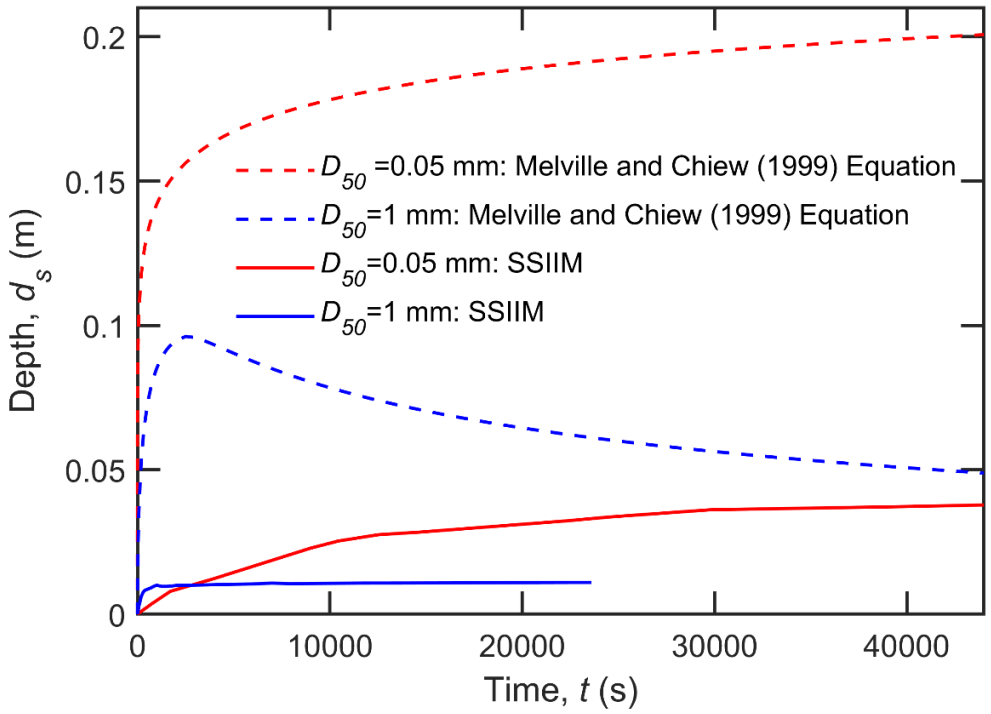

Figure 3.2: Model 1a scour depth versus time

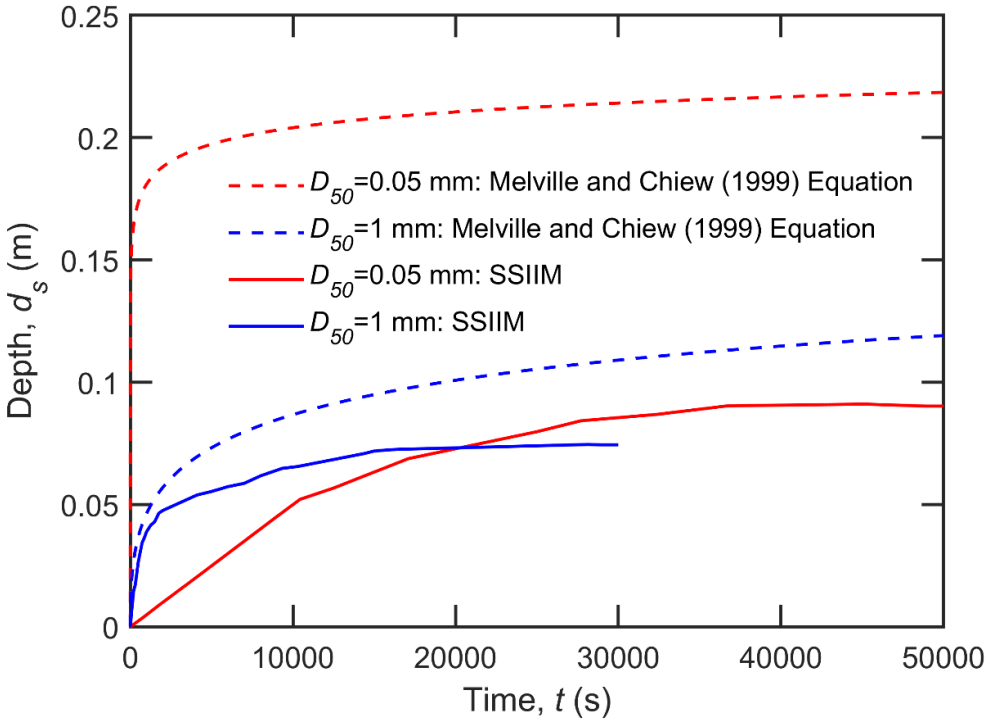

Figure 3.3: Model 1b scour depth versus time

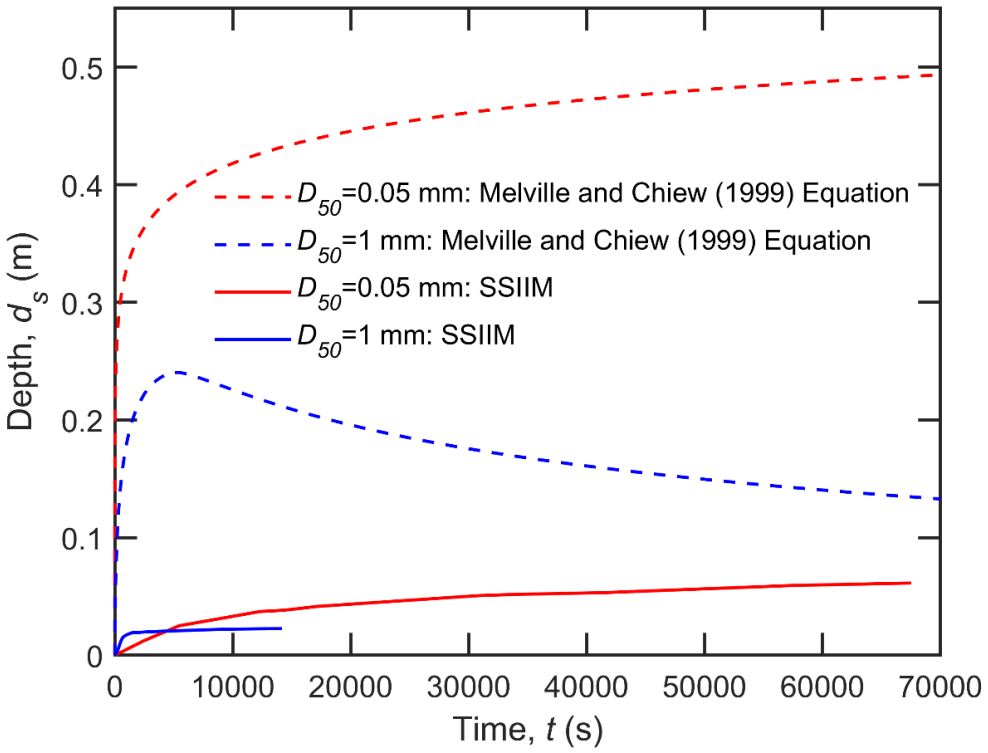

Figure 3.4: Model 2a scour depth versus time

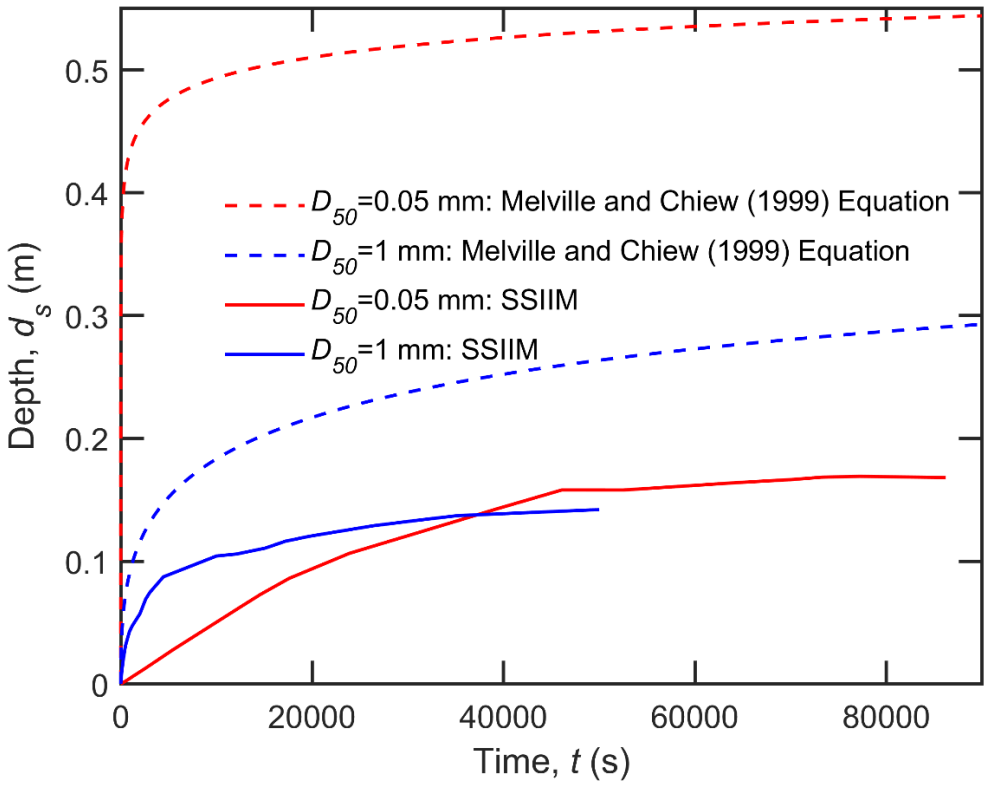

Figure 3.5: Model 2b scour depth versus time

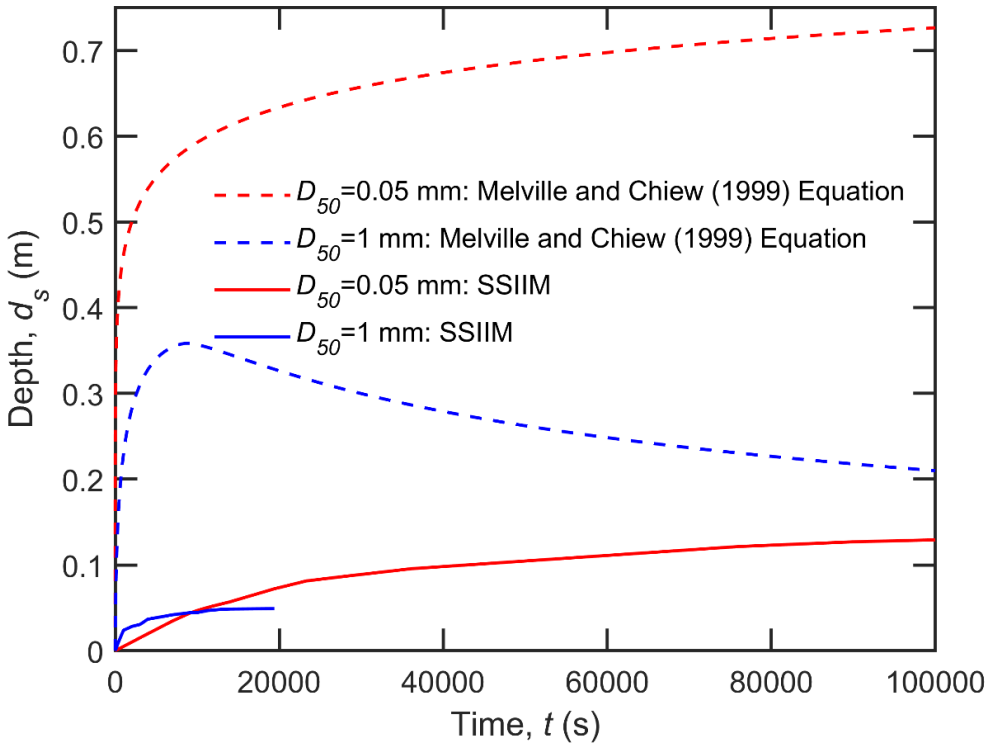

Figure 3.6: Model 3a scour depth versus time

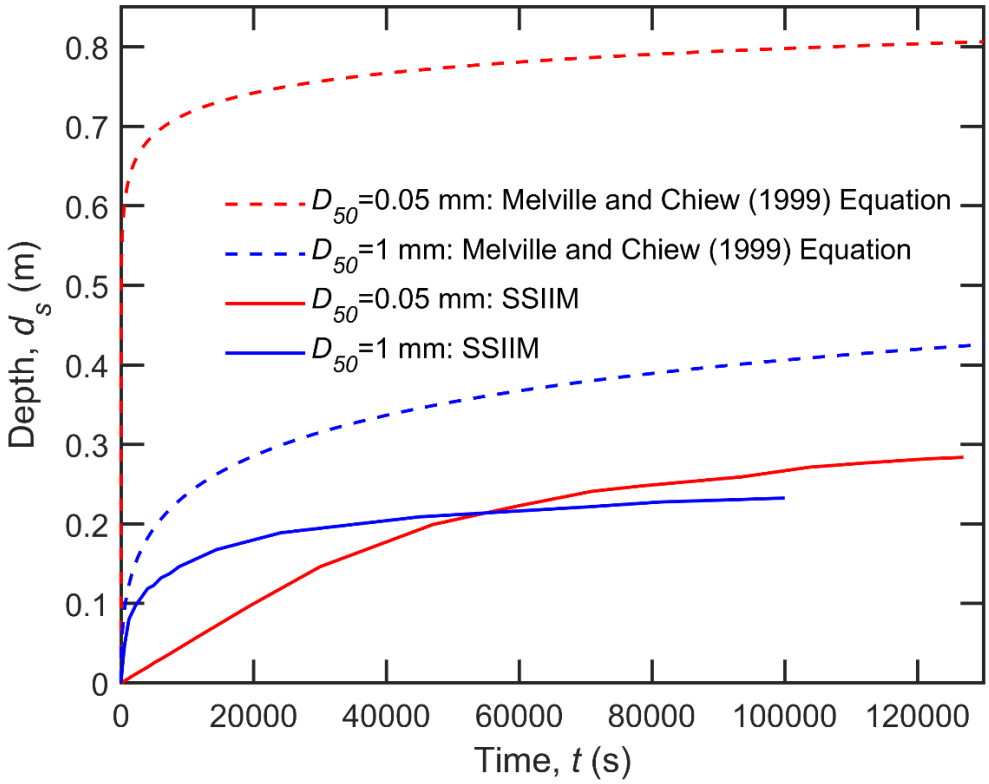

Figure 3.7: Model 3b scour depth versus time

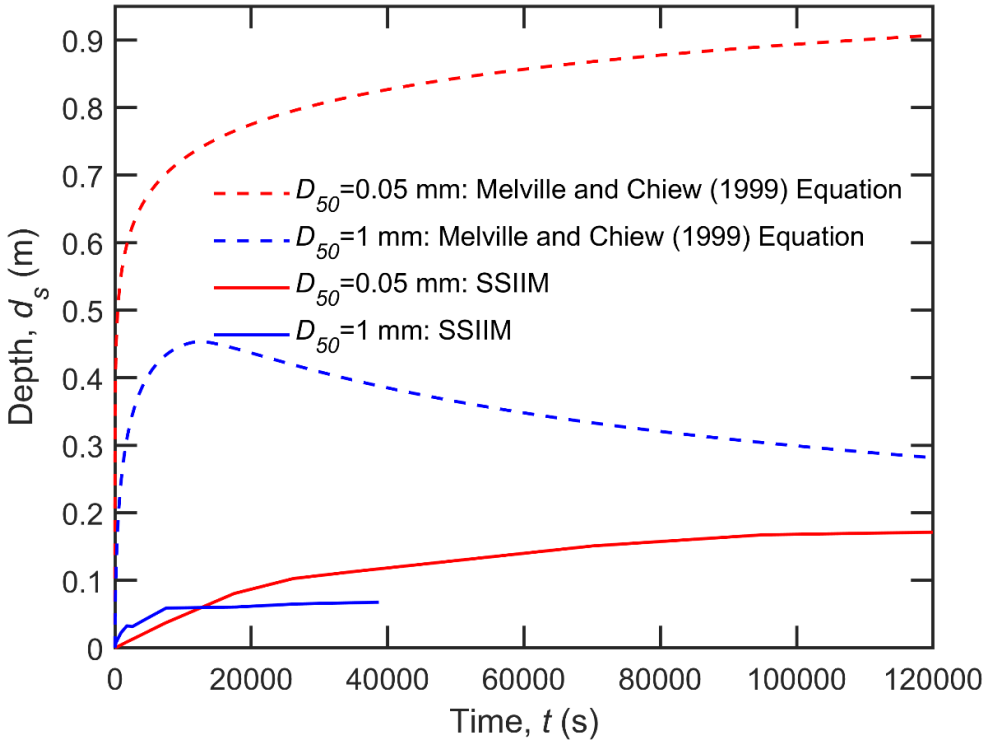

Figure 3.8: Model 4a scour depth versus time

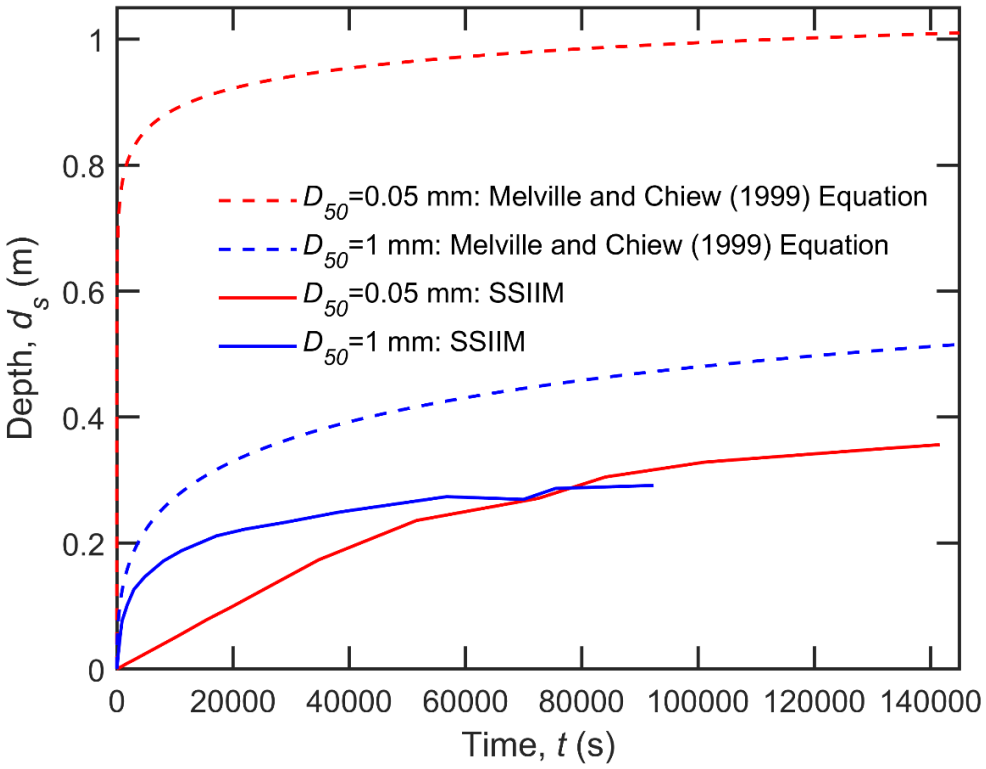

Figure 3.9: Model 4b scour depth versus time

From Figure 3.2 – Figure 3.9 the shape of the curves can grouped in similarity by the flow intensity where all a-flows show a larger difference in scour between 1 mm and 0.05 mm grains. The 1 mm grains with lower flow intensity rapidly reach their equilibrium depth while the 0.05 mm grain take a much longer time. For the b-flows the 1 mm and 0.05 mm curves are much closer to each other in times of equilibrium depths and times. While the maximum or equilibrium scour depths may seem to be the only concern for designing foundation depths, they are not the end of the story. The significance of understanding and modeling scour over time is that it can drastically improve the accuracy of depth predictions for non-unform flows. For a steady flow velocity, the equilibrium depth is a good approximation, however many real bridges experience temporal variations in flows due to weather and flooding events. As discussed in Chapter 1: Section 1.1.3, the probabilistic nature of channel flow means that velocity hydrographs would provide more meaningful data then an average velocity. Methods such as that by Briaud et al. (2007, 2014) seek to calculate the total scour at piers as the superposition of scour over intervals of steady flow. In order to accurately estimate scour over a short interval instead of an infinite amount of time, realistic temporal scour models are required. Basing scour depths on only the maximum flow

velocities leads to severe overprediction of depths and expensive design costs. The non-linear relationships between scour factors does not allow simple averaging of velocity without consequences in accuracy. Thus, with improvements to temporal equations such as Melville and Chiew (1999) and velocity hydrographs scour prediction accuracy would drastically improve. Melville and Chiew (1999) used experimental scour data with sands grains sizes between 0.8 mm to 5.35 mm to develop their temporal equations. While the equation may not be applicable to finer soil around 0.05 mm, it can provide some insight to the depth over time relationships. As expected, the Melville and Chiew (1999) equations overpredict the depths in all cases by a significant amount in all cases. The equilibrium depths and times for the 1 mm and 0.05 mm cases are listed in Table 3.6.

Table 3.6: Equilibrium depths, d_s, and times, t_e

Model	D (m)	D_{50} = 0.05 mm		D_{50} = 1 mm	
		d_s (m)	t_e (s)	d_s (m)	t_e (s)
1a	0.10	0.0372	30000	0.0099	2000
1b	0.10	0.0910	40000	0.0726	17000
2a	0.25	0.0605	60000	0.0222	10000
2b	0.25	0.1691	77000	0.1419	50000
3a	0.50	0.1293	100000	0.0486	14000
3b	0.50	0.2837	126000	0.2275	81000
4a	0.80	0.1713	120000	0.0676	30000
4b	0.80	0.3562	141000	0.2915	92000

The equilibrium times in Table 3.6 were used as run times for rest of the cases in the parametric study. The 1 mm and b-flow cases were the curves to closeted resemble the Melville and Chiew (1999) curves while the 0.05 mm cases showed the largest difference in shape. The main difference was in the initial erosion rates for the 0.05 mm where SSIIM had values so low that the initial erosion was significantly lower than that of the 1 mm model. Unlike the SSIIM results, the initial erosion rates for Melville and Chiew (1999) are inversely proportion to the grain size, so the initial erosions of the 0.05 mm cases were very large. To further investigate the smaller

linear initial erosion rate for the 0.05 mm cases and compare with the 1 mm cases, the results were plotted together by grain size in Figure 3.10 and Figure 3.11.

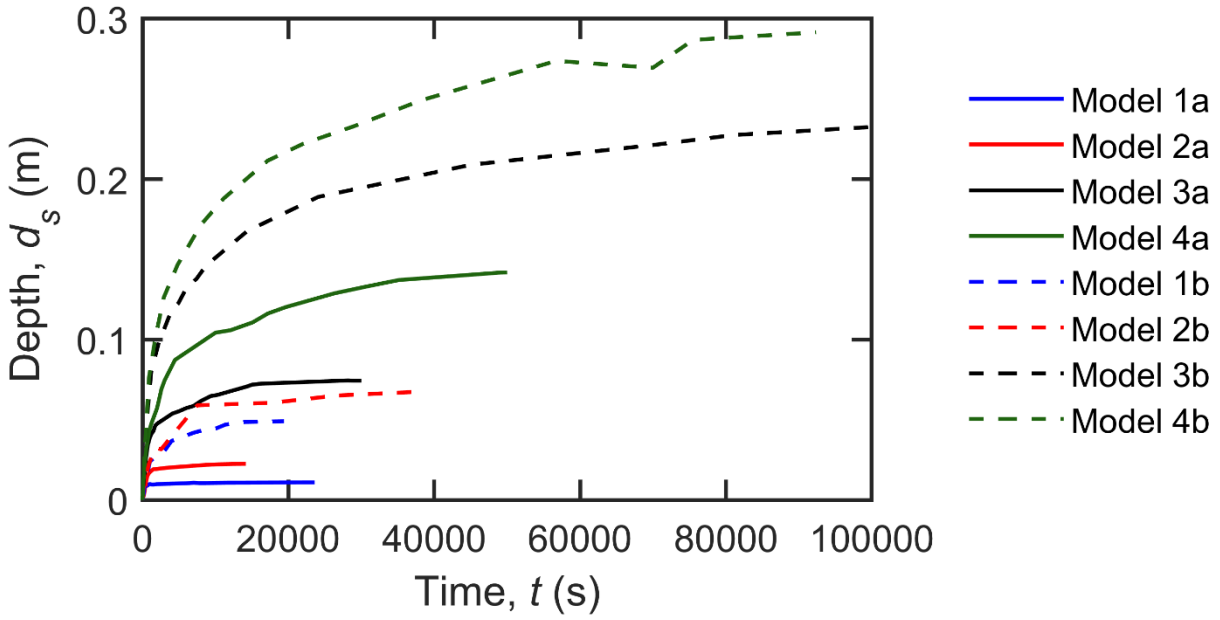

Figure 3.10: Scour depth versus time for D_{50} = 1 mm

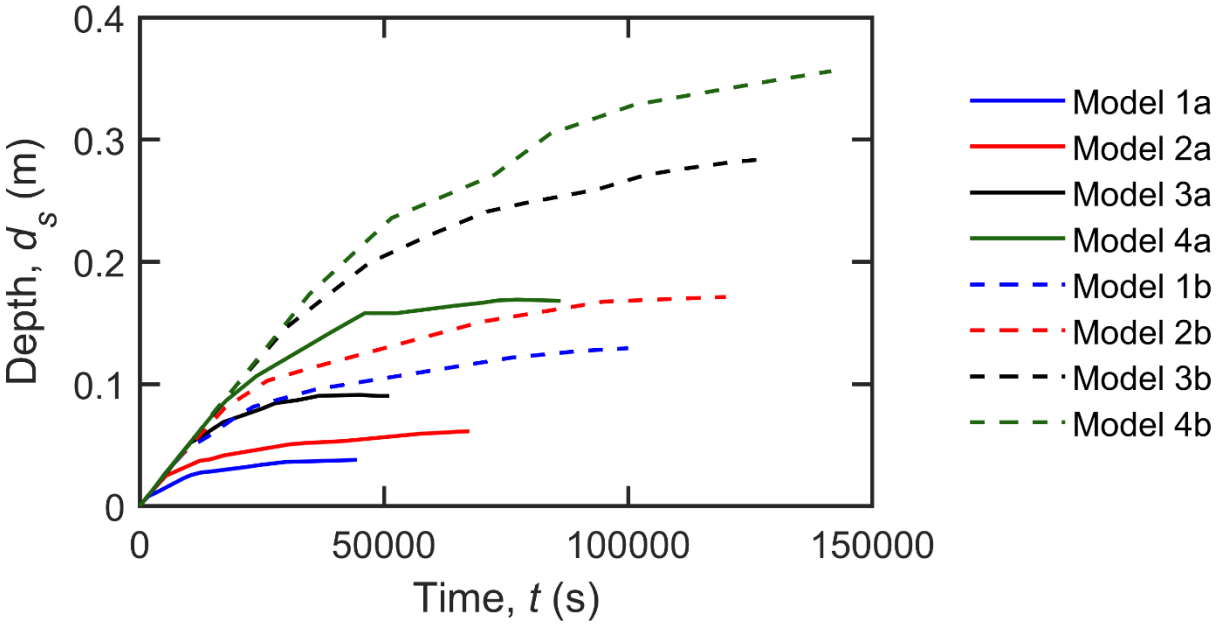

Figure 3.11: Scour depth versus time for D_{50} = 0.05 mm

Without experimental data for the 0.05 mm cases its is difficult to say what the true initial erosion rates should look like. It is assumed that the true value may lie somewhere in between the

SSIIM and the Melville and Chiew (1999) results. From Figure 3.11 it can be seen that all models regardless of velocity and pier size experience the same initial erosion rate of 5.0 x 10^{-06} m/s or D_{50}/10 s, where 10 s was also the numerical timestep. This provides information on how SSIIM's numerical sediment models describes transport. As the active sediment layer was left to the default value of D_{50}, it was the likely control factor for the initial erosion rate with the timestep. Further proof that the active sediment layer controls initial erosion rates was shown in Chapter 2: Section 2.3.2. In the validation of Case 2 in Chapter 2 where two models were simulated in SSIIM. Model B with the larger active sediment layer experienced larger initial erosion rates although the equilibrium depths were close. Thus, while the equilibrium depths are consistent in SSIIM, the temporal modeling requires improvement. Numerical sediment models should be tested and compared with large sets of experimental data to ensure that erosion rate are acute for the provide graduation.

3.3.2 Stable Slope Angle

Investigations into the stable slope angle effects on pier scour were conducted for all eight SSIIM models. Stable slope angles tested ranged between 20° - 40°, while D_{50} and cohesion were constant at 1 mm and 0 Pa respectively. The scour depths for all stable slope angles were plotted together in Figure 3.12.

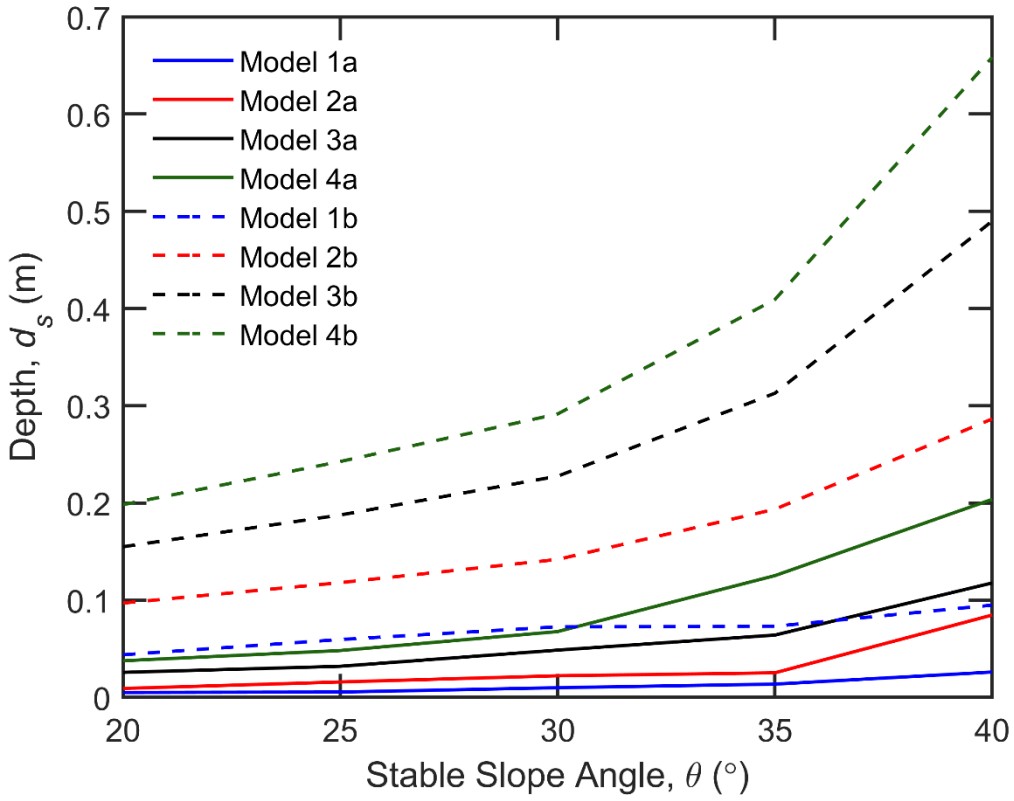

Figure 3.12: Scour depth versus stable slope angle for all models

As expected, scour depth was proportional to the stable slope angles as steeper slopes implied deeper scour depths. Lower slope angles resulted in slope collapses and filling of the scour hole for shallower depths. Inversely the steep slope angles resulted in scour holes holding their shape and maintaining deeper depths over time. Due to the slope collapses with shallower stable slope angles a wider scour hole may be produced. As seen in Figure 3.12 the variation in depth increased with larger piers and faster flow velocities. The largest increase in scour depth occurred when increasing the stable slope angle from 35° to 40°. Further data analyse is conducted in Section 3.4.2 on exactly how much scour depth is impacted by the stable slope angle.

3.3.3 Soil Grain Size (D_{50})

The uniform sediment D_{50} values ranged from 0.05 mm to 10 mm to cover the entire range of sands which is defined as 0.06 mm to 2 mm by the M.I.T soil classification system. The scour depths for all eight models are plotted on Figure 3.13 using the runtimes listed in Section 3.3.1.

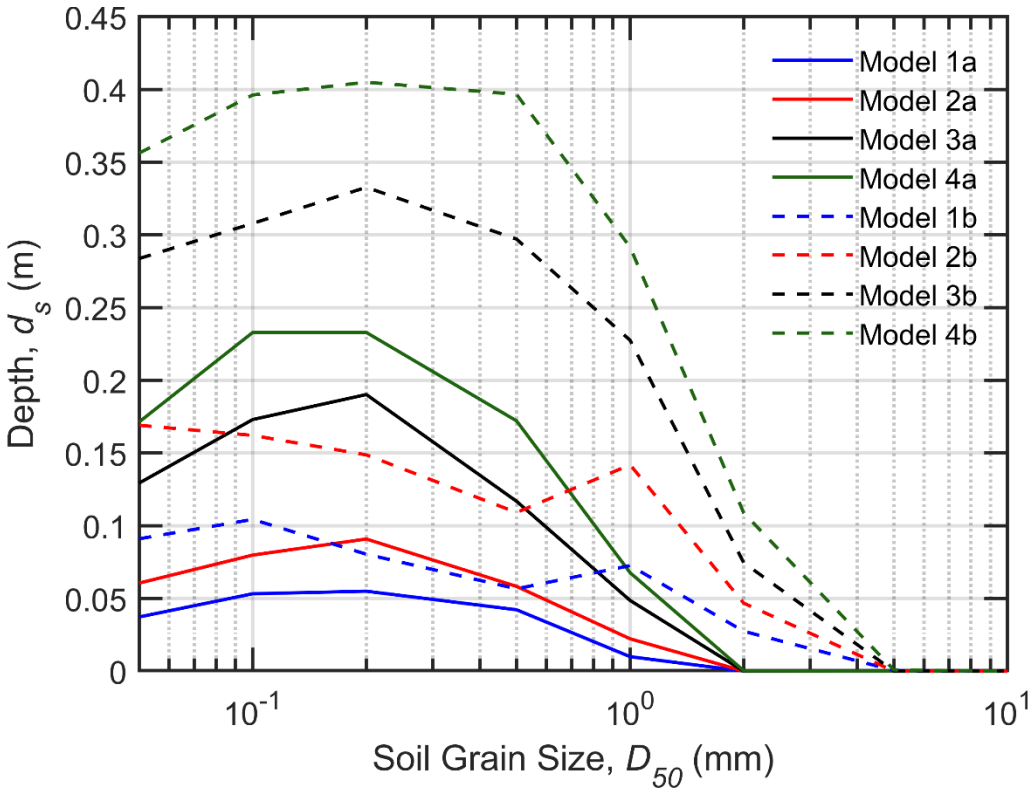

Figure 3.13: Scour depth versus D_{50} for all models

The results for each model ware also plotted individually to compare with the 12 empirical equations. The D_{50} results were ideal for comparing with the empirical equations as D_{50} was the only soil inputs used by some of the equations. The D_{50} tests all used 0 Pa cohesion which was reasonable as clean sands typically will not exhibit any cohesive strength. However, the angle of repose for sands may vary from 20° to 40°, thus so can the stable slope angles (Al-Hashemi and Al-Amoudi 2018). As seen in Section 3.3.2 the stable slope angle had a large impact on scour depths for larger piers and faster flows, so it is important to consider for sands. The decision was made to make 30° the control stable slope angle for the D_{50} tests but the true value for sands may vary. To visualise the range of scour depths which may occur for sands with different repose angles the slope results from Section 3.3.2 were added to the D_{50} plots. The SSIIM scour depth versus D_{50} curves with stable slope data for D_{50} = 1 mm are displayed in Figure 3.14 – Figure 3.21.

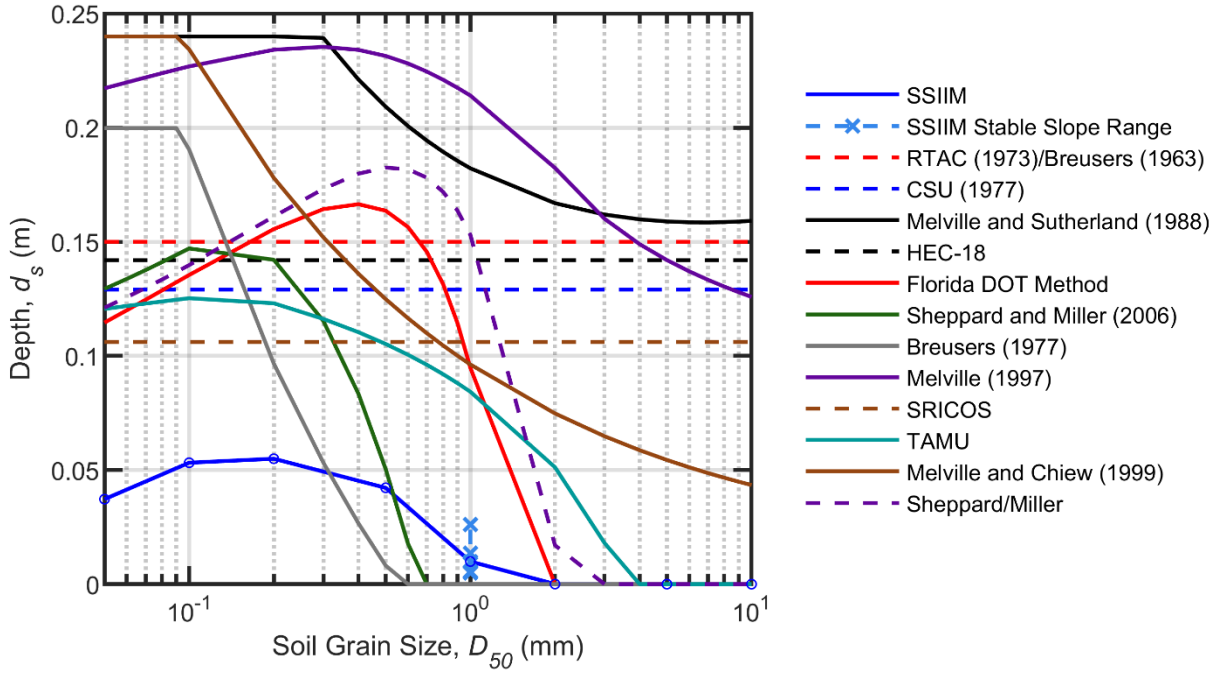

Figure 3.14: Model 1a scour depth versus D_{50} with empirical equations

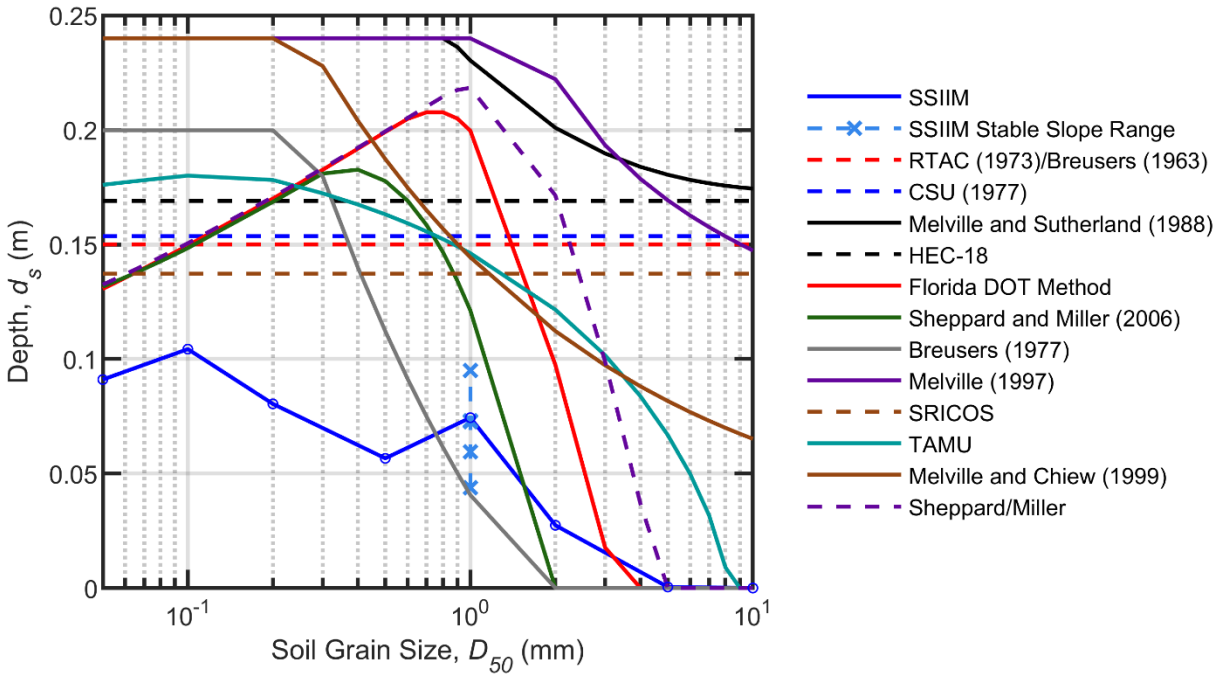

Figure 3.15: Model 1b scour depth versus D_{50} with empirical equations

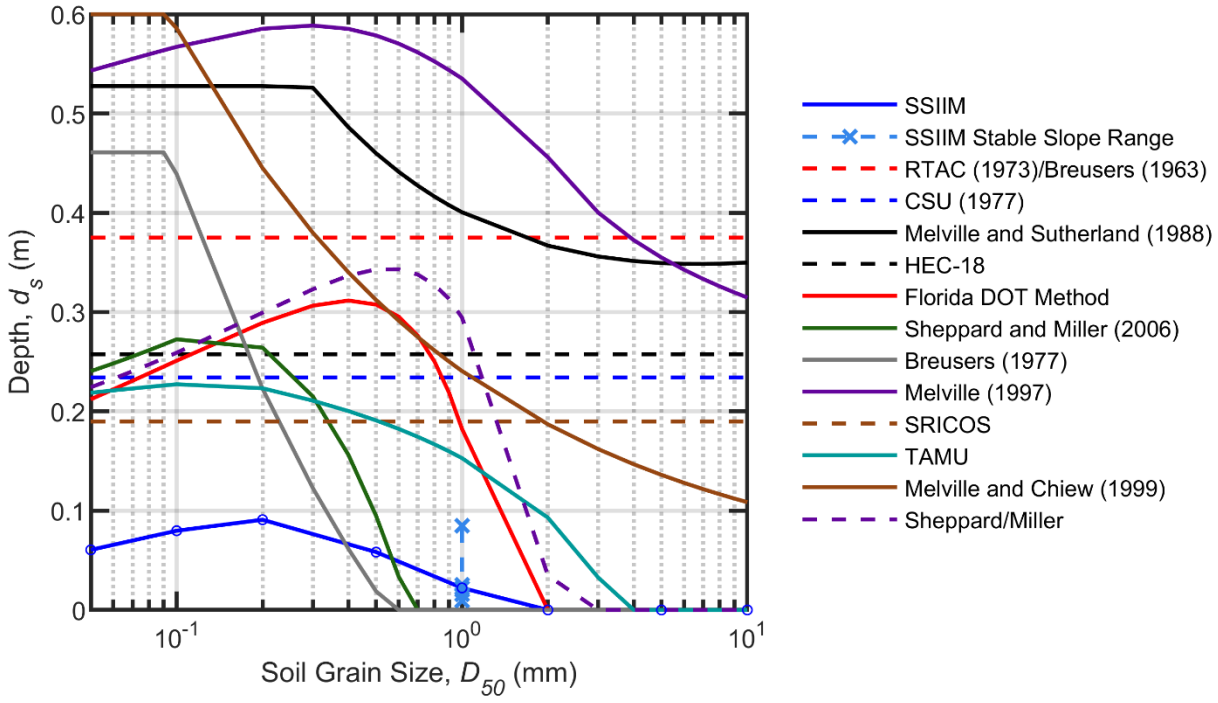

Figure 3.16: Model 2a scour depth versus D_{50} with empirical equations

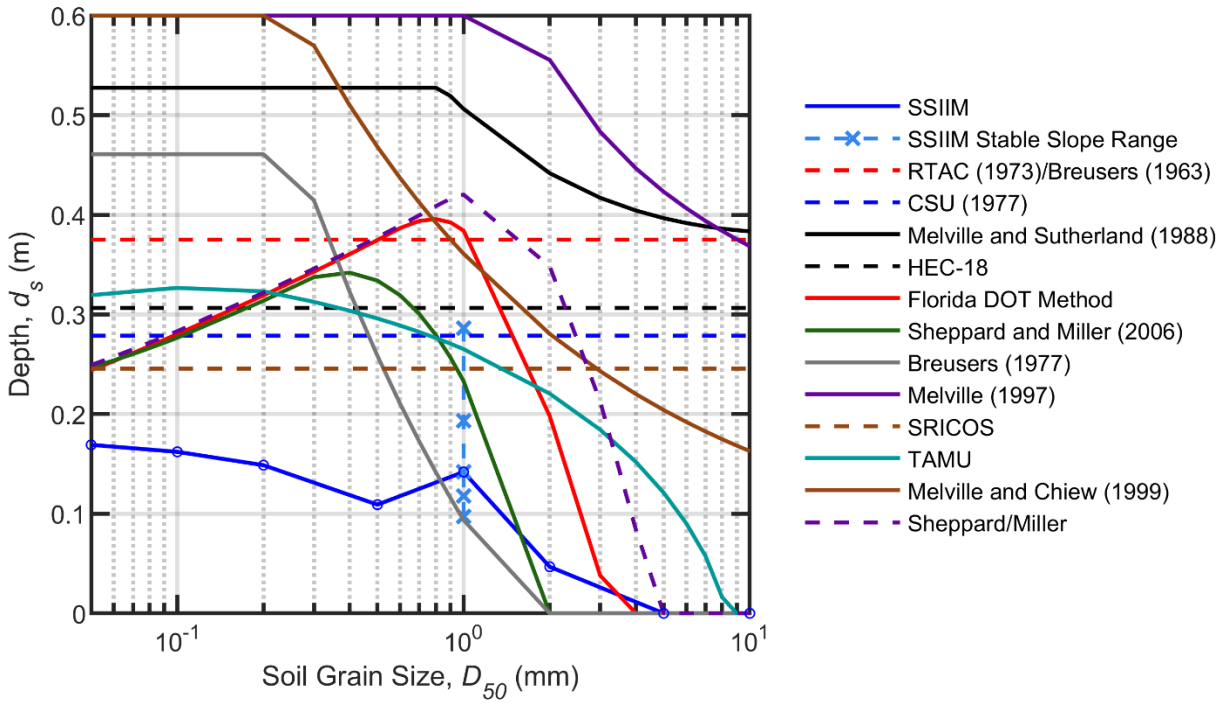

Figure 3.17: Model 2b scour depth versus D_{50} with empirical equations

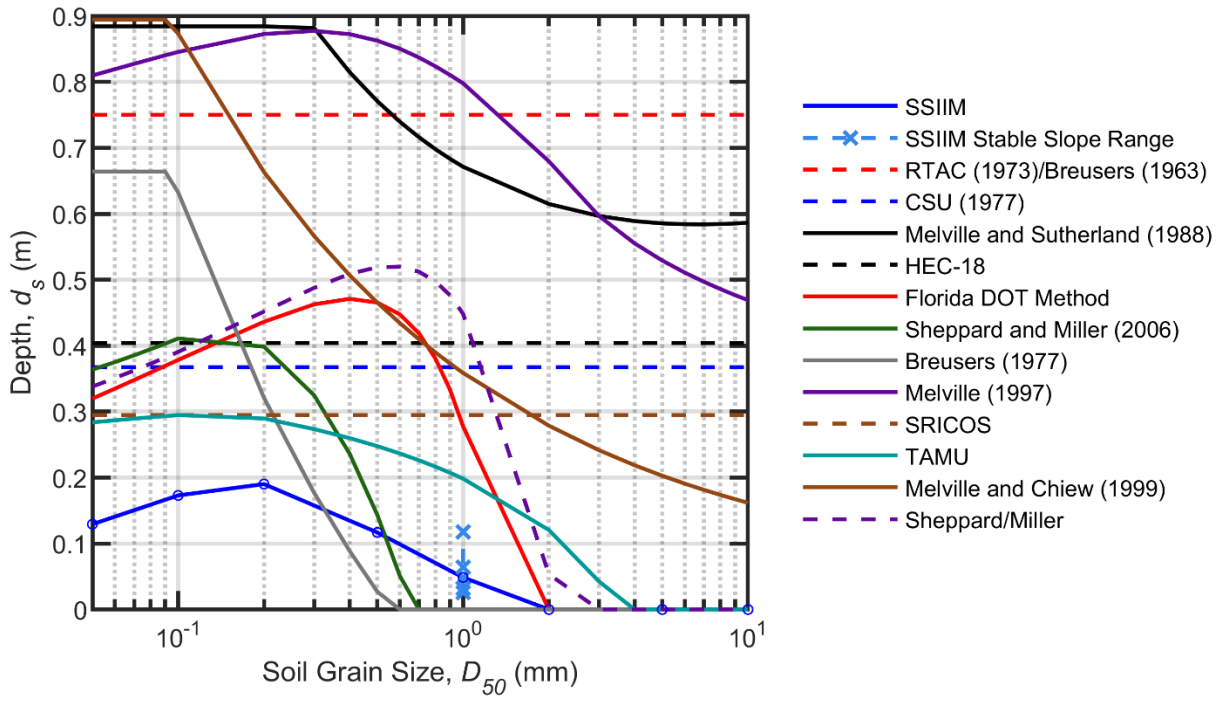

Figure 3.18: Model 3a scour depth versus D_{50} with empirical equations

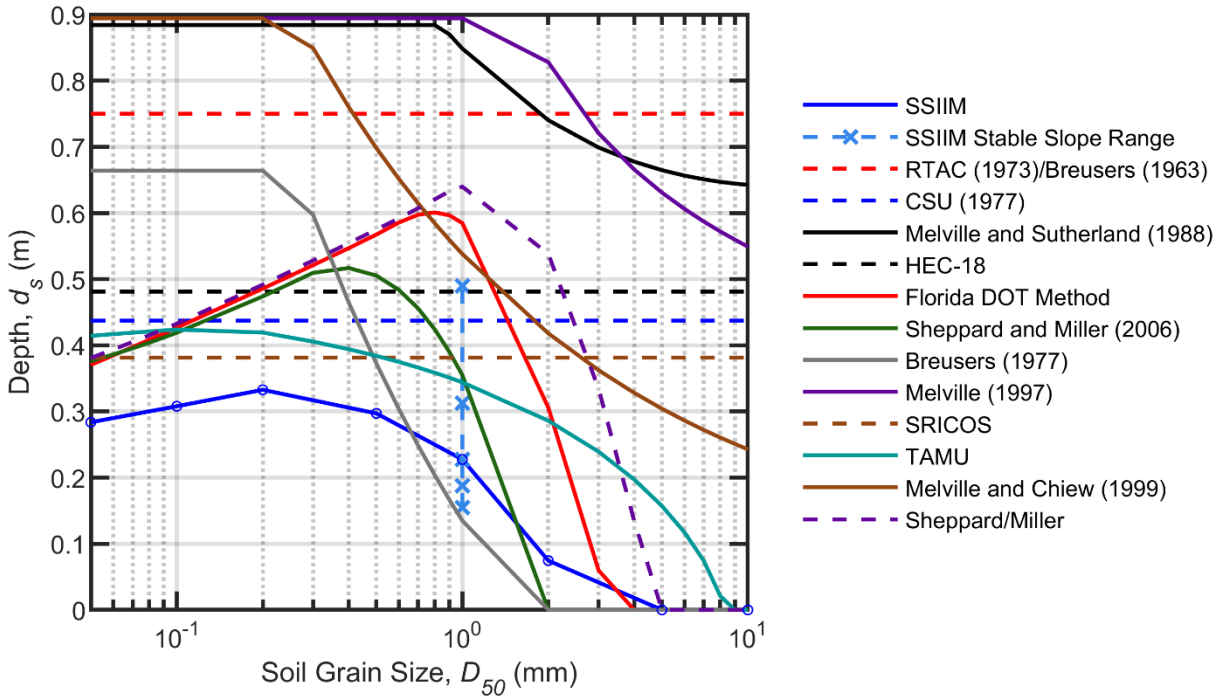

Figure 3.19: Model 3b scour depth versus D_{50} with empirical equations

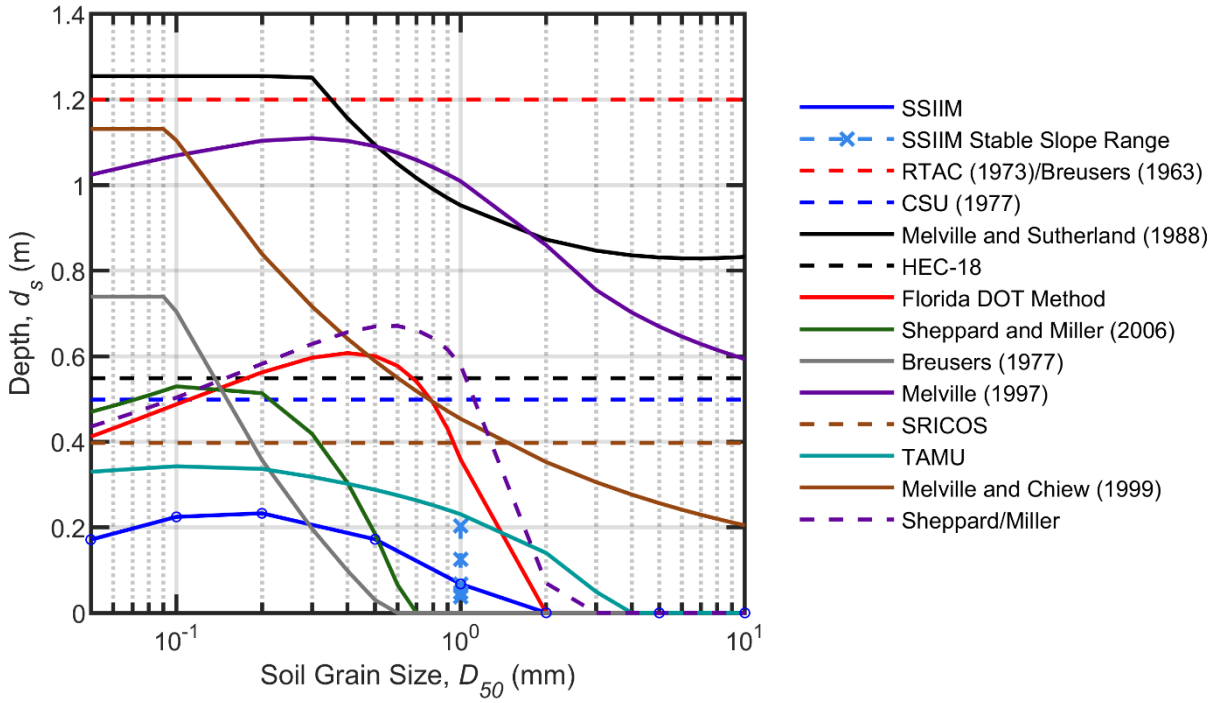

Figure 3.20: Model 4a scour depth versus D_{50} with empirical equations

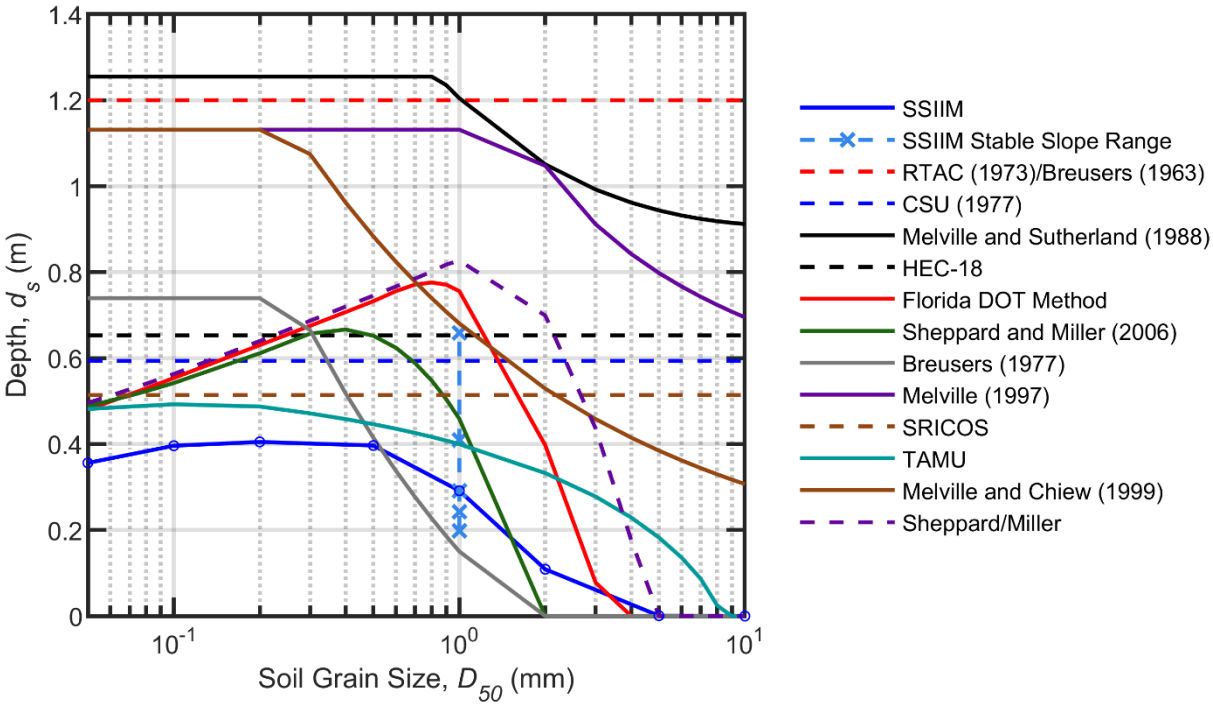

Figure 3.21: Model 4b scour depth versus D_{50} with empirical equations

The results demonstrated that scour in SSIIM was usually overpredicted by most equations. The SRICOS, CSU, and HEC-18 equations provided close estimates while not using any soil parameters. The older RTAC (1973)/Breusers (1963) equations are much too dated and overly conservative. The Melville and Sutherland (1988) and Melville and Chiew (1999) equations not only over predict but also demonstrate a relationship curve between depth and D_{50} opposite of what is observed in SSIIM. SSIIM indicated maximum scour depth between the sizes of 0.2 mm – 1 mm with depths decreasing for larger and smaller grain sizes. The Breusers (1977) equation underpredicted depths too often to be a safe choice. The Melville (1997) curve was able to capture the shape seen in SSIIM but was too conservative for depth estimates. The Sheppard and Miller (2006) equation showed some close matches with SSIIM in terms of the curve shape and which grains sizes produced the largest scour depths. The F-DOT equation was developed as an improvement to the Sheppard and Miller (2006) which is evident with its better match for larger grain sizes with SSIIM results. How ever both the Sheppard and Miller (2006) and F-DOT equation had some minor cases of underprediction for the larger grain sizes. The Sheppard/Miller equation was also an updated version of the Sheppard and Miller (2006) method. The Sheppard/Miller equation appeared have corrected the underprediction by the Sheppard and Miller (2006) method for the median sand D_{50} values. The SRICOS method developed by Briaud was originally used to describe the temporal variation of scour but required data from EFA testing. The SRICOS equation for the maximum depth was simply a function of the flow Froude number and was found to provide a good estimate of scour depth. The empirical equation with no underprediction and the closest match with SSIIM were the TAMU and Sheppard/Miller methods. Further quantitative data analysis is conducted in Section 3.4.1 for the D_{50} cases.

The approximate flow intensities from Table 3.5 can be compared with the results herein. From many methods for predicting scour such as the F-DOT and Sheppard/Miller equations, the point of zero scour depth occurs for flow intensities lower than 0.4. This implied that at a flow intensity of 0.4, the amplification of bed shear stress due to a pier presence increases that flow intensity to around 1.0. The flow intensity of 1.0 occurs somewhere near the upstream corners and is the starting point for the scour hole formation. This behaviour was also observed in SSIIM where there was negligible scour for $D_{50} > 1$ mm with a-flows and $D_{50} > 2$ mm with b-flows. The stable slope study depths were included on the plots to demonstrate how much scour depths may vary for sands of different repose angles. If one were to imagine the stable slope lines acting as

an envelope over the SSIIM D_{50} curve one can get a sense of the depth variations which may occur. The large variation in depths emphasize the need for taking into consideration soil repose angles when estimating pier scour depths. While the TAMU method performed well with no underestimation, there was cases with potential underestimation of scour depth. In models 2b, 3b and 4b the high stable slope models in SSIIM reported scour depths larger than those estimated by the TAMU method. Thus, even the best methods for estimating pier scour can benefit from the inclusion of cohesion and angle of repose effects. For sands of higher stable slope or repose angles the Breusers (1977) and Sheppard and Miller (2006) are also more likely to under predict scour depths.

3.3.4 Cohesion

The cases thus far have used 0 Pa of cohesion with the sediment of focus being clean sands. However, non-uniform sands may contain a little clay or silt content leading to some cohesive strength. To investigate the effects cohesion due to fines in sands, tests were performed with cohesive strength ranging from 0 Pa - 0.5 Pa. The tests were conducted with the control values of with D_{50} = 1 mm and stable slope angle of 30°. The results for all eight SSIIM models are plotted in Figure 3.22.

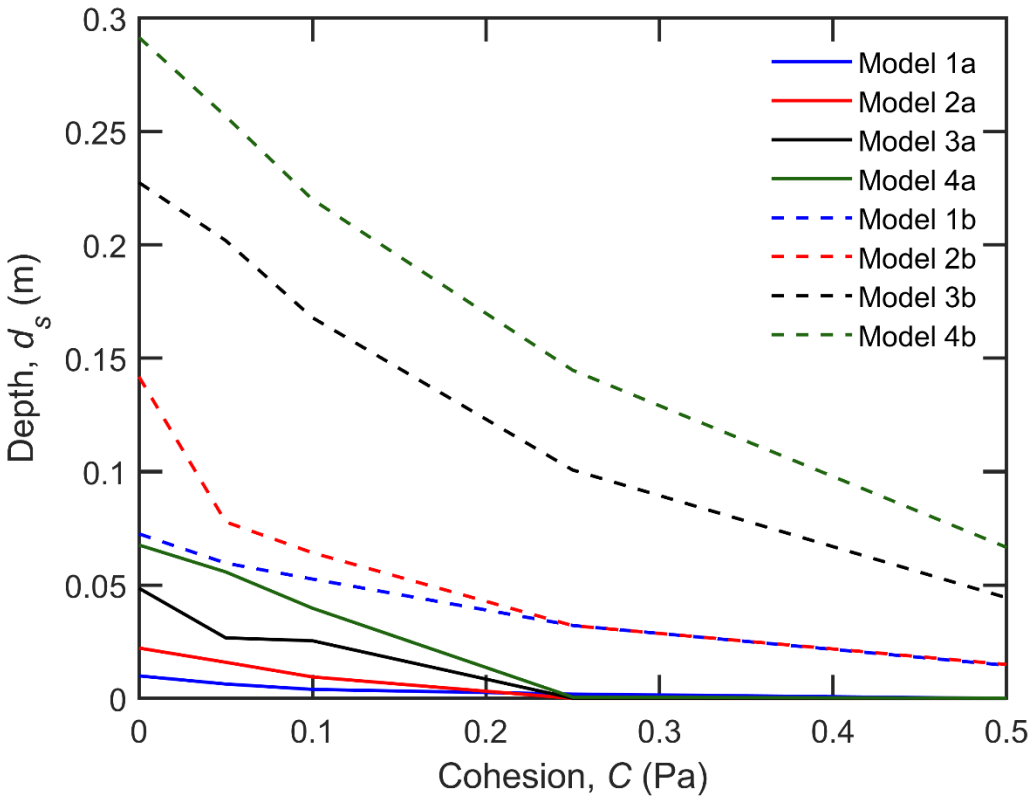

Figure 3.22: Scour depth versus stable slope angle for all models

Adding cohesion to the models resulted in dramatic scour depth decreases. Further data analysis in quantifying the depth variation is shown in Section 3.4.2.

3.4 Data Analysis and Discussion

The results of the parametric study presented in Section 3.3 are further analysed quantitatively in this section. Error analysis was conducted for the empirical equations to score the performance and provide recommendations for engineers on which methods to use. Depth variation with soil parameters was examined to further emphasize the need for methods to include more soil parameters for accurate depth estimates. Lastly a discussion is made on the current methods for numerically modeling scour in SSIIM and which improvements are recommended for future research.

3.4.1 Empirical Equations Versus SSIIM

This section seeks to quantitatively express the results of the D_{50} study presented in Section 3.3.3. The D_{50} cases from SSIIM were used for the error analysis of the 12 empirical equations.

Only D_{50} cases were used because it was the only soil parameter used in any of the empirical methods. From the figures in Section 3.3.3 it was apparent that the TAMU equation was the best performing while the older RTAC (1973)/Breusers (1963) and Melville and Sutherland (1988) equations were much too conservative. To determine the exact error in depth prediction for each empirical equation, the SSE (sum of the squares error) was calculated for each equation. The SSE for each equation was calculated using the formula

$$SSE\ \% = \frac{\sum\left(d_s{}^{SSIIM} - d_s{}^{Equation}\right)^2}{\sum\left(d_s{}^{SSIIM}\right)^2} \times 100 \tag{3.1}$$

where d_s is the scour depth obtained from SSIIM and the empirical equation. A table of all errors calculated for each model and equation is included Appendix B. In addition to the total error represented by the SSE, the underprediction of each equation was addressed. The underprediction of scour must be avoided as its disastrous effects are much worse than expensive overprediction. To calculate the UE (underprediction error) for each case the following expression was used

$$UE\ \% = \frac{\sum\left(d_s{}^{SSIIM} - d_s{}^{Equation}\right)}{\sum(D)} \times 100 \tag{3.2}$$

where d_s is the scour depth obtained from SSIIM or the empirical equation and D is the pier diameter. An important note to remember is that these errors are not actual error relative to site measurements but differences from SSIIM numerical results. Once the SSE and UE was calculated by model and equations, all model results were averaged for each equation and plotted in Figure 3.23.

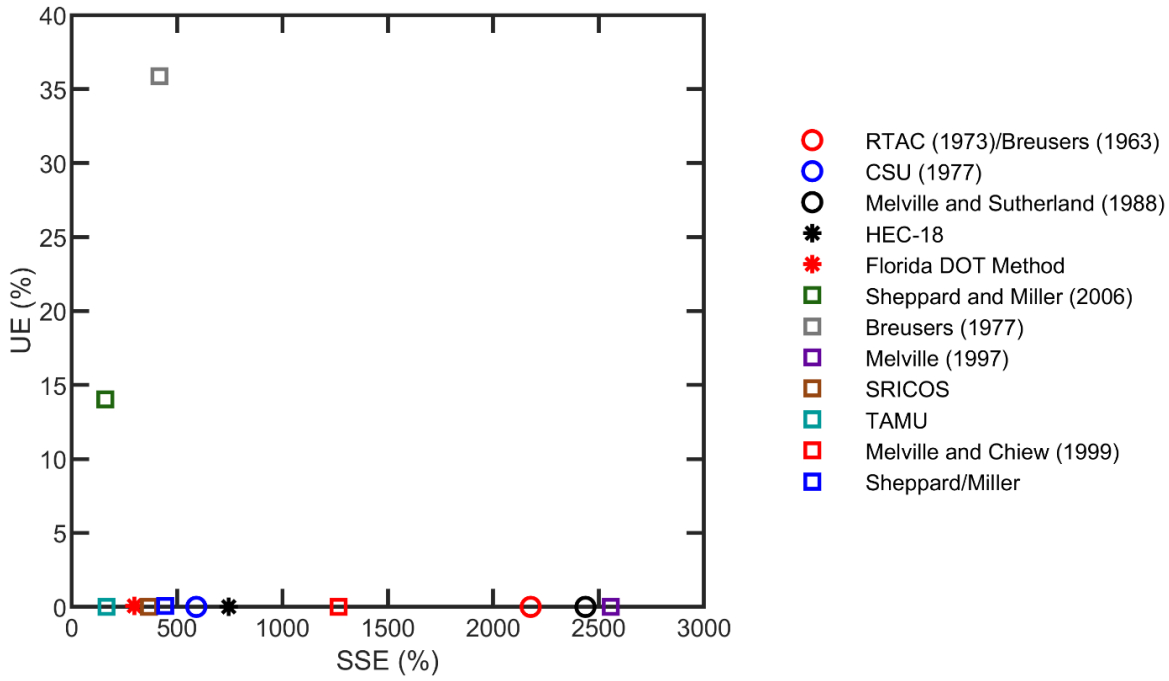

Figure 3.23: SSE and UE for empirical pier scour equations

In Figure 3.23, the bottom left corner represents good performance while the top right indicates poor performance. Right away the Sheppard and Miller (2006) and Breusers (1977) methods are not recommended for use due to significant underprediction of scour depths. As previously discussed, the best performing equation for predicting pier scour depths was the TAMU equation by Briaud et al (2014). Some of next best were the F-DOT and HEC-18/CSU (1977) equations which are currently recommended by the FHWA as discussed in Chapter 1: Section 1.2.1. With more SSIIM data points the SSE and UE could be better defined by being able to integrate the exacts areas of errors on the d_s versus D_{50} plots. From the plots in Section 3.3.3 the F-DOT equation may exhibit more underprediction error for larger D_{50} values while the Sheppard/Miller equation avoids this. The Sheppard/Miller provides a safer alternative to the F-DOT equation which may underpredict scour for larger grain sizes as seen in Section 3.3.3. From Chapter 1: Section 1.2.1 the MTO drainage manual had recommended the use of the CSU (1977), Melville and Sutherland (1988) and RTAC (1973)/Breusers (1963) equations. While the CSU (1977) performed fine, the other two equations were observed to significantly overestimate scour depths in SSIIM. The D_{50} versus depth plots in Section 3.3.3 included the stable slope study results to demonstrate how much scour depths may vary for different angle of repose. As with the different stable slope angles, the assumptions, and sources of potential errors in SSIIM may have

shifted the SSIIM result from what may be true experimental scour depths. While the exact magnitude of error may be incorrect, the relative errors between the equations is useful. Thus, the SSIIM curve shapes and relative errors are reliable for evaluating the performance of equations.

3.4.2 Variation in Scour Depth with Stable Slope Angle and Cohesion

This section discusses how much scour depth may vary with soil parameters not considered by any empirical equations. While there is not enough data to develop new equation or correction factors, general conclusions are made. The results presented in Section 3.3 demonstrated that both the stable slope angle and cohesion had considerable impacts on pier scour depths. A soils stable slope angle is indicative of its repose angle, and its cohesive strength is a function of the amount of fines present. The stable slope angle controls scour hole shapes and depths while the cohesion reduces scour depths. The variation in scour depth from the control soil parameter depth was calculated using the formula

$$Variation\,\% = \frac{{d_s}^{test} - {d_s}^{control}}{{d_s}^{control}} \times 100 \tag{3.3}$$

where ${d_s}^{test}$ is the scour depth with varied parameters and ${d_s}^{control}$ is the scour depth with control soil parameters. The depth variations with the stable slope angle deviation from the control 30° are listed in Table 3.7.

Table 3.7: Scour depth variation with stable slope angle

Model	Diameter (m)	Depth Variation from 30° Stable Slope Angle			
		20°	25°	35°	40°
1a	0.10	-49.5%	-45.3%	37.3%	162.4%
1b	0.10	-39.6%	-18.0%	0.7%	30.8%
2a	0.25	-59.0%	-28.7%	13.6%	281.3%
2b	0.25	-31.6%	-16.8%	36.4%	101.9%
3a	0.50	-47.1%	-34.2%	31.9%	142.2%
3b	0.50	-31.9%	-17.5%	37.5%	115.3%
4a	0.80	-44.4%	-28.8%	85.1%	201.1%
4b	0.80	-32.0%	-16.8%	40.4%	125.9%
Average		-41.9%	-25.8%	35.4%	145.1%

The depth variations in Table 3.7 quantify what was visually presented in Figure 3.12. Lowering the stable slope angles to 20° reduced scour depths by an average of 45.2% while a steeper stable slope of 40° increased depths by a substantial 153.3% on average. It cannot be said that these results are a full representation of repose angle effects without also investigating the reduction of critical shear stress on slopes. However, the results are useful as the Brooks (1963) formula provided good matches in results during the validation in Chapter 2. Therefore, the larger potential variation in scour depths with stable slope angles demonstrates the importance of the repose angle when estimating pier scour depths. The depth variations with soil cohesion from the control 0 Pa of cohesive strength are listed in Table 3.8.

Table 3.8: Scour depth variation with cohesion

Model	Diameter (m)	Depth Variation from 0 Pa Cohesion			
		0.05 Pa	0.1 Pa	0.25 Pa	0.5 Pa
1a	0.10	-36.1%	-60.1%	-81.0%	-100.0%
1b	0.10	-17.8%	-27.5%	-55.7%	-79.9%
2a	0.25	-28.3%	-57.4%	-100.0%	-100.0%
2b	0.25	-45.2%	-54.7%	-77.4%	-89.5%
3a	0.50	-45.1%	-47.7%	-99.9%	-100.0%
3b	0.50	-11.3%	-26.2%	-55.7%	-80.5%
4a	0.80	-17.6%	-41.2%	-99.2%	-99.9%
4b	0.80	-11.9%	-24.5%	-50.4%	-77.2%
Average		-26.6%	-42.4%	-77.4%	-90.9%

As the cohesion acted to increase the critical shear stress the increasing cohesion lowered scour depths drastically. Whether through soil gradation analysis or laboratory testing for cohesive strength, a soil's cohesion should be used in predicting pier scour depth. Ignoring soil cohesion may lead to severally overestimating scour depth and expensive design recommendations.

3.4.3 Live-Bed Scour Depth Over Time Example

An observation made from Figure 3.13, d_s versus D_{50}, was that the SSIIM curves for b-flows were different from the a-flows. The a-flow curves were smoother and resembled the TAMU curve while the b-flows saw a dip in depths for D_{50} values between 1 mm – 5 mm. The reason for

the lower scour depths in that range was due to the fact that the sediment was in the live bed condition. Table 3.5 listed the flow intensity where all grains smaller than 1 mm were in the live bed range for the b-flow intensity. The runtimes for those sediments were based on the equilibrium time, t_e, for the 0.05 mm case to ensure that equilibrium depths would be meet for larger grains. However, the depth over time in live bed scour does not reach a steady state solution like clear water conditions. From Figure 1.5, the difference between clear water and live-bed scour over time was illustrated. Live-bed scour will reach a peak depth and then experience cyclic behaviour due to patterns of erosion and deposition occurring. Therefore, the plotted depths in Figure 3.13 were not the equilibrium depths nor the peak depth but rather a random depth occurring after the peak. Depth over time plots were not created for all cases as only clear water scour was within the scope. To illustrate an example of a live-bed scour over time the 0.5 mm case for Model 1b was presented Figure 3.24.

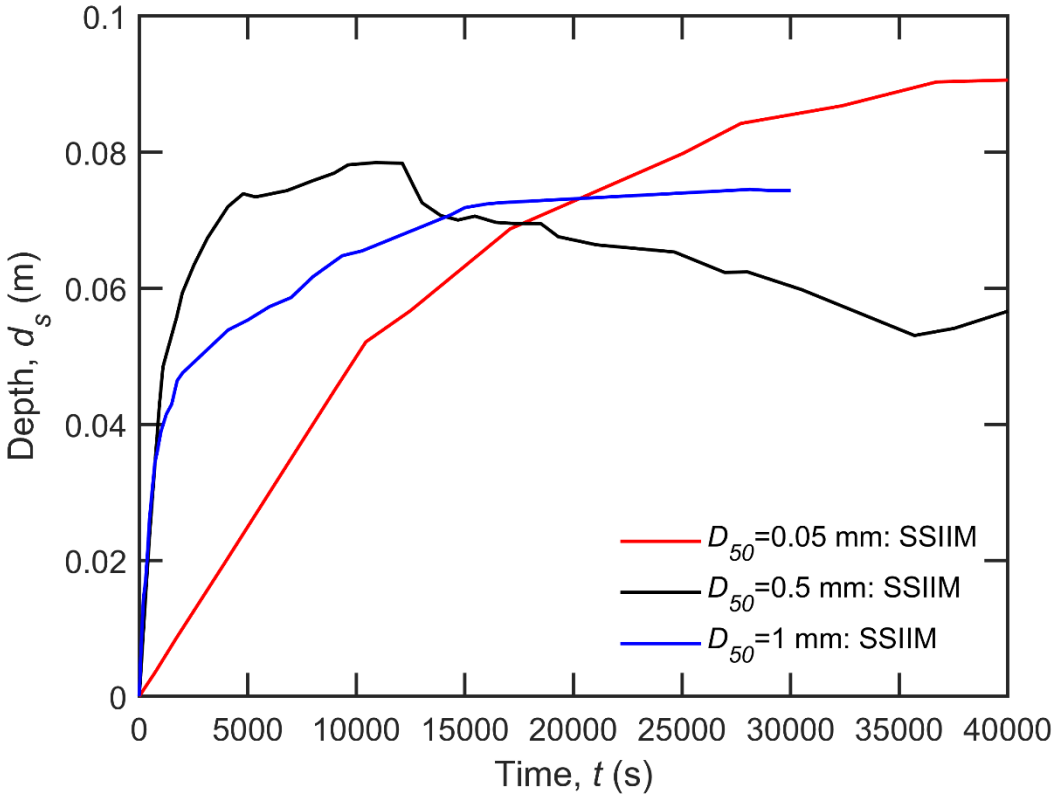

Figure 3.24: Live bed scour in model 1b

The live-bed behaviour is evident with the 0.5 mm curve with its peak, dip, and then increase in depth. The 0.5 mm curve peaked at 10900 s with a depth of 0.0785 m, dipped to a

depth of 0.0530 m at 35700 s and then the simulation was stopped at 40000 s for a recorded depth of 0.0566 m. The variation in depth between the live bed peak and trough was 0.0254 m, which is around 25% of diameter or 32% of the peak depth. Although the 0.05 mm case was stopped once it reached its supposed equilibrium depth it was likely at the initial peak depth. If the 0.05 mm case was ran for longer times it would be expected to decrease in depth and experience cyclic behaviour just as the 0.5 mm case. The error in equilibrium depths presented in Section 3.3.3 was not of concern for the purposes of the present investigation. As the primary goal was to evaluate the performance of empirical equations the change in relative error does not impact results of the study. The relative errors would not change so the empirical equation performances and recommendations would remain the same. While the curves for the 1b and 2b models very strongly exhibited this behaviour it was not observed for the 3b and 4b models with larger piers.

3.4.4 Numerically Modeling Pier Scour in SSIIM

This section summarises the numerical scour modeling capabilities in SSIIM after analyzing the results of the parametric study. The algorithms and solvers in SSIIM were discussed in detail in Chapter 2. While SSIIM was found to produce satisfactory matches in scour depths during the validations in Chapter 2 it is not yet an ideal numerical scour modeling tool. The three validation cases from Chapter 2 had produced modest errors of 0.8%, 12.6 % and 0.2% in predicting the maximum scour depths. The validations cases consisted of sands with D_{50} values of 0.385 mm for Case 2 and 1.8 mm for Cases 3 and 4. The errors in scour depth results from the present parametric study may be assumed to be in the range of 0.2% - 12.6% although the confidence is low without experimental data to compare for every case. A constraint in SSIIM's fluid modeling capabilities is that the RANS solver is the steady state algorithm SIMPLE. The SIMPLE algorithm neglects transient terms which model the cyclic wake vortices sheading responsible for much of the downstream scour. The addition of a transient RANS solver such as PISO would reduce scour underestimation in SSIIM at both the downstream and upstream faces of piers. Another limitation on the present study was the construction of the computational grids to avoid lengthy simulation times. Due to the limited meshing options in SSIIM a uniform grid was used which required a reduction in grid refinement around the piers. The coarser than ideal grid around the piers may have resulted in minor errors in scour hole shapes and depths. The only major simulation error observed in SSIIM was the inlet and outlet boundary erosion discussed in

Section 3.3.1. With the adequate inlet and domain lengths used in the present study the inlet erosion should not have impacted the scour holes results.

The sediment transport in SSIIM was modelled with Van Rijn's formula and Shields's Diagram (1936) described sediment critical shear stresses. An alternative to using these formulae and adaptive meshing would be to model the sediment bed using DEM or Smoothed Particle Hydrodynamics (SPH). However, a CFD and DEM coupled software would be required with all relevant soil parameters captured. A DEM sediment model would be computationally expensive but could provide more accurate sediment modeling during scour. SSIIM's reliance on simple empirical sediment modeling algorithms may limit its scour modeling capabilities especially in the modeling of slope effects. The modeling of cohesion in SSIIM was limited to its effects on the critical shear stress which was well documented. However, SSIIM neglected cohesion influences on a soil's failure mode during erosion with its active sediment layer input. The chunk-by-chunk erosion which occurs in clays and silts is unique as sands and gravels erode grain by grain. The initial erosion rates for smaller D_{50} values like the 0.05 mm case was rather low which may not be realistic. Finer soils may erodes faster then shown by SSIIM due to the removal of larger chunks of soil by the flow. Further studies into erosion rates of finer soils is recommended for developing sediment models for numerically modeling scour. A novel DEM should include the effects of cohesion through the transport process to accurately model the tempol evolution of scour holes. The importance of modeling temporal scour comes up when using velocity hydrographs to calculate scour at different intervals with non-uniform flow. An important soil parameter for modeling local scour holes was the repose angle of a soil. The repose angle is used to describe a soil's shear strength and sloping behaviour. However, SSIIM did not include explicit inputs for the repose angles because its effects were modeled with two separate algorithms. The Brooks (1963) formula reduced the critical shear stress of soil on sloped beds while a second algorithm modeled sand slides. The sand slides algorithm was found to successfully model scour hole slopes using inputted stable slope angles in Chapter 2. The empirical Brooks (1963) parameters were kept constant with the values which provided the best match in results in Chapter 2. The critical shear stress reduction model on slopes should be replaced by a more robust model that factors in a soil's repose angle instead of just empirical parameters. An ideal sediment model would use an inputted repose angle to model both sand slides and critical shear stress reduction on slopes.

Further studies into the slopes of local pier scour hole are required to fully understand how to numerally model sediment slopes.

3.5 Conclusions

This chapter focused on conducting a parametric study in SSIIM on clear water pier scour in clean sands. Four cylindrical piers of varying diameter and two flow velocities were explored alongside 16 types of sands for a total of 128 numerical simulation cases. The first objective was to quantify the effects stable slope angles and cohesion on pier scour depths as these parameters are not considered by current methods. The control soil parameters were set to a median grain size of 1 mm, stable slope angle of 30° and cohesive strength of 0 Pa. Testing of stable slope angles between 20° and 40° revealed a variation in scour depth of -41.9% to +145.1%. These large variations in depth with stable slope angles revealed the enormous influences the repose angle has on bridge scour hole shapes and sizes. The exclusion of repose angles from methods for estimating pier scour was shown to have been a probable cause for past scour depth underestimation, especially for larger grain sizes. Testing cohesive strengths between 0 Pa and 0.5 Pa resulted in significant scour depth reductions with 0.5 Pa cohesion reducing scour by -90.9% on average. Cohesion acted to increase soil critical shear stress and its exclusion from scour prediction methods would results in overly expensive design recommendations. The second objective was to use the D_{50} study results to evaluate the performance of empirical equations for predicting pier scour. The best performing and recommended equation for predicting pier scour was found to be the TAMU (Briaud 2015a, 2015b) method based on total and underprediction error analysis.

Chapter 4: Concluding Remarks

This thesis covered a review of contraction and local scour which occur at bridge foundations in channels. Scour theory and prediction methods were discussed in detail along with the influencing factors. The research scope was focused on addressing the prediction of local scour depth at bridge piers. A major gap in existing methods for predicting bridge scour was the consideration of soil parameters other than grain sizes. Methods such as the Sheppard/Melville (2011) and HEC-18 equations were documented to have good performance but could be greatly improved by incorporating soil parameters. Reviewing published literature revealed that the most significant soil parameters on scour are grains size, gradation, cohesion, and the angle of repose. These soil parameters were found to control the inception of motion, erosion behaviour, and shape of scour holes which all control maximum scour depths at piers. Furthermore, most methods have been derived from limited experimental scenarios in which scaling effects contribute to inaccuracies when predicting field scour with larger structures. Thus, the current methods in design tend to overly predict scour leading to expensive construction costs. Additionally, the lack of soil parameter inputs has led to underprediction of scour depths resulting in scour becoming the most common cause for bridge failures. To develop better methods of predicting scour further research was required into the influence of soil parameters on scour depths.

For full control of parameters and no scaling effects numerical simulation was the optimal approach. The software SSIIM was used to model pier scour for its sediment modeling capabilities coupled with CFD. Validations were conducted with SSIIM where pier scour depth was able to match experimental depths to within 12.6%. Once SSIIM was validated the next step was to investigate the influence of sediment properties. The objectives were to identity the best performing methods for predicting pier scour and quantify the variation in scour depth with the promin soil parameters. With 4 piers, 2 flow intensities and 16 types of soils a total of 128 simulations were conducted in SSIIM. The scope was limited to clear water scour in clean sands with control soil parameters of a 1 mm grain size, 30° angle of repose, and 0 Pa cohesion. While two soil parameters were kept constant, the third was varied to investigate the influence on scour depth. The scour depths for ten grain sizes were examined to evaluate the performance of 12 empirical methods for predicting pier scour. Of the empirical equations examined, the TAMU

(Texas A&M University) method was found to be the best scour depth prediction equation. The angle of repose was modeled using stable slope angles between 20° and 40°. Variation of the stable slope angle was found to vary scour depths by –41.9% to +145.1%. Cohesive strength was added to the sediment to simulate the presence of fines and was found to significantly impact scour depths. A cohesion of 0.5 Pa was enough to reduce scour depths by about 90%. The significant variations in scour depth as functions of angle of repose and cohesion highlighted the need for their inclusion in scour prediction equations and methods.

SSIIM's ability to simulate numerical scour was discussed and improvements were recommended for future numerical scour research. As the TAMU method was identified as the best performing it should be used as the based equation for future improvements. Numerical scour modeling should be improved with better sediment modeling algorithms which realistically capture soil behavior on slopes and cohesion effects on temporal scour. With a robust sediment model coupled with CFD a large number of simulations should be conducted with different types of soil, flows and structural to developed correction factors or even new prediction methods. With the inclusion of gradation, repose angles and cohesion effects new scour prediction methods will provide both safe and cost-efficient design recommendations.

References

Ahmad, N., Bihs, H., Myrhaug, D., Kamath, A., & Arntsen, Ø. (2018). Three-dimensional numerical modelling of wave-induced scour around piles in a side-by-side arrangement. Coastal Engineering (Amsterdam), 138, 132–151. https://doi.org/10.1016/j.coastaleng.2018.04.016

Ahmed, F., & Rajaratnam, N. (1998). Flow around Bridge Piers. Journal of Hydraulic Engineering (New York, N.Y.), 124(3), 288–300. https://doi.org/10.1061/(ASCE)0733-9429(1998)124:3(288)

Akib, S., Jahangirzadeh, A., & Basser, H. (2014). Local scour around complex pier groups and combined piles at semi-integral bridge. Vodohospodársky Časopis, 62(2), 108–116. https://doi.org/10.2478/johh-2014-0015

Alemi, M., & Maia, R. (2018). Numerical Simulation of the Flow and Local Scour Process Around Single and Complex Bridge Piers. International Journal of Civil Engineering, 16(5), 475–487. https://doi.org/10.1007/s40999-016-0137-8

Amini Baghbadorani, D., Beheshti, A., & Ataie-Ashtiani, B. (2017). Scour hole depth prediction around pile groups: review, comparison of existing methods, and proposition of a new approach. Natural Hazards (Dordrecht), 88(2), 977–1001. https://doi.org/10.1007/s11069-017-2900-9

Amini, A., Melville, B., Ali, T., & Ghazali, A. (2012). Clear-Water Local Scour around Pile Groups in Shallow-Water Flow. Journal of Hydraulic Engineering (New York, N.Y.), 138(2), 177–185. https://doi.org/10.1061/(ASCE)HY.1943-7900.0000488

Annandale, G. (1995). Erodibility. Journal of Hydraulic Research. 33. 471-494.

Annandale, G., Smith, S., Nairns, R., & Jones, J. (1996). Scour power. Civil Engineering (New York, N.Y. 1983), 66(7), 58–60.

Annandale, G. (2000). Prediction of scour at bridge pier foundations founded on rock and other earth materials. Transportation Research Record, 2(1696), 67–70.

Ataie-Ashtiani, B., & Beheshti, A. (2006). Experimental Investigation of Clear-Water Local Scour at Pile Groups. Journal of Hydraulic Engineering (New York, N.Y.), 132(10), 1100–1104. https://doi.org/10.1061/(ASCE)0733-9429(2006)132:10(1100)

Ataie-Ashtiani, B., Baratian-Ghorghi, Z., & Beheshti, A. (2010). Experimental Investigation of Clear-Water Local Scour of Compound Piers. Journal of Hydraulic Engineering (New York, N.Y.), 136(6), 343–351. https://doi.org/10.1061/(ASCE)0733-9429(2010)136:6(343)

Babu, M., Sundar, V., & Rao, S. (2003). Measurement of scour in cohesive soils around a vertical pile - simplified instrumentation and regression analysis. IEEE Journal of Oceanic Engineering, 28(1), 106–116. https://doi.org/10.1109/JOE.2002.808198

Barbhuiya, A., & Dey, S. (2004). Local scour at abutments: A review. Sadhana (Bangalore), 29(5), 449–476. https://doi.org/10.1007/BF02703255

Bieniawski, Z. T. (1989). Engineering rock mass classifications: a complete manual for engineers and geologists in mining, civil, and petroleum engineering. John Wiley & Sons.

Bierawski, L., & Maeno, S. (2006). DEM-FEM Model of Highly Saturated Soil Motion Due to Seepage Force. Journal of Waterway, Port, Coastal, and Ocean Engineering, 132(5), 401–409. https://doi.org/10.1061/(ASCE)0733-950X(2006)132:5(401)

Bonnefille, R. (1963). Essais de synthese des lois du début d'entrainement des sédiments sous l'action d'un courant en regime continu. Bull. du Centre de Rech. et d'ess. de Chatou. 5. 17-22.

Brandimarte, L., Montanari, A., Briaud, J., & D'Odorico, P. (2006). Stochastic Flow Analysis for Predicting River Scour of Cohesive Soils. Journal of Hydraulic Engineering (New York, N.Y.), 132(5), 493–500. https://doi.org/10.1061/(ASCE)0733-9429(2006)132:5(493)

Breusers H N C 1963 Discussion of 'Sediment transportation mechanics: erosion of sediment' by Task Force on Preparation of Sedimentation Manual.J. Hydraul. Div, Am. Soc. Civ. Eng. 89: 277–281

Breusers, H., Nicollet, G., & Shen, H. (1977). Local Scour Around Cylindrical Piers. Journal of Hydraulic Research, 15(3), 211–252. https://doi.org/10.1080/00221687709499645

Briaud, J., Ting, F., Chen, H., Gudavalli, R., Perugu, S., & Wei, G. (1999). SRICOS: Prediction of Scour Rate in Cohesive Soils at Bridge Piers. Journal of Geotechnical and Geoenvironmental Engineering, 125(4), 237–246. https://doi.org/10.1061/(ASCE)1090-0241(1999)125:4(237)

Briaud, J., Ting, F., Chen, H., Cao, Y., Han, S., & Kwak, K. (2001a). Erosion Function Apparatus for Scour Rate Predictions. Journal of Geotechnical and Geoenvironmental Engineering, 127(2), 105–113. https://doi.org/10.1061/(ASCE)1090-0241(2001)127:2(105)

Briaud, J., Chen, H., Kwak, K., Han, S., & Ting, F. (2001b). Multiflood and Multilayer Method for Scour Rate Prediction at Bridge Piers. Journal of Geotechnical and Geoenvironmental Engineering, 127(2), 114–125. https://doi.org/10.1061/(ASCE)1090-0241(2001)127:2(114)

Briaud, J., Chen, H., Li, Y., & Nurtjahyo, P. (2004). SRICOS-EFA Method for Complex Piers in Fine-Grained Soils. Journal of Geotechnical and Geoenvironmental Engineering, 130(11), 1180–1191. https://doi.org/10.1061/(ASCE)1090-0241(2004)130:11(1180)

Briaud, J., Chen, H., Li, Y., Nurtjahyo, P., & Wang, J. (2005). SRICOS-EFA Method for Contraction Scour in Fine-Grained Soils. Journal of Geotechnical and Geoenvironmental Engineering, 131(10), 1283–1294. https://doi.org/10.1061/(ASCE)1090-0241(2005)131:10(1283)

Briaud, J., Brandimarte, L., Wang, J., & D'Odorico, P. (2007). Probability of scour depth exceedance owing to hydrologic uncertainty. Georisk, 1(2), 77–88. https://doi.org/10.1080/17499510701398844

Briaud J.-L., Chen H.-C., Chang K.-A., Oh S.J., Chen S., Wang J., Li Y., Kwak K., Nartjaho P., Gudaralli R., Wei W., Pergu S., Cao Y.W., Ting F (2011). Summary Report: The SRICOS–EFA Method. Texas A&M University

Briaud, J., & Govindasamy, A. (2014). Application of the Observation Method for Scour to Two Texas Bridges. In Geo-Congress 2014 (pp. 2640–2654). https://doi.org/10.1061/9780784413272.255

Briaud, J., Gardoni, P., & Yao, C. (2014). Statistical, Risk, and Reliability Analyses of Bridge Scour. Journal of Geotechnical and Geoenvironmental Engineering, 140(2), 4013011–. https://doi.org/10.1061/(ASCE)GT.1943-5606.0000989

Briaud, J. (2015a). Scour Depth at Bridges: Method Including Soil Properties. I: Maximum Scour Depth Prediction. Journal of Geotechnical and Geoenvironmental Engineering, 141(2), 4014104–. https://doi.org/10.1061/(ASCE)GT.1943-5606.0001222

Briaud, J. (2015b). Scour Depth at Bridges: Method Including Soil Properties. II: Time Rate of Scour Prediction. Journal of Geotechnical and Geoenvironmental Engineering, 141(2), 4014105–. https://doi.org/10.1061/(ASCE)GT.1943-5606.0001223

Brooks, H. N. (1963), discussion of "Boundary Shear Stresses in Curved Trapezoidal Channels", by A. T. Ippen and P. A. Drinker, ASCE Journal of Hydraulic Engineering, Vol. 89, No. HY3

Chen, G., Schafer, B., Lin, Z., Huang, Y., Suaznabar, O., Shen, J., & Kerenyi, K. (2015). Maximum scour depth based on magnetic field change in smart rocks for foundation stability evaluation of bridges. Structural Health Monitoring, 14(1), 86–99. https://doi.org/10.1177/1475921714554141

Chen, Q., Yang, Z., & Wu, H. (2019). Evolution of Turbulent Horseshoe Vortex System in Front of a Vertical Circular Cylinder in Open Channel. Water (Basel), 11(10), 2079–. https://doi.org/10.3390/w11102079

Chen, S., Tfwala, S., Wu, T., Chan, H., & Chou, H. (2018). A hooked-collar for bridge piers protection: Flow fields and scour. Water (Basel), 10(9), 1251–. https://doi.org/10.3390/w10091251

Cheng, Nian-Sheng. (2015). Representative Grain Size and Equivalent Roughness Height of a Sediment Bed. Journal of Hydrologic Engineering. 142. 10.1061/(ASCE)HY.1943-7900.0001069.

Chiew, Y., & Melville, B. (1987). Local scour around bridge piers. Journal of Hydraulic Research, 25(1), 15–26. https://doi.org/10.1080/00221688709499285

Coleman, S., Lauchlan, C., & Melville, B. (2003). Clear-water scour development at bridge abutments. Journal of Hydraulic Research, 41(5), 521–531. https://doi.org/10.1080/00221680309499997

Coleman, S. (2005). Clearwater Local Scour at Complex Piers. Journal of Hydraulic Engineering (New York, N.Y.), 131(4), 330–334. https://doi.org/10.1061/(ASCE)0733-9429(2005)131:4(330)

Dargahi, B. (1987). ‘‘Flow field and local scouring around a pier.’’ Bulletin No. TRITA-VBI-137, Hydraulic Laboratory, Royal Institute of Technology, Stockholm, Sweden.

Dargahi, B. (1989). The turbulent flow field around a circular cylinder. Experiments in Fluids, 8(1-2), 1–12. https://doi.org/10.1007/BF00203058

Dargahi, B. (1990). Controlling Mechanism of Local Scouring. Journal of Hydraulic Engineering (New York, N.Y.), 116(10), 1197–1214. https://doi.org/10.1061/(ASCE)0733-9429(1990)116:10(1197)

Debnath, K., Nikora, V., Aberle, J., Westrich, B., & Muste, M. (2007). Erosion of Cohesive Sediments: Resuspension, Bed Load, and Erosion Patterns from Field Experiments. Journal of Hydraulic Engineering (New York, N.Y.), 133(5), 508–520. https://doi.org/10.1061/(ASCE)0733-9429(2007)133:5(508)

Debnath, K., & Chaudhuri, S. (2010a). Bridge Pier Scour in Clay-Sand Mixed Sediments at Near-Threshold Velocity for Sand. Journal of Hydraulic Engineering (New York, N.Y.), 136(9), 597–609. https://doi.org/10.1061/(ASCE)HY.1943-7900.0000221

Debnath, K., & Chaudhuri, S. (2010b). Laboratory experiments on local scour around cylinder for clay and clay–sand mixed beds. Engineering Geology, 111(1), 51–61. https://doi.org/10.1016/j.enggeo.2009.12.003

Debnath, K., Chaudhuri, S., & Manik, M. (2014). Local scour around abutment in clay/sand-mixed cohesive sediment bed. ISH Journal of Hydraulic Engineering, 20(1), 46–64. https://doi.org/10.1080/09715010.2013.835103

Deng, L., & Cai, C. (2010). Bridge Scour: Prediction, Modeling, Monitoring, and Countermeasures—Review. Practice Periodical on Structural Design and Construction, 15(2), 125–134. https://doi.org/10.1061/(ASCE)SC.1943-5576.0000041

Dey, S. (1999). Time-variation of scour in the vicinity of circular piers. Proceedings of the Institution of Civil Engineers. Water, Maritime and Energy, 136(2), 67–75. https://doi.org/10.1680/iwtme.1999.31422

Dey, S. (2003) "Threshold of sediment motion on combined transverse and longitudinal sloping beds", Journal of Hydraulic Research, Vol. 41, No. 4, pp. 405-415.

Ehteram, M., & Mahdavi Meymand, A. (2015). Numerical modeling of scour depth at side piers of the bridge. Journal of Computational and Applied Mathematics, 280, 68–79. https://doi.org/10.1016/j.cam.2014.11.039

Escauriaza, C., & Sotiropoulos, F. (2011). Initial stages of erosion and bed form development in a turbulent flow around a cylindrical pier. Journal of Geophysical Research: Earth Surface, 116(F3). https://doi.org/10.1029/2010JF001749

Ettema, R., Constantinescu, G., & Melville, B. (2017). Flow-Field Complexity and Design Estimation of Pier-Scour Depth: Sixty Years since Laursen and Toch. Journal of Hydraulic Engineering (New York, N.Y.), 143(9), 3117006–. https://doi.org/10.1061/(ASCE)HY.1943-7900.0001330

Froehlich, D.C. (1988) Analysis of On-Site Measurements of Scour at Piers. In: Abt, S.R. and Gessler, J., Eds., Hydraulic Engineering—Proceedings of the 1988 National Conference on Hydraulic Engineering, American Society of Civil Engineers, New York, 534-539.

Froehlich, D. C. (1989). Local scour at bridge abutments. In Proceedings of the 1989 national conference on hydraulic engineering (pp. 13-18).

Ge, L., & Sotiropoulos, F. (2005a). 3D Unsteady RANS Modeling of Complex Hydraulic Engineering Flows. I: Numerical Model. Journal of Hydraulic Engineering (New York, N.Y.), 131(9), 800–808. https://doi.org/10.1061/(ASCE)0733-9429(2005)131:9(800)

Ge, L., Lee, S., Sotiropoulos, F., & Sturm, T. (2005b). 3D Unsteady RANS Modeling of Complex Hydraulic Engineering Flows. II: Model Validation and Flow Physics. Journal of Hydraulic

Engineering (New York, N.Y.), 131(9), 809–820. https://doi.org/10.1061/(ASCE)0733-9429(2005)131:9(809)

Govindasamy, A., Briaud, J., Kim, D., Olivera, F., Gardoni, P., & Delphia, J. (2013). Observation Method for Estimating Future Scour Depth at Existing Bridges. Journal of Geotechnical and Geoenvironmental Engineering, 139(7), 1165–1175. https://doi.org/10.1061/(ASCE)GT.1943-5606.0000838

Guan, D., Chiew, Y., Wei, M., & Hsieh, S. (2019). Characterization of horseshoe vortex in a developing scour hole at a cylindrical bridge pier. International Journal of Sediment Research, 34(2), 118–124. https://doi.org/10.1016/j.ijsrc.2018.07.001

Hamzah M. Beakawi Al-Hashemi, Omar S. Baghabra Al-Amoudi, A review on the angle of repose of granular materials, Powder Technology, Volume 330, 2018, Pages 397-417, ISSN 0032-5910, https://doi.org/10.1016/j.powtec.2018.02.003.

Huang, W., Yang, Q., & Xiao, H. (2009). CFD modeling of scale effects on turbulence flow and scour around bridge piers. Computers & Fluids, 38(5), 1050–1058. https://doi.org/10.1016/j.compfluid.2008.01.029

Ismail, A., Jeng, D., Zhang, L., & Zhang, J. (2013). Predictions of bridge scour: Application of a feed-forward neural network with an adaptive activation function. Engineering Applications of Artificial Intelligence, 26(5-6), 1540–1549. https://doi.org/10.1016/j.engappai.2012.12.011

Jahangirzadeh, A., Basser, H., Akib, S., Karami, H., Naji, S., & Shamshirband, S. (2014). Experimental and numerical investigation of the effect of different shapes of collars on the reduction of scour around a single bridge pier. PloS One, 9(6), e98592–e98592. https://doi.org/10.1371/journal.pone.0098592

Jain, S. C. (1981). Maximum clear-water scour around circular piers. Journal of the Hydraulics Division, 107(5), 611-626.

Jain, S. C., and Fischer, E. E. (1979). “Scour around bridge piers at high Froude numbers.” FHWA-RD- 79-104, Federal Highway Administration, U.S. Dept. of Transportation, Washington, DC.

Jiang, H., Cheng, L., & An, H. (2017). On numerical aspects of simulating flow past a circular cylinder. International Journal for Numerical Methods in Fluids, 85(2), 113–132. https://doi.org/10.1002/fld.4376

Jones, J. S., & Sheppard, D. M. (2000). Local scour at complex pier geometries. In Building Partnerships (pp. 1-9).

Karami, H., Basser, H., Ardeshir, A., & Hosseini, S. (2014). Verification of numerical study of scour around spur dikes using experimental data. Water and Environment Journal: WEJ, 28(1), 124–134. https://doi.org/10.1111/wej.12019

Kaya, A. (2010). Artificial neural network study of observed pattern of scour depth around bridge piers. Computers and Geotechnics, 37(3), 413–418. https://doi.org/10.1016/j.compgeo.2009.10.003

Keaton, J. (2013). Estimating erodible rock durability and geotechnical parameters for scour analysis. Environmental & Engineering Geoscience, 19(4), 319–343. https://doi.org/10.2113/gseegeosci.19.4.319

Keaton, J. R. (2011). Modified Slake Durability Test Applicability for Soil. In International Symposium on Erosion and Landscape Evolution (ISELE), 18-21 September 2011, Anchorage, Alaska (p. 7). American Society of Agricultural and Biological Engineers.

Khalid, M., Muzzammil, M., & Alam, J. (2019). A reliability-based assessment of live bed scour at bridge piers. ISH Journal of Hydraulic Engineering, 1–8. https://doi.org/10.1080/09715010.2019.1584543

Khan, M., Azamathulla, H., Tufail, M., & Ab Ghani, A. (2012). Bridge pier scour prediction by gene expression programming. Proceedings of the Institution of Civil Engineers. Water Management, 165(9), 481–493. https://doi.org/10.1680/wama.11.00008

Kocaman, S., Seckin, G., & Erduran, K. (2010). 3D model for prediction of flow profiles around bridges. Journal of Hydraulic Research, 48(4), 521–525. https://doi.org/10.1080/00221686.2010.507340

Kumar, A., Kothyari, U., & Ranga Raju, K. (2012). Flow structure and scour around circular compound bridge piers – A review. Journal of Hydro-Environment Research, 6(4), 251–265. https://doi.org/10.1016/j.jher.2012.05.006

Lagasse PF, Clopper PE, Zevenbergen LW et al (2007) National cooperative highway research program (NCHRP Report 593): countermeasures to protect bridge piers from scour. Transportation research Board, Washington DC

Larras, J. (1963). Profondeurs Maximales d'Erosion des Fonds Mobiles Autour des Piles en Rivere. Ann. Ponts Chaussees, 133, 411-424.

Laursen, E. M., & Toch, A. (1956). Scour around bridge piers and abutments (Vol. 4). Ames, IA: Iowa Highway Research Board.

Laursen, E. M., 1960, Scour at Bridge Crossings, ASCE Hyd. Div. Jour., V 89, No. Hyd 3, May.

Laursen, E M. (1963) An analysis of relief bridge scour. [Journal Article]. ASCE Journal of Hydraulic Division, 89(HY3), 93-109.

LEE, T., JENG, D., ZHANG, G., & HONG, J. (2007). Neural network modeling for estimation of scour depth around bridge piers. Journal of Hydrodynamics. Series B, 19(3), 378–386. https://doi.org/10.1016/S1001-6058(07)60073-0

Liang, F., Wang, C., Huang, M., & Wang, Y. (2017). Experimental observations and evaluations of formulae for local scour at pile groups in steady currents. Marine Georesources & Geotechnology, 35(2), 245–255. https://doi.org/10.1080/1064119X.2016.1147510

Liang, F., Wang, C., & Yu, X. (2019). Widths, types, and configurations: Influences on scour behaviors of bridge foundations in non-cohesive soils. Marine Georesources & Geotechnology, 37(5), 578–588. https://doi.org/10.1080/1064119X.2018.1460644

Link, O., Mignot, E., Roux, S., Camenen, B., Escauriaza, C., Chauchat, J., Brevis, W., & Manfreda, S. (2019). Scour at bridge foundations in supercritical flows: An analysis of knowledge gaps. Water (Basel), 11(8), 1656–. https://doi.org/10.3390/w11081656

Lu, J., Hong, J., Su, C., Wang, C., & Lai, J. (2008). Field Measurements and Simulation of Bridge Scour Depth Variations during Floods. Journal of Hydraulic Engineering (New York, N.Y.), 134(6), 810–821. https://doi.org/10.1061/(ASCE)0733-9429(2008)134:6(810)

Manes, C., & Brocchini, M. (2015). Local scour around structures and the phenomenology of turbulence. Journal of Fluid Mechanics, 779, 309–324. https://doi.org/10.1017/jfm.2015.389

Melville, B. W. (1975). ‘‘Local scour at bridge sites.’’ Rep. No. 117, Dept. of Civil Engineering, School of Engrg., Univ. of Auckland, Auckland, New Zealand.

Melville, B., & Raudkivi, A. (1977). FLOW CHARACTERISTICS IN LOCAL SCOUR AT BRIDGE PIERS. Journal of Hydraulic Research, 15(4), 373–380. https://doi.org/10.1080/00221687709499641

Melville, B. (1984). Live-bed Scour at Bridge Piers. Journal of Hydraulic Engineering (New York, N.Y.), 110(9), 1234–1247. https://doi.org/10.1061/(ASCE)0733-9429(1984)110:9(1234)

Melville, B., & Sutherland, A. (1988). Design Method for Local Scour at Bridge Piers. Journal of Hydraulic Engineering (New York, N.Y.), 114(10), 1210–1226. https://doi.org/10.1061/(ASCE)0733-9429(1988)114:10(1210)

Melville, B. (1992). Local Scour at Bridge Abutments. Journal of Hydraulic Engineering (New York, N.Y.), 118(4), 615–631. https://doi.org/10.1061/(ASCE)0733-9429(1992)118:4(615)

Melville, B., & Raudkivi, A. (1996). Effects of Foundation Geometry on Bridge Pier Scour. Journal of Hydraulic Engineering (New York, N.Y.), 122(4), 203–209. https://doi.org/10.1061/(ASCE)0733-9429(1996)122:4(203)

Melville, B. (1997). Pier and Abutment Scour: Integrated Approach. Journal of Hydraulic Engineering (New York, N.Y.), 123(2), 125–136. https://doi.org/10.1061/(ASCE)0733-9429(1997)123:2(125)

Melville, B., & Chiew, Y. (1999). Time Scale for Local Scour at Bridge Piers. Journal of Hydraulic Engineering (New York, N.Y.), 125(1), 59–65. https://doi.org/10.1061/(ASCE)0733-9429(1999)125:1(59)

Melville, B. W., and Coleman, S. E. (2000). Bridge scour, Water Resources, Colo.

Ministry of Transportation of Ontario (MTO). 1997. Drainage Management Manual, Ministry of Transportation Ontario. Drainage and Hydrology Section, Transportation Engineering Branch, Quality and Standards Division.

Mohamed, T., Noor, M., Ghazali, A., & Huat, B. (2005). Validation of Some Bridge Pier Scour Formulae Using Field and Laboratory Data. American Journal of Environmental Sciences, 1(2), 119–125. https://doi.org/10.3844/ajessp.2005.119.125

Mohamed, Y., Abdel-Aal, G., Nasr-Allah, T., & Shawky, A. (2013). Experimental and theoretical investigations of scour at bridge abutment. Journal of King Saud University. Engineering Sciences, 28(1), 32–40. https://doi.org/10.1016/j.jksues.2013.09.005

Nagel, T., Chauchat, J., Bonamy, C., Liu, X., Cheng, Z., & Hsu, T. (2020). Three-dimensional scour simulations with a two-phase flow model. Advances in Water Resources, 138, 103544–. https://doi.org/10.1016/j.advwatres.2020.103544

Najafzadeh, M., Barani, G., & Hessami Kermani, M. (2013a). GMDH based back propagation algorithm to predict abutment scour in cohesive soils. Ocean Engineering, 59, 100–106. https://doi.org/10.1016/j.oceaneng.2012.12.006

Najafzadeh, M., Barani, G., & Azamathulla, H. (2013b). GMDH to predict scour depth around a pier in cohesive soils. Applied Ocean Research, 40, 35–41. https://doi.org/10.1016/j.apor.2012.12.004

Namaee, M., & Sui, J. (2019). Local scour around two side-by-side cylindrical bridge piers under ice-covered conditions. International Journal of Sediment Research, 34(4), 355–367. https://doi.org/10.1016/j.ijsrc.2018.11.007

Nasr-Allah, T., Moussa, Y., Abdel-Aal, G., & Awad, A. (2016). Experimental and numerical simulation of scour at bridge abutment provided with different arrangements of collars. Alexandria Engineering Journal, 55(2), 1455–1463. https://doi.org/10.1016/j.aej.2016.01.021

National Cooperative Highway Research Program, 2010b, "Estimation of Scour Depth at Bridge Abutments," NCHRP Project 24-20, Draft Final Report, Transportation Research Board, National Academy of Science, Washington, D.C. (Ettema, R., T. Nakato, and M. Muste).

Neill, C. R. 1964. Local scour around bridge piers. Council of Alberta, Highway and River Eng. Div., Alberta, Canada.

Neill, C. R. (ed) (1973). RTAC Guide to Bridge Hydraulics, University of Toronto Press.

Nielsen, A., Liu, X., Sumer, B., & Fredsøe, J. (2013). Flow and bed shear stresses in scour protections around a pile in a current. Coastal Engineering (Amsterdam), 72, 20–38. https://doi.org/10.1016/j.coastaleng.2012.09.001

Olabarrieta, M., Medina, R., & Castanedo, S. (2010). Effects of wave–current interaction on the current profile. Coastal Engineering (Amsterdam), 57(7), 643–655. https://doi.org/10.1016/j.coastaleng.2010.02.003

Olsen, Nils Reidar B. (2018). SSIIM User's Manual. Department Of Civil and Environmental Engineering the Norwegian University of Science and Technology

Olsen, Nils Reidar B. (1999). Class Notes: Computational; Fluid Dynamics in Hydraulic and Sedimentation Engineering. Department Of Civil and Environmental Engineering the Norwegian University of Science and Technology

Pal, M., Singh, N., & Tiwari, N. (2011). Support vector regression based modeling of pier scour using field data. Engineering Applications of Artificial Intelligence, 24(5), 911–916. https://doi.org/10.1016/j.engappai.2010.11.002

Pandey, M., Ahmad, Z., & Sharma, P. (2018). Scour around impermeable spur dikes: a review. ISH Journal of Hydraulic Engineering, 24(1), 25–44. https://doi.org/10.1080/09715010.2017.1342571

Park, C., Park, H., & Cho, Y. (2017). Evaluation of the applicability of pier local scour formulae using laboratory and field data. Marine Georesources & Geotechnology, 35(1), 1–7. https://doi.org/10.1080/1064119X.2014.954658

Patankar, S. V. (1980) "Numerical Heat Transfer and Fluid Flow", McGraw-Hill Book Company New York

Qi, W., & Gao, F. (2014). Physical modeling of local scour development around a large-diameter monopile in combined waves and current. Coastal Engineering (Amsterdam), 83, 72–81. https://doi.org/10.1016/j.coastaleng.2013.10.007

Qi, M., Li, J., & Chen, Q. (2016). Comparison of existing equations for local scour at bridge piers: parameter influence and validation. Natural Hazards (Dordrecht), 82(3), 2089–2105. https://doi.org/10.1007/s11069-016-2287-z

Rambabu, M., Rao, S., & Sundar, V. (2003). Current-induced scour around a vertical pile in cohesive soil. Ocean Engineering, 30(7), 893–920. https://doi.org/10.1016/S0029-8018(02)00063-X

Raudkivi, A., & Ettema, R. (1985). Scour at Cylindrical Bridge Piers in Armored Beds. Journal of Hydraulic Engineering (New York, N.Y.), 111(4), 713–731. https://doi.org/10.1061/(ASCE)0733-9429(1985)111:4(713)

Rhie, C.-M and Chow, W.L. (1983) "Numerical study of the turbulent flow past and airfoil with trailing edge separation", AIAA Journal, Vol. 21, No. 11.

Richardson, E., & Lagasse, P. (1996). Stream Stability and Scour at Highway Bridges. Water International, 21(3), 108–118. https://doi.org/10.1080/02508069608686502

Richardson EV, Davis SR (2001) Evaluating scour at bridges. Hydraulic engineering circular no. 18 (HEC-18), Report no. FHWA: NHI 01-001, Federal Highway Administration, Washington, DC

Richardson, J., & Panchang, V. (1998). Three-Dimensional Simulation of Scour-Inducing Flow at Bridge Piers. Journal of Hydraulic Engineering (New York, N.Y.), 124(5), 530–540. https://doi.org/10.1061/(ASCE)0733-9429(1998)124:5(530)

Roulund, A., Sumer, B., Fredsøe, J., & Michelsen, J. (2005). Numerical and experimental investigation of flow and scour around a circular pile. Journal of Fluid Mechanics, 534, 351–401. https://doi.org/10.1017/S0022112005004507

Salaheldin, T., Imran, J., & Chaudhry, M. (2004). Numerical Modeling of Three-Dimensional Flow Field Around Circular Piers. Journal of Hydraulic Engineering (New York, N.Y.), 130(2), 91–100. https://doi.org/10.1061/(ASCE)0733-9429(2004)130:2(91)

Salim, M. and J.S. Jones, 1995, "Effects of Exposed Pile Foundations on Local Pier Scour," Proceedings ASCE Water Resources Engineering Conference, San Antonio, TX.

Salim, M. and J.S. Jones, 1996, "Scour Around Exposed Pile Foundations," Proceedings ASCE North American and Water and Environment Congress, '96, Anaheim, CA (also issued as FHWA Memo).

Salim, M. and J.S. Jones, 1999, Scour Around Exposed Pile Foundations," ASCE Compendium, Stream Stability and Scour at Highway Bridges, Richardson and Lagasse (eds.), Reston, VA.

Schlichting, H. (1979) "Boundary layer theory", McGraw-Hill.

Sheppard, D., & Miller, W. (2006). Live-Bed Local Pier Scour Experiments. Journal of Hydraulic Engineering (New York, N.Y.), 132(7), 635–642. https://doi.org/10.1061/(ASCE)0733-9429(2006)132:7(635)

Sheppard, D., Demir, H., & Melville, B. (2011). Scour at wide piers and long skewed piers. Transportation Research Board.

Sheppard, D., Melville, B., & Demir, H. (2014). Evaluation of Existing Equations for Local Scour at Bridge Piers. Journal of Hydraulic Engineering (New York, N.Y.), 140(1), 14–23. https://doi.org/10.1061/(ASCE)HY.1943-7900.0000800

Sheppard, D., Odeh, M., & Glasser, T. (2004). Large Scale Clear-Water Local Pier Scour Experiments. Journal of Hydraulic Engineering (New York, N.Y.), 130(10), 957–963. https://doi.org/10.1061/(ASCE)0733-9429(2004)130:10(957)

Shields, A. (1936). Application of similarity principles and turbulence research to bed-load movement (translated version). Mitteilungen der Preußischen Versuchsanstalt für Wasserbau.

Smith, W.L., 1999, "Local Structure-Induced Sediment Scour at Pile Groups," M.S. Thesis, University of Florida, Gainesville, FL.

Sonia Devi, Y., & Barbhuiya, A. (2017). Bridge pier scour in cohesive soil: a review. Sadhana (Bangalore), 42(10), 1803–1819. https://doi.org/10.1007/s12046-017-0698-5

Sturm, T., Ettema, R., & Melville, B. (2011). Evaluation of bridge-scour research abutment and contraction scour processes and prediction. National Cooperative Highway Research Program, Transportation Research Board of the National Academies.

Sumer, B., Fredsøe, J., & Christiansen, N. (1992a). Scour Around Vertical Pile in Waves. Journal of Waterway, Port, Coastal, and Ocean Engineering, 118(1), 15–31. https://doi.org/10.1061/(ASCE)0733-950X(1992)118:1(15)

Sumer, B. M., Christiansen, N., and Fredsoe, J. (1992b). "Time scale of scour around a vertical pile." Proc., 2nd Int. Offshore and Polar Engrg. Conf., International Society of Offshore and Polar Engineers, San Francisco, Calif., Vol. III, 308-315.

Sumer, B., Christiansen, N., & Fredsøe, J. (1993). Influence of Cross Section on Wave Scour around Piles. Journal of Waterway, Port, Coastal, and Ocean Engineering, 119(5), 477–495. https://doi.org/10.1061/(ASCE)0733-950X(1993)119:5(477)

Sumer, B., & Fredsøe, J. (1998). Wave Scour around Group of Vertical Piles. Journal of Waterway, Port, Coastal, and Ocean Engineering, 124(5), 248–256. https://doi.org/10.1061/(ASCE)0733-950X(1998)124:5(248)

Sumer, B., & Fredsøe, J. (2001). Wave Scour around a Large Vertical Circular Cylinder. Journal of Waterway, Port, Coastal, and Ocean Engineering, 127(3), 125–134. https://doi.org/10.1061/(ASCE)0733-950X(2001)127:3(125)

Sumer, B., Whitehouse, R., & Tørum, A. (2001). Scour around coastal structures: a summary of recent research. Coastal Engineering, 44(2), 153–190. https://doi.org/10.1016/S0378-3839(01)00024-2

Sumer, B., Hatipoglu, F., & Fredsøe, J. (2007). Wave Scour around a Pile in Sand, Medium Dense, and Dense Silt. Journal of Waterway, Port, Coastal, and Ocean Engineering, 133(1), 14–27. https://doi.org/10.1061/(ASCE)0733-950X(2007)133:1(14)

Toth, E., & Brandimarte, L. (2011). Prediction of local scour depth at bridge piers under clear-water and live-bed conditions: Comparison of literature formulae and Artificial Neural networks. Journal of Hydroinformatics, 13(4), 812–824. https://doi.org/10.2166/hydro.2011.065

Van Rijn, L. C. (1993). Principles of sediment transport in rivers, estuaries and coastal seas.

Vanoni, V.A., ed., 1975, Sedimentation Engineering: American Society of Civil Engineers, Manuals and Reports on Engineering Practice, No. 54, 745 p.

Wang, C., Yu, X., & Liang, F. (2017). A review of bridge scour: mechanism, estimation, monitoring and countermeasures. Natural Hazards (Dordrecht), 87(3), 1881–1906. https://doi.org/10.1007/s11069-017-2842-2

Wardhana, K., & Hadipriono, F. (2003). Analysis of Recent Bridge Failures in the United States. Journal of Performance of Constructed Facilities, 17(3), 144–150. https://doi.org/10.1061/(ASCE)0887-3828(2003)17:3(144)

White, C. M. (1940). The Equilibrium of Grains on the Bed of a Stream. Proceedings of the Royal Society of London. Series A, Mathematical and Physical Sciences, 174(958), 322–338. https://doi.org/10.1098/rspa.1940.0023

Whitehouse, R. (2004). Marine scour at large foundations. In: Second international conference on scour and erosion (ICSE-2), Singapore

Wu, Peng. Hirshfield, Faye. Sui, Jue-yi. (2015). Local scour around bridge abutments under ice covered condition-an experimental study. International Journal of Sediment Research, 30(1), 39–47. https://doi.org/10.1016/S1001-6279(15)60004-X

Wu, P., Balachandar, R., & Sui, J. (2016). Local Scour around Bridge Piers under Ice-Covered Conditions. Journal of Hydraulic Engineering (New York, N.Y.), 142(1), 4015038–. https://doi.org/10.1061/(ASCE)HY.1943-7900.0001063

Wu, W., Rodi, W., & Wenka, T. (2000). 3D Numerical Modeling of Flow and Sediment Transport in Open Channels. Journal of Hydraulic Engineering (New York, N.Y.), 126(1), 4–15. https://doi.org/10.1061/(ASCE)0733-9429(2000)126:1(4)

Xiong, W., Cai, C., Kong, B., & Kong, X. (2016). CFD Simulations and Analyses for Bridge-Scour Development Using a Dynamic-Mesh Updating Technique. Journal of Computing in Civil Engineering, 30(1), 4014121–. https://doi.org/10.1061/(ASCE)CP.1943-5487.0000458

Yalin, M. S. (1971). Theory of hydraulic models. Macmillan International Higher Education.

Yankielun, N., & Zabilansky, L. (1999). Laboratory Investigation of Time-Domain Reflectometry System for Monitoring Bridge Scour. Journal of Hydraulic Engineering (New York, N.Y.), 125(12), 1279–1284. https://doi.org/10.1061/(ASCE)0733-9429(1999)125:12(1279)

Zaid, M., Yazdanfar, Z., Chowdhury, H., & Alam, F. (2019). Numerical modeling of flow around a pier mounted in a flat and fixed bed. Energy Procedia, 160, 51–59. https://doi.org/10.1016/j.egypro.2019.02.118

Zanke, U., Hsu, T., Roland, A., Link, O., & Diab, R. (2011). Equilibrium scour depths around piles in noncohesive sediments under currents and waves. Coastal Engineering (Amsterdam), 58(10), 986–991. https://doi.org/10.1016/j.coastaleng.2011.05.011

Zhao, M., Zhu, X., Cheng, L., & Teng, B. (2012). Experimental study of local scour around subsea caissons in steady currents. Coastal Engineering (Amsterdam), 60(1), 30–40. https://doi.org/10.1016/j.coastaleng.2011.08.004

Zheng, S., Zheng, S., Xu, Y., Xu, Y., Cheng, H., Cheng, H., Wang, B., Wang, B., Lu, X., & Lu, X. (2018). Assessment of bridge scour in the lower, middle, and upper Yangtze River estuary with riverbed sonar profiling techniques. Environmental Monitoring and Assessment, 190(1), 1–13. https://doi.org/10.1007/s10661-017-6393-5

Zhu, H., Zhou, Z., Yang, R., & Yu, A. (2007). Discrete particle simulation of particulate systems: Theoretical developments. Chemical Engineering Science, 62(13), 3378–3396. https://doi.org/10.1016/j.ces.2006.12.089

Zhu, H.P. Zhou, Z.Y. Hou, Q.F. Yu A.B. (2011). Linking discrete particle simulation to continuum process modelling for granular matter : Theory and application. Particuology, 9(4), 342–357. https://doi.org/10.1016/j.partic.2011.01.002

Zhu, Zw., Liu, Zq.. (2012). CFD prediction of local scour hole around bridge piers. Journal of Central South University, 19(1), 273–281. https://doi.org/10.1007/s11771-012-1001-x

Appendices

Appendix A: Parametric Study Depth Results

		D50 (mm)										Stable Slope Angle (°) [1mm and 0 Pa				Cohesion (Pa) [30° and 1mm]			
		0.05		0.1	0.2	0.5	1		2	5	10	20	25	35	40	0.05	0.1	0.25	0.5
Model	D (m)	ds (m)	te (s)	ds (m)	ds (m)	ds (m)	ds (m)	te (s)	ds (m)	ds (m)	ds (m)	ds (m)	ds (m)	ds (m)	ds (m)	ds (m)	ds (m)	ds (m)	ds (m)
1a	0.10	0.0372	30000	0.0532	0.0550	0.0422	**0.0099**	**2000**	0.0000	0.0000	0.0000	0.0050	0.0054	0.0136	0.0260	0.0063	0.0040	0.0019	0.0000
1b	0.10	0.0910	40000	0.1043	0.0804	0.0566	**0.0726**	**17000**	0.0274	0.0004	0.0000	0.0438	0.0595	0.0731	0.0949	0.0597	0.0526	0.0322	0.0146
2a	0.25	0.0605	60000	0.0798	0.0909	0.0583	**0.0222**	**10000**	0.0000	0.0000	0.0000	0.0091	0.0158	0.0252	0.0847	0.0159	0.0095	0.0000	0.0000
2b	0.25	0.1691	77000	0.1621	0.1487	0.1091	**0.1419**	**50000**	0.0467	0.0000	0.0000	0.0970	0.1180	0.1935	0.2864	0.0778	0.0642	0.0321	0.0150
3a	0.50	0.1293	100000	0.1730	0.1902	0.1168	**0.0486**	**14000**	0.0000	0.0000	0.0000	0.0257	0.0320	0.0641	0.1177	0.0267	0.0254	0.0000	0.0000
3b	0.50	0.2837	126000	0.3079	0.3327	0.2971	**0.2275**	**81000**	0.0745	0.0000	0.0000	0.1549	0.1876	0.3128	0.4899	0.2019	0.1679	0.1007	0.0444
4a	0.80	0.1713	120000	0.2329	0.2329	0.1721	**0.0676**	**30000**	0.0002	0.0000	0.0000	0.0376	0.0482	0.1252	0.2037	0.0558	0.0398	0.0006	0.0001
4b	0.80	0.3562	141000	0.3962	0.4050	0.3967	**0.2915**	**92000**	0.1088	0.0008	0.0000	0.1982	0.2426	0.4092	0.6584	0.2567	0.2200	0.1447	0.0666

Appendix B: Parametric Study Error Analysis

	Model	RTAC (1973)	CSU (1977)	Melville & Sutherland (1988)	HEC-18	F-DOT	Sheppard & Miller (2006)	Breusers (1977)	Melville (1997)	SRICOS	TAMU	Melville & Chiew (1999)	Sheppard/Melville
SSE %	1a	1424.48%	1002.26%	2701.58%	1253.26%	491.78%	274.98%	529.47%	2648.53%	627.90%	317.14%	1248.17%	726.90%
	1b	241.39%	257.53%	617.97%	332.44%	149.71%	82.54%	114.57%	613.24%	189.46%	148.95%	302.15%	210.49%
	2a	4119.62%	1419.41%	5831.47%	1768.88%	809.41%	457.35%	1392.39%	7585.30%	866.50%	485.45%	3833.20%	1167.51%
	2b	587.27%	269.06%	1055.83%	347.44%	180.50%	96.67%	268.56%	1444.00%	190.41%	157.47%	792.22%	262.23%
	3a	3654.81%	703.34%	3478.62%	883.84%	316.79%	159.95%	530.90%	3501.46%	410.97%	103.95%	1682.05%	489.50%
	3b	613.24%	145.79%	701.11%	189.37%	69.37%	24.57%	92.94%	718.70%	100.36%	29.80%	361.31%	118.80%
	4a	5710.15%	767.57%	4197.25%	964.42%	299.60%	158.03%	352.74%	3252.29%	440.44%	65.07%	1556.79%	465.94%
	4b	1072.58%	170.90%	918.16%	222.16%	71.56%	26.54%	58.20%	699.88%	114.76%	18.39%	352.56%	122.38%
UE %	1a	0.00%	0.00%	0.00%	0.00%	0.04%	9.96%	44.03%	0.00%	0.00%	0.00%	0.00%	0.00%
	1b	0.00%	0.00%	0.00%	0.00%	0.44%	27.83%	61.60%	0.00%	0.00%	0.00%	0.00%	0.44%
	2a	0.00%	0.00%	0.00%	0.00%	0.00%	8.88%	24.70%	0.00%	0.00%	0.00%	0.00%	0.00%
	2b	0.00%	0.00%	0.00%	0.00%	0.00%	18.69%	38.00%	0.00%	0.00%	0.00%	0.00%	0.00%
	3a	0.00%	0.00%	0.00%	0.00%	0.00%	9.72%	27.68%	0.00%	0.00%	0.00%	0.00%	0.00%
	3b	0.00%	0.00%	0.00%	0.00%	0.00%	14.90%	33.43%	0.00%	0.00%	0.00%	0.00%	0.00%
	4a	0.00%	0.00%	0.00%	0.00%	0.03%	8.49%	26.24%	0.00%	0.00%	0.00%	0.00%	0.00%
	4b	0.00%	0.00%	0.00%	0.00%	0.10%	13.70%	31.36%	0.00%	0.00%	0.00%	0.00%	0.10%
Average SSE %		2177.94%	591.98%	2437.75%	745.23%	298.59%	160.08%	417.47%	2557.92%	367.60%	165.78%	1266.06%	445.47%
Average UE %		0.00%	0.00%	0.00%	0.00%	0.08%	14.02%	35.88%	0.00%	0.00%	0.00%	0.00%	0.07%
Total Score		**2178%**	**592%**	**2438%**	**745%**	**302%**	**861%**	**2212%**	**2558%**	**368%**	**166%**	**1266%**	**449%**